IMAGE BASED FRAMEWORK FOR CONDITION ASSESSMENT OF RCC BRIDGE GIRDERS

Submitted in partial fulfilment of the requirements
for the award of the degree of

DOCTOR OF PHILOSOPHY
in
CIVIL ENGINEERING

by

B. Murali Krishna

(Roll No: 716003)

Supervisor

Dr. T. P. Tezeswi

Assistant Professor

STRUCTURES DIVISION

DEPARTMENT OF CIVIL ENGINEERING

NATIONAL INSTITUTE OF TECHNOLOGY

WARANGAL- 506 004 (T.S.) INDIA

AUGUST 2020

NATIONAL INSTITUTE OF TECHNOLOGY

WARANGAL

CERTIFICATE

This is to certify that the thesis entitled "**Image Based Framework for Condition Assessment of RCC Bridge Girders"** being submitted by **Mr B. Murali Krishna** for the award of the degree of **Doctor of Philosophy** to the Faculty of Engineering and Technology of **National Institute of Technology, Warangal** is a record of bonafide research work carried out by him under my supervision and it has not been submitted elsewhere for award of any degree.

Dr. T. P. Tezeswi
Thesis Supervisor
Assistant Professor
Department of Civil Engineering
National Institute of Technology, Warangal
Warangal (T.S.) – INDIA

APPROVAL SHEET

This Thesis entitled "**Image Based Framework for Condition Assessment of RCC Bridge Girders**" by **Mr B. Murali Krishna** is approved for the degree of Doctor of Philosophy.

Examiners

_____

_____

_____

Supervisor

_____

Chairman

_____

Date: _____

DECLARATION

This is to certify that the work presented in the thesis entitled **"Image Based Framework for Condition Assessment of RCC Bridge Girders"** is a bonafide work done by me under the supervision of **Dr. T. P. Tezeswi** and was not submitted elsewhere for the award of any degree. I declare that this written submission represents my ideas in my own words and where other ideas or words have been included, I have adequately cited and referenced the original sources. I also declare that I have adhered to all principles of academic honesty and integrity and have not misrepresented or fabricated or falsified any idea / data / fact /source in my submission. I understand that any violation of the above will be a cause for disciplinary action by the Institute and can also evoke penal action from the sources which have thus not been properly cited or from whom proper permission has not been taken when needed.

_____

(**B. Murali Krishna**)

(Roll No: **716003**)

Date: _____

Dedicated To

My

Beloved Parents

Mr B. Satyanarayana & Mrs B. Suguna

&

Elder Brother

B. Prasanna Jaya Krishna

ACKNOWLEDGEMENTS

With great pleasure and proud privilege, I manifest my heartiest thankfulness to my research supervisor, **Dr. T. P. Tezeswi**, Department of Civil Engineering, for his invaluable suggestions, sagacious guidance, scholarly advice and comprehensive critical remarks in bringing out this research work with artistry.

I express my sincere gratefulness to **Prof. M. Chandrasekhar**, Head, Department of Civil Engineering and Chairman, Doctoral Scrutiny Committee for his enlightening guidance and immense help rendered in bringing out this work.

I am grateful and thankful to **Prof. P. Rathish Kumar**, Department of Civil Engineering, **Dr. K. Venkata Reddy**, Assistant Professor in the Department of Civil Engineering, **Dr. P. V. Suresh**, Assistant Professor in Department of Chemical Engineering members of Doctoral Scrutiny Committee, for their guidance and help during the investigation. I would sincerely like to thank **Dr. M. Raja Vishwanathan**, Department of Humanities & Social Sciences, National Institute of Technology, Warangal.

I am also thankful to **Prof. C. B. Kameswara Rao**, **Prof. T. D. Guneswara Rao**, **Prof. G. Rajesh Kumar**, **Sri M. Sudhakar**, **Dr. S. Venkateswara Rao**, **Dr. K. Gopi Krishna**, **Dr. M. V. N. Siva Kumar** and **Dr. Ravi Prasad**, the faculty members of Structures Division, NITW for the moral support given during the period of research work.

I thank my friends and fellow research scholars Dr. Hanuma Kasagani, Mr. Oggu Praveen, Dr. M Venu, Dr. T. Chaitanya Krishna, Mr. Koteswara Rao, Dr. Harsha Praneeth, Dr. N. Venkatesh, Ms. B. Raja Rajeswari, Dr. P. Madhuri, Mr. A. Pranay Kumar, Mr. M. Santosh, Mr. P. Chandra Sai, Mr. M. Sudhakar, Mr. Y. Lahir, Ch. Aravind Swamy and Mr. Y. Lakshmi Vinayak for their direct or indirect suggestions throughout the period of my research work.

I am thankful to Sri A. Laxman Mechanics in Structural Engineering Laboratories, Sri P. Rajendra Prasad, Sri Md. Hussain and Administrative staff for the help done during the research period.

Finally, I thank everyone, who contributed either directly or indirectly in the successful completion of this work.

- **B. Murali Krishna**

ABSTRACT

An image-based methodology for condition assessment of Reinforced Cement Concrete (RCC) road bridge components is presented. The study consists of experiments on RCC rectangular beams and scaled (1:12) T-beams, validation of numerical models for T-beams and training of corresponding Artificial Neural Networks (ANN). In experimental work, Digital Image Correlation (DIC) is used as a virtual sensor for data extraction. Image processing was done using an open-source Ncorr v1.2.2 algorithm for the results obtained using a random speckle pattern and Quick Response (QR) code-based speckle pattern. A novel QR code-based speckle pattern is evaluated for 2D (two dimensional) DIC measurements and shows an improved correlation with conventional measurements when compared to the random speckle pattern. The ultimate Moment (M)-Curvature (κ) values computed from the QR code-based speckled pattern are found to be in good agreement with conventional measurements and Finite Element Method (FEM) results. QR code encrypts the structural information which enables integration with Building Information Modelling (BIM).

Rectangular RCC beams of size 1800 mm x 150 mm x 200 mm and scaled (1:12) RCC T-beams are tested under four-point flexural loading. Using the law of similitude, the small-scale T-beams were designed, cast and tested under four-point bending so that the nonlinear constitutive behaviour can be correctly scaled up. A model concrete has been developed consisting of cement, water and fine aggregates based on geometrically scaling down the coarse aggregate. Load-deflection curves of RCC beams are plotted for the results obtained using both contact and non-contact (DIC) sensors, and further, Moment (M)-Curvature (κ) relationship of RCC beams is developed. The experimental stress-strain curves obtained from compression test on prism specimens at 28 days are used as input data for material model parameters for finite element analysis. Validation of FEM results with the scaled (1:12) experimental results enables further derivation of Moment (M)-Curvature (κ) backbone curve for full-scale bridge girders, which further enables quantification of damage and residual moment capacity of full-scale bridges considered from Ministry of Road Transport and Highways (MoRTH). The correlation between the experimental, numerical and ANN was found to be very satisfactory.

After validation of data obtained using QR code-based speckle pattern for different bridge girders ANNs, input data is obtained from experiments and validated simulations (Phase-I & Phase-II). To assess the condition of structural components, a Local Damage Index (LDI) is developed, which helps in the quantification of the damage.

CONTENTS

LIST OF TABLES

LIST OF FIGURES

ABBREVIATIONS

Symbols

%	Percentage
*	Multiplication
R^2	Correlation Coefficient

Weight and Measures

µm	Micrometer (micron)
b_f	Breadth of Flange
b_w	Breadth of Web
d	Depth of Web
d_f	Depth of Flange
E_c	Young's Modulus, N/mm²
f_u	Ultimate Stress, N/mm²
g/L	Gram per Liter
kN	Kilo Newton
kg	Kilogram
kg/m^3	Kilogram per cubic meter
L	Liter
M	Moment
m	Meter
N	Newton
w/c	Water cement ratio
ε	Strain
ε_u	Strain corresponding to ultimate stress
κ	Curvature
l	Length

Text Abbreviations

2D	Two Dimensional
ANN	Artificial Neural Networks
BIM	Building Information Module

CDP	Concrete Damage Plasticity
CRN	Condition Rating Number
DI	Damage Index
DIC	Digital Image Correlation
DSLR	Digital Single-Lens Reflex Camera
FEA	Finite Element Analysis
GUI	Graphical User Interface
LVDTs	Linear Variable Differential Transformers
MAE	Mean Absolute Error
MoRTH	Ministry of Road Transport and Highways
OPC	Ordinary Portland Cement
OR	Over Reinforced
QR	Quick Response
RCC	Reinforced Cement Concrete
RMSE	Root Mean Square Error
ROI	Region of Interest
SHM	Structural Health Monitoring
UPV	Ultra Pulse Velocity
UR	Under Reinforced
UTM	Universal Testing Machine

CHAPTER 1

Introduction

1.0 General

As our civil infrastructure ages, the challenge of keeping it operational grows. Hence the need for improved condition assessment on which to make cost-effective maintenance decisions. Indian Railways has more than 0.13 million bridges, out of which 800 are important, 11,000 are major, and 0.12 million are minor bridges. Also, in India, there are 5174 large dams (with a maximum height of more than 15m) with more than half of these aged at least 30 years. The cost of monitoring these structures is astronomical.

1.1 Motivation

Currently, the most common methods of Structural Health Monitoring (SHM) in India are visual inspection and sounding. However, this is subjective and dependent on the skill level of the inspector. Methods utilizing the material properties of a structure, such as ultrasonic wave attenuation, electrical conductivity, as well as dynamic response based methods often have practical problems with cabling and difficulty in establishing reliable communication for data transmission and control, in field conditions. Gathering this condition information requires SHM and inspection on a grand scale, which must be accurate, inexpensive and easy to interpret. Moreover, the sheer number of critical facilities necessitates selective monitoring using sensors to reduce the cost to the exchequer. For large civil engineering structures, such as bridges, buildings and power generation infrastructure, manual inspection techniques are often used. This leads to inspections that can be influenced by subjectivity due to environmental and physical conditions.

1.2 Overview of Digital Image Correlation (DIC)

DIC is a full-field non-contact optical method for measuring displacements based on the correlation of the digital images taken during test execution. DIC can be used for monitoring by imaging a bridge periodically and computing strains and displacements from images recorded at different operating conditions. This data can track the deterioration history of a defect and inform its cause and suitable intervention. Structural health monitoring of different bridge components (local analysis) and an entire bridge (global analysis) can be studied using DIC.

A simple, cost-effective and practical imaging-based technique is adopted in this study for monitoring damage in bridges. The basic premise of this method is based on correlating the digital images associated with an object before and after deformation and, additionally identifying the displacement and strain field for an object, depending on the position of the image (Sutton et al. 2009). DIC enables determination of the surface deformation of an object (Mudassar and Butt 2016). Portable DIC and non-interferometric methods are widely used in the field of structural health monitoring (Antos et al. 2017). The non-interferometric method determines the surface distortion by evaluating the grey intensity variations of the object surface before as well as after deformation, and usually have less rigorous expectations under experimental conditions (Pan Bing et al. 2009). DIC technique has been extensively accepted and frequently used as an effective and versatile tool for surface distortion measurement as part of experimental solid mechanics.

A portable DIC and photogrammetric data acquisition system using only digital cameras for SHM that is simple and robust enough to be used in the field without specialized training is proposed. The proposed device and procedure will enable the two dimensional (2D) DIC as well as out of plane measurements using photogrammetry, without sacrificing accuracy and at a lower cost. This system will enable global as well as localized measurements of structural deformation and provide data for periodic maintenance. The flowchart showing the image processing technique in Figure 1.1 explains the overall procedure adopted for DIC technique.

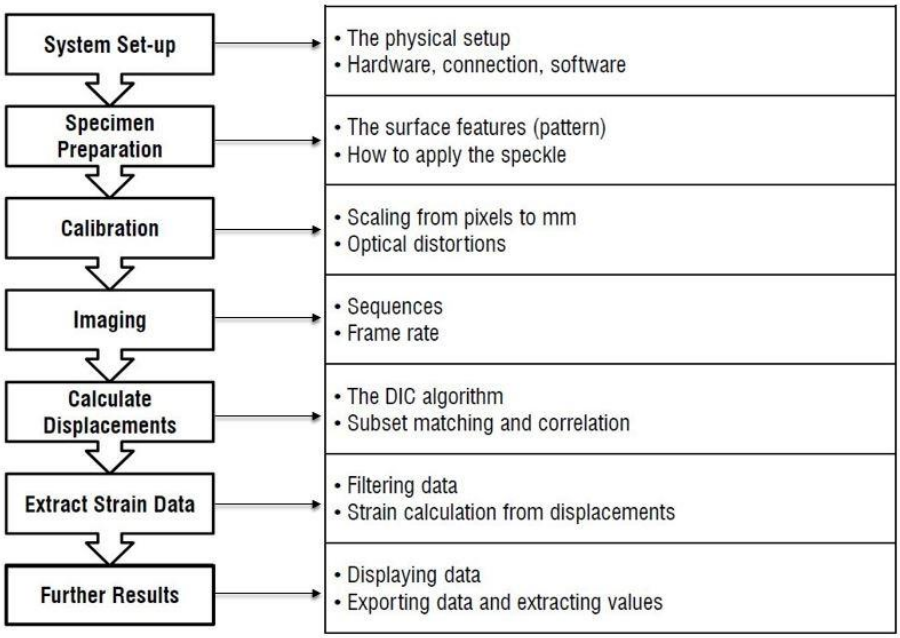

Figure 1.1 Flowchart showing the typical image processing procedure for DIC

1.3 Reinforced Cement Concrete (RCC) Scaled (1:12) T-Beams

Most of the bridges in India are constructed of RCC of which T-girder bridges are most common wherein the flange portion (slab) carries the compressive loads and the reinforcing bars placed at the bottom of the web (stem portion) bear tension. The T-beam girder bridge is most commonly adopted in a span range of 10 to 25 m.

1.3.1 Law of similitude analysis for scaled concrete

The requirement of developing small-scale reinforced concrete models came into existence with the increased use of reinforced concrete for various complex structures (White 1964). Physical modelling techniques for small-scale reinforced concrete T-beam subjected to a four-point bending test presented. The field models are scaled down to reduced models which replicate full scale reinforced concrete structure with model concrete and reinforcement is the same as that of the full-scale model. Portland cement scale model, is adopted in this study because this model has the advantage of being made from the same material as a full-scale specimen.

The laws of similitude (Harris and Sabnis 1999) place strict requirements on the relationship between full scale and reduced scale model, which need to remain constant in order to ensure complete similitude requirements. If concrete and steel are two materials used in reinforced concrete, then these two materials must maintain the scale ratios with their respective counterpart models. It is essential to find materials which will maintain the same stress-strain behaviour as full-scale models. The ideal condition would be to use the same materials in the model as in full-scale specimen (Harris et al. 1966). The difficulty in using this type of model lies in scaling the aggregate according to the law of similitude. If the standard aggregate size is reduced by 1:12, the maximum size of aggregate is that of sand, and the mixture compares to that of mortar (El-Ariss 2006). The idea is to develop a model which is similar in all the aspects right from reinforcing bar to deformations. The size of the model must be large enough to measure the deformations (Wolowicz et al. 1979) and assertion properties like compressive strength, stress-strain relationship and tensile strength (Simitses and Rezaeepazhand, 1992).

In this study, small-scale T-beams are designed using the law of similitude and tested. Maintaining the law of similitude requirements in materials proposed by Harris and Sabnis is a crucial aspect of these type of models. In the current study, standard RCC Ministry of Road Transport and Highways (MoRTH) bridge dimensions are scaled-down. Image processing is done using an open-source Ncorr v1.2.2, a MATLAB R2018a based algorithm to obtain results

using random speckle pattern and QR code-based speckle pattern which is imposed on the beams.

1.4 Damage Index (DI) Using Artificial Neural Networks (ANN)

ANNs have been successfully implemented in damage identification of structural systems by several researchers. Hasançebi et al. (2013) presented an ANN based approach for damage detection in RCC T-beam bridges using Finite Element Analysis (FEA) based model updating method. Cao Vui V. et al. (2014) developed a methodology to find the residual moment capacity of the structure using the DI method. Jadid and Fairbairn (1996) proposed a model to predict the Moment (M)-Curvature (κ) relationship of a beam-column joint. Jeyasehar and Sumangala (2006) presented the damage assessment of prestressed concrete beams using the feed-forward back-propagation algorithm. Wu X Ghaboussi and Garrett (1992) proposed the self-organisation and learning capabilities of neural networks in both damaged and undamaged structural assessment.

1.5 Thesis Organization

The complete thesis is organized as follows:

i. **Chapter 1,** of the thesis motivates the necessity of this study and discusses: a) Advantages and disadvantages of DIC; b) Testing of scaled RCC T-beams using the law of similitude analysis; c) Development of a Damage Index (DI) suitable for flexure dominated bridge girders using ANN.

ii. **Chapter 2,** reviews the literature on DIC speckle patterns, Scaled RCC T-beams, and existing DI developed using ANN. The gaps in the literature are summarized.

iii. **Chapter 3,** details the scope and objectives of the investigation.

iv. **Chapter 4,** establishes the QR code as a speckle pattern suitable for DIC based measurements of RCC beams and presents the validation of corresponding FEA models.

v. **Chapter 5,** describes the experimental investigation of 1: 12 scaled RCC T-beams using DIC and comparison with experimental, numerical and analytical results.

vi. **Chapter 6,** develops the DI based condition assessment methodology for RCC beam girders using ANN.

vii. **Chapter 7,** presents the conclusions and the scope for further study.

The literature review of the present study is presented in **Chapter 2**.

CHAPTER 2

Review of Literature

2.0 General

In the previous chapters, the need for optimal speckle pattern in the field of Digital Image Correlation (DIC) was brought out. The need for similitude analysis regarding scaled Reinforced Cement Concrete (RCC) T-beam studies was discussed, and the necessity of deep learning techniques based on Artificial Neural Networks (ANN) were also addressed. In the present chapter, the details of literature available on the above are discussed. The extensive research that is being conducted in the field of Structural Health Monitoring (SHM) is delineated. In the present chapter studies that were reported earlier with regard to SHM, are reviewed. This section presents a state of art report on the development of SHM using DIC. A brief report of the literature study is presented below.

2.1 Review of Literature on Digital Image Correlation (DIC)

Lucas Bruce D and Takeo Kanade (1981), presented a new image registration technique using Newton-Raphson iteration method between consecutive images to find a good match among these images. This technique is fast because it inspects far fewer possible matches' among the images. This registration technique can handle scaling, shearing and rotations of images. These type of techniques are used mainly in image processing fields. The strategy adopted in this algorithm is a combined coarse-fine method which is basically for low-resolution matches. For better convergence of images in several iterations, image smoothening is adopted in this algorithm. The performance and implementation of the algorithm is also discussed in this study.

Sutton M.A et al. (1983), determined an improved DIC method for full-field in-plane deformations of an object. The surface deformations are calculated based on selecting subsets from the deformed and undeformed images. After calculation of deformations, the corresponding strains were obtained using green Lagrangian function. In this algorithm, after several iterations, the iteration routine terminates once the acceptable correlation coefficient is reached. Several laboratory experiments were conducted using correlation method to check the suitability of employing the algorithm in DIC field. Using bilinear interpolation procedure, the computed displacements were approximately 0.10 pixels. Comparison of experimental with theoretical results shows good agreement with the algorithm.

Zyung et al. (1988), conducted experiments on poly methyl methacrylate (PMMA), commonly known as Plexiglas samples, for which the strains were recorded at various location using DIC. The experiment was conducted using two modes of loading. Mode-I was symmetric loading and Mode-II was unsymmetrical loading. The cracks were observed at mid-span, and strain measurements were calculated at a distance from the tip of the crack. The tip of the crack was taken as origin, and radial distances were taken in the form of (r, θ). DIC was developed in the 1980s employing pixels for displacement and strain measurements.

Lu and cary (2000), incorporated a process for refining DIC method by applying a 2^{nd} order Taylor series approximation of the displacement field. It was observed that twelve parameters consisting of displacements, 1^{st} and 2^{nd} order displacement gradients represent a much wider range of deformation. A 13^{th} parameter introduced in the form of grey-scale value offset of the bicubic spline interpolation (determines grayscale values at any location in the grey-scale image fields) for the deformed image allows us to make assumption that the grey-scale value "h" in the deformed image is nearly the same as grey-scale value "g" in the reference image. The above assumption was used in the approximation of Hessian matrix, which is used for the calculation of displacement parameters. In the case of 2^{nd} order deformation test, the results showed that by measuring and accounting for higher-order gradients, displacements and 1^{st} order gradients (used in the calculation of strains) could be measured more accurately.

Hung et al. (2003), proposed a Fast and Simple (FAS) algorithm based on the DIC for the measurement of surface deformation of planar surfaces. Different specimens were investigated to check the feasibility of this algorithm. The algorithm uses fine search on the pixel level within the fixed region, and the position of the local minimum sub-pixel level is then obtained based on the fitting area to the range of discrete pixels surrounding the solution on the pixel level. An aluminium plate was subjected to uniaxial tension test. The strain results from strain gauges were compared, using Newton-Raphson and FAS methods. Similarly, a circular disk was subjected to a diametrical compression test, and the various strain results obtained from the test were compared. In the case of uniaxial tension test, there is good agreement with strain gauge results. On the contrary, limited accuracy was achieved in the latter case. Also, tests were conducted adopting various speckle sizes, and the optimal speckle size (2-10 pixels) was found out.

Tong (2005), presented a study on the robustness, reliability, computational cost of commonly used four image correlation criteria by comparing strain mapping results of three sets of

digitally modified images (using paint shop pro, Eden prairie, etc.) with varying brightness, contrast, uneven local lighting and blurring. Only SSD correlation coefficients were evaluated as C_C coefficients can be related to SSD correlation coefficients. It was observed that the fourth correlation criterion didn't fail at any of the variable lighting and exposure conditions but took larger computational time for processing when compared with other three. The reliability and accuracy of strain mapping results were assessed at both global level and local level (average and standard deviation of local strains). The test results obtained using fourth correlation criterion were more robust. Point-to-point difference between test mapping results and reference ones for all three in-plane strain components (e_{xx}, e_{xy}, e_{yy}) was made, and it was found that second correlation criterion was nearly as reliable as the second correlation criterion (though it fails at certain modified conditions) whereas first and third weren't very much reliable (first correlation criterion being the least reliable).

Kozicki and Tejchman (2007), conducted experiments for strain localization of concrete with the help of DIC. They measured surface displacements using digital images recorded at consecutive intervals of time while conducting experiments. They carried-out model tests with notched concrete specimens under three-point bending. Three different beam sizes and two different concrete mixes were used in the study. They determined load-deflection curves and evolution of fracture process during experiments. They also compared measured size effect in strength with the deterministic size effect law proposed by Bazant (1984) and experimental results reported by Bell et al. (2003). It was observed that strong size effect occurs in concrete beams subject to bending. The beam ductility and nominal strength increase with decreasing specimen size. It was also discovered that DIC is a very simple and effective method for determination of strains with large accuracy and without physical contact and the width of the fracture process zone increases during deformation and is equal to about 6-7 mm before the failure. The zone can be almost straight or strongly curved. He also informed that the current algorithm could be improved by applying Fast Fourier Transformation to accelerate the computation of strains and displacements.

Yaofeng and Pang (2007), investigated the effect of subset size, which is related to image pattern quality and subset displacement functions, as well as on the accuracy of deformation estimations using DIC. A parameter, called subset entropy (average of absolute intensity divergences at any point in the subset from the neighbouring points normalised by the pixel depth of the image) was proposed to quantify the subset image quality for image correlation and therefore the interaction between subset entropy, and subset size was studied. DIC was

performed on the images with scattered subset entropies under rigid body translation test, and a plot of the standard deviation of displacement vs mean subset entropy was obtained. It was observed that the standard deviation of translation decreases when the subset entropy increases. Images with uniform subset entropy were studied under rigid body translation, and it was observed that the standard deviation of displacement decreases with respect to subset size. Then, the specimen was subjected to tensile test, and it was observed that with uniform subset entropy a significant error of more than 50% was observed in the mean strain compared to mean translation when a smaller subset was used. It was assumed that a larger subset has more mutual pixels involved in the correlation and can also reduce the influence of imaging noise and pixel intensity quantisation during image acquisition. In the case of non-homogenous deformation field, the systematic errors increase faster in displacement measurements of higher strain gradients due to mismatch of displacement functions and true deformation and equilibrium between the influence of systematic and random errors was observed at a smaller subset.

Moon and Kim. (2011), developed a technique of classifying the image, whether it is cracked or uncracked beam. The test beams were cast and cured at room temperature. Then the testing of the beams was done in universal testing machine under laboratory conditions. As the load increases the beams starts deflecting. Photographs were taken, and the photos are in the form of RGB Images. To ensure better accuracy the images taken must be processed, i.e. they must be converted from RGB image to binary images. This process is called image processing. Once image processing is done, the images need to be trained in neural networks. After a sufficient amount of training, the neural network finally classifies the image into the cracked and un-cracked images.

Vassoler et al. (2010), investigated the accuracy of the displacement measurement for different sets of DIC algorithm using numerically simulated images for zero, 1^{st} and 2^{nd} order displacement fields considering only algorithm error. Images containing 256 x 256 pixels were numerically generated for three different deformations: rigid translation, 1^{st} order displacement field and 2^{nd} order displacement field. In the case of rigid translation, the maximum absolute error decreases with increase in speckle size (maximum up to 5 pixels in all the cases) for a given subset size and the mean error showed a sinusoidal shape with no dependency on subset size and a period of 1 pixel. In the case of 1^{st} order displacement (analysed up to 10% stretching), maximum absolute error varied similarly as that of rigid translation for a given

subset size and the mean error varied randomly. In both the above cases, the maximum absolute error decreases with increase in subset size. In the last case, the observations suggest that absolute error may vary exponentially with respect to strains due to inappropriate relationship between the pattern and subset sizes. It was observed that for 2^{nd} order displacements, under lower strains, larger subsets performed better and under higher strains while smaller subsets showed less absolute error. It was worth noting that though the evidence didn't provide information about ideal granule or subset size, they lay emphasis on the choice of these parameters for high-order displacement field.

Stoilov et al. (2012), studied random patterns that are used for DIC. They generated three random patterns with different textures for the work. He generated them numerically using a computer. They carried out several studies on the shape of autocorrelation functions and behaviour of cross-correlation functions under several degrees of tensile deformation. They introduced a criterion for evolution of random pattern quality. The characteristics of the proposed synthetic random pattern are obtained by applying a very sophisticated technique. A computer-generated random pattern is applied to the area of interest. Three groups of specimens with three artificial patterns are printed, and they are subjected to tensile test. The conventional tensile test shows the quality of patterns is good enough despite lower signal to noise ratio of respective patterns. From his observation, he added that the proposed synthetic patterns are best until real deformation reaches 20%.

Salmanpour et al. (2013), reported the measurement procedure and the applicability of DIC for measuring strains and full-field displacements when testing large masonry walls at full-scale. Eleven static-cyclic tests were performed in two phases (preliminary phase and main phase) on different wall types. Setup was built on thick concrete foundations, and the shear forces were applied through a steel beam connected to the walls by means of mortar. Two different cameras (Nikon D3 camera and Nikon D800E) were used during testing and processing was done using Vic2D commercial code. The confidence interval was calculated using covariance matrix of the correlation equation to estimate the accuracy of measurements which confirms expected displacement accuracy of 0.01 pixels. The test results proved that 2D DIC might be considered effective for displacement and strain measurements.

Shih and Sung (2013), proposed a paper based on the feasibility of using DIC to observe cracks developed in reinforced concrete beams. Depending on the relative motion between the blocks on either side of the cracking line, crack width and dislocation length were calculated

theoretically. To study the feasibility of DIC for the purpose, two different specimens were subjected to a three-point bending test. From the displacement diagrams for 1st specimen, the occurrence of minor cracking on the specimen surface was observed using digital speckle images. Further, the angular displacement diagram showed the process of cracking extension and the angular degree revealed that cracking had infiltrated the test specimen. In addition to this, the strain concentration shown on Von Mises strain diagram was more obvious in slightly larger stages of loading, and the strain diagram revealed that the specimen rupture was shear based. From the displacement diagrams of 2nd specimen, it was observed that the rupture started from pre-laid defective notch without 45^o displacement, which concludes that the mode of rupture was controlled by open tension fissure. Further, from Von Mises diagram, strain concentration was observed in the middle of the beam bottom with several cracks seen in the specimen but not obvious at 45^o cracking, indicating the rupture to be flexural in nature. The results from the displacement and strain diagrams agreed with the digital images taken after the cracking of the specimens, which implies that identifying early crack development is possible through DIC.

Pan (2014), proposed a paper on the convergence characteristics of IC-GN algorithm in terms of convergence speed and convergence radius. The influence of initial guess of deformation, subset size and interpolation scheme on the convergence criteria were also carefully examined using experimental images. Two sets of images, one from three-point bending test of rubber specimen and the other from the tensile test on aluminium sample were analysed under four different convergence criteria (in the ascending order of stringency). It was observed that quicker convergence with fewer iterations was obtained with a larger subset size. It was also observed that with the increase in offset distance, the number of iterations increased and the success rate of convergence decreased. It was worth noting that an efficient initial guess transfer scheme ensured rapid convergence of IC-GN algorithm at least iteration. The relative differences between displacements measured using 4th criterion and the other three criteria were depicted graphically along with maximum and standard deviation in each of the cases. Because the differences between displacements measured using 2nd and 4th criterion are small enough to be neglected, the 2nd criterion is highly recommended. 1st criterion may also be used with slightly lower accuracy compensated using proper smoothing methods.

Liang et al. (2015), investigated on strain measurements of damaged areas using DIC. They found that DIC measurements for damaged areas differ from conventional DIC. In conventional DIC, calculation path is generally from left to right or top to bottom. Separate

methods were given for path calculation for damaged areas. From the method of path calculation (higher correlation to lower correlation), calculation errors are decreased by 35% compared to conventional DIC. To reduce calculation time, a threshold is set so that correlation stops automatically when the correlation result is lower than it. The efficiency of the proposed technique is compared with simulated images. He came to a conclusion based on the results that his method is useful for many applications such as crack opening, drilling measurement etc.

Ab Ghani et al. (2016), studied DIC technique for calculating the strains and displacement. The test was conducted to measure the tensile strength of GFRP. The surface was first prepared, and speckle pattern was drawn on using paints. A high-resolution camera was used to take photographs of the specimen. Then the images were converted from RGB images to grayscale. Ncorr application in MATLAB was used to perform DIC. Firstly, the unloaded image was kept as reference image, and then the current images were loaded in the toolbox. Then the process of DIC was carried out using Ncorr, and finally, the output of the result was displacements and strains. The contour of the displacement and strain profile is also shown as output in Ncorr. The values of the output were compared with the actual values of the experiment, and the necessary graphs are plotted.

Blaysat et al. (2016), proposed formulae for the displacement measurement while including and excluding the influence of sub-pixel interpolation. A noiseless DIC tangent operator was defined to minimise the noise propagation from images to displacement maps. When the two predictive formulas were validated with noisy simulated data, it was found that one of them provides reasonable global assessment for the displacement resolution, since on average there was a 16% deviation from the experimental resolution and, the other gave on average a predicted displacement resolution closer to the experimental one since the divergence was only 4%. When these formulae were validated with experimental data, it was found that the ratio obtained between predicted and empirical resolutions was much higher than one. Generalised Anscombe Transform (GAT) was applied to transform a homoscedastic Gaussian noise into a heteroscedastic Poisson-Gaussian noise, and the scatter was much lower, but it was observed that resolution distribution still depends on the lighting intensity. The reason was the micro-movements between camera and specimen were resolved by considering a pre-processing procedure called non-random signal reduction (applied only on regular markings). Thus, the formulae were verified satisfactorily.

Chen et al. (2018), presented a study concerned with the optimisation of Digital Speckle Pattern (DSP) for DIC by considering both accuracy and efficiency. The RMS error of IC-GN algorithm, average no. of iterations, influence of subset sizes and the noise level of images (noiseless, 1% noise level, 3% noise level, 5% noise level) were basic parameters in quality assessment formulations. In the design of 1-R and Multi-R speckle patterns, a pseudo-random function was defined so that a random DSP can be perturbed with a random factor 'rand' from the regular speckle array. The imaging of Gaussian speckle patterns was more realistic than binary images, but it's challenging to obtain Gaussian patterns; therefore, the recorded DSPs were used as primary DSPs for optimisation. The four-step experimental procedure for optimisation consisted of shifting the recorded DSPs with a displacement step of 0.05 pixels, adding 1%, 3% and 5% noise using MATLAB, calculating the required data and giving statistical results in box plots to display the iteration distributions and RMSE of corresponding DSP. The RMSE of the displacements can be expected to decrease as the value of rand decreases, but the variation in number of iterative cycles isn't obvious as the value of rand varies. With the noise-level fixed, it was observed that large subsets have fewer iterations and higher precision. It was concluded that on comparing multi-R DSPs with the smallest radius and 1-R with a radius of two, 1-R was superior in both precision and efficiency. The results obtained from downloaded and experimental DSPs indicated that experimental speckle patterns experience more significant fluctuations in both displacement error and number of iterative cycles.

2.1.1 Review of literature on experimental RCC beam testing

Srikanth et al. (2007), developed a relationship between Moment (M)-Curvature (κ) using experimentation and validated the result using six confinement models. The six confinement models of M-κ were compared with experimental data, and observations are made. Some assumptions were made such as the stress-strain relationship was assumed to be stress block of the beam, tensile strength of concrete was neglected, while strain profile across the section remains linear until failure, etc. For obtaining the relationship between discrete values of concrete strains. The concrete strain was assumed in the range of 0.0001 to 0.01, and the neutral axis was initially assumed to be 0.5 times effective depth. The experiment beams contained six beams, three are over reinforced, and other three are under reinforced. The predicted confined models were then compared with experimental data, both numerically and graphically. For numerical comparison, three points were selected, i.e. ultimate moment and corresponding

curvature (M_u, κ_u), moment corresponding to 85% of the ultimate moment ($0.85M_u$ and $0.85\kappa_u$) in ascending portion and 85% of the ultimate moment ($0.85M_u$ and $0.85\kappa_u$) in descending portion.

Swamy Naga Ratna Giri et al. (2017), conducted several experiments in the laboratory on RCC beams under flexural testing and the corresponding Moment (M)-Curvature (κ) relationship was drawn. A comparative study was proposed for both wet-cured and self-cured in terms of Moment (M)-Curvature (κ) relationship. Analytical stress-strain model was proposed for different curing conditions using Saenz's model, and after that, using stress block parameters, the corresponding analytical Moment (M)-Curvature (κ) was derived. The non-dimensional stress-strain relationship was proposed in this study. A significant difference in strength was observed among the beams and the ultimate moment of self-cured beams were in good agreement with wet-cured beams. A high moment carrying capacity was observed in conventional water-cured beams when compared with self-cured beams. The Moment (M)-Curvature (κ) relationship for both the ascending portion and the descending portion of the stress-strain curve are proposed.

2.1.2 Review of literature on numerical modelling of RCC beams

Jankowiak and Lodygowski (2005), presented a methodology for material parameter identification using Concrete Damage Plasticity (CDP) model in ABAQUS software. The constitutive parameters identified from the laboratory experiments are presented in this study. To test the constitutive model of concrete, two standard applications are shown here. The softening and hardening scalar damage variables for both tension and compression are presented. Mesh sensitivity analysis is done for accurate prediction of models. A single-edge notched concrete beam is used for both three-point and four-point bending tests in the laboratory under static loading condition. A comparative study is proposed based on crack patterns for both experimental and numerical investigations. The realistic behaviour of concrete from the experimental investigation is compared with numerical modelling.

George et al. (2017), carried out an investigation regarding non-linear behaviour of concrete using CDP model in ABAQUS software. A modified Drucker-Prager criterion was adopted for tensile and compression plasticity of concrete to predict the inelastic behaviour of concrete in association with damaged elasticity. In this model, the concrete tensile cracking and concrete compression crushing were considered in this study. Based on experimental results, the load-

deflection curves obtained from the three-point bending test are given as input parameters in ABAQUS software. In order to predict accurate behaviour, a mesh sensitivity analysis is done. Different elements are used in this study to predict the variations in terms of accuracy. CPS3 a two-node triangular element and CPS4R a four-node quadrilateral element is used in this investigation. By increasing the span to depth ratio, the load carrying capacity of the beam decreased.

2.2 Review of Literature on Scaled RCC T-Beams Using Model Concrete

Deniaud et al. (2003), studied the effect of shear strengthening of Reinforced Concrete T-beams with Fiber Reinforced Polymer (FRP) Sheets. A total of four laboratory concrete T-beams were cast, and eight tests were conducted on those specimens. A four-point bending test was performed on T-beam specimens. The maximum shear capacity increased from 15.4% to 42.2% from the beams. The shear capacity increased due to the amount of internal shear reinforcement and corresponding FRP technique.

El-Ariss (2006), reports the effects of reducing the coarse aggregate quantity in mix proportions on the compressive strength of concrete. For desert regions, the availability of coarse aggregate was very low in order to overcome this issue, the amount of coarse aggregate was reduced, and the empirical formula was framed for optimizing a concrete mix design for desert regions. Extensive laboratory experiments were performed, and about 1350 samples were tested with 30 different concrete mixes. Influence of coarse and fine aggregates, curing methods, and water/cement ratio on the compressive strength of concrete was analysed. Two separate formulas were developed for the quantity of coarse and fine aggregates as a function of compressive strength.

Knappett et al. (2010), developed a model concrete which consists of water, fine sand as a geometrical scaled coarse aggregate, gypsum-based plaster can produce a model concrete having a range of compressive strength 25-80 MPa at very high scale factors. Reinforcement was modelled using wire mesh and roughened steel wire in order to satisfy similitude requirements. A series of laboratory experiments were conducted regarding four-point, and three-point bending tests on model beams of size 0.5*0.5 m^2 section prototype beam of using a scale factor 1:40. However, using the law of similitude analysis, results show that this technique allows for strength, ductility and stiffness of structural element under bending tests, and failure modes are accurately reproduced.

Syed et al. (2012), conducted structural testing in the laboratory, which requires scaled models. In general, bridges have massive piers and heavy loads; so for these models, scale factors need to be applied by satisfying law of similitude requirements. A series of laboratory experiments were conducted on scaled bridge columns in which quasi-static cyclic testing was done with free vibration tests. A detailed explanation of several requirements of similitude analysis regarding dynamic and static tests are different from each other. Here the scale factor for bridge columns is considered as 1:4, which would be a reasonable and manageable test specimen for laboratory conditions.

Petry and Beyer (2012), presented an overview of the difficulties related to scaling. Using 1:2 scale factor, a modern four-story building with unreinforced masonry brick wall is tested using a shake table to investigate the interaction between structural elements. Generally, large dimension structures are difficult for testing, so scaling factors are applied uniformly based on the law of similitude requirements. A comparison of mechanical properties are made between full-scale and reduced-scale masonry models where using scaled model testing's real size structures can be assessed correctly. The results obtained from the half-scale masonry structure and tested under proposed shake table test give desired results.

Balawi et al. (2015), investigated scaling laws based on the law of similitude theory for plates and beams which are loaded statically and on low-velocity impact. An important aspect of scale-down models is about understating the relation between prototype and scaled model behaviour. Dimensional analysis was used to find similitude requirements between the scaled models. In most of the cases, it is not possible to satisfy the similarity between scaled models and corresponding prototype models due to environmental conditions, shape, size, material properties and boundary conditions. Theoretical prediction of a prototype was compared with the theoretical prediction of the scaled model. Numerical and experimental results were compared among the scaled models. Experimental and numerical results are in good agreement with similitude theory.

WU and XIONG (2017), studied about thirty six-storey high-rise structure with a height of 149 m. The main objective was to strengthen the hybrid structure as well as to evaluate the earthquake-resistant behaviour. A scaled model of the steel-concrete hybrid structure with a scale factor of 1/20 was tested on a shaking table. Based on the testing, the dynamic properties and seismic behaviour were analysed. The prototype structural component had a micro concrete

strength grade of M6, M8, M10 and M12. For different seismic actions, the model structure mainly remains bending deformation according to the damage in the model structure.

Altunisik et al. (2018), investigated similitude requirements between prototype and scaled models for load-bearing systems. In this study, they considered different structural elements with different scale factors. The structural elements were frame, column, simple beam and cantilever beam with scale factors of 1/5, 1/2, and 1/10 scale factors. Using similarity relationship, one can model as scaling up and scaling down depending on the situation and available facilities. This similitude analysis can be adopted using dimensional analysis or by field equations of the system. For different load-bearing systems, the scale factors are constant depending on the scale type, and the corresponding results were examined. The experimental results were compared with numerical results obtained using SAP2000 software.

2.3 Review of Literature on Damage Indices

Stubbs and Kim (1996), developed a method of damage indices to quantify the damage done to the structure. They assumed a beam can be considered as Euler Bernoulli beam. They started a research project on beams, and then they calculated damage indices as a function of strain energy. The beam is divided into N number of nodes, and the strain energy is calculated on each node. The strain energy was evaluated for both damaged and undamaged structure. The strain energy at a particular node is divided by the strain energy of the total beam and then calculated for damaged beams. The ratio of flexural rigidity of the undamaged structure to damaged structure will give the Damage Index (DI) at a particular node. Hence, DI was calculated at each node, and then with the help of statistical analysis, normalized DI was calculated. A threshold value of the DI was set, and if the obtained value of the damage must be lower than the threshold value to ensure safety of the structure.

Fitzner and Henrichs (2001), analysed damage diagnosis, which is required for comprehensive characterization, interpretation and rating of the stone damage. They developed a comprehensive monument mapping method as a non-destructive procedure for in-situ studies on weathering damages at natural stones. This procedure allows the phenomenological response of the natural stones to weathering processes. New tools damage categories and damage indices have been introduced for consequent quantification and rating of stone damage as a significant scientific contribution to damage diagnosis and monument preservation. There are three steps in the control of damage due to weathering. These are Anamnesis, which deals with monument identification, location, art-historical portrayal, case history, utilization, and

environment. Diagnosis which deals with building materials, material properties, state of deterioration, factors and processes of deterioration, need/ urgency of preservation measures and therapeutically steps which deal with conception, calculation, test-application, execution and control certification of preservation measures long-term observation and maintenance of monuments. Out of these three steps, diagnosis is an essential and laborious procedure. It involves in situ investigations which deal with measurements, monument mapping, sampling, laboratory analysis, which consist of analysis of physical, chemical and mechanical material properties and weathering simulations, which consist of outdoor exposure chamber tests. They have also developed scales of deterioration, which consists of non-visible deterioration and visible deterioration. After the detail, description of cause and state of deterioration of damage is quantified in terms of DI.

Sung et al. (2012), discussed SHM of large span bridges, especially cable-stayed bridges. They developed Finite Element Method (FEM) models, comparing different damage indices based on the frequency of load and designing a new DI denoted by the letter "W", utilizing exited damage indices. The paper consists of the determination of DI of Wenhui Cable-Stayed Bridge and finding out the various damage indices and comparing it. The noise was also added to the data to check for variation, and which gives more reliable result. We know that noises are inevitable in measuring; the correction for noise was also taken care of by using the correction formula proposed by them. In the analysis of Wenhui Bridge, they have come out with eight cases out of which first four are the single damaged case, and other four are multiple damage case. The analysis has been done for all eight cases, and they came with the W damage index for all damage cases.

Cao V. V. et al. (2014), reviewed the available concepts of DI in order to propose a new concept of DI, which is based on residual deformations. In general, DI are classified into two categories. The first category is about non-cumulative DI, which does not include the effect of cyclic loading. The second category is about cumulative DI, which produces a rational indication of the extent of damage in case of earthquakes. Generally, DI varies from 0 to 1, where 0 indicates no damage and 1 indicates a collapsed state of damage. A new DI is proposed based on energy for both cyclic and static loading conditions and compared with established DI proposed by several researchers. Most of the researchers widely use DI proposed by Park and Ang (1985). Damage classification proposed in this current investigation is as follows;

Table 2.1: Proposed damage indices for different states

Damage States	Range of Proposed Damage Index (DI)
Minor	0.0-0.05
Light	0.05-0.25
Moderate (Repairable)	0.25-0.50
Severe (Irreparable)	0.50-0.75
Collapse	0.75-1.00

Wang et al. (2017), conducted experiments to find out the residual capacity of the bridge before and after collision. The main concern of the research is accidents between over height vehicles and Bridges. The damaged and undamaged results are plotted, and FEM analysis was done on the bridge, and the results were compared. Based on the experimentation and FEM analysis result, the damage coefficient was obtained, and the flexural capacity of the beam was calculated. The results of the research show that the typical section failure at mid-span arises from the edge position of the damaged region. FEM analysis was done using Abacus software. Concrete was simulated with solid element and rebar was simulated with bar element in Abaqus. FEM model shows the strain results at $1/4^{th}$, mid-span and $3/4^{th}$ of the section. Both strains in concrete and rebar were calculated. Wang et al. provides us with the theoretical and experimental foundation for the evaluation of the technical state of RCC Bridge after a collision.

Mechbal and Rebillat (2017), studied the behaviour of composite material for aeronautical industry. They worked extensively on SHM. Composite materials may be more appealing in aeronautical industry because of their advantages over conventional materials, but they are prone to damage, which is much more complicated. The damage to composite material was studied, and conclusions were made. The studies were made on composite stiffened plate, which is made up of monolithic carbon epoxy. The health monitoring is done using Lamb waves which propagate through the structure without any interferences if there is no damage to the structure. If there is any damage to the structure, Lamb waves interfere with the damage that can be recorded by receivers. The damage indexes are classified into several families, and then studies were carried out on different materials, and the corresponding damage indexes were calculated. The results in the above process can be tabulated, and effective SHM system was designed for stiffened composite structures.

Hait et al. (2019), reviewed several available experimental and analytical methods for both global and local DI. These damage indices were reviewed for buildings and bridges, and their impact due to seismic loading and material deterioration are studied. For different levels of

seismicity, several case-studies were addressed for assessment of bridges and buildings to understand the variation of DI. The authors addressed the future scope of research in different aspects of damages like progressive development, damage estimation, and time-dependent damage assessment for various non-structural and structural components using different materials. He proposed the limitations of DI for various available methods.

2.4 Review of Literature on Application of ANN

Karamodin et al. (2008), carried out the investigation on SHM using experimental data, and used that data for training artificial neural networks for prediction of the DI. Two neural networks were designed separately at each time step to monitor storey damage. The input given to the first neural network was maximum drift of each story, and the next stories and damage due to maximum drift of the story as output. Second neural network identified damage due to energy dissipated at each story. From shear to drift story diagram, the input for the data was calculated, and it was appropriated to the energy dissipated. For the first neural network, a feed-forward neural network with one hidden layer consisting of ten nodes was selected. Tangent sigmoid transfer function was used for hidden layer nodes, linear (*purelin*) is used for output nodes and Levenberg-Marquardt back-propagation for training. The training required 1000 training epochs to achieve a Mean Square Error (MSE). For the second neural network, the training algorithm remains the same, but it had two hidden layers consisting of 10 nodes in each hidden layer.

Abd et al. (2015), estimated the deflection of continuous deep beam using both experimental data and artificial neural networks. They did a comparative study on Statistical modelling and neural networks. Deep beams are beams, which have high depth when compared to its width. The depth of the beam can be compared with its span. According to IS 456:2000, in a simply supported beam, if l/d ratio is less than 2, it is considered as deep beam whereas in case of continuous beam its value must be less than 2.5. The behaviour of deep beam is different from that of a regular beam. The elastic solution is reliable if the beam is uncracked. If the cracks are formed in the beam, there will be redistribution of the stresses in the beam, and hence elastic principles cannot be applied to the beam. Non-elastic analysis of the beam must be done. Most importantly, ANN is capable of learning from examples. Multilayer ANN with a feed-forward algorithm with back-propagation is developed to model the nonlinear relationship between the deflections under the ultimate strength of deep beam. 75 samples were studied, which had two spans continuous beam, which was loaded by two-point load symmetric on both the spans.

Imam et al. (2015), determined the residual strength of the corroded reinforced beam subjected to various degrees of corrosion damage. The estimation of the residual flexural capacity of an RCC member was studied for more than three decades. The output of the study deals with the determination of factor C_f that gives residual strength on multiplying with the original capacity. Factor C_f is an empirical formula which depends on diameter (D) of the bar, corrosive current I_{corr} and T (time) in days for which the rebar was subjected to corrosive currents. We know in a corrosion process that corrosive current flows in a structural member in which water acts as an electrolyte and rebar act as an anode, which gets corroded. This type of corrosion is called galvanic corrosion. The value of the factor C_f always lies between 0 and 1. This means that when the value is close to 1, the damage due to corrosion is less and vice-versa. Experimental values were determined, and ANN model was developed. The input layer consists of diameter D and I_{corr} and T. The hidden layers consist of more than 50 neurons in each layer. Finally, in the output layer, we have C_f factor. The training epochs were 100, error goal was 0.001, training algorithm used was Levenberg-Marquardt, and transfer function was *sigmoidal* from input to the hidden layer and *purelin* from hidden layer to the output layer.

S. Philip Bamiyo et al. (2016), discussed the complex behaviour of reinforced concrete slab, i.e. to study load-deflection of the two-way slab using artificial neural networks. A set of 30 slabs were cast with dimensions of 700 mm x 600 mm x 75 mm and cured for 28 days. The load applied to the slabs ranged from 10 kN to 155 kN with 5 kN increments. The maximum deflection was 6.97 mm, which occurred at 155 kN producing a stress 369.05 kN/m^2. As we know in neural networks, we need to have the training, testing and validating of experimental data. About 54% were used for training, 23% for testing and 23% for validation. The input layer consists of four input neurons. It had two layers of hidden layers consisting of five neurons in each layer and output layer consisting of two neurons, i.e. stress and deflection. In his study, the number of learning cycles used was 16. The activation function used was *tan-sigmoidal* function. The correlation factor was $R^2 = 0.9316$, which is a good sign as the accuracy of ANN and experimental data was more than 95%. The maximum percentage error measured in deflection was only 0.23%. In linear regression model, the straight line passed maximum points.

2.5 Summary of Literature Review

From a detailed literature review on SHM using DIC, it can be concluded that

- Limited research is available in the context of Indian Bridges on the development of a framework for health monitoring of flexure dominated structural elements using DIC.

- To achieve an effective correlation, the pattern must be random, isotropic, highly contrasting, and speckles should be neither too small nor too large. Correlation may fail with extremely large or small speckle patterns.

- The accuracy of the measured displacement is influenced by the size of the speckle and the corresponding size of the used pixel subset.

- Systematic experiments were performed by previous researchers to determine the properties of speckle patterns which have a dominant influence on the spatial resolution and accuracy of results.

- The algorithms available in the literature are Curve Fitting Gradient-Based and Newton-Raphson Algorithms. Among these algorithms, Newton-Raphson Algorithm gives stable results with more accuracy. Based on the literature review, a QR code-based speckle pattern is an innovative approach in the field of DIC.

- The laws of similitude place strict requirements on the relationship between full scale and reduced scale model, which need to remain constant in order to ensure complete similitude requirements.

- Literature review indicates that ANN is established as a vital tool in SHM. The accuracy of the network depends upon the consistency of the training data.

- In comparison with ANN training algorithms, such as Bayesian Regularization, and Scaled Conjugate Gradient, the Levenberg-Marquardt algorithm gives acceptable results with fewer iterations and better accuracy.

- Literature study indicates that there is no universally accepted DI scale is present.

The objectives and scope of the investigation are defined in **chapter 3**.

CHAPTER 3

Objectives and Scope of Investigation

3.0 General

This research work presents an innovative approach of using Quick Response (QR) code as a speckle pattern in the field of DIC. From the detailed literature review, it is clear that there is a lack of research available to develop QR code as a speckle pattern in the field of DIC. The main objective of the study is estimation of DI, and Condition Rating Number (CRN) based on curvature of flexurally dominated RCC members which are obtained using DIC. A framework is developed for bridge girder condition assessment using DIC based SHM. The study also compares the performance of the two different types of speckle patterns, i.e. QR Code based speckle pattern and Random speckle pattern on bridge deck components (rectangular and T-beams).

3.1 Scope of the Present Investigation

- Experimental testing and validation of numerical models of rectangular flexure dominated RCC beams and scaled (1:12) T-beams under laboratory conditions.
- Performance of two different types of speckle patterns, i.e. QR code-based speckle pattern and Random speckle pattern are compared.
- Develop a framework for bridge girder condition assessment using DIC based SHM.

3.2 Research Significance

- An innovative approach to use QR code as a speckle pattern in the field of DIC is established with comparative results. QR code-based speckle pattern may be used as an integrated non-contact optical sensor for SHM and data embedment for BIM. (**Patent Filed**)
- An image-based condition assessment methodology is developed to enable quantification of existing damage and residual moment capacity based on curvature for flexure dominated RCC Bridge T-girder.
- Correlation between mechanistic based superstructure DI and bridge CRN is established.

3.3 Objectives of the Study

- Determination of the suitability of QR code-based speckle patterns for obtaining local damage as well as global deformation of components.
- Determination of the capacity of full-scale RCC T-beams based on experimental results obtained from scaled models and corresponding correlation with FE models.
- Development of DI for RCC rectangular beams and T-beams based on ANN.

3.4 Research Methodology

In order to achieve the objectives of the investigation, detailed experimental work is planned in three phases:

3.4.1 Phase-I: Determination of optimal speckle pattern

The first phase of the study is aimed at investigating the performance of a proposed QR code-based speckle pattern and its experimental validation. The QR code pattern is proposed as a replacement for the random speckle pattern generally used in the DIC method. To validate this new technique, flexural strength test using four-point loading is conducted for six different rectangular RCC beams. The deflection and curvature obtained from QR code-based speckle pattern is compared with the results obtained using speckle pattern-based DIC method as well as conventional dial gauges and Linear Variable Differential Transformer (LVDTs). The work involves testing of rectangular concrete beam specimens tested in flexure under a Universal Testing Machine (UTM). Strains and deformations were computed using both random speckle and QR code-based random speckle patterns applied to the specimens. MATLAB based open-source DIC software package Ncorr v1.2.2 (Blaber et al. 2015) is employed for image processing. Ncorr is an open-source subset based Two Dimensional (2D) DIC software that includes modern DIC algorithms with some additional enhancements (Harilal 2014).

The flexural performance of RCC beams, was investigated both experimentally and numerically. Different experimental methods are employed to measure the RCC beams flexural deformations and strengths, including traditional direct method by gauges/LVDTs, innovative noncontact methods by DIC (random speckle pattern and QR code speckle pattern). Results show that the data obtained from QR code-based speckle is closer to the values obtained from conventional methods (LVDT/dial gage) as compared to random speckle pattern. Then, ABAQUS is used to verify the experimental findings. Concrete Damage Plasticity (CDP)

model is applied for concrete. The related material parameters are calibrated and input into ABAQUS. Good agreement between experiment and numerical simulations are found.

3.4.2 Phase-II: Investigation on scaled (1:12) RCC T-beams

The second phase of the study is aimed at studying the behaviour of small scale (1:12) RCC flexure dominated T-beams using DIC technique. In the present investigation, an innovative QR code-based speckle pattern and Random speckle pattern are used. Using the law of similitude, the small-scale T-beams are designed, cast and tested under four-point bending so that the nonlinear constitutive behaviour can be correctly scaled to prototype. A model concrete consisting of cement, water and fine aggregates is developed by geometrically scaling the coarse aggregate and rebar. Load-Deflection and Moment (M)-Curvature (κ) curves for RCC beams obtained using conventional contact sensors and DIC are compared. Numerical analysis is carried out by using finite element-based software SAP2000. The identical component was simulated in SAP2000 and was found to be in good agreement with ABAQUS and experimental data

3.4.3 Phase-III: Prediction of DI using ANN

In the third phase, development of DI for both rectangular and T-beams using ANNs are investigated. ANN input data is obtained from experiments and validated simulations (Phase-I & Phase-II). The approach of Phase-III is using experimental data and artificial intelligence methods for the prediction of the damage state of RCC beams.

Chapter 4 deals with the experimental, analytical and numerical programs of RCC scaled (1:12) T-beams using DIC.

CHAPTER 4

Determination of Suitability of QR-Code Based Speckle Pattern Using DIC

4.0 General

This study presents QR code as a speckle pattern in the field of DIC. The objective is to compare the experimental results obtained from the readings of the deformations from the dial gauges and curvature meters with those obtained from the DIC technique and further, correlation with corresponding Finite Element (FE) models. An enhancement to random speckle pattern in DIC is developed, for the traditional four-point bending experiment using QR code as a speckle pattern.

4.1 Experimental Programme

The experimental program comprises of casting two beams each of three different concrete grades M30, M50 and M70 (M means Mix and 30, 50 and 70 implies the characteristic compressive of concrete in Mpa) with Under-Reinforced (UR) and Over-Reinforced (OR) sections (total 24 beams). For each grade, two different types of speckle-patterns are used; one each for UR and OR sections. The random speckle pattern and QR code-based speckle pattern are used for both UR and OR sections with normal, medium and high strength concretes. The schematic representation of experimental programme is shown in Figure 4.1.

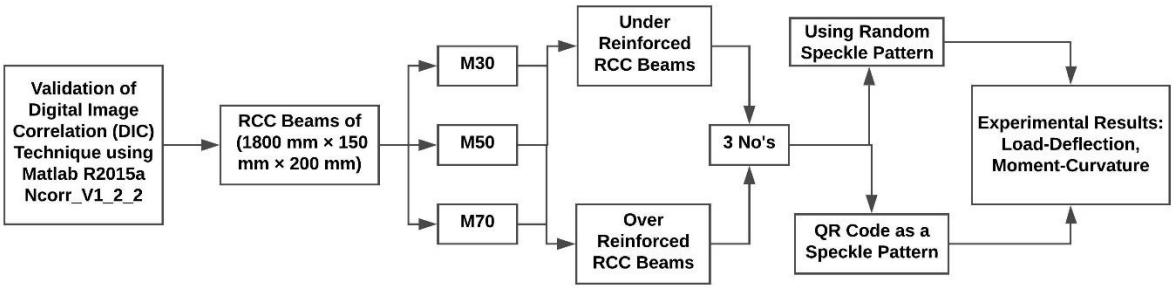

Figure 4.1 Schematic view of the experimental program

4.1.1 Materials

Locally available river sand is used as fine aggregate, whereas, crushed granite is used as coarse aggregate. Fine aggregate corresponds to Zone II, while coarse aggregate with a maximum size of aggregate 20 mm is used in this study**.** The physical properties of fine and coarse aggregates are shown in Table 4.1.

Table 4.1 Physical properties of fine and coarse aggregates

Physical Properties	Fine Aggregate	Coarse Aggregate
Specific Gravity	2.64	2.81
Fineness Modulus	2.56	7.40
Bulk density (gm/cc)	1.46	1.40

4.1.2 Mix proportions

The final mix proportions for different grades of RCC beams are presented in Table 4.2.

Table 4.2 Mix proportions obtained for RCC beams

Mix	Coarse aggregate (kg/m^3)	Fine aggregate (kg/m^3)	Cement (kg/m^3)	Fly-ash (kg/m^3)	Silica fume	SP430 (ml/kg)	W/B
M30	1145	764	300	100	-	10	0.43
M50	1004	669	430	100	-	20	0.37
M70	945	650	500	110	40	30	0.30

4.1.3 Specimen preparation and testing

The reinforced concrete beams of three different grades of concrete M30, M50 and M70 for both UR and OR sections are cast and tested under four-point loading to failure with deformations measured using dial gauges and curvature meters simultaneously DIC technique is also used to obtain the deformations. The unsupported length of RCC beams is 1800 mm with a cross-section size of 150 mm width and 200 mm depth. The suitability of employing both random speckle pattern and QR based random speckle pattern for the beams is investigated. The details of test setup are shown in Figure 4.2.

4.2 Digital Image Correlation (DIC)

4.2.1 General principle

DIC is based on comparing two images (reference image and deformed image) which are acquired at different states before and after deformations. After the acquisition, of the digitized images, and two subsets are picked respectively from the reference and deformed images for correlation in the form of a matrix (n×m). A fine pixel by pixel search is performed within the region of interest in the deformed image. The nearest location of the point of interest at the pixel level is selected based on the occurrence of the best-matched pattern, which has the minimum value of mutual cross-correlation coefficient. Ncorr v1.2.2 uses an algorithm for correlation, which is programmed to detect the local displacement of a particular point by comparing the two image subsets, and the result is in the form of pixel displacement. Pixel

displacement is then converted to engineering units by using Ncorr v1.2.2; the pixel blocks need to be random and unique with a range of contrast of 8-bit grayscale image intensity levels that vary from 0 to 255 shown in Figures 4.3 and 4.4. It doesn't require any special lighting, and in several cases, the natural surface of the structure or component has sufficient texture for DIC to work without the necessity of special surface preparation. The parameters for the low-cost Digital Single-Lens Reflex (DSLR) camera employed in this study are shown in Table 4.3.

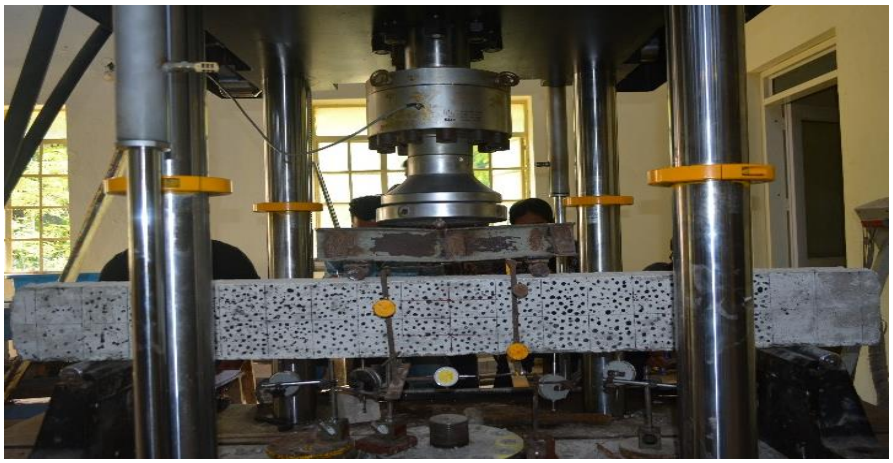

(a)

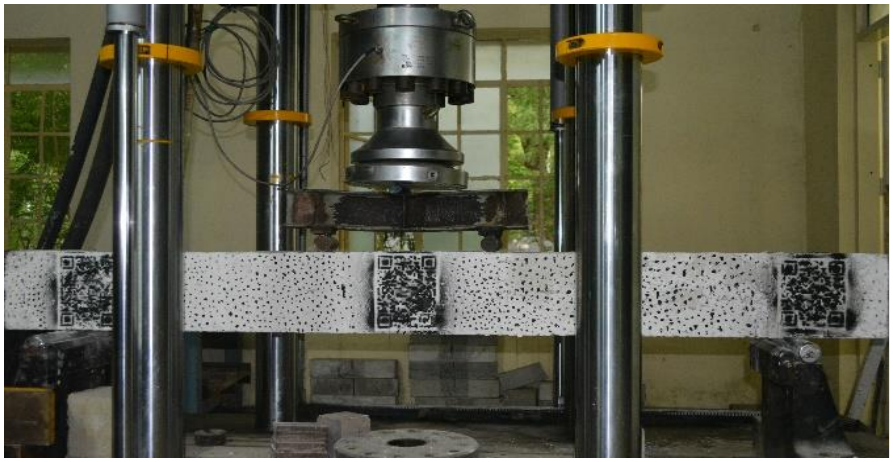

(b)

Figure 4.2 Testing of beams using (a) Random speckle (b) QR code speckle patterns

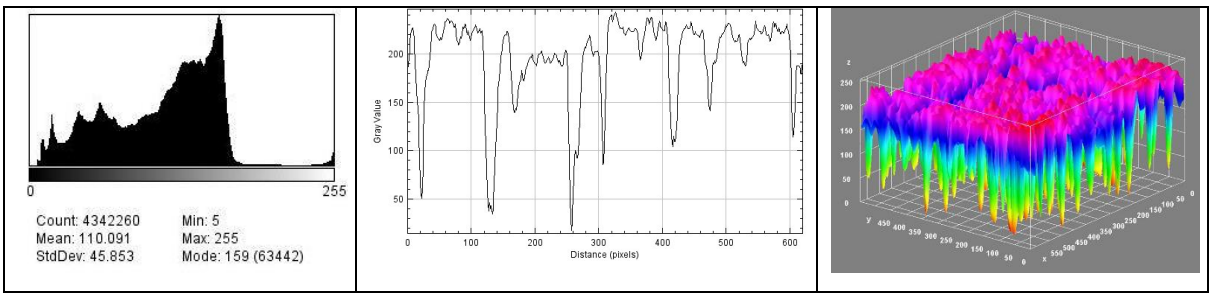

Figure 4.3 Surface histogram of mid-span RCC beam of gray intensity for random speckle

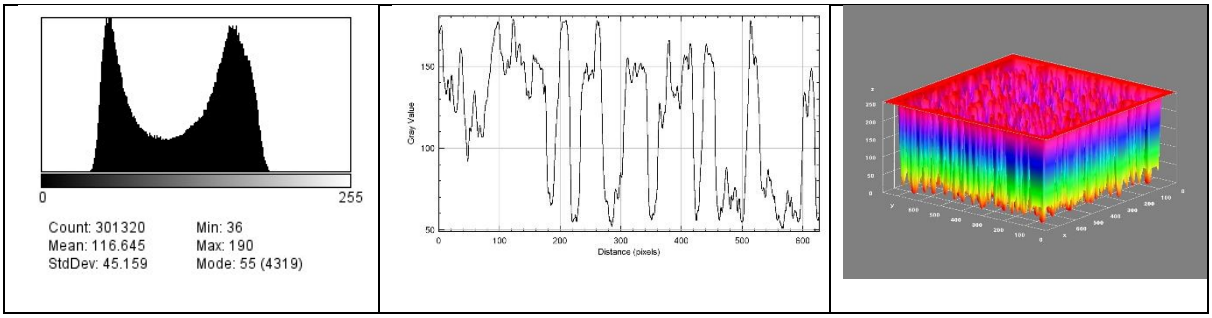

Figure 4.4 Surface histogram of mid-span RCC beam of gray intensity for QR code speckle

The captured images are pre-processed from RGB colour to grayscale (8-bit) and then analyzed using ImageJ software. Grayscale images have distinct black and white colours. The grayscale value varies from 0 to 256 (0 indicates black; 256 indicates white, and the values in between represent different shades of gray). The gray image value of pixel is stored based on the intensity of light. Histogram is a graphical representation of a number of pixels with different intensity values of the image. Histogram can identify pixel values at each point in an image and show the total number of pixels in an image.

Table 4.3 Camera parameters (Nikon DSLR Camera D5200)

Width	6000 pixels
Height	4000 pixels
Horizontal resolution	300 dpi
Vertical resolution	300 dpi
Pixel depth	24 bit
Manufacturer	NIKON CORPORATION
Model	Nikon DSLR Camera
Colour display	sRGB
Shutter speed	1/125 S
Aperture	f/3.5
Iris Aperture	w/o flash
Focal length	18mm
Focal ratio	f/3.5
Exposure time	1/125 S
ISO speed	ISO-400
Exposure compensation	0

Digital images are divided into a number of smaller regions which are termed subsets, and these subsets undergo deformations when the image distortion takes place. The deformation location of the subset might not be at the integer location. That is why interpolation functions need to be used to get the gray intensity value at a non-integer location.

The correlation function (C) is defined as the similarity between the deformed state and the undeformed state of the image subset. In general, the Pearson correlation coefficient lies between (-1 to +1) for optimal speckle patterns. To correlate the similarity index between the reference image subset and deformed image subset, a correlation analysis is done. In order to obtain the deformation subset, 2D DIC algorithm arrives at values of the extreme correlation cost function (Nguyen et al. 2017). This function can be written in the form:

$$C = \frac{\int_{\Delta M} \left(F(x,y)\right)\left(G(x_0+U, y_0+V)\right) dA}{\left[\int_{\Delta M} [F(x,y)]^2 dA \int_{\Delta M} [G(x_0+U, y_0+V)]^2 dA\right]^{1/2}} \quad (4.1)$$

Where F and G are respectively references and deformed images are having grayscale intensity functions at a specified location (x_0, y_0) and (x, y) a function of deformed location in (4.1).

The maximum correlation coefficient can be easily calculated using a simple MATLAB function. The function "normxcorr2" available in MATLAB is used to find the correlation between two subsequent images (reference and deformed). It is clear that the overall correlation is found to be higher in the case of QR code-based speckle pattern images from a three-dimensional graph plotted between calculated correlation value and pixels, as shown in Figure 4.5.

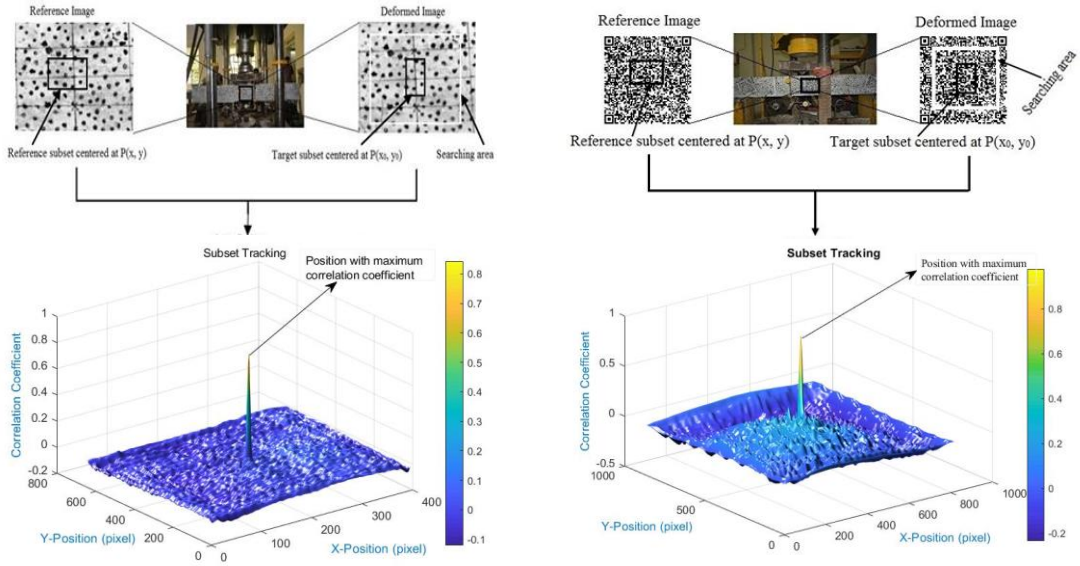

(a) Random speckle pattern (b) QR code speckle pattern

Figure 4.5 Subset tracking procedure using DIC

The physical size of 1 pixel might range between 1 nanometer to 1 centimetre approximately. DIC compares digital photographs of the test piece or component at different stages of

deformation by identifying blocks of pixels. The system can also measure surface deformation and full-field 2D deformation vector fields and strain maps.

4.2.2 Computation of strain

In Cartesian coordinate system (x, y, z), the strain metrics can be calculated based on measured tangential displacement field (u, v, w) as expressed in (4.2), (4.3) and (4.4). Strains are calculated from displacement data, and the four displacement gradients are used to find the Lagrangian strains (Nguyen et al. 2017). Which are as follows:

$$E_{xx} = 0.5\left[2\frac{\partial u}{\partial x} + \left(\frac{\partial u}{\partial x}\right)^2 + \left(\frac{\partial v}{\partial x}\right)^2\right] \tag{4.2}$$

$$E_{xy} = 0.5\left[\frac{\partial u}{\partial y} + \frac{\partial v}{\partial x} + \frac{\partial u}{\partial x}\frac{\partial u}{\partial y} + \frac{\partial v}{\partial x}\frac{\partial v}{\partial y}\right] \tag{4.3}$$

$$E_{yy} = 0.5\left[2\frac{\partial v}{\partial y} + \left(\frac{\partial u}{\partial y}\right)^2 + \left(\frac{\partial v}{\partial y}\right)^2\right] \tag{4.4}$$

Schematic representation of subset deformation before and after deformation of subsequent images is shown in Figure 4.6.

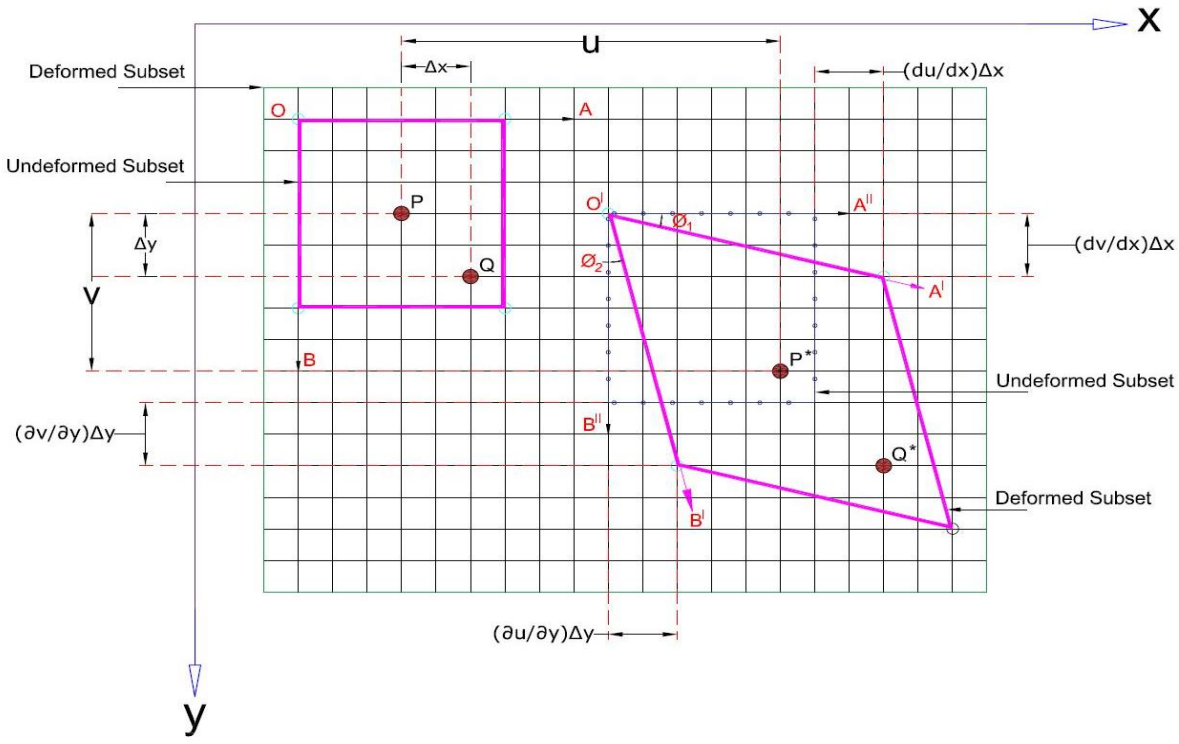

Figure 4.6 Schematic representation of subsets before and after deformation

The flowchart shown in Figure 4.7 briefly explains the procedure adopted for validation of DIC software along with the contact sensor devices.

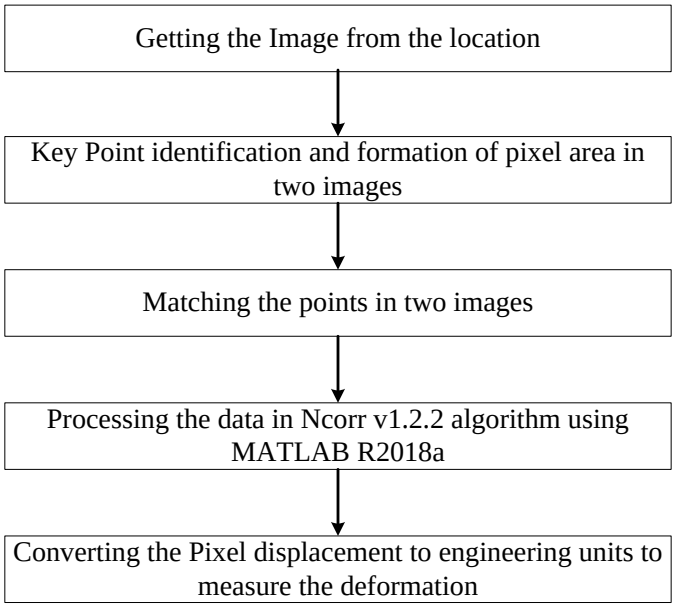

Figure 4.7 Flowchart showing the image processing technique

This approach has also been utilized successfully for large deformation measurements. Due to its simplicity, the DIC technique has been further extended to deformation and curvature studies. According to the technique, if the specimen attains the natural texture of random gray intensity value, there is no necessity of specimen preparation for DIC.

4.2.3 DIC system setup

Two-dimensional DIC technique presented in this study involves three consecutive steps, (i) Spraying black speckle pattern on the prepared white specimen surface in order to obtain the random gray colour intensity distribution; (ii) Capturing the digital images of both undeformed and deformed specimen surfaces using low-cost DSLR camera; (iii) Post-processing with Ncorr v1.2.2 DIC software for obtaining full-field displacement and strain. The minimum deflections/strains measured is in the order of 0.01 mm/micro strains. The size of the QR code is 150 mm by 150 mm, which is sprayed on the flexural portion of the beam. The minimum radius of the subset considered in this study is 1.5 mm escribed circle with a step size of 1.5 mm up to 21 mm (as there was no significant difference in the results after 18 mm until 21 mm). The optimal radius of subset was found to be 13 mm with a subset spacing of 6 based on the results obtained, which are in good agreement with conventional measurement technique (LVDTs/dial gauges).

In view of the intricacy and the accuracy involved in the measurement of surface distortions, an important aspect of DIC is to create an appropriate pattern on the sample to be tested. This has a significant impact on the quality of results; hence, it is important to determine the optimal pattern at the very outset. Irrespective of length scales all patterns should be spatially random. The randomness of a speckle pattern will influence the DIC monitoring algorithm. For DIC to work effectively, the pixel blocks need to be random and unique with a range of contrast and intensity levels. It requires no special lighting, and in many cases, the natural surface of the structure or component has sufficient image texture for DIC to work without the need for any special surface preparation. In general, the implementation of the DIC method comprises the following three steps: (i) specimen preparation; (ii) recording images of the specimen's surface before and after deformation; (iii) processing the acquired images. The flowchart showing the image processing technique in Figure 1.1 explains the overall procedure adopted for DIC technique.

4.2.4 Fundamentals of DIC

Experimental solid mechanics includes surface deformation measurement of materials and structures under mechanical or thermal loading. Contact sensor devices are used to measure object distortion while loading the test. The most extensively adopted instruments are Linear Variable Differential Transformers (LVDTs), dial gauges and strain gauges, which measure displacement with respect to the rate of loading applied on the specimen (Carter et al. 2015). These devices are well established, with an accuracy of ±1μm or even lower, where real-time data can be captured. On the other hand, these contact sensors can measure in one dimension only, limited to the area where the sensor is fixed. Sensors, when used with a controller unit, are prone to damage during destructive tests (Yuan et al. 2015). Therefore, LVDTs or strain gauges are not suitable in case of extreme testing conditions. Contact sensors are used traditionally for measurement of deformations, but due to inherent difficulties in terms of accuracy, the necessity of flat surfaces and issues related to the attachment of these devices, non-contact methods of measurements are becoming popular.

4.2.5 Advantages of 2D DIC:

DIC has several advantages over conventional NDT methods.

- Needs simple experimental test setup and specimen preparation.
- Low requirements in field conditions during testing.
- Wide range of measurement sensitivity and resolution.

4.2.6 Disadvantages of 2D DIC:

- The test planar object surface must have random gray intensity distribution.
- The measurements depend heavily on the quality of the imaging system.
- At present, the strain measurement accuracy of the 2D DIC method is lower than the interferometric techniques.

4.2.7 Speckle pattern studies

The optical speckle pattern is very much important in DIC. Several studies have been conducted to understand the non-contact optical DIC method using different speckle patterns (Lecompte et al. 2006). Systematic experiments were performed by previous researchers to determine the quality of contrasting speckle patterns on the surface of test specimens that have a dominant influence on the spatial resolution and accuracy of results (Carter et al. 2015, Bossuyt 2013). It was concluded from the studies that to achieve an effective correlation, the pattern must be random, isotropic and highly contrasting.

Further, speckles should neither be too small nor too large. Correlation may fail with extremely large or small speckle patterns. The size of the speckles, combined with the size of the used pixel subset influences the accuracy of the measured displacements (Salmanpour and Mojsilovic 2013, Lecompte et al. 2006). Consistent speckle sizes have to be maintained-ideally 3-5 pixels in size. If the pattern is too large, certain subsets may be entirely on a black field or entirely on a white field. Conversely, very minute speckles can cause aliasing effect resulting in images that often show a pronounced Moire pattern in the measurement result (Mudassar and Butt 2016).

It was proposed by (Hung Po-Chih et al. 2003) that the strain resolution increases with increase in speckle density from 23% to 58% of area fraction. Speckle patterns containing medium-sized speckles and exhibiting a limited spectral content yield the most accurate displacement measurements. Patterns well-suited for DIC exhibit a sharp correlation peak, a broad correlation margin, and neither have features too small to be resolved by the imaging system to be used nor large featureless areas. Applying speckles on the surface of the specimen using a permanent marker can be a good technique for creating optimal speckle pattern (Pan Bing et al. 2009). This type of technique is used on the surface of the specimens which are involved in measuring very high strains. To achieve this, dots on the surface are marked off the desired size (Suryanto et al. 2017). A black marker provides excellent contrast on a white base coat. An optimal speckle pattern is necessary for using DIC with ease for practical applications.

4.2.7.1 Need for a good pattern

- For the proper tracking of the subsets of the image.
- Correlation can be made with high confidence and produce low noise.

4.2.7.2 Pattern requirements (CSI application note AN-525)

- High Contrast: Either black dots on a bright white background or bright white dots on a dark background.
- 50% coverage: Equal amounts of white and black on the surface.
- Consistent speckle sizes: Ideally 3-5 pixels in size. Correlation may fail with extremely large or small speckle pattern.
- Isotropic: Pattern shouldn't exhibit bias in any particular orientation.
- Random: Repeating patterns causes false matching hence speckle pattern should be random.

4.2.7.3 Common application methods

- Speckle pattern application kit: It contains an array of stamp rollers/rockers, spray paints and stencil tools to produce optimal speckle patterns.
- Spray paint: The surface of the specimen is coated white in light coats and the speckles are applied.
- Permanent marker patterns: Speckles are applied with a permanent marker on a white base coat.
- Printed patterns: Pattern is printed onto vinyl appliqué or adhesive labels, making sure it adheres to the specimen well enough to deform with the surface.

Standard paints and inks may crack or change at higher temperatures, therefore, paints designed for extreme temperature conditions are used (CSI application note AN-525).

4.2.8 Implementation steps

- Specimen and experimental preparations.
- Recording images of the planar specimen surface before and after loading.
- Processing the acquired images using a computer program to obtain the desired displacement and strain information.
- Target specimen surface must be flat and remain in the plane parallel to the optic sensor during measurement.

- Corresponding distortion correction techniques should be used to remove the influence of distortion to provide accurate measurements.

The estimated motion of each image point multiplied by the magnification of the imaging system will not accurately equal to that of the actual physical point on the specimen surface unless the following requirements are met. DIC is simple to implement while enabling cost-effective measurements in a range of potential applications including examining the evolution and uniformity of strain in materials testing, crack tip and crack propagation studies, detecting damage development in composites, structural deflections, high-temperature strain mapping, and dynamic response analysis.

The deformation components on the surface of an object are obtained using DIC algorithms by recording the images of the surface before as well as after loading (Feng et al. 2015). The algorithms available in the literature are Curve Fitting Gradient-Based and Newton-Raphson algorithms. Among these algorithms, Newton-Raphson algorithm gives stable results with more accuracy (Lu and Cary 2000, Vassoler and Fancello 2010, Cofaru et al. 2010, Yuan et al. 2015). In the algorithms suspected by Su and Anand (2003), the accuracy and speed were not verified, while algorithms developed by Kozicki and Tejchman (2007) proved to be highly expensive. Some researchers have applied the Gradient-Based algorithm to DIC (Long et al. 2013, Wittevrongel et al. 2015).

4.2.9 Quick Response (QR) code as a speckle pattern in DIC

The QR code was invented by Denso Corporation in 1994 and Affirmed as Automatic Identification Manufacturers (AIM) International standard along International Standards (ISO/IEC) in 2000. In DIC, two images of reference and deformed images are captured. After the acquisition, the images are digitized, and two subsets are chosen respectively from the reference and deformed images for correlation in the form of a matrix (n×m). A fine search routine, pixel by pixel, is performed within the specified range in the deformed image. The nearest location of the point of interest at the pixel level is selected based on the occurrence of the best-matched pattern, which has the minimum value of mutual cross-correlation coefficient. A correlation algorithm detects the local displacement of a particular point by comparing the two image subsets, and the result is in the form of pixel displacement. Pixel displacement is converted into engineering units by using camera calibration parameters. The converted displacement gives the deformation in the structures. The DIC-based non-contact

measurements can be compared directly with strains obtained from FE simulations as well as to inverse identification of test parameters at the structural level.

4.2.10 Ncorr v1.2.2 workflow

In order to assist a non-contact strain measurement system, an open-source DIC software "Ncorr" is used for computing the deformation from the initial unloaded stage to failure. This method is relatively easy to set up and deploys a cost-effective ordinary optical digital camera like a DSLR or smartphone camera, adapted according to the situations (Suryanto et al. 2017).There are various commercial software available in the market, which uses 2D DIC as a tool to estimate displacement and strain fields. Ncorr is one such open-source 2D DIC code based on MATLAB software developed at Georgia Institute of Technology by Antonia Antoniou's group. Ncorr is capable of estimating displacement and strain fields from the given input speckle images.

Flexural behaviour of RCC beams are tested under four-point bending condition, corresponding displacement and strain fields are estimated using Ncorr. There are various contact and non-contact techniques in the fields of experiment mechanics for measurement of surface deformation and strain. The flowchart showing the image processing technique in Figure 4.8 explains the overall procedure adopted for Ncorr software.

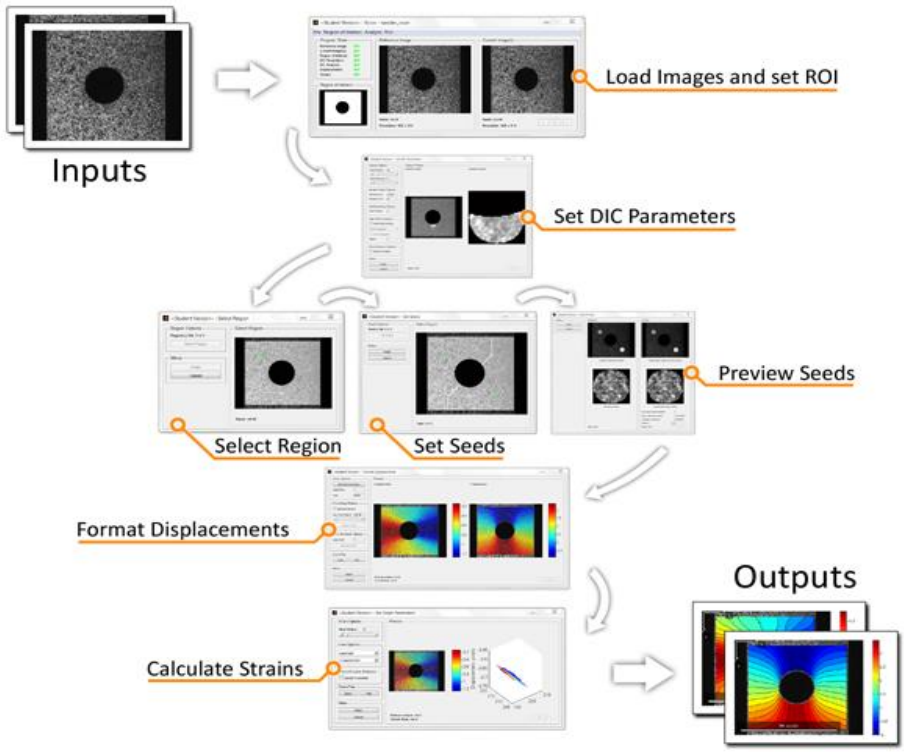

Figure 4.8 Flowchart showing the image processing technique used in Ncorr v1.2.2

4.3 Testing Procedure

The experimental program is focused on the comparison of the flexural behaviour of RCC beams which is extracted using the DIC technique for different speckle patterns. A comparison of the conventionally measured moment and deformation/curvature obtained using a combination of both QR Code speckle pattern and random speckle pattern is conducted. Low-cost off-the-shelf equipment (Nikon D5200 DSLR camera with 24.1 MEGAPIXEL DX-format CMOS sensor) is used to capture the images while testing the RCC beams. After capturing the sequence of images, image processing is done by Ncorr, an open-source DIC code using MATLAB R2015a. The parameters varied in the investigation are normal (M30), medium (M50) and high strength (M70) concretes as well as variation in the speckle patterns. Two different types of speckle patterns; random speckle pattern and QR Code based speckle pattern are used. The dimensions of the beams are 1800 mm × 150 mm × 200 mm. These beams are cast and tested for both UR and OR design category. Dial gauges (least count 0.01 mm) are used as conventional contact sensors and placed on the bottom surface of the beams to measure the deflections. The position of the dial gauges is shown in Figure 4.9. Curvature meters are used in compression zone as well as in tension zone and are 200 mm apart from the middle frame. The schematic drawing of the equipment, used for testing with a random speckle pattern applied throughout the cross-section is shown in Figure 4.9.

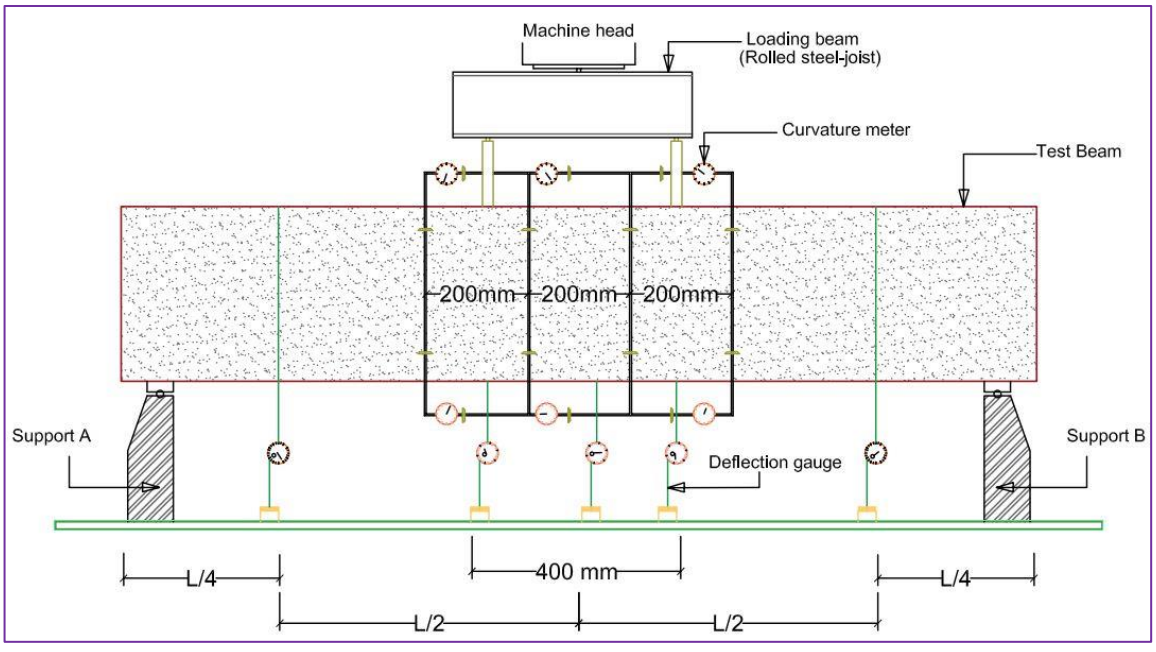

Figure 4.9 Schematic diagram of random speckle pattern test set-up

The beams are quasi-statically tested using a UTM having a capacity of 1000 kN with a strain rate loading of 1.5 mm/min. With the application of loading and as the testing starts, images

are captured at consecutive uniform intervals of loading using a DSLR camera. The consecutive images are considered to calculate the horizontal curvatures at top and bottom portion of the beam using Ncorr software. From the curvature readings, strain in concrete (ε_c) and strain in steel (ε_s) are calculated, using these strain values the corresponding M-κ values are calculated. The conventional results from the dial gauges and curvature meters are then compared with DIC results.

A typical QR code pattern stencil, as shown in Figure 4.10 is applied at critical locations of the beam surface for different beams (grades of concrete, OR and UR). In order to attain randomness of the pattern, QR codes are rotated and applied at critical locations. QR code-based speckle pattern finds applications in structural health monitoring (Meadati et al. 2015). As QR code is being used for numerous applications in data encryption, data transmission and as information carrier in web applications. Therefore, using QR code as a speckle pattern for DIC in real-time SHM provides us with certain advantages such as the QR code being encrypted with details of the structure helps in easy identification of the structure by scanning. DIC results obtained using QR, and random speckle is computed with deformation, curvature and strains obtained from conventional sensors. The schematic drawing of the equipment used for testing QR code random speckle pattern is shown in Figure 4.11.

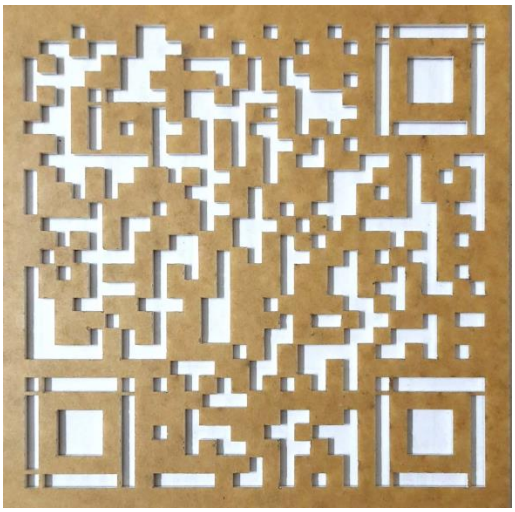

Figure 4.10 QR code pattern employed in this study

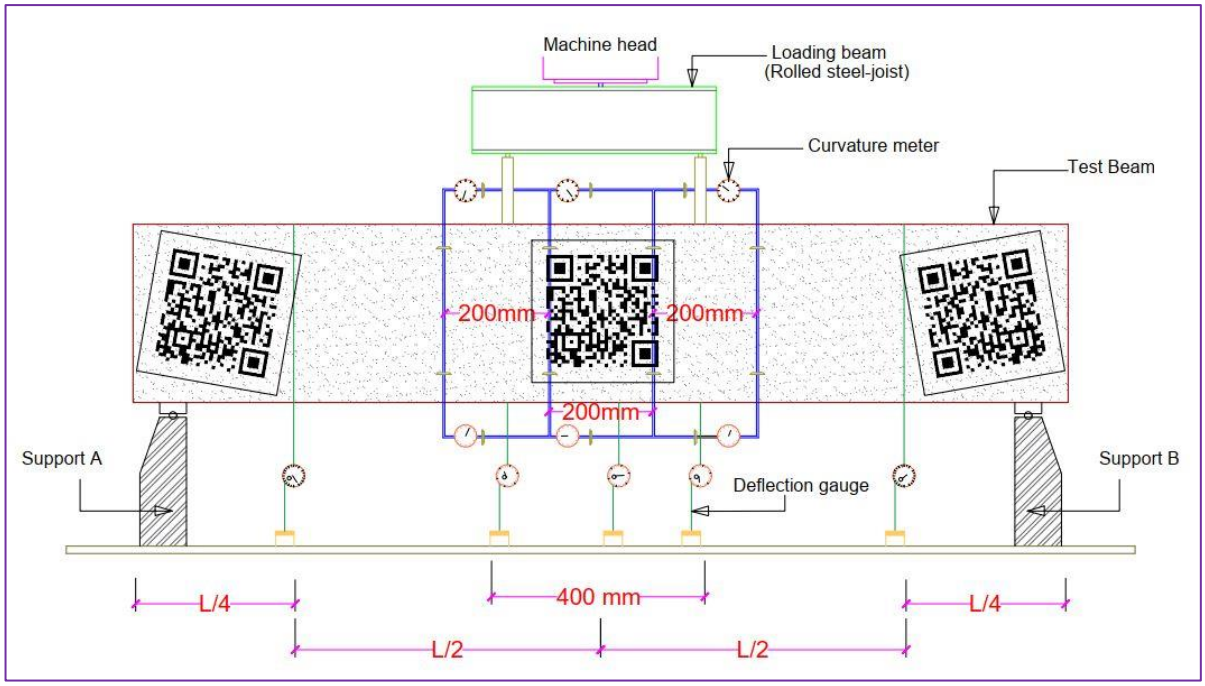

Figure 4.11 Schematic diagram of QR code with random speckle pattern test set-up

4.4 Finite Element Method (FEM)

FEM is one of several numerical simulation methods to obtain solutions to problems, which otherwise are difficult to obtain. In FEM, the solution to a problem is obtained by dividing a larger system into several smaller parts, which are called finite elements (discretization) (Grassl et al. 2013, Kalyana Rama et al. 2017). In this paper Concrete Damage Plasticity (CDP) constitutive model is used for modelling concrete, available in standard numerical tool ABAQUS v6.14/CAE (FEM software), which is a powerful engineering numerical simulation program. With the help of this tool, the results obtained from experimental tests on RCC beams for different grades of concrete are validated. A simple plasticity model is used to simulate the nonlinear monotonic behaviour of steel in concrete. The flexural response of RCC beams obtained using DIC is compared with those obtained from conventional tests and numerical simulations.

4.4.1 Concrete Damage Plasticity (CDP) model

Accurate material modelling is the most challenging aspect in finite element modelling of concrete structures and especially the modelling of concrete. The concrete beam is modelled using CDP constitutive model, available in ABAQUS v6.14/CAE software, which is suitable for modelling both plain and reinforced concrete, under varying types of static and dynamic loads such as monotonic, cyclic etc. The concrete behaviour in the axial concrete damaged plasticity model was given by Lubliner et al. (1989) and the yield surface of this model was

later modified by Lee and Fenves (1998). In this model, it is assumed that the concrete fails mainly due to tensile cracking and crushing of concrete due to compression. The combined behaviour of steel and concrete is replicated by using embedded element technique. CDP model assumes non-associated plastic flow. The flow potential G used in the present investigation is based on Drucker-Prager hyperbolic function as expressed in (4.5).

$$G = \sqrt{(\in \sigma_{t0}\ tan\,\Psi)^2} + \overline{q}^2 - \overline{p}\,tan\,\Psi \qquad (4.5)$$

Where,

σ_{t0} - Uniaxial tensile stress at failure

$\overline{p}$ - Hydrostatic pressure stress

$\overline{q}$ - Mises equivalent effective stress

Ψ - Dilation angle

∈ - Eccentricity

The stress-strain behaviour of concrete (i.e., uniaxial tensile and compressive response of concrete) is characterized by damaged plasticity, as shown in Figure 4.12.

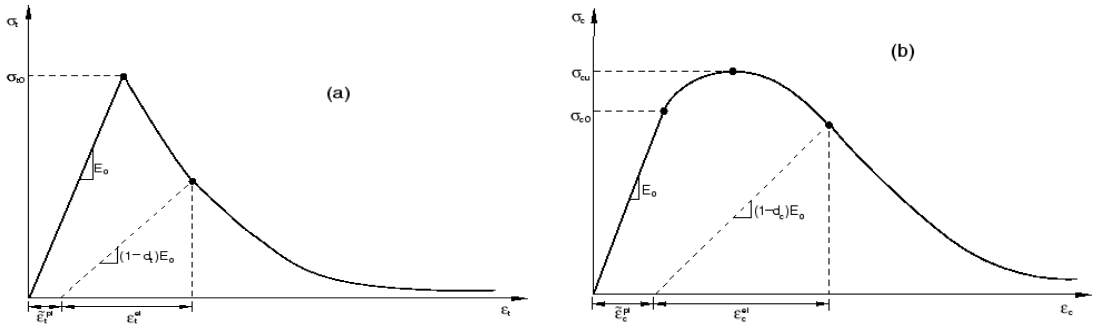

(a) Uniaxial tension **(b)** Uniaxial compression

Figure 4.12 The stress-strain behaviour of concrete (ABAQUS user's manual, 2011)

The strength of concrete under uniaxial tension and compression determines the shape of flow potential and the corresponding load surfaces. The changes made for the CDP model was that the failure surface considered in the deviatoric plane need not be a circle as shown in Figure 4.13, and the shape of deviatoric plane is given by a parameter K_C. As recommended by the user's manual of ABAQUS, the failure surface for K_C = 2/3 was used in the analysis.

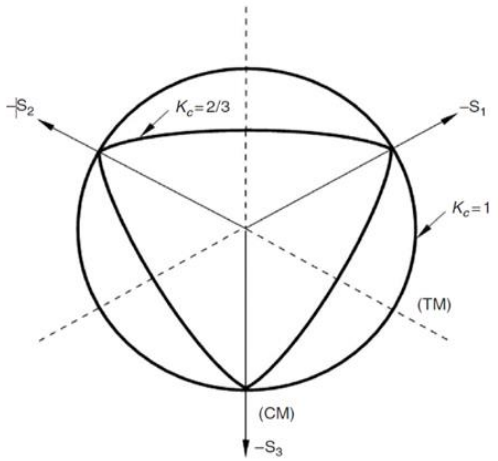

Figure 4.13 CDP deviatoric plane for different values of K_C (Jankowiak and Lodygowski, 2005)

The input parameters used in the analysis by CDP constitutive models are shown in Tables 4.4 and 4.5 Simulia ABAQUS user's manual (2011).

Table 4.4 Input parameters used in CDP

Ψ	dilation angle	35°
e	eccentricity	0.1
F	σ_{bo}/σ_{co}	1.12
K_c	q_{TM}/q_{CM}	0.67
Viscosity parameter		0

Table 4.5 Input parameters used for concrete damage in CDP

Concrete compression damage		**Concrete tension damage**	
Damage parameter (C)	**Inelastic strain**	**Damage parameter (T)**	**Cracking strain**
0	0.000828016	0	0
0.81	0.003573541	0.99	0.001494322

4.4.2 FE simulation

Non-linear 3D solid finite element analysis is performed on RCC beam under four-point loading test to determine its ultimate moment capacity. The geometry of rebar sections and concrete beam sections are created in ABAQUS. These sections can be extruded in 3D space. A solid 3D deformable model of the reinforced concrete beam with 200 mm depth and 150 mm width with a length of 1800 mm is developed. Reinforcement of length 1800 mm and appropriate stirrups (dimensions are given in Table 6) for M30, M50, M70 (OR and UR) beams

are developed. Properties of both concrete and rebar materials used in simulations were created in property module and assigned to the respective parts and are shown in Tables 4.6-4.7.

Table 4.6 Reinforcement details of RCC tested beams

Beam Designation	Top bars (mm)	Bottom bars (mm)	8ϕ stirrups spacing (mm)
M30 UR	2-8ϕ	3-10ϕ	130
M30 OR	2-8ϕ	2-16ϕ, 2-10ϕ	95
M50 UR	2-8ϕ	4-12ϕ	75
M50 OR	2-8ϕ	3-20ϕ	60
M70 UR	2-8ϕ	3-16ϕ	75
M70 OR	2-8ϕ	4-20ϕ	50

In numerical simulation, concrete specimen is loaded by creating a rigid body surface (applicator) and imparting load to the applicator. Between rigid body surface and concrete beam specimen, where the load is applied, contact conditions are used. Hence, the pressure force applied on the specimen is distributed to replicate experimental conditions. Using an embedded region option in ABAQUS constraints tab, rebars are embedded in concrete with the same degrees of freedom, hence, creating a perfect bond between concrete and rebar. For concrete, an 8-noded linear brick element (C3D8R element) with reduced integration formulation is used. For rebar, T3D2 (Truss element) a 2-noded linear 3D truss element is used in modelling. The geometry of the meshed RCC beam is shown in Figure 4.14.

Table 4.7 Concrete and reinforcement steel properties used in simulation model

Grade of Concrete (MPa)	Concrete Mechanical Properties			Steel Properties	
	Density (kg/m^3)	Elastic Modulus (MPa)	Poisson's ratio	Density (kg/m^3)	Poisson's ratio
M30	2400	27400	0.15	7850	0.3
M50	2400	35350	0.15	7850	0.3
M70	2400	41830	0.15	7850	0.3

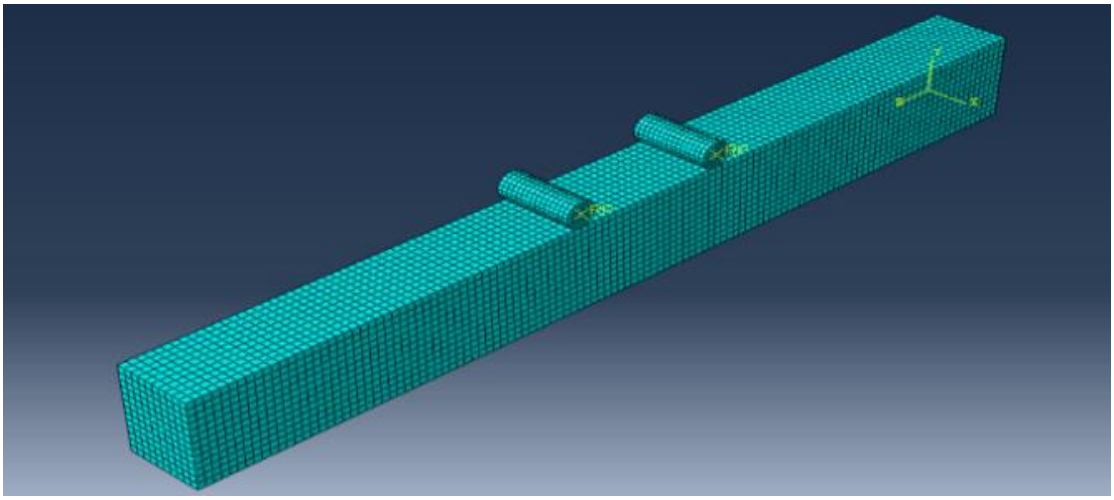

Figure 4.14 Meshed RCC beam using ABAQUS software

Pinned support boundary condition is prescribed on both the sides of RCC beam at 100 mm from the edges (in initial step). Also, applicator is constrained to move only in the direction of loading. Step1 is created, and load is assigned using displacement control. The deflections at the end of analysis for the entire beam and reinforcements within is shown in Figure 4.15. Comparison of simulation results with both DIC and conventional mid-span deflection is done.

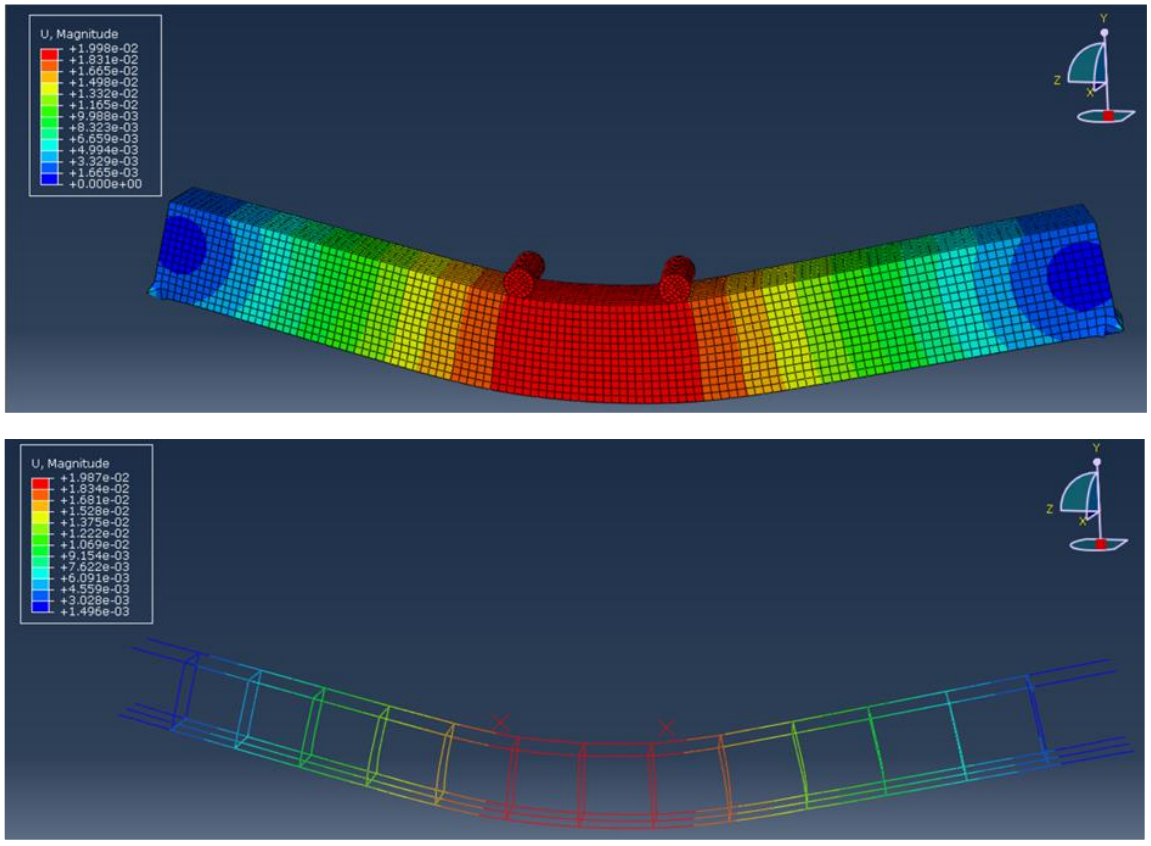

Figure 4.15 Deflection profile of RCC beam using ABAQUS software

DIC results are compared with standard numerical tool ABAQUS v6.14/CAE software and conventional results obtained using dial gauges and actuator data for both the specimens. A 3D solid finite element analysis ABAQUS 6.14/CAE numerical simulation tool is used to validate the results obtained from RCC beams of both conventional and DIC measurements.

4.5 Results and Discussions

The deflection curves are plotted with the corresponding loads obtained from the UTM using the results obtained from both conventional and DIC measurements. These curves are also compared with FEA results. The contour of X and Y axis deformations obtained from random speckle pattern (DIC) is shown in Figure 4.16. The load-deflection curves are plotted using DIC and compared with conventional crosshead motion of RCC beam and FEM results shown in Figures 4.17-4.22. The average load-deflection curves plotted are taken as the average of three beams.

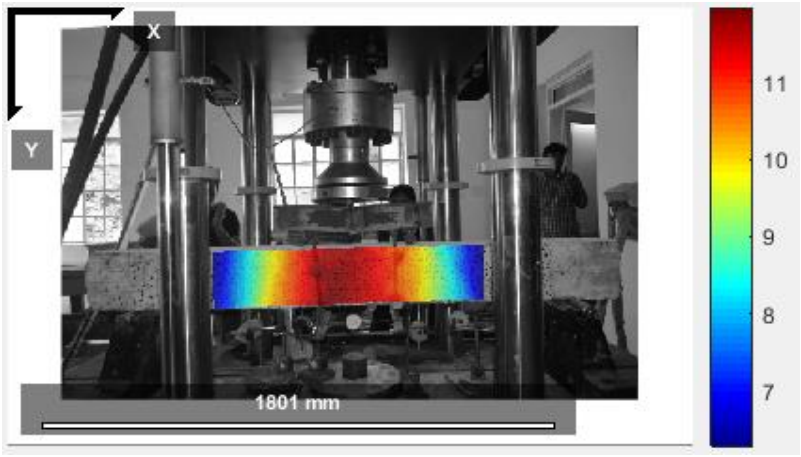

(a)

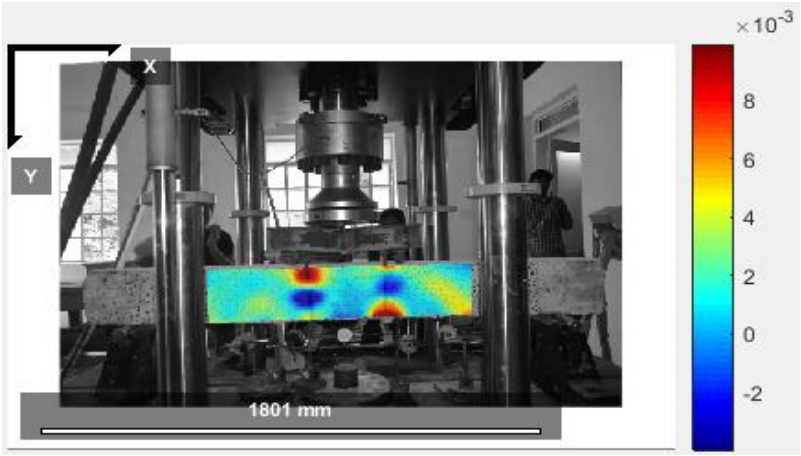

(b)

Figure 4.16 Contour obtained using random speckle pattern (a) Vertical displacement (mm) (b) Horizontal displacement (mm)

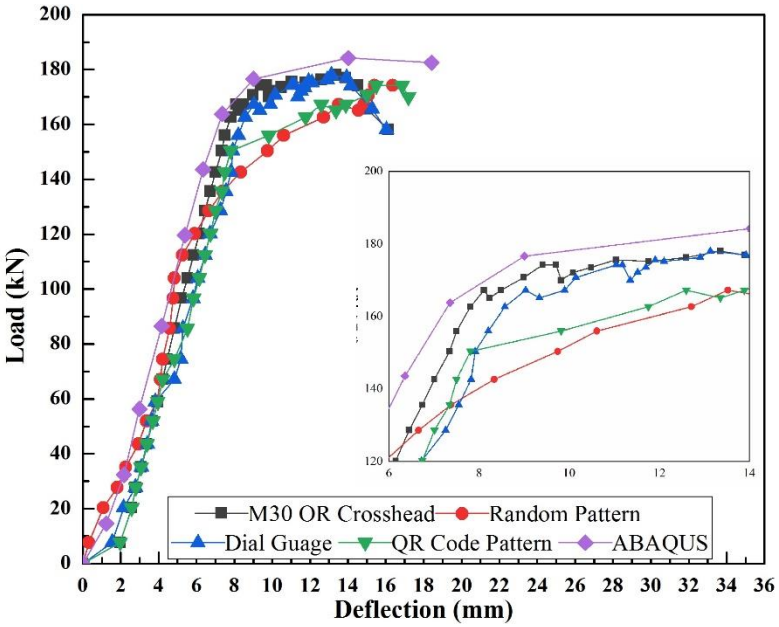

Figure 4.17 Load vs Mid-span deflection of M30 over-reinforced RCC beam

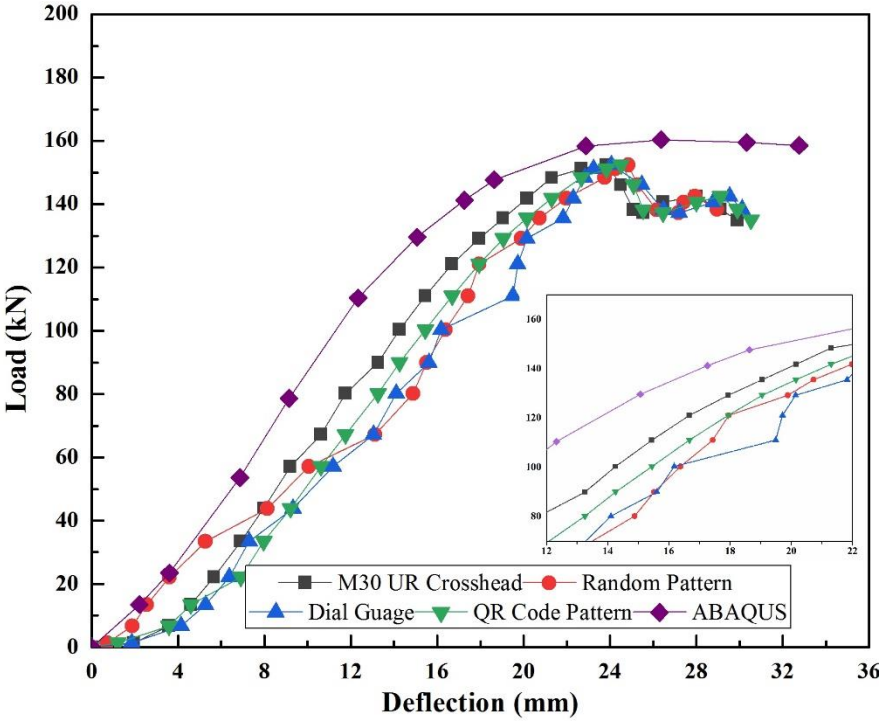

Figure 4.18 Load vs Mid-span deflection of M30 under-reinforced RCC beam

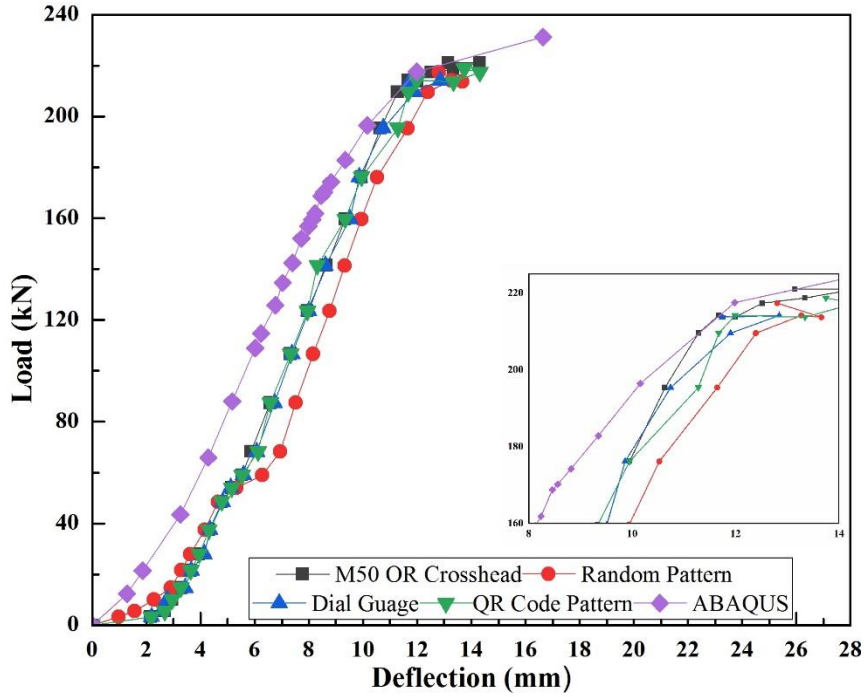

Figure 4.19 Load vs Mid-span deflection of M50 over-reinforced RCC beam

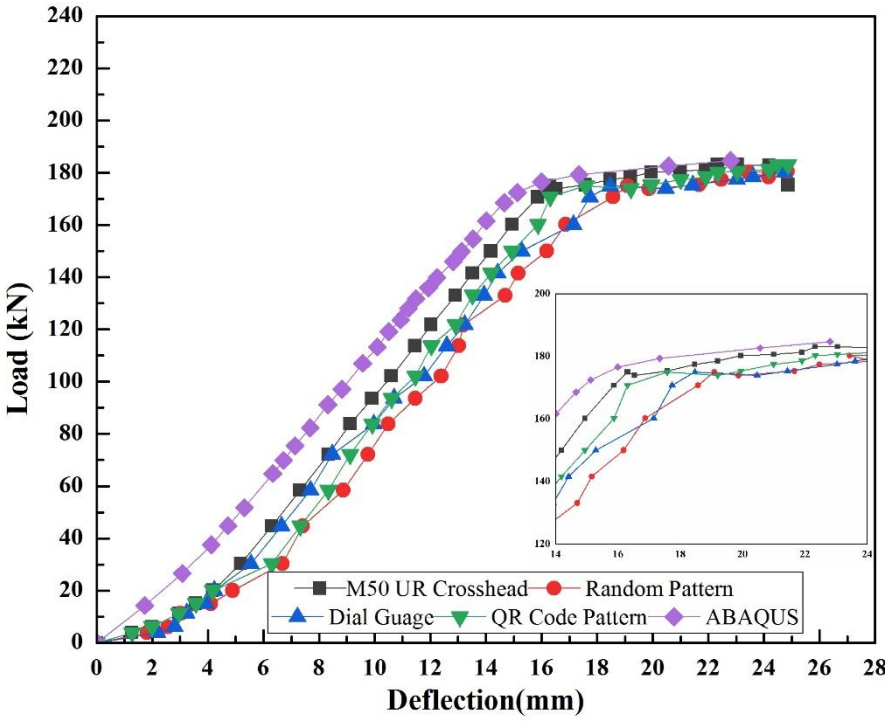

Figure 4.20 Load vs Mid-span deflection of M50 under-reinforced RCC beam

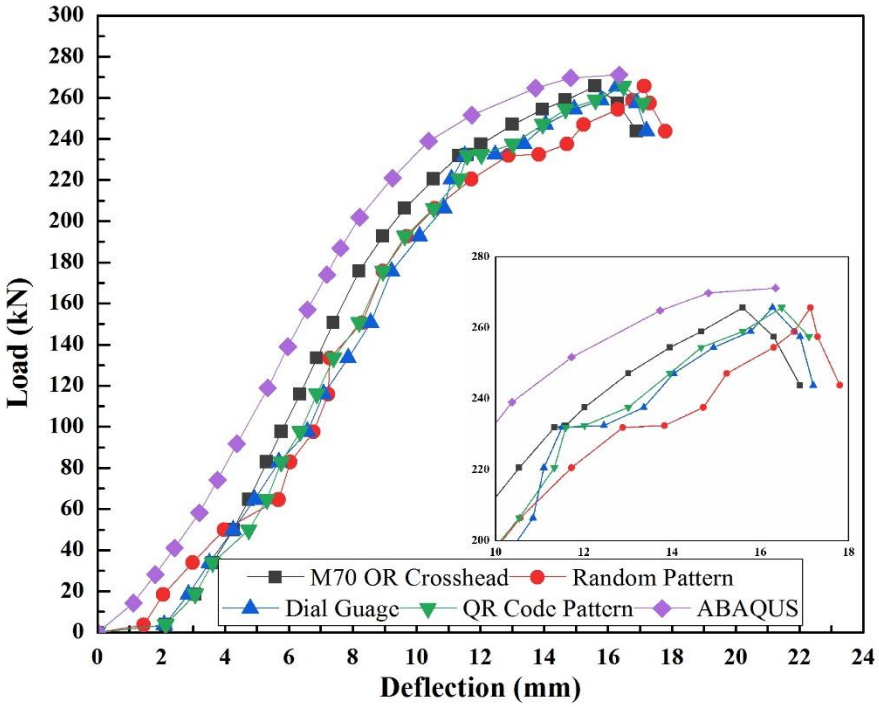

Figure 4.21 Load vs Mid-span deflection of M70 over-reinforced RCC beam

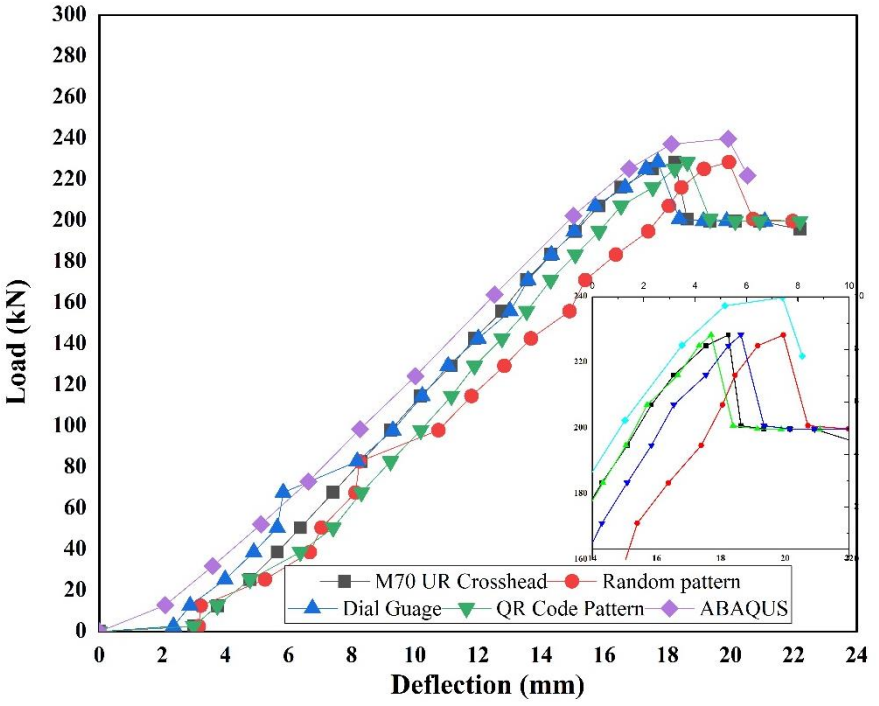

Figure 4.22 Load vs Mid-span deflection of M70 under-reinforced RCC beam

4.5.1 Moment (M)-Curvature (κ) relationship obtained from LVDTs/dial gauges

The curvature of the beams is measured by placing curvature meters in both the compression as well as in tension zones. Curvature meters having least count of 0.001 mm are fixed between two rectangular frames, one at the top and another at the bottom. Schematic view of the test setup is shown in Figure 4.23. Based on the radius of the top and bottom curvature meters, the

average curvature is calculated. The deflections are measured using two load points, which is at the midpoint of the beam and at the points located midway between the supports and the midpoint, using dial gauges.

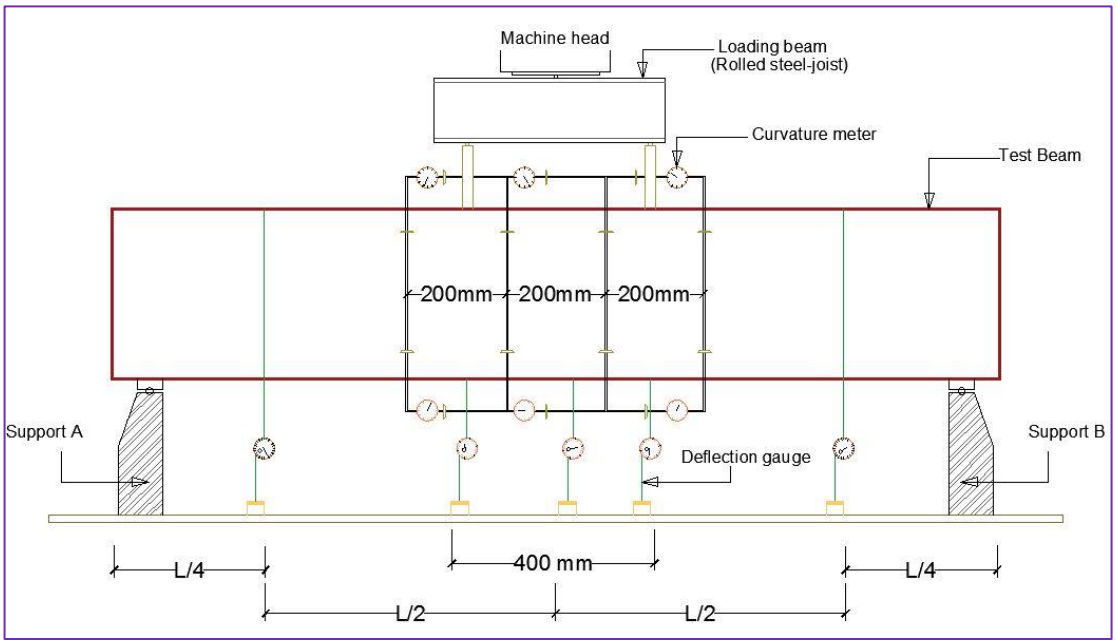

Figure 4.23 Schematic view of the test setup for RCC beam

4.5.2 Comparison of the measured flexural behaviour of concrete beams

M-κ relationship developed with the results obtained using DIC is compared with results developed using conventionally obtained results and FEM results. The method adopted for developing M-κ relationship is similar (MLV Prasad and Rathish, 2012, Dutton et al. 2013, Swamy Naga Ratna Giri et al. 2018). It is observed that the moment carrying capacity of UR beams is less than OR beams. The grade of concrete increases with the moment carrying capacity, while the curvature of the beam at ultimate moment will decrease as shown in Figures 4.24-4.26. It is observed that the conventional and numerical results are matching with those of DIC technique. Tables 4-6 show the ultimate M-κ values of both UR and OR concrete RCC beams obtained from both conventional measurements and DIC technique using different speckle patterns.

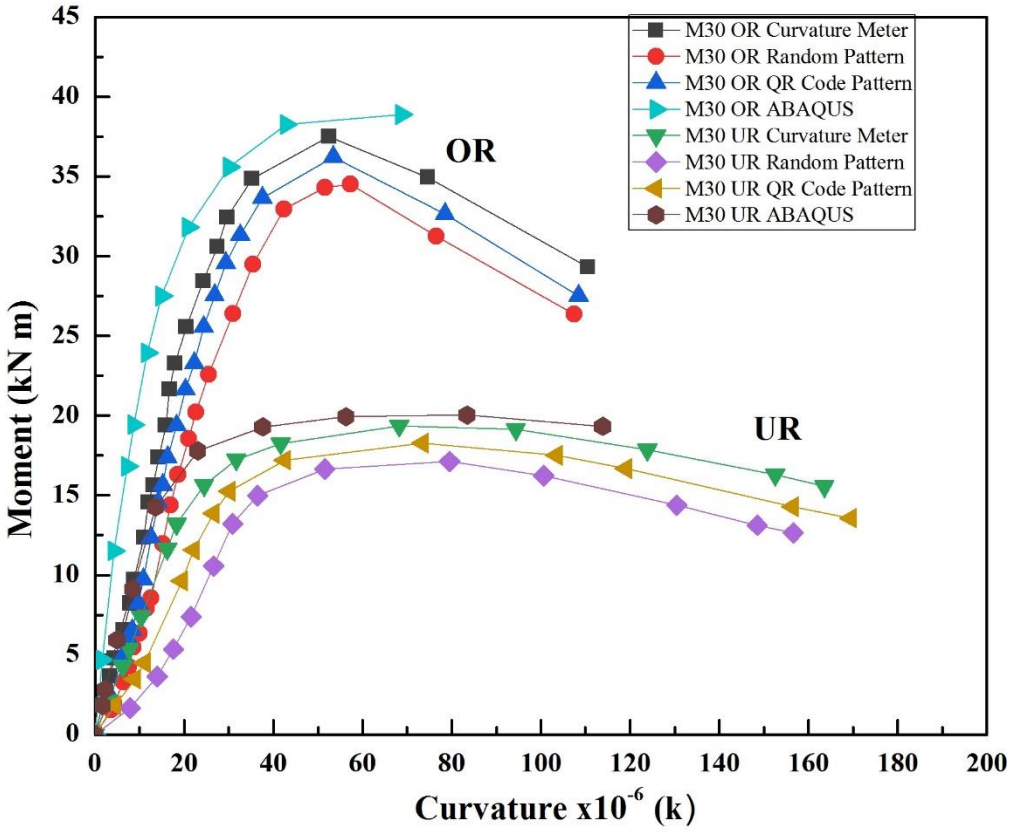

Figure 4.24 M-κ curve for M30 concrete grade

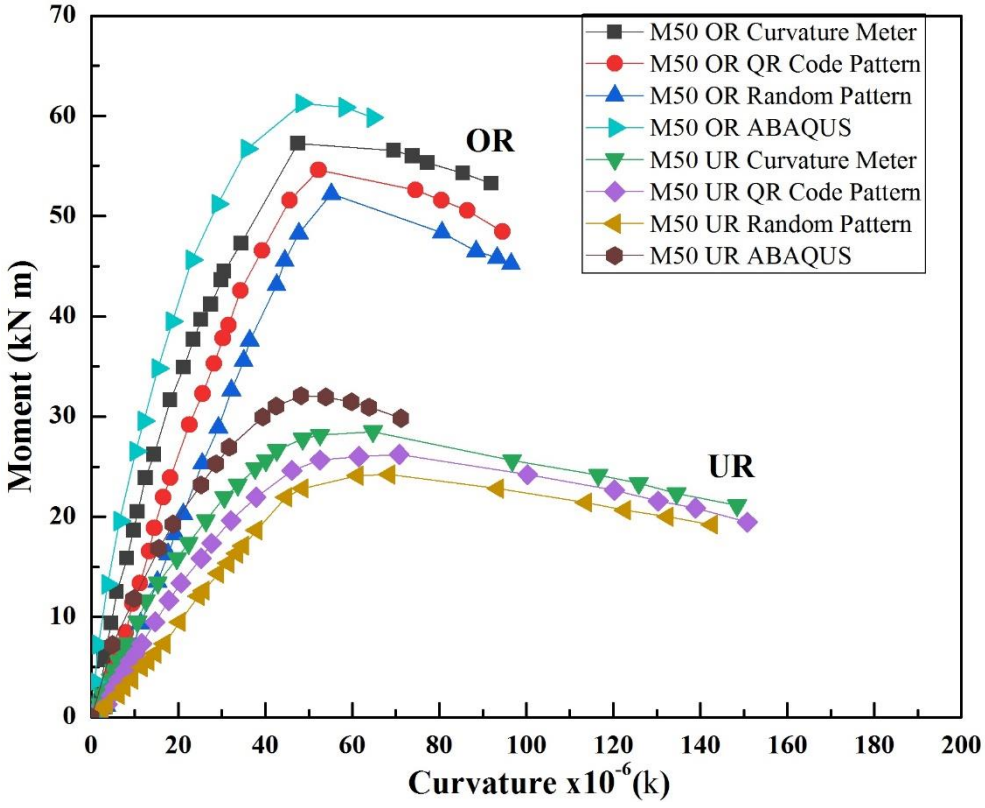

Figure 4.25 M-κ curve for M50 concrete grade

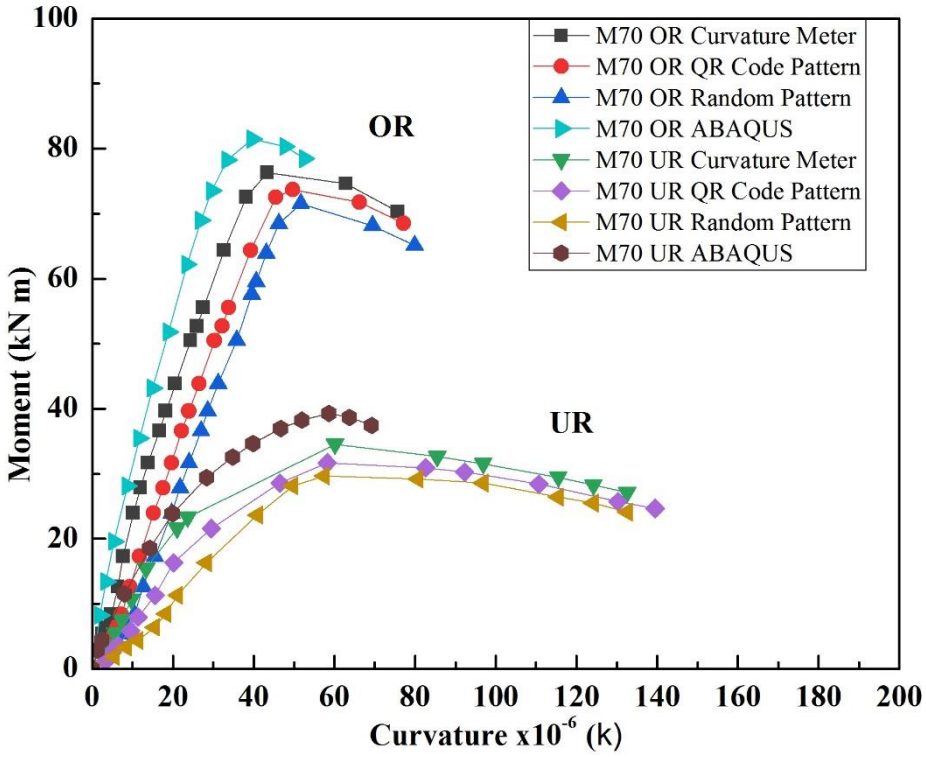

Figure 4.26 M-κ curve for M70 concrete grade

It is observed that the M-κ curves extracted using QR code speckle pattern closely match the curves obtained from conventional measurements. As expected, the moment carrying capacity of OR beams is higher compared to UR beams. However, with the increase in grade of concrete, the moment carrying capacity increases while the curvature of the beam at the ultimate moment (M_u) decreases.

4.5.3 Conventionally measured M-κ at ultimate values: Table 4.8 shows the *M-κ* data for which ultimate values are compared between normal (M30), medium (M50) and high strength (M70) concretes for both UR and OR categories obtained from conventional measurements (LVDTs/Dial gauges).

Table 4.8 Compression and tensile strains of ultimate M-κ

Grade	M (kN-m)	$\kappa \times 10^{-6}$	$\epsilon_c \times 10^{-6}$	$\epsilon_s \times 10^{-6}$
M30 UR	19.35	68.23	2416	9865
M30 OR	37.5	52.5	5054	4410
M50 UR	28.5	64.77	2865	8794
M50 OR	57.24	47.52	5375	3178
M70 UR	34.54	60.21	3168	7670
M70 OR	76.28	43.35	5841	1965

(a) M-κ obtained from DIC at ultimate values using random speckle pattern: Table 4.9 shows the DIC M-κ data at ultimate values where the beam is tested with random speckle pattern throughout the cross-section of the beam.

Table 4.9 Compression and tensile strains of ultimate M-κ obtained using DIC (random speckle pattern)

Grade	M (kN-m)	$\kappa \times 10^{-6}$	$\epsilon_c \times 10^{-6}$	$\epsilon_s \times 10^{-6}$
M30 UR	17.12	79.48	4333	9975
M30 OR	34.51	57.33	6120	4200
M50 UR	24.21	68.55	3760	8580
M50 OR	52.21	55.18	5813	4120
M70 UR	29.64	57.52	3121	7234
M70 OR	71.55	51.65	7096	2201

(b) M-κ obtained from DIC at ultimate values using QR code as speckle pattern Table 4.10 shows M-κ DIC data at ultimate values for which the beam is tested with QR Code based speckle pattern.

Table 4.10 Ultimate M-κ results for compressive strain and tensile strain obtained using DIC (QR code)

Grade	M (kN-m)	$\kappa \times 10^{-6}$	$\epsilon c \times 10^{-6}$	$\epsilon s \times 10^{-6}$
M30 UR	18.26	73.45	4007	9215
M30 OR	36.21	53.46	5755	3869
M50 UR	26.23	70.76	3922	8815
M50 OR	54.58	52.26	5422	3986
M70 UR	31.65	58.24	3125	7269
M70 OR	73.71	49.68	6932	2012

Table 4.11 Comparison of ultimate M-κ results obtained from contact and non-contact sensors

	Conventional		Random speckle pattern				QR code speckle pattern			
Specimens	M	κ	M	κ	M^1	κ^1	M	κ	M^1	κ^1
M30 UR	19.36	68.24	17.13	79.49	11.51	16.48	18.27	73.46	5.63	7.64
M30 OR	37.52	52.51	34.52	57.34	7.99	9.19	36.22	53.47	3.46	1.82
M50 UR	28.51	64.78	24.24	68.56	14.97	5.83	26.24	70.77	7.96	9.24
M50 OR	57.25	47.53	52.22	55.19	8.78	16.11	54.59	52.27	4.64	9.97
M70 UR	34.53	60.22	29.65	57.53	14.13	4.44	31.66	58.25	8.31	3.27
M70 OR	76.29	43.36	71.56	51.66	6.20	19.14	73.72	49.69	3.36	14.59
				MAE	10.59	11.86			5.56	7.75

MAE: Mean Absolute Error; M^1: % error in moment (kN-m); κ^1: % error in curvature

From Table 4.11, it can be observed that higher moment capacities for RCC beams are consistently observed in case of QR code-based speckle pattern when compared to random

speckle pattern. The maximum percentage error in the ultimate moment is 15% in the case of random speckle pattern whereas it reduces to 8% in case of combined QR code and random speckle patterns. The maximum percentage error in ultimate curvature is 19% in the case of random speckle pattern whereas it reduces to 14% in case of combined QR code and random speckle patterns. The results obtained from the QR code speckle pattern are closer to the results obtained from conventional measurements using LVDT and dial gauges.

Table 4.12 Comparison of ultimate M-κ results obtained from experimental and numerical

Specimens Designation	Conventional		FEM results			
	M	κ	M	κ	M^1	κ^1
M30 UR	19.36	68.24	20.04	79.26	3.51	16.14
M30 OR	37.52	52.51	38.87	61.72	3.59	17.53
M50 UR	28.51	64.78	32.08	53.25	12.52	17.79
M50 OR	57.25	47.53	61.24	48.42	6.96	1.87
M70 UR	34.53	60.22	39.28	58.64	13.75	2.62
M70 OR	76.29	43.36	81.46	39.65	6.77	8.55
				MAE	7.85	10.75

MAE: Mean Absolute Error; M^1: % error in moment (kN-m); κ^1: % error in curvature

From Table 4.12, it can be observed that the mean absolute error percentage in the ultimate moment is 7.85% in case of FEM results and it reduces to 5.56% for the results obtained from DIC using QR code-based speckle pattern. The mean absolute error percentage in ultimate curvature is 10.75% in case of FEM results, and it reduces to 7.75% for the results obtained from DIC using QR code-based speckle pattern. The results obtained from DIC using QR code-based speckle pattern are in good agreement with both conventional measurements as well as FEM results.

4.6 Summary

The non-linear flexural behaviour of rectangular RCC beams for both Under-Reinforced (UR) and Over-Reinforced (OR) beams are tested using random speckle pattern as well as QR code-based speckle pattern. Load-Deflection graphs are plotted for both specimens and Moment (M) – Curvature (κ) relationship is obtained using RCC beams for M30 (normal), M50 (medium) and M70 (high) compressive strengths. The following conclusions are drawn:

- The non-linear constitutive modelling adopted herein is a CDP model applied in the finite element code, ABAQUS. This constitutive model is used to predict the realistic flexural non-linear behaviour of RCC beams.

- ❖ The more random the pattern is, the closer are the DIC results obtained from both FEM and conventional measurements.
- ❖ QR code-based speckle pattern serves a dual purpose of having an additional advantage of data encryption and may be used as consistent non-contact optical sensor in real-time SHM techniques.

CHAPTER 5

Flexural Behaviour of (1:12) Scaled RCC T-Beams

5.0 General

A scaled model which represents a reinforced concrete T-beam has the same geometrical shape as a full-scale model. The scaled T-beam specimens are quasi statically tested in flexure to determine the ultimate load and failure patterns. Four-Point bending tests were conducted on model beams of 2 m span designed to represent 24 m span full-scale beam at 1:12 scale factor. The obtained results were used in the validation of the numerical and analytical models.

DIC is used to validate the response of experimental, analytical and numerical validations of RCC T-beam response. An alternative to traditionally used random speckle pattern in DIC is developed, using QR code-based speckle pattern which encrypts the data for regular structural condition monitoring of critical infrastructure, as well as incorporating data for Building Information Modelling (BIM). The schematic representation of experimental programme is shown in Figure 5.1.

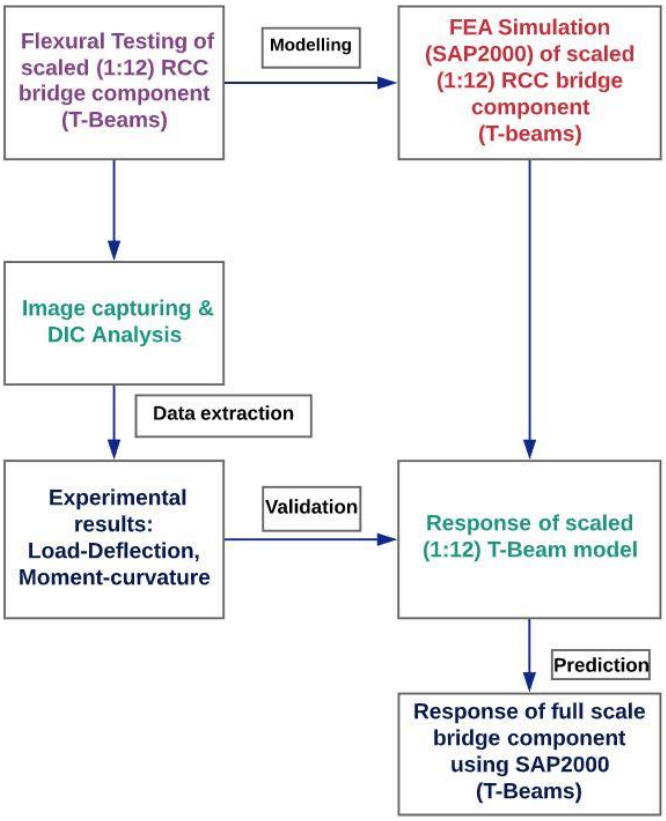

Figure 5.1 Schematic view of the experimental program

5.1 Geometric Scale

Experiment on the field scale models requires more time, sophisticated and substantial machinery and skilled personnel. If the size of the model is minimal, then the fabrication of the model and load application is complicated. To avoid the above complexities, one has to get optimal scale factors for the model prototype. The scaling factors given by Harris and Sabnis (1999) are used in the present work and presented in Table 5.1.

Table 5.1 Geometric scale factors (Harris and Sabnis, 1999)

Structural Type	Strength Models	Elastic Models
Highway bridge	1/20 to 1/10	1/25
Shell roof	1/30 to 1/10	1/200 to 1/50
Dams	1/400	1/75
Wind effects	1/300 to 1/50	Not applicable
Reactor vessel	1/20 to 1/4	1/100 to 1/50
Beam/slab structures	1/10 to 1/4	1/25

Strength models of concrete structures have many dimensional parameters, such as cover, bar spacing, minimum thickness, etc. Law of similitude requirements in materials is a crucial part of this type of models. In this study, a standard Ministry of Road Transport and Highways (MoRTH) bridge with dimensions shown in Table 5.2, is considered for small scale model on which laboratory testing is performed.

Table 5.2 Standard MoRTH Bridge dimensions (Ministry of Surface Transport, 1991)

T-beam Dimensions (mm)	Standard full-scale Model Dimensions (mm)	Scale Factor	Small Scale Model Dimensions (mm)
Span (L)	24000	1/12	2000
Flange (b_f)	2880		240
Flange (D_f)	360		30
Web (b_w)	780		65
Web (d)	2160		180

Similitude requirements for true practical model are shown in Table 5.3. All scale factors are either unity or a function of S_l (scale factor of linear dimension).

5.2 Testing Program

The testing program comprises of casting three T-beams (QR code-based and random) of M30 grade of concrete and using two different types of speckle-patterns on two faces of the same beam with Under-Reinforced (UR) section.

5.2.1 Materials used

53 grade Ordinary Portland Cement (OPC) confirming to IS 12269 (BIS, 1987) is used in this study. River sand corresponding to Zone-II according to IS 383 (BIS, 1970) is used as fine aggregate. The specific gravity of fine aggregate is 2.63 and fineness modulus is about 2.54 with a bulk density of 1.46 gm/cc. The mortar specimens are prepared with a sand-cement ratio (S/C) of 2 and Water-Cement ratio (W/C) of 0.4. Standard steel cubical moulds having a dimension of 150 mm are used for casting the cubes. After curing for 28 days, the average quasi-static compressive strength of cement mortar specimens as stipulated by IS 2250-1981 is approximately 39 MPa.

Table 5.3 Scale factors for RCC models (Harris and Sabnis, 1999)

	Quantity	Dimension	Practical True Model
Material-Related Property	Concrete stress, σ_c	FL^{-2}	1
	Concrete strain, ε_c	--	1
	Young's modulus, E_c	FL^{-2}	1
	Poisson's ratio, v	--	1
	Reinforcing stress, σ_t	FL^{-2}	1
	Reinforcing strain, ε_t	--	1
	Modulus of reinforcing, E_t	FL^{-2}	1
	Bond stress, u	FL^{-2}	1
Geometry	Linear dimension, l	L	S_l
	Displacement, δ	L	S_l
	Angular displacement, β	--	1
	Area of reinforcement, A_r	L^2	S_l^2
Loading	Concentrated load, Q	F	S_l^2
	Line load, w	FL^{-1}	S_l
	Pressure, q	FL^{-2}	1
	Moment, M	FL	S_l^3

5.2.2 Mix proportions

Mix proportions are done based on information available from the literature review. The final mix proportions for M30 grade concrete are presented in proportions of 1:2.

5.2.3 Specimen preparation and testing

Under reinforced (UR) T-beams with 30Mpa of strength are cast and tested. Dial gauges and Linear Variable Differential Transformers (LVDTs) are used to determine the deformations in the beam. The suitability of QR code-based and random speckle pattern are investigated using the DIC technique. The cross-section size of T-beam is shown in Figure 5.2.

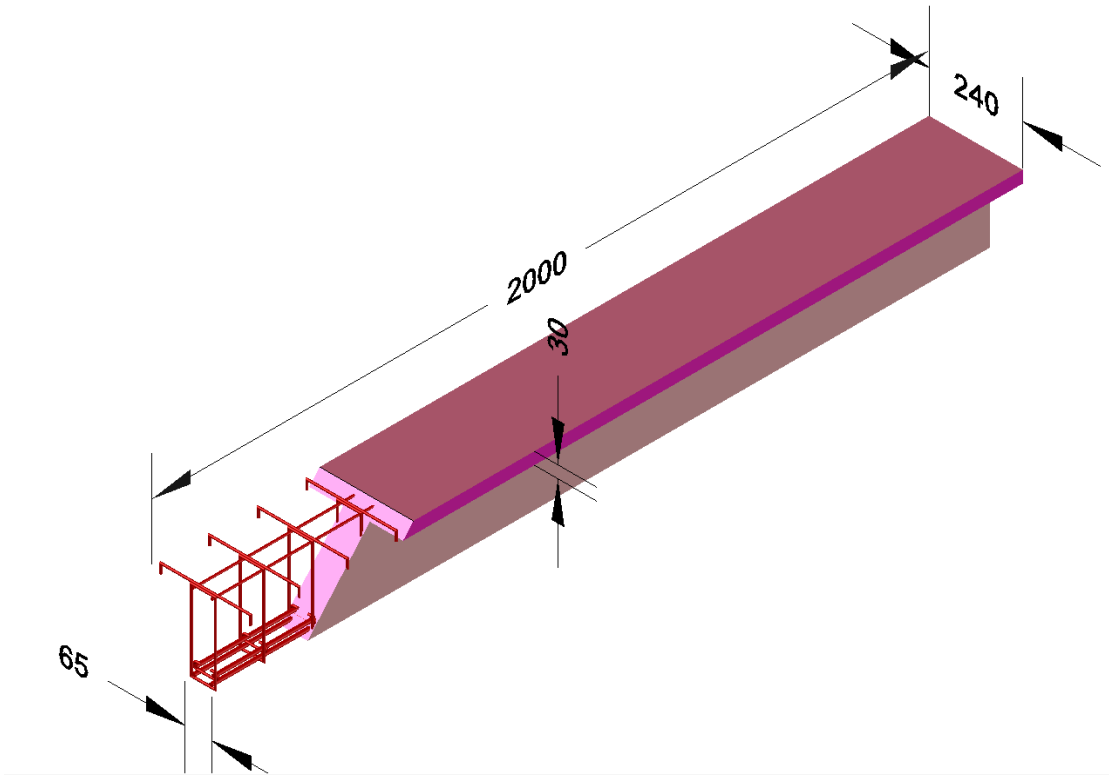

Figure 5.2 Cross-section of T-beam

For the T-beam tested under simply supported condition (refer Figures 5.3a and 5.3b), the deformations are measured using QR based speckle pattern and random speckle pattern which are embossed on the two side faces of the beam. An experimental programme was designed to study the stress-strain behaviour of scaled concrete prism of size 100 mm x 100 mm x 200 mm under axial compression as shown in Figure 5.4. The stress-strain behaviour of scaled concrete is shown in Figure 5.5. Dial gauges and LVDTs are used as contact sensors placed at the bottom surface of the RCC T-beam to find out the deflections. The dial gauges having least count 0.01 mm are used for deflection measurement. LVDTs are used in tension and compression zones and are 200 mm apart from the middle frames. The curvature is measured by placing LVDT at the top (compression) and bottom (tension) surfaces of tested beams. Figure 5.6 shows the test setup for reinforced T-beams.

The beams are quasi-statically tested under 1000 kN Universal Testing Machine (UTM) with a strain rate of 1.0 mm/min. As soon as testing starts, images of the T-beam are taken continuously with the help of two commercially available low-cost DSLR cameras focusing on each side of the T-beam (Nikon D5200 and Nikon D3300) with a lens of f =55mm (DSLR camera), without interrupting the testing process. The specifications of the two cameras used while testing the beams are shown in Table 5.4. The camera was used to capture the consecutive images while loading the specimen. These static images were used for DIC technique using

image processing Ncorr v1.2.2 MATLAB R2018a programming software**.** Using gray scale images, DIC analysis was done and then compared with conventional results obtained from dial gauges and LVDTs.

(a)

(b)

Figure 5.3 Testing of beams using (a) QR code-based speckle pattern (b) Random speckle pattern

(a)

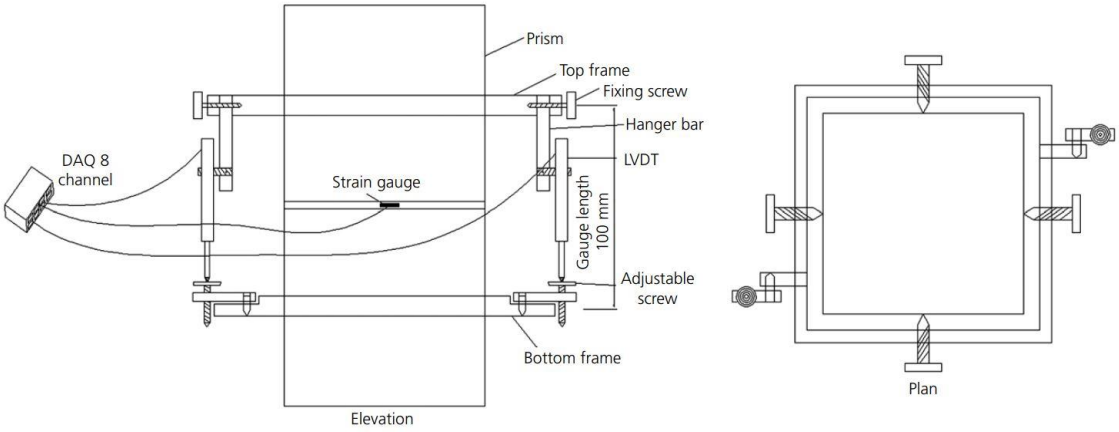

(b)

Figure 5.4 Test setup (a) Experimental (b) Schematic representation

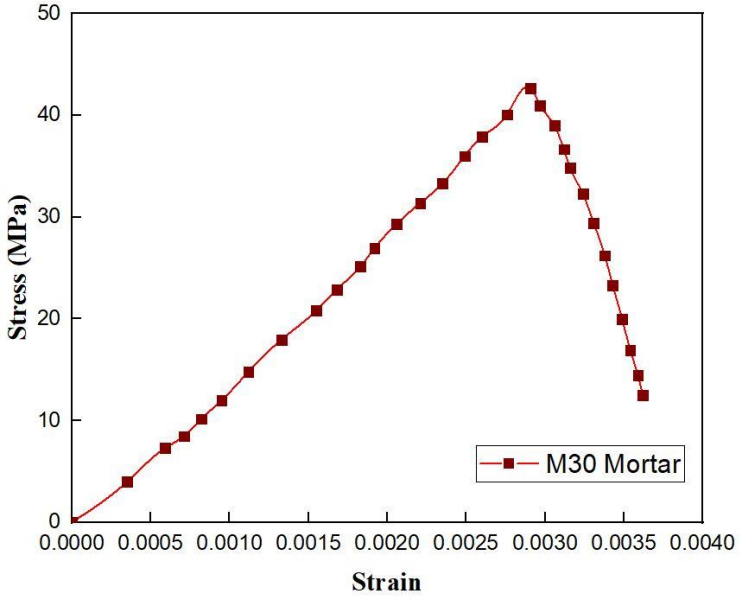

Figure 5.5 M30 stress-strain scaled concrete prism (1:2 ratio)

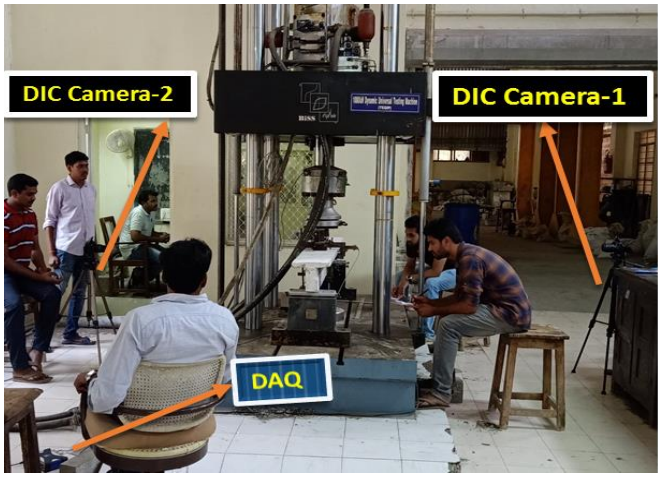

Figure 5.6 Typical flexural loaded T-beam test setup

Table 5.4 Camera parameters (Nikon D5200 and D3300)

Camera Specifications	D5200	D3300
Width	6000 pixels	6000 pixels
Height	4000 pixels	4000 pixels
Horizontal resolution	300 dpi	300 dpi
Vertical resolution	300 dpi	300 dpi
Pixel depth	24 bit	24 bit
Manufacturer	NIKON CORPORATION	NIKON CORPORATION
Model	Nikon DSLR Camera D5200	Nikon DSLR Camera D3300
Colour display	sRGB	sRGB
Shutter speed	1/125 S	1/125 S
Aperture	f/3.5	f/4.5
Iris Aperture	w/o flash	w/o flash
Focal length	18mm	22mm
Focal ratio	f/3.5	f/3.5
Exposure time	1/125 S	1/80 S
ISO speed	ISO-400	ISO-800
Exposure compensation	0	0

5.2.4 Surface histograms of T-beam

Surface histograms for T-beams are obtained, as discussed in section 4.2.1, as shown in Figures 5.7 and 5.8.

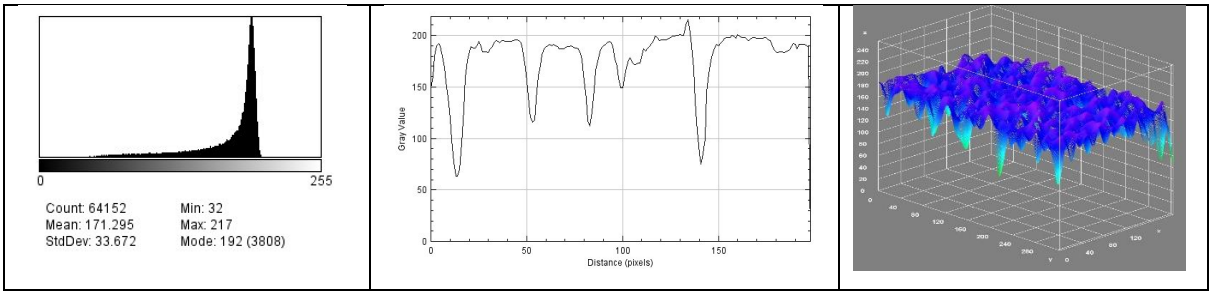

Figure 5.7 Surface histogram of concrete beam showing grayscale intensity for random speckle pattern

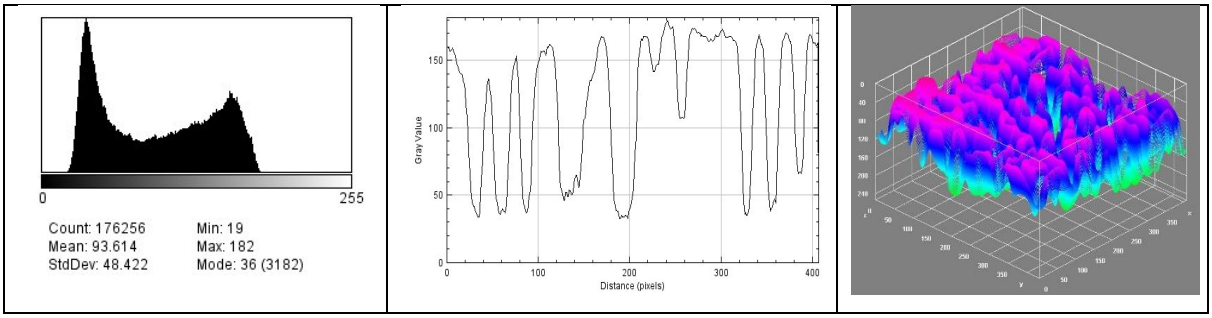

Figure 5.8 Surface histogram of concrete beam showing grayscale intensity for QR code-based speckle pattern

The intention behind using the DIC technique widely is the drop-down prices of Charge Coupled Device (CCD) and Complementary Metal-Oxide-Semiconductor (CMOS) sensor-based cameras. DIC compares digital photographs of the test piece or component at different stages of deformation by identifying blocks of pixels, as shown in Figure 5.9. The system can also measure surface deformation and come up with full-field 2D deformation vector fields and strain maps.

5.2.5 QR Code-based DIC technique

DIC technique has been utilised successfully for large deformation measurements. Due to its simplicity, DIC technique has been extended to curvature studies as well. According to the technique, if the specimen attains the natural texture of random grey intensity value, there is no need to prepare the surface of the specimen. The use of QR code-based speckle pattern is for applications in structural health monitoring. QR code is used for numerous applications in data encryption, data transmission and also as information carrier in web applications. Therefore, using QR code as a speckle pattern for DIC in real-time structural health monitoring provides us with certain advantages, such as QR code encrypted with details of the structure enabling easy identification of the structure by scanning. RCC T-beams were examined using Ncorr v1.2.2, shown in Figure 5.10.

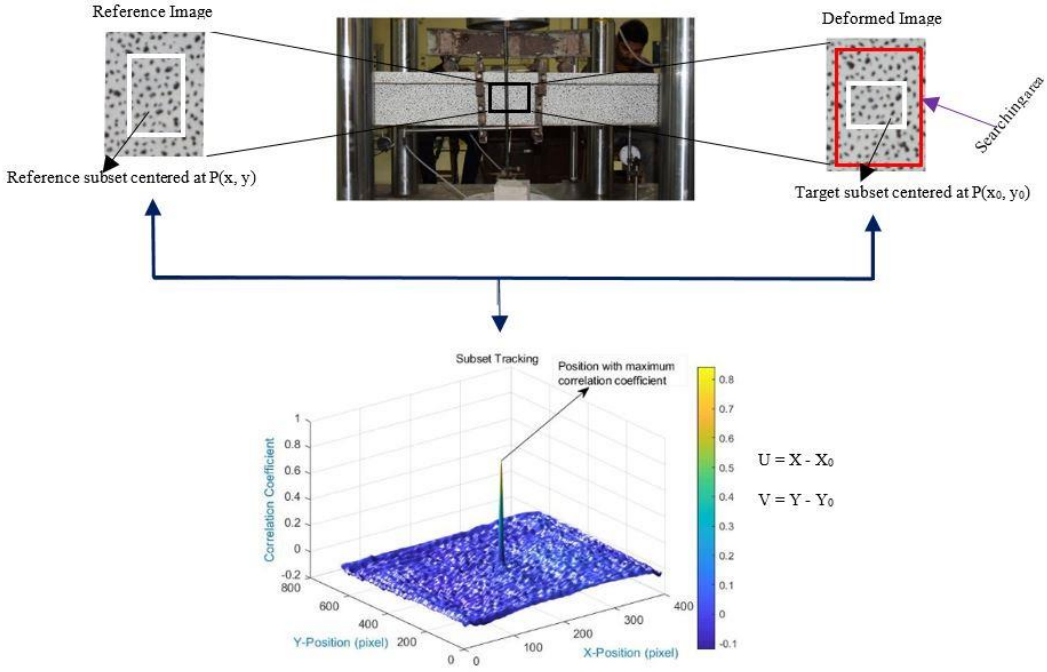

(a)

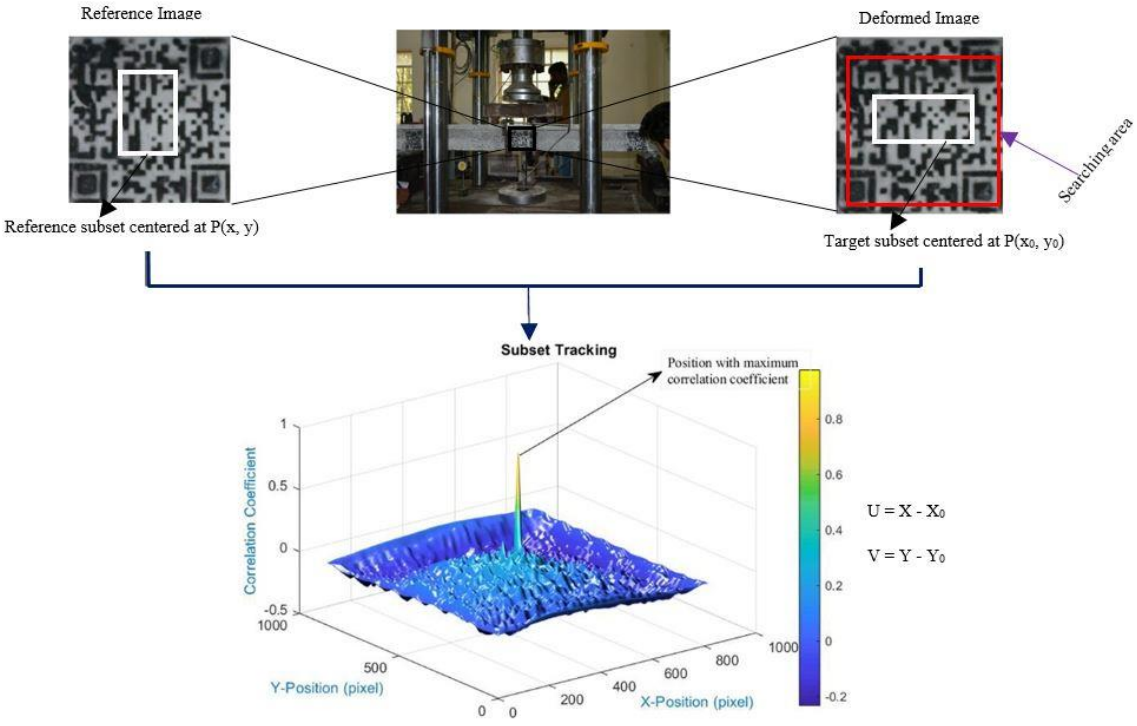

(b)

Figure 5.9 Subset tracking procedure using DIC (a) Random speckle (b) QR code-based speckle pattern

(a)

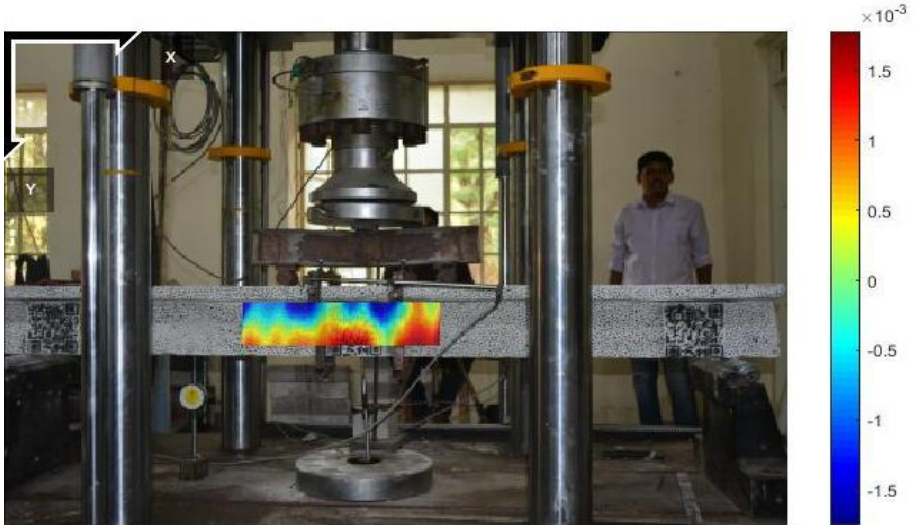

(b)

Figure 5.10 Deflection profile of QR pattern using Ncorr v1.2.2 for T-beams (a) Vertical displacement (mm) (b) Horizontal displacement (mm)

The present work uses QR code-based speckle pattern, verify and validate its results with currently used random speckle pattern in DIC. From this study, it was observed that the results based on QR code-based speckle pattern is on par with those random speckle pattern.

5.3 Finite Element Simulation

T-beams are modelled using the Concrete Damage Plasticity (CDP) Model with same elements and boundary conditions as discussed in section 4.4

5.3.1 T-beam FE simulation

A solid 3D deformable model of reinforced concrete T-beam with a length of 1800 mm was developed. Reinforcement of length 1800 mm and appropriate stirrups (dimensions are given

in Table 5.6) for M30 UR beams were developed, as shown in Figure 5.11. Properties of both concrete and rebar materials used in simulations were created in property module and assigned to the respective parts, as shown in Table 5.5.

Table 5.5 Reinforcement details of RCC T-beams

Beam Designation	Top bars (mm)	Bottom bars (mm)	6ϕ stirrups spacing (mm)
M30 UR	2-6ϕ	2-10ϕ	125

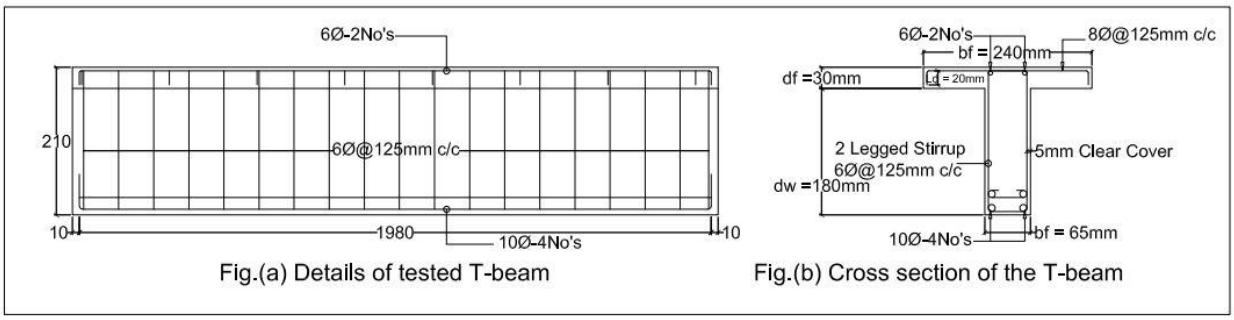

Figure 5.11 Reinforcement details of T-section

Material properties used in the simulation are shown in Table 5.6. The geometry of the meshed RCC beam is shown in Figure 5.12.

Table 5.6 Concrete and reinforcement steel properties used in simulation model

Grade of Concrete in (MPa)	Concrete Mechanical Properties			Steel Properties	
	Density (kg/m^3)	Elastic Modulus (MPa)	Poisson's ratio	Density (kg/m^3)	Poisson's ratio
M30	2400	27400	0.15	7850	0.3

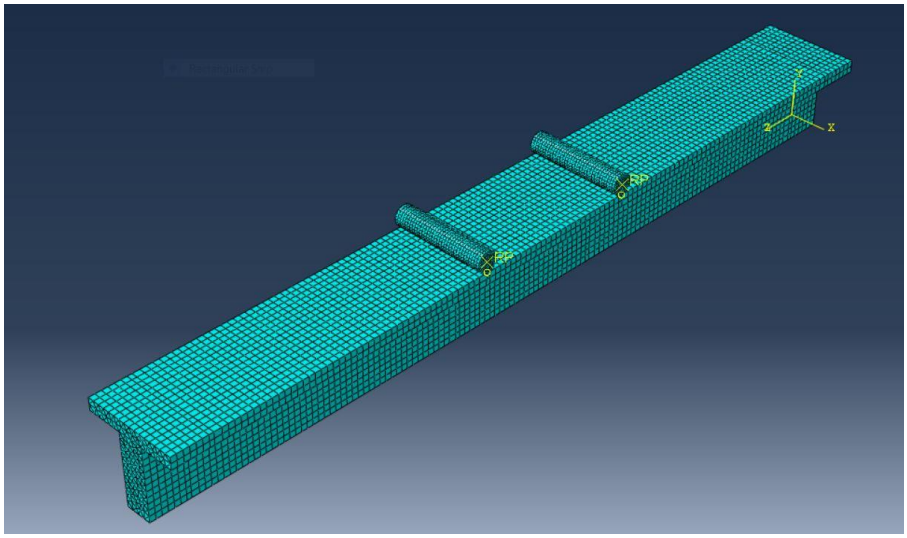

Figure 5.12 Meshed RCC beam using ABAQUS software

The deflections at the end of analysis for the entire beam and reinforcements within is shown in Figure 5.13. Comparison of simulation results with both DIC and conventional mid-span deflection was done.

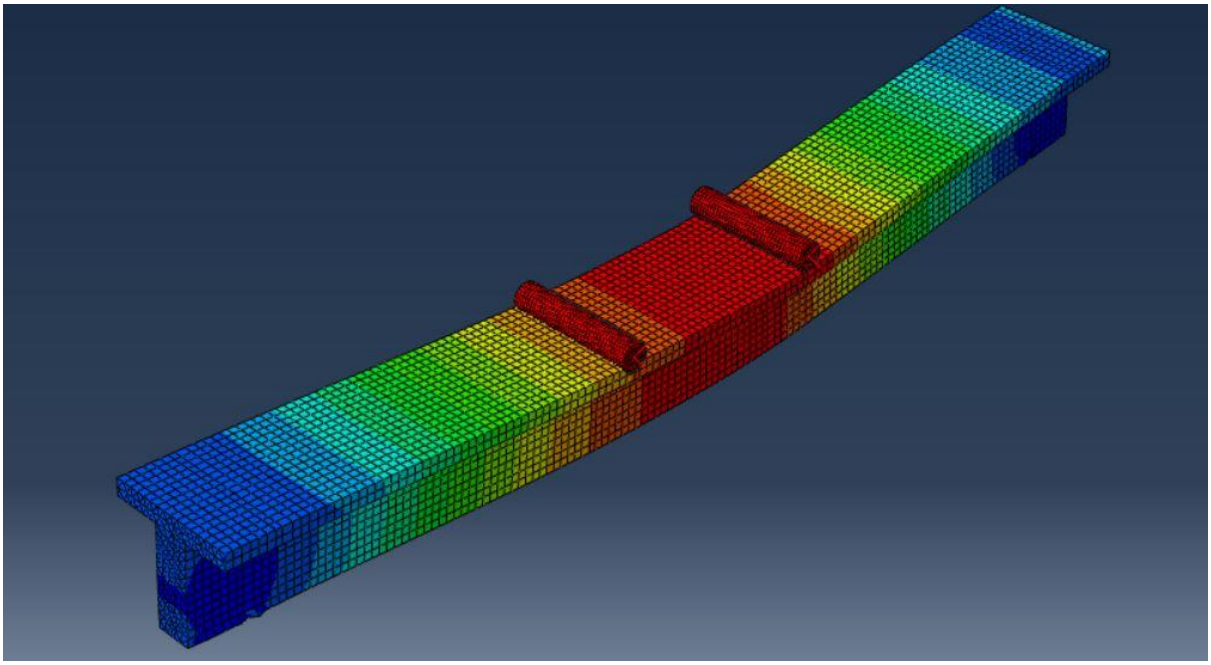

(a)

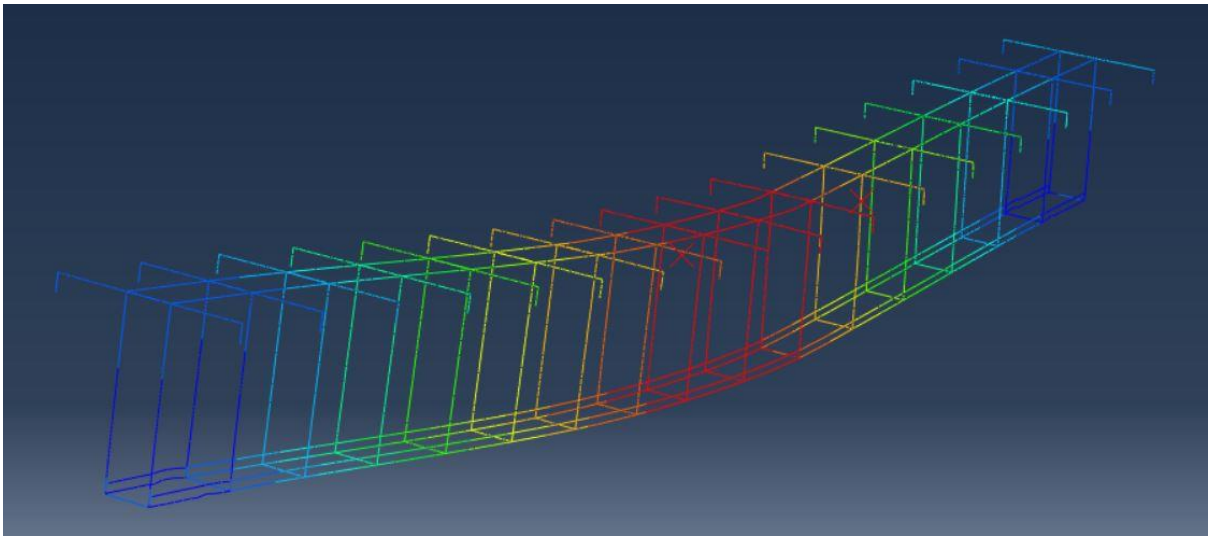

(b)

Figure 5.13 Deflection profile of (a) Solid RCC beam (b) Reinforcement

5.4 Analytical Stress-Strain Model for Scaled Concrete T-Beam

Before the analysis of scaled RCC T-beam, one should understand the stress-strain behaviour of the constitutive materials used in the beams, i.e. steel and scaled concrete. The steel is

manufactured from the industry so there should not be more variation of stress-strain, but concrete is manufactured on-site, so many variations impact the behaviour of concrete (Swamy Naga Ratna Giri et al. 2017). The stress-strain relationship of mortar prism was developed using Saenz's model (1964), who proposed (5.1), given below, initially for ordinary concrete.

$$F = \frac{A_\varepsilon + D}{1 + B_\varepsilon + C_{\varepsilon^2}} \tag{5.1}$$

To determine the stress-strain curve of scaled concrete, the stress ratio and strain ratio are considered as dependent and independent variables instead of stress and strain proposed by Saenz. Equation (5.2) was proposed for non-dimensional stress-strain curve of concrete in axial compression.

$$\frac{f}{f_u} = \frac{A\left(\frac{\varepsilon}{\varepsilon_u}\right)}{1 + B\left(\frac{\varepsilon}{\varepsilon_u}\right) + C\left(\frac{\varepsilon}{\varepsilon_u}\right)^2} \tag{5.2}$$

A, B, C are constants to be evaluated and to evaluate these constants, and the following boundary conditions need to be considered shown in Table 5.7.

Table 5.7 Boundary conditions for scaled RCC T-beams

Boundary condition 1	Boundary condition 2	For ascending portion	For descending portion
At $\frac{\varepsilon}{\varepsilon_u}$ = 1, $\frac{f}{f_u}$ = 1	At $\frac{\varepsilon}{\varepsilon_u}$=1, $\frac{d(\frac{f}{f_u})}{d(\frac{\varepsilon}{\varepsilon_u})}$ = 0	At $\left(\frac{\varepsilon}{\varepsilon_u}\right)$=0.80, $(\frac{f}{f_u})$=0.85	At $\left(\frac{\varepsilon}{\varepsilon_u}\right)$=1.07, $(\frac{f}{f_u})$=0.85

Two sets of A,B, C values are to be proposed, in that one set is for ascending portion, and another set is for descending portion of the stress-strain curve. From the stress-strain curve, it was noticed that a single equation could not explain the entire behaviour of scaled concrete. Two separate equations were proposed based on *Saenz's model* for ascending and descending portion of the stress-strain curve. The boundary conditions are different for ascending and descending portions of the stress-strain curve. By satisfying the boundary conditions, constants A, B, C are shown in Table 5.8, for ascending and descending portion of the stress-strain curve. The experimental and analytical stress ratio vs strain ratio are shown in Figure 5.14.

Table 5.8 Constants for ascending and descending portion of the stress-strain curve

Mortar	A	B	C
Ascending portion	1.2	0.1	0.1
Descending portion	-0.335	0.3	1.02

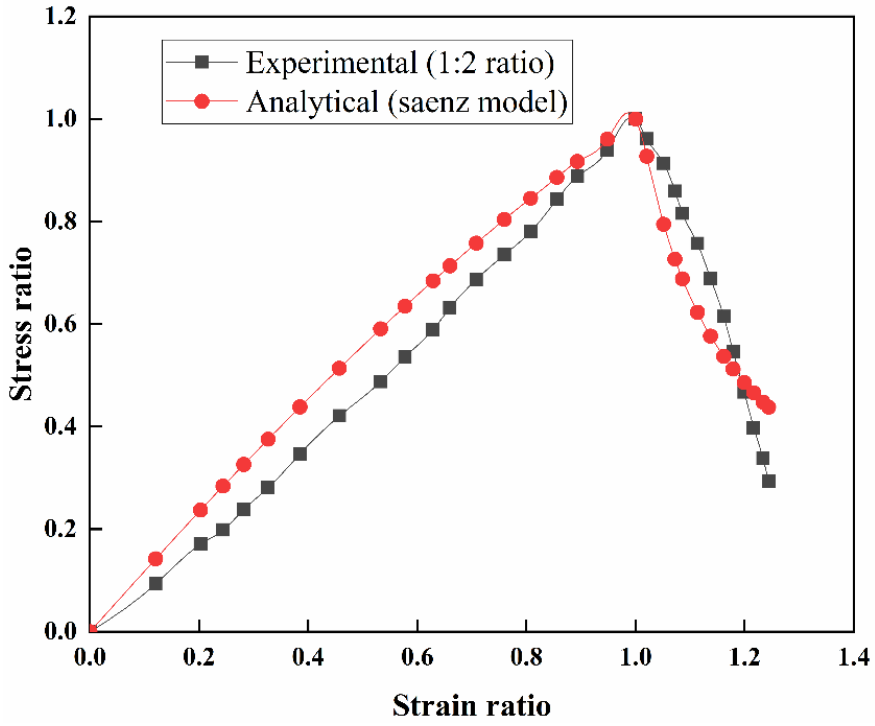

Figure 5.14 Stress ratio vs Strain ratio

5.5 Analytical Moment (M)-Curvature (κ) for Scaled (1:12) T-Beams

Analytical model detailed in section 5.4 describes the behaviour of scaled concrete prism in compression, and now it is proposed to predict the M-κ behaviour of scaled concrete. In deriving a moment-curvature relationship for scaled concrete T-beam section, following are the assumptions:

5.5.1 Assumptions

i. Stress-strain in the selected section is considered as stress block.
ii. The tensile strength of concrete is neglected.
iii. The variation of strain across the section is linear up to the point of failure.
iv. The steel is perfectly bonded.
v. Idealised stress-strain relation for the tension and compression steel is used.
vi. The concrete compressive strain (ε_c) at extreme fibre was assumed to be in the range of 0.0001 up to the failure strain (i.e. 0.01).
vii. Initially, at 0.5 times the effective depth, neutral axis (nd) was assumed (i.e. 0.5d).
viii. For the neutral axis depth values, the compressive force in concrete, Cc, is arrived based on the stress-strain model developed.

ix. The stress in tension and compression is calculated based on the assumption of strain compatibility.

x. Based on the stress-strain curve of steel, the corresponding stresses will be considered.

5.5.2 Procedure adopted for determining analytical M-κ

i. The concrete compressive strain (ε_c) at extreme fibre is assumed to be in the range of 0.0001 up to the failure strain (i.e. 0.01).

ii. Initially, at 0.5 times the effective depth, neutral axis (*nd)* is assumed (i.e. 0.5d).

iii. For the neutral axis depth values, the compressive force in concrete, C_c, is arrived based on the stress-strain model developed in section 5.4.

iv. The stress in tension and compression is calculated based on the assumption of strain compatibility.

v. Based on the stress-strain curve of steel, the corresponding stresses will be considered.

vi. The total tensile force (T) is calculated as tension.

vii. In order to calculate the compressive force (C_s) in compression steel, a similar procedure is adopted (as C_c is calculated).

viii. From the expression $C = C_c+C_s$, the total compressive force (C) acting in the section is calculated.

ix. If C = T, then the assumed value of the neutral axis depth *(nd)* is correct; otherwise, the neutral axis depth is modified until the condition C = T is achieved.

x. After satisfying the condition (C = T), moment (M) and the corresponding curvature (Ø) is calculated.

Now, the total moment at the neutral axis is given in (5.3).

$$M = M_t+M_c+M_{cs}, \quad (5.3)$$

Where M_t is the moment of force in steel subjected to tension, M_c is the moment of compressive force in concrete and M_{cs} is the moment of force in compression steel about the neutral axis. The MATLAB code for this analysis is included in Appendix-A.

5.6 Results and Discussions

T-beams of cross-section size (L=1800 mm, b_f = 240 mm, d_f = 30 mm, b_w = 65 mm and d_w = 200 mm) are cast and tested to evaluate the load-deflection and Moment (M)-Curvature (κ) relationships for UR section. After completion of both conventional and DIC analysis, deflection profiles are plotted with the corresponding load obtained from Universal Testing Machine (UTM). DIC results are compared with standard numerical tool ABAQUS v6.14/CAE

software and conventional results obtained using DIC, LVDT's, dial gauges and actuator data for all the specimens as shown in Figure 5.15.

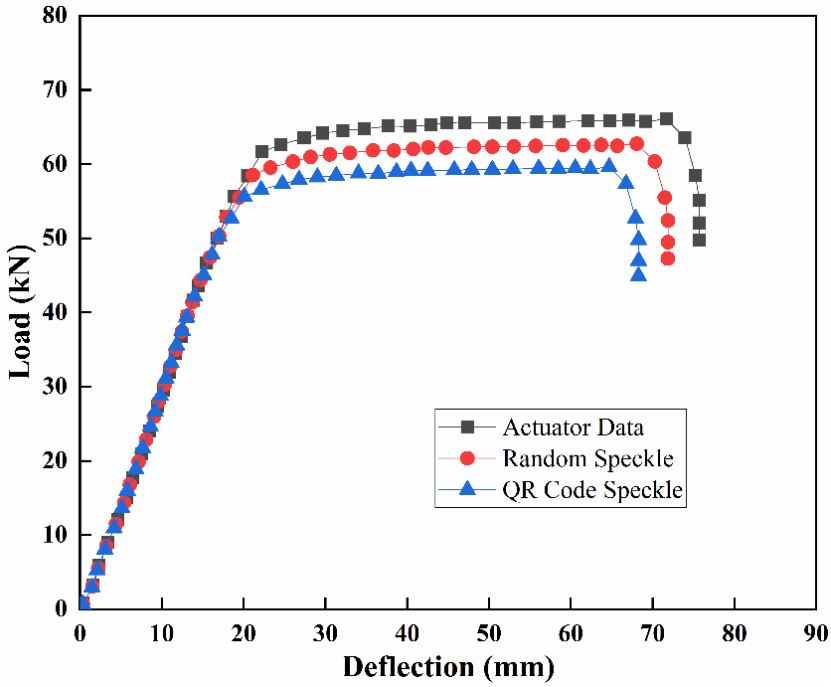

Figure 5.15 Experimental load vs deflection for scaled (1:12) RCC T-beam

5.6.1 Moment (M)-Curvature (κ) relationship for scaled T-beams

The curvature of the beams is measured by placing curvature meters in both the compression as well as in tension zones. Curvature meters having least count of 0.001 mm are fixed between two rectangular frames, one at the top and another at the bottom. Schematic view of the test setup is shown in Figure 5.2. Based on the radius of the top and bottom curvature meters, the average curvature is calculated. The deflections are measured using two load points, which is the midpoint of the beam and at the points located midway between the supports and the midpoint, using dial gages.

A comparison of the Moment (M)-Curvature (κ) values obtained from conventional (dial gauge, curvature meter and crosshead motion) measurements and DIC with different speckle patterns is shown in Figures 5.16 and 5.17. The ultimate M-κ values of T-beams obtained from conventional, analytical and numerical measurements, along with DIC technique using different speckle patterns is shown in Tables 5.9 and 5.10.

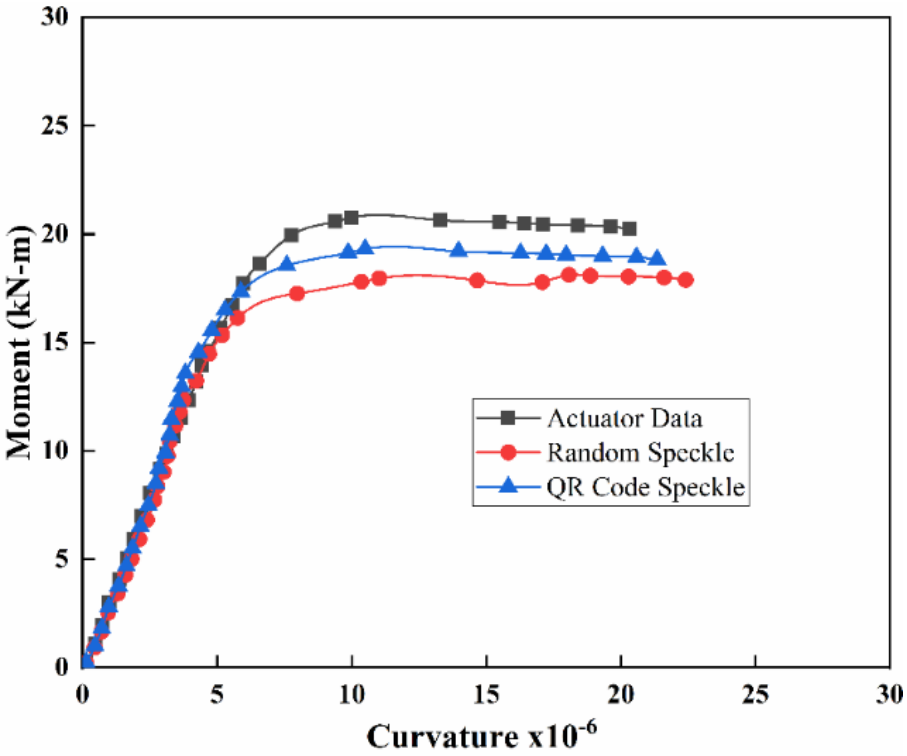

Figure 5.16 M-κ curve for scaled (1:12) RCC T-beam

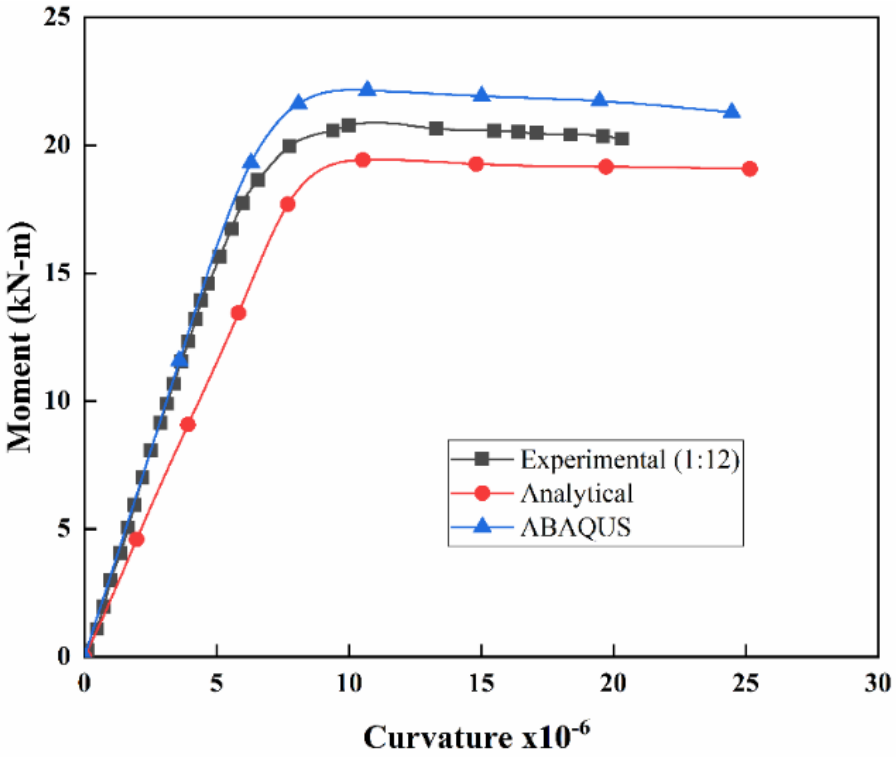

Figure 5.17 Comparison of M-κ curve for scaled (1:12) RCC T-beam

It is observed that M-κ curves extracted using QR code random speckle pattern closely match the curves obtained from conventional measurements.

5.6.2 M-κ results at ultimate values using random and QR speckle patterns

Table 5.9 shows the DIC M-κ data at ultimate values where the beam is tested with both speckle patterns throughout the cross-section of the beam. After testing the beam, results are extracted using Ncorr. The results obtained from the software are compared with conventionally obtained data. Table 5.10 shows M-κ DIC data at ultimate values obtained using analytical and FEM with that of conventional method of testing.

Table 5.9 Comparison of ultimate M-κ values of beams obtained using random and QR code speckle patterns with that of a conventional method of testing

Specimens Designation	Conventional		Random speckle pattern				QR code speckle pattern			
	M	**κ**	**M**	**κ**	**M^1**	**$κ^1$**	**M**	**κ**	**M^1**	**$κ^1$**
M30	20.76	10.12	18.15	11.025	12.57	8.94	19.31	10.5	6.98	3.74
				MAE	12.57	8.94			6.98	3.74

MAE: Mean Absolute Error; M^1: % error in moment (kN-m); $κ^1$: % error in curvature

Table 5.10 Comparison of ultimate M-κ of beams obtained using analytical and FEM with that of the conventional method of testing

Specimens Designation	Conventional		Analytical				FEM results			
	M	**κ**	**M**	**κ**	**M^1**	**$κ^1$**	**M**	**κ**	**M^1**	**$κ^1$**
M30	20.76	10.12	19.41	10.52	6.47	4.01	22.14	10.7	5.63	5.73
				MAE	6.47	4.01			5.63	5.73

MAE: Mean Absolute Error; M^1: % error in moment (kN-m); $κ^1$: % error in curvature

The maximum percentage error in ultimate moment is 12.57% in the case of random speckle pattern whereas it reduces to 6.98% in case of QR code speckle patterns. The maximum percentage error in ultimate curvature is 8.94% in the case of random speckle pattern whereas it reduces to 3.74% in case of QR code speckle patterns. Similarly, the maximum percentage error in ultimate moment is 6.47% in the case of analytical results, whereas it reduces to 5.63% with FEM based results. The maximum percentage error in ultimate curvature is 4% in the case of analytical results whereas it increases to 5.73% in case of FEM based results. The results obtained from the QR code-based random speckle pattern are closer to the results obtained from conventional measurements and also with analytical behaviour. Greater moment capacity was consistently observed when QR code-based random speckle pattern is used in comparison with random speckle pattern.

5.7 Conclusions Drawn from the Study

The nonlinear flexural behaviour of RCC T-Beams for M30 UR beams are measured using random speckle pattern as well as QR code-based speckle pattern. Load-Deflection graphs are plotted for both specimens and Moment (M)-Curvature (κ) relationship is obtained using RCC beams for M30 compressive strengths. The following conclusions are drawn:

- The M-κ relationships for T-beams obtained from conventional dial gauge and crosshead readings compare well with DIC results obtained using different speckle patterns.
- The scaling factors are derived from the standard law of similitude procedure and their accuracy in satisfying the similarity conditions.
- The designed scaled-down T-beam is cast and tested in a four-point bending test configuration under incremental loads while DIC cameras measured the displacement field and calculated the strain distribution of the T-beam.
- Analytical stress-strain relationship for scaled (1:12) RCC T-beam is validated based on experimental results.
- The QR code serves the dual purpose of embedding data in the structural component as well as functioning as a random pattern for DIC which is helpful for non-contact sensor-based condition monitoring, as well as the integration of component-level data with BIM.

CHAPTER 6

Development of Damage Index Using ANN

6.0 General

In this phase of the study, a feed-forward back-propagation algorithm is used for training the Artificial Neural Networks (ANNs) on experimental and numerical data. Separate ANNs are prepared for rectangular beams and T-beams. The output parameters of ANNs are i) Remaining capacity of the beam component, ii) Corresponding Damage Index (DI). To begin with, numerical simulations are validated with corresponding experimental results of tested scaled RCC beams. For identifying the damage in beams, validated experimental and numerical simulation results are given as input parameters into the ANN and damage status is obtained from the ANN output. Load-deflection curves of rectangular beams and T-beams obtained using both conventional and virtual (DIC) sensors are compared, and a normalized Moment (M)-Curvature (κ) relationship generally applicable for flexural dominated RCC beams is developed.

6.1 Damage Index (DI)

Damage identification is a critical issue in terms of safety and functionality of any engineering structure. DI has been recognised as a useful tool for quantitatively expressing the extent of damage in such structures. This study proposes a neural-network-based SHM scheme using geometric, material and load response (DIC) data as input parameters. MATLAB R2018a (*fitting tool*) software is employed for data processing. After that, samples of training data obtained from virtual sensors are tested and classified, to indicate the health condition of the monitored structure.

Till date, there is no universally accepted DI, although several scales, usually varying between 0 (no damage) to 1 (total collapse), have been proposed by Kappos (1997), Cao Vui (2014) and Kanwar et al. (2007). Among these, the damage index proposed by Cao Vui (2014) is employed in this study because it enables higher resolution of the damage states. Ideally, DI should range within a scale of 0 to 1, as shown in Table 6.1, with 0 representing the state of elastic response, and 1 referring to the state of total collapse. DI can be calculated using (6.1) given below.

$$\text{Damage Index (DI)} = 1 - \frac{\text{Current Capacity}}{\text{Original Capacity}} \quad (6.1)$$

Table 6.1 Proposed damage indices for different states (Cao Vui 2014)

Damage States	Range of Proposed Damage Index (DI)
Minor	0.0-0.05
Light	0.05-0.25
Moderate (Repairable)	0.25-0.50
Severe (Irreparable)	0.50-0.75
Collapse	0.75-1.00

The DI is mapped to the corresponding Condition Rating Number (CRN) as proposed by Bridge inspection and maintenance by Indian Railways Pune. The proposed damage indices and corresponding CRN are shown in Table 6.2.

Table 6.2 Proposed Condition Rating Number (CRN) (Bridge Inspection Manual, 2014)

CRN	Description
1	A condition which warrants rebuilding/rehabilitation immediately
2	A condition which requires rebuilding/rehabilitation on a programmed basis
3	A condition which requires major/special repairs
4	A condition which requires routine maintenance
5	Sound condition
6	Not applicable
0	Not inspected

6.2 Artificial Neural Networks (ANN) Modelling:

ANN are non-linear multi-dimensional regression analysis tools, which may be used to model complex relationships between inputs and outputs (Onal and Ozturk 2010). This technique allows investigation of the relationship between the curvature of the test component and development of a corresponding DI by simulating the component. ANN are composed of several interconnected neurons or simple nodes. Weightage (synaptic weights) is assigned to each neuron. ANN are a family of self-adaptive, flexible computational tools with the capability of capturing non-linear behaviour of complex problems. Similar to a biological neuron in the human brain, the individual neuron in ANN gathers the information, processes and transmits it to other neurons; the input signals in ANN are multiplied by their corresponding synaptic weights and biases, and they are aggregated in a summation layer, which is excited by an activation function, after which the signal is transferred to other neurons. The input vector [x_1, x_2, x_3……x_k] is multiplied by synaptic weights which are fed to the

summing junction. The sum is a dot product of synaptic weight matrix and vector x. The bias μ is also added in the summation layer, which is subjected to an activation function, in order to excite or activate the neurons. The synaptic weight vector is given by (6.2).

$$w = \begin{pmatrix} w_{11} & \cdots & w_{1k} \\ \vdots & \ldots & \vdots \\ w_{i1} & \cdots & w_{ik} \end{pmatrix} \tag{6.2}$$

The mathematical function for the output is given in (6.3).

$$y_i = f\left(\sum_k w_{ik} x_k + \mu_i\right) \tag{6.3}$$

Where x_k is the input signal applied to the neurons, w_{ik} are the weights attached to the input neurons, μ_i is the offset or bias, f is a transfer function, and y_i is the output. One of the most widely used function is the sigmoid transfer function. This transfer function adjusts the input (which may have any value between plus and minus infinity) to output values between the ranges 0 to 1. The sigmoid transfer function is extensively used in neural networks that are trained using the back-propagation algorithm because this function is differentiable. From (6.3) the output can be a non-linear, linear or *sigmoidal* function of the input.

There are two phases for the ANN chosen in this study, i.e. feed-forward phase and back-propagation phase. During the feed-forward phase, the synaptic weights (either defined or random) are applied to the input matrix and are propagated through hidden layers and from hidden layer to output layer. At the output layer, the model is evaluated as part of the training process, and the error between predicted versus actual values is determined. If the error is more than the targeted error, the back-propagation of the neural network takes place wherein readjustment of the weights takes place at every neuron. Then, after the weights are adjusted, the process repeats until the prescribed target error is achieved.

In this study the feed-forward, back-propagation neural network has one input layer with four number of inputs variables, one hidden layer with ten number of neurons and an output layer with two number of output variables for rectangular beams. Whereas one input layer with eight number of inputs variables, one hidden layer with ten number of neurons and an output layer with two number of output variable for T-beams. The algorithm adopted for the training is Levenberg-Marquardt (*trainlm*). Training input parameters considered in the present investigation are shown in Table 6.3.

Table 6.3 Training input parameters used in ANNs

Show Window	true	**Min_grad**	1e-07
Show Command line	false	**Max_fail**	6
Show	25	$\mathbf{M_u}$	0.001
epochs	1000	$\mathbf{M_{u\_dec}}$	0.1
time	inf	$\mathbf{M_{u\_inc}}$	10
goal	0	$\mathbf{M_{u\_max}}$	10000000000

The number of hidden layers and the number of neurons in the hidden layers is determined by the complexity of the problem. The more complex the problem, more the number of neurons required. In fact, it is the most crucial part of ANN architecture. However, it has been observed from the literature that one hidden layer is sufficient for most problems (Hecht-Nielsen 1992, De Villiers & Barnard 1993, Cybenko 1989). For complex problems, where increasing the number of neurons in a single layer does not increase the predictive efficiency of the network two hidden layers may be required.

In the present investigation, the necessary data was input into the MATLAB R2018a *neural fitting* toolbox. Among the input data, 70% are selected as training samples. 15% of the data are selected for testing, and the remaining 15% are selected for validation. MATLAB R2018a neural fitting toolbox automatically divides and arranges the input data in the input layers to [-1, 1], and output data in the output layer to [0, 1] and this process is called data pre-processing. Several iterations are required for the selection of hidden layer neurons based on minimum absolute training error. To calculate the performance of the trained model, statistical indices such as the Correlation coefficient (R), Mean Absolute Error (MAE), and Root Mean Square Error (RMSE) are used as given in (6.4), (6.5) and (6.6). Correlation coefficient (R) is used as the initial model evaluation criteria for different combinations of network architecture with a varying number of nodes in the hidden layer. Detailed performance measures of the ANNs architectures with different statistical indices are given in Tables 6.4, 6.5 and 6.6.

$$\mathrm{RMSE} = \sqrt{\frac{1}{N}\sum_{i=1}^{N}(p_i - o_i)^2} \tag{6.4}$$

$$R = \frac{\sum_{i=1}^{N}(p_i - \overline{p})(o_i - \overline{o})}{\sqrt{\sum_{i=1}^{N}(p_i - \overline{p})^2 \sum_{i=1}^{N}(o_i - \overline{o})^2}} \tag{6.5}$$

$$\mathrm{MAE} = \frac{1}{N}\sum_{i=1}^{N}(p_i - o_i) \tag{6.6}$$

Table 6.4 Parametric study of ANN configurations for rectangular UR beam training data

Hidden Neurons	R	MAE	RMSE
N_h= 2	0.99077	0.03599	0.05697
N_h= 3	0.98963	0.04189	0.06131
N_h= 4	0.98919	0.04163	0.06165
N_h= 5	0.99305	0.03826	0.05697
N_h= 6	0.99541	0.03515	0.05208
N_h= 7	0.99576	0.02924	0.04994
N_h= 8	0.99651	0.03601	0.05531
N_h= 9	0.99875	0.03007	0.04652
N_h=10	**0.99953**	**0.02909**	**0.04376**
N_h= 11	0.99373	0.03739	0.05428
N_h= 12	0.99109	0.04254	0.06013
N_h= 13	0.99324	0.03321	0.0477
N_h= 14	0.99226	0.03484	0.05139
N_h= 15	0.99206	0.03706	0.05376
N_h= 16	0.99285	0.03327	0.04982
N_h= 17	0.99288	0.03379	0.0532

Table 6.5 Parametric study of ANN configurations for rectangular OR beam training data

Hidden Neurons	R	MAE	RMSE
N_h= 2	0.99577	0.04099	0.06197
N_h= 3	0.99463	0.04289	0.06231
N_h= 4	0.99419	0.04263	0.06265
N_h= 5	0.99605	0.03926	0.05797
N_h= 6	0.9974	0.03615	0.05308
N_h= 7	0.99776	0.03024	0.05094
N_h= 8	0.99651	0.03701	0.05631
N_h= 9	0.99875	0.03107	0.04752
N_h=10	**0.99920**	**0.03009**	**0.04476**
N_h= 11	0.99673	0.03839	0.05528
N_h= 12	0.99609	0.04354	0.06113
N_h= 13	0.99824	0.03421	0.0487
N_h= 14	0.99726	0.03584	0.05239
N_h= 15	0.99706	0.03806	0.05476
N_h= 16	0.99785	0.03427	0.05082
N_h= 17	0.99788	0.03479	0.0542

Table 6.6 Parametric study of ANN configurations for scaled RCC T-beam training data

Hidden Neurons	R	MAE	RMSE
N_h = 2	0.99177	0.03699	0.05797
Nh = 3	0.99063	0.04289	0.06231
Nh = 4	0.99019	0.04263	0.06265
Nh = 5	0.99205	0.03926	0.05797
Nh = 6	0.9934	0.03615	0.05308
Nh = 7	0.99376	0.03024	0.05094
Nh = 8	0.99251	0.03701	0.05631
Nh = 9	0.99475	0.03107	0.04752
N_h =10	**0.99576**	**0.03009**	**0.04476**
Nh = 11	0.99273	0.03839	0.05528
Nh = 12	0.99209	0.04354	0.06113
Nh = 13	0.99424	0.03421	0.0487
Nh = 14	0.99326	0.03584	0.05239
Nh = 15	0.99306	0.03806	0.05476
Nh = 16	0.99385	0.03427	0.05082
Nh = 17	0.99388	0.03479	0.0542

Based on the parametric study of ANN configurations, a network with 10 neurons is found to be optimum. The calculated and predicted values of DI are O_i and P_i. Where N is the number of validated samples. The average values of $\overline{O}$ and $\overline{P}$ are O_i and P_i values respectively. The very common choice for feed-forward neural networks is sigmoidal activation function which is shown in Figure. 6.1 and it is also expressed in (6.7). Network output values are restricted between 0 and 1.

$$\phi_x = \frac{1}{1+e^{-x}} \tag{6.7}$$

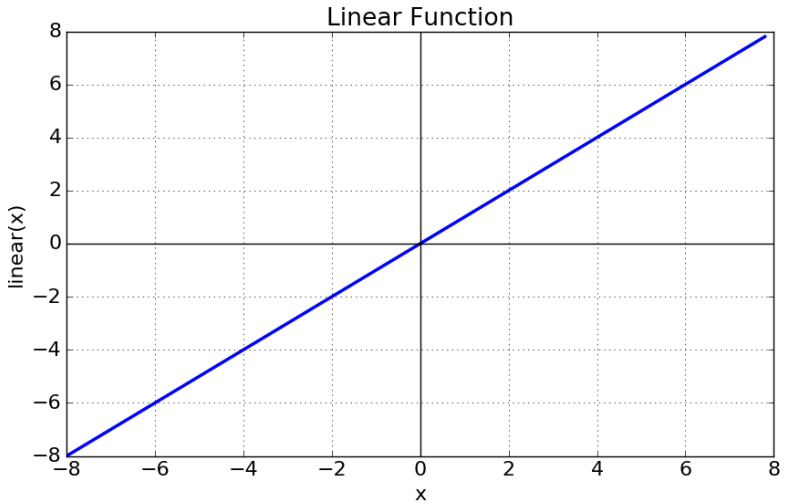

Figure 6.1 Function used in ANNs

6.3 Validation of Rectangular Beams Using ANNs

Simply supported RCC beams (24 no's) of size 1800 mm x 150 mm x 200 mm are tested in flexure. DIC is used to extract Moment (M)-Curvature (κ) relationships using random speckle patterns and QR code-based random speckle patterns. A feed-forward, back-propagation neural network is employed. It has one input layer with four input variables, one hidden layer with ten neurons and an output layer with two output variables. The algorithm adopted for the training is Levenberg-Marquardt (*trainlm*). The input vectors for the rectangular beams are (grade, deflection, curvature, load), and the output vectors are (residual moment, damage index). The schematic neural network is shown in Figure 6.2. The transfer function between input and the hidden layer is *sigmoidal* function, and from hidden to output layer is *purelin*. Two separate neural networks are trained, one for Over-Reinforced (OR) and other for Under-Reinforced (UR) concrete. There are other input parameters which are also used in addition to these parameters for prediction of DI. By performing a number of trails with various input parameters. The predicted output mainly depends upon these four input vectors for the rectangular beams, for that reason, the authors have chosen these parameters.

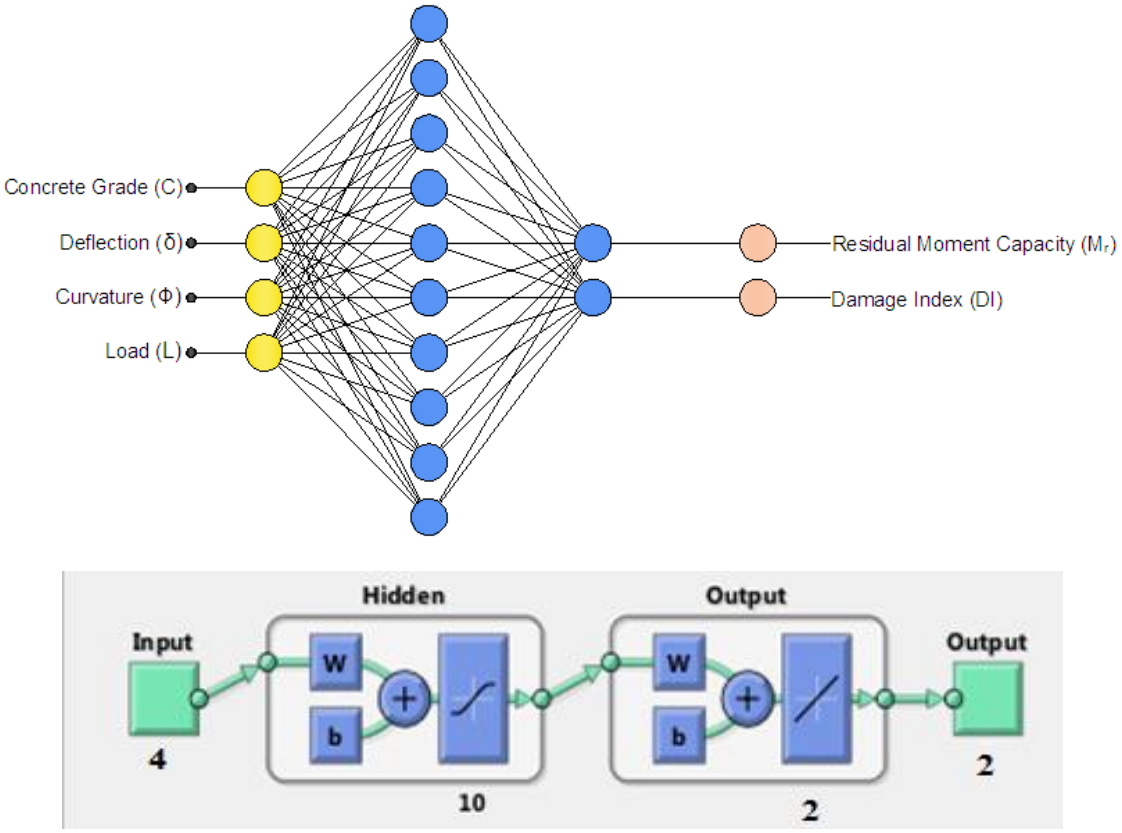

Figure 6.2 Schematic representation of ANNs architecture for rectangular beams (Ref: MATLAB R2018a *neural fitting* toolbox)

In Figure 6.2, one of the input vectors is load. The load is a force (kN, N) applied on the beam specimen while performing the experimental testing, and corresponding images are captured at various loads up to failure. Using these images corresponding deflections and curvatures are obtained from the image-processing technique (DIC). The deflections and curvatures obtained from DIC are validated by comparison with conventionally obtained (LVDT & dial gauge) data. These deflections are given as input vectors, and the corresponding load has to be estimated by the trained ANNs.

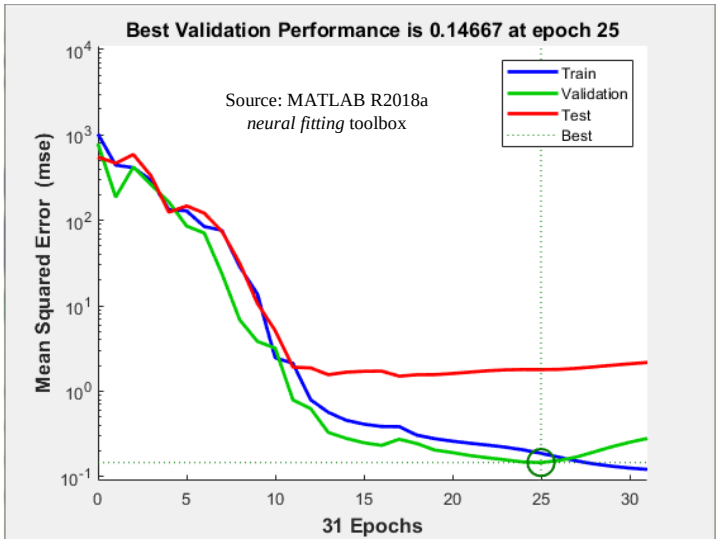

Figure 6.3 Schematic representation of performance graph for rectangular UR beam (Ref: MATLAB R2018a *neural fitting* toolbox)

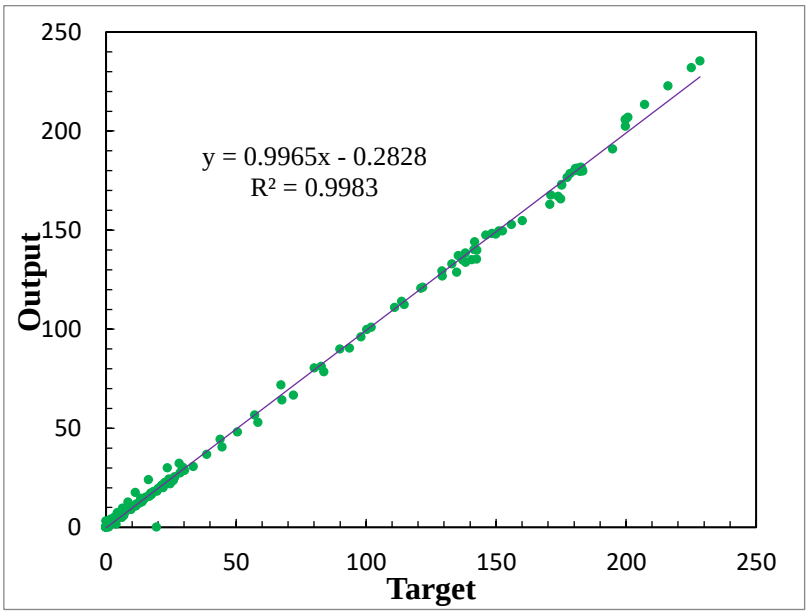

Figure 6.4 Regression graph for rectangular UR beams using ANN

From Figure 6.3, the neural network stops at 25th Epoch and error at that point is closer to 10^{-1}. The R^2-value from the regression analysis is 0.9983, shown in Figure 6.4.

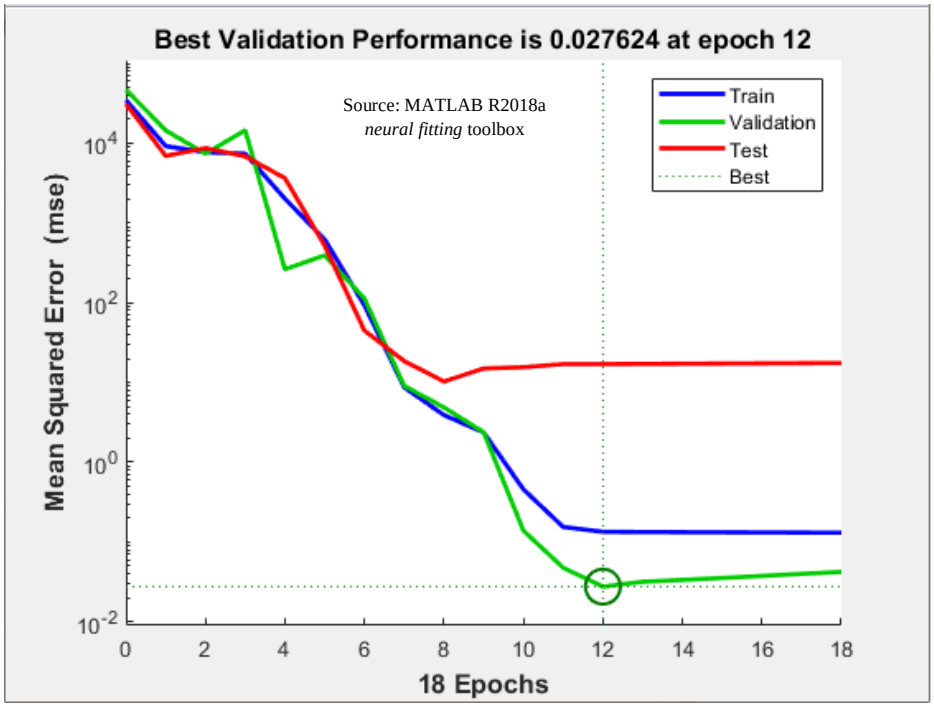

Figure 6.5 Performance graph for rectangular OR beam (Ref: MATLAB R2018a *neural fitting* toolbox)

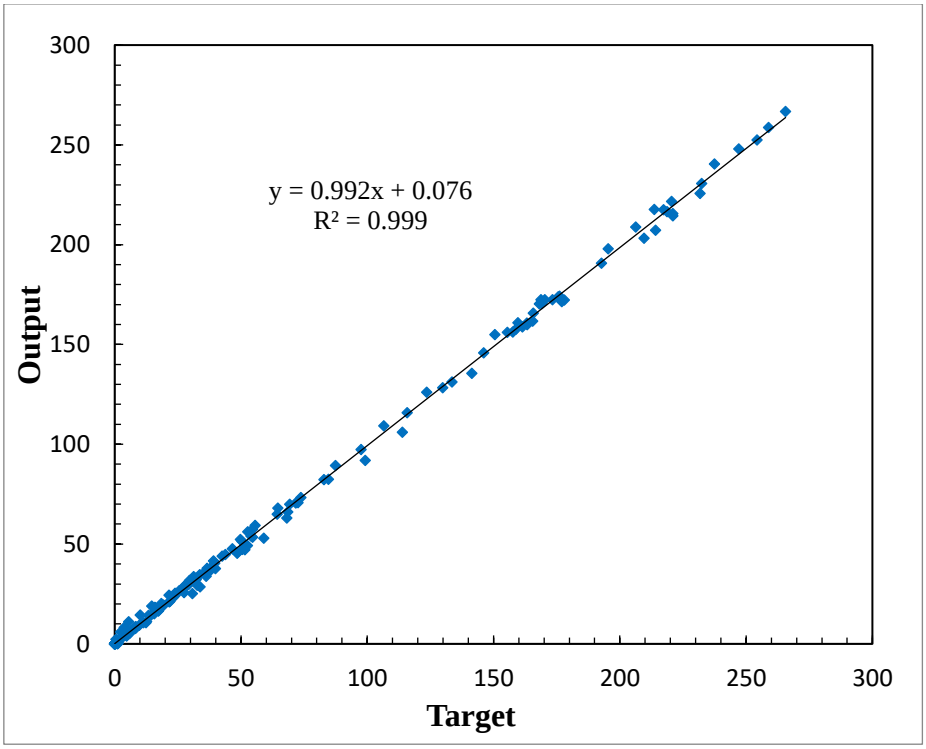

Figure 6.6 Regression graph for rectangular OR beams using ANN

From Figure 6.5, the training of neural network stops at 12th Epoch at a mean squared error (mse) near 10^{-2}. The R^2 value from the regression analysis is 0.999, shown in Figure 6.6.

6.3.1 Results obtained for rectangular beams using ANNs approach

From the experiment and imaged-based ANNs prediction, the following results are obtained for rectangular OR and UR sections, as shown in Figures 6.8-6.13. The results obtained from ANNs prediction are close to experimental results. For most of the specimens, the error is less than 5%. Experimentally examined RCC rectangular beam using Ncorr v1.2.2 is shown in Figure 6.7.

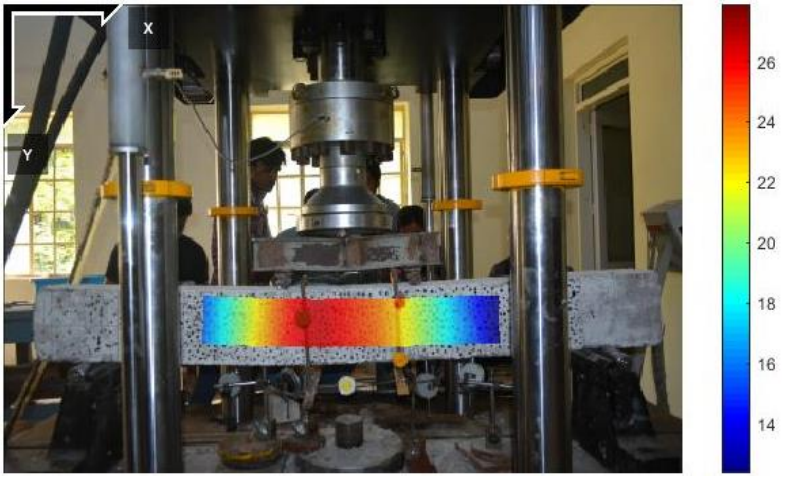

(a)

(b)

Figure 6.7 Deflection profile using Ncorr v1.2.2 for rectangular beams (a) Vertical displacement (mm) (b) Horizontal displacement (mm)

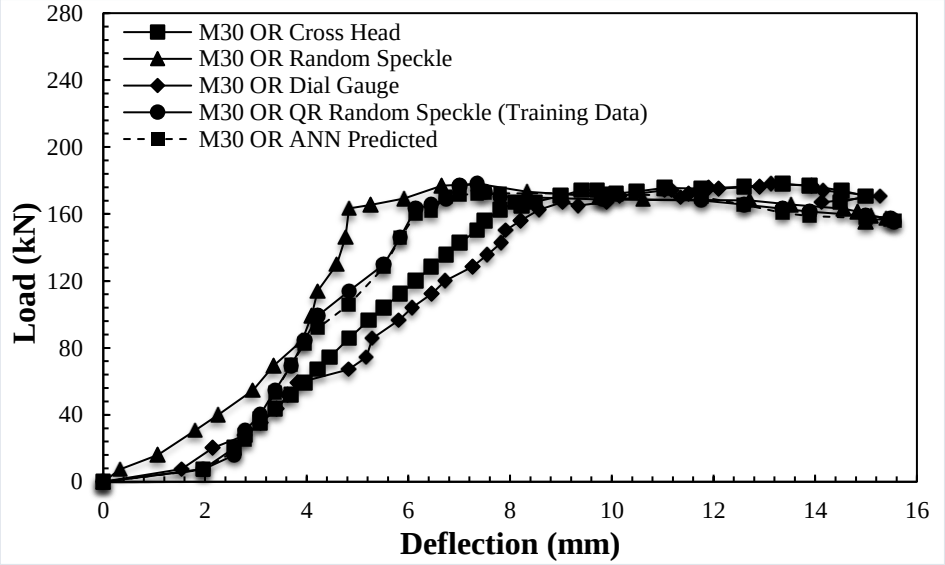

Figure 6.8 Load vs Deflection for M30 OR section

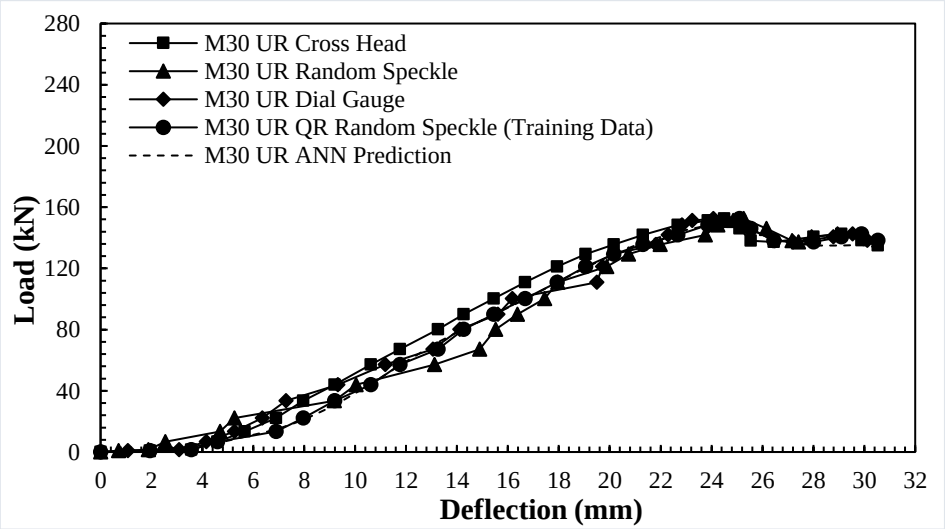

Figure 6.9 Load vs Deflection for M30 UR section

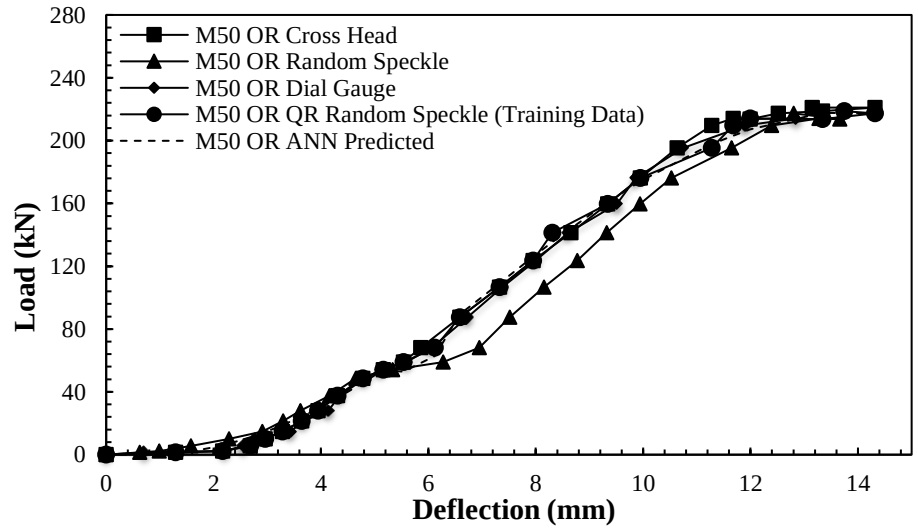

Figure 6.10 Load vs Deflection for M50 OR section

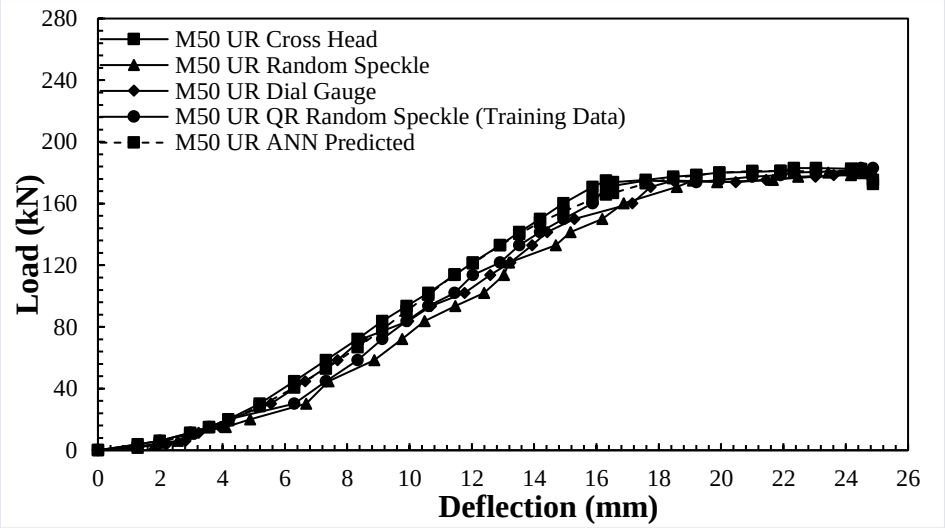

Figure 6.11 Load vs Deflection for M50 UR section

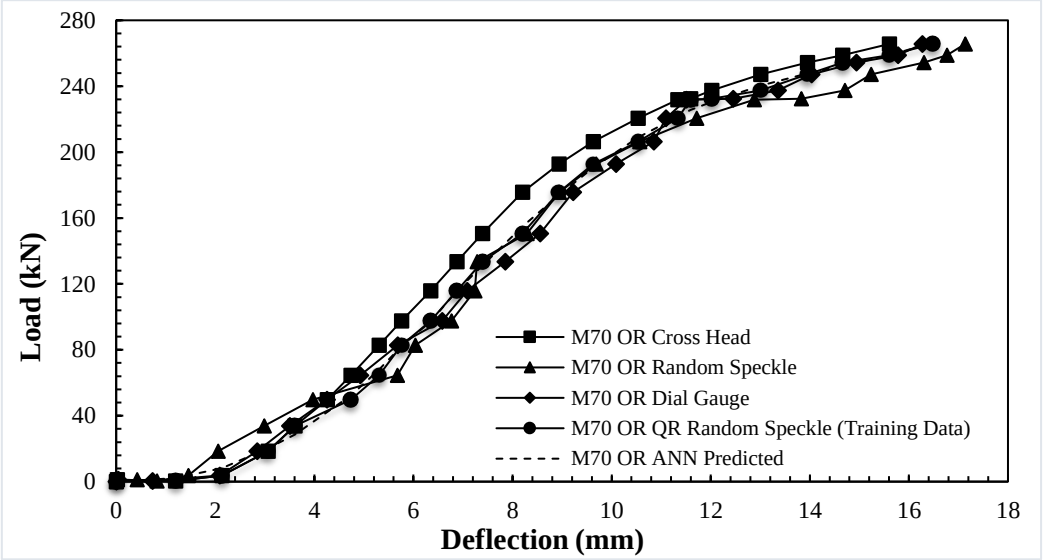

Figure 6.12 Load vs Deflection for M70 OR section

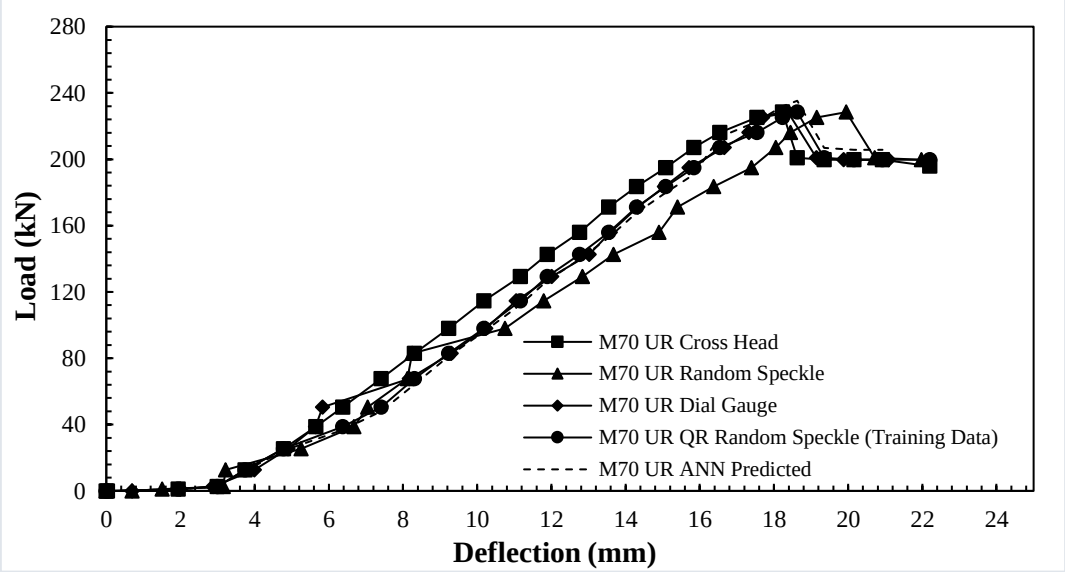

Figure 6.13 Load vs Deflection for M70 UR section

DIC enables measurement of the deformation field and calculation of the strain distribution of the beam. The values extracted from DIC with QR code-based random speckle pattern compare well with conventionally obtained (LVDT & dial gauge) results. Only the QR code-based experimental data are used for the training of ANNs. From Figures 6.8-6.13 provided the legend with training data as input parameters and predicted as output parameters. In most of the specimens, it is observed that ANNs prediction results closely match experimental results.

6.3.2 Moment (M)-Curvature (κ) results for rectangular beams

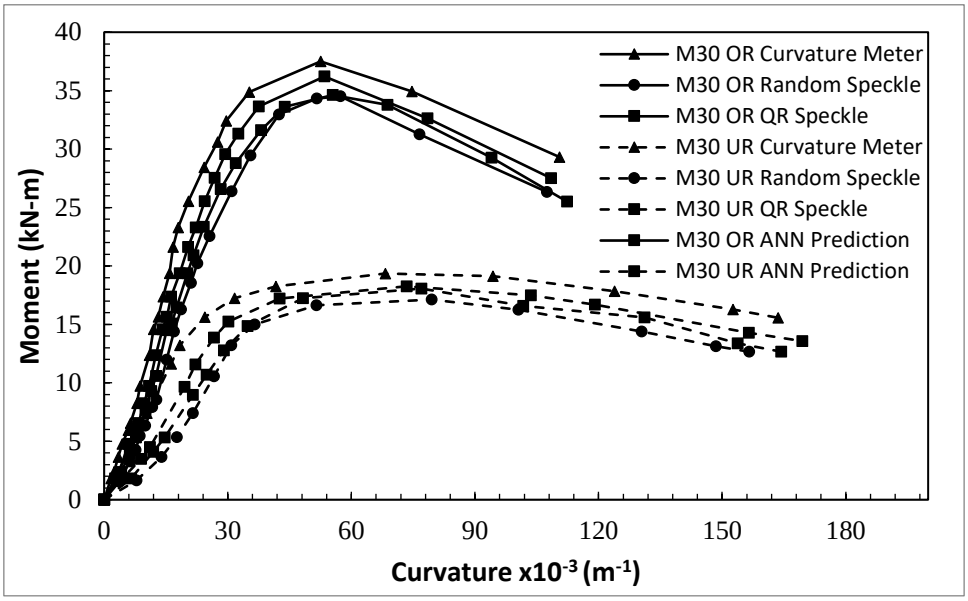

Figure 6.14 Moment (M)-Curvature (κ) for M30 beams

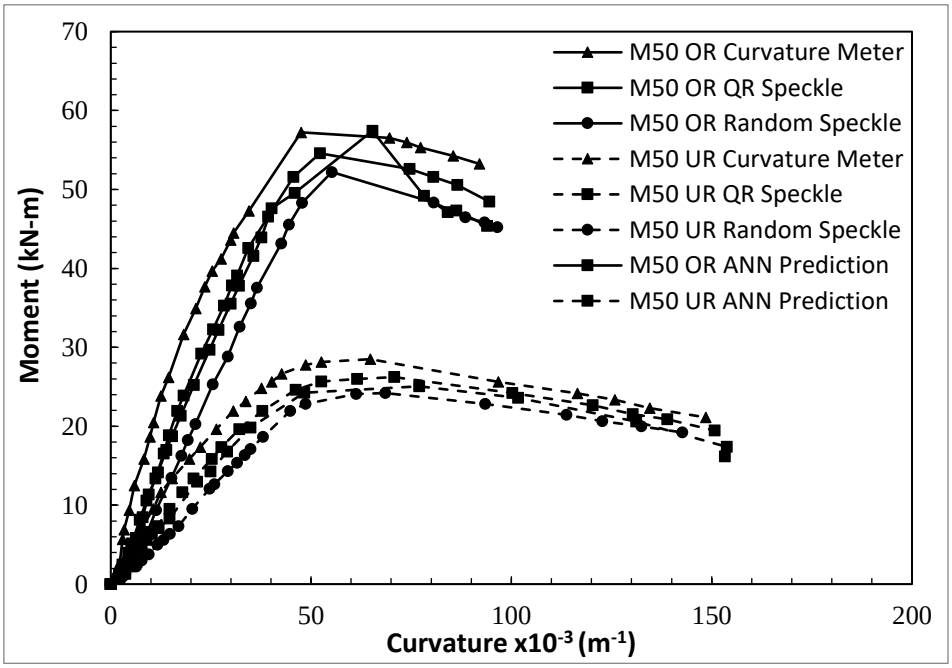

Figure 6.15 Moment (M)-Curvature (κ) for M50 beams

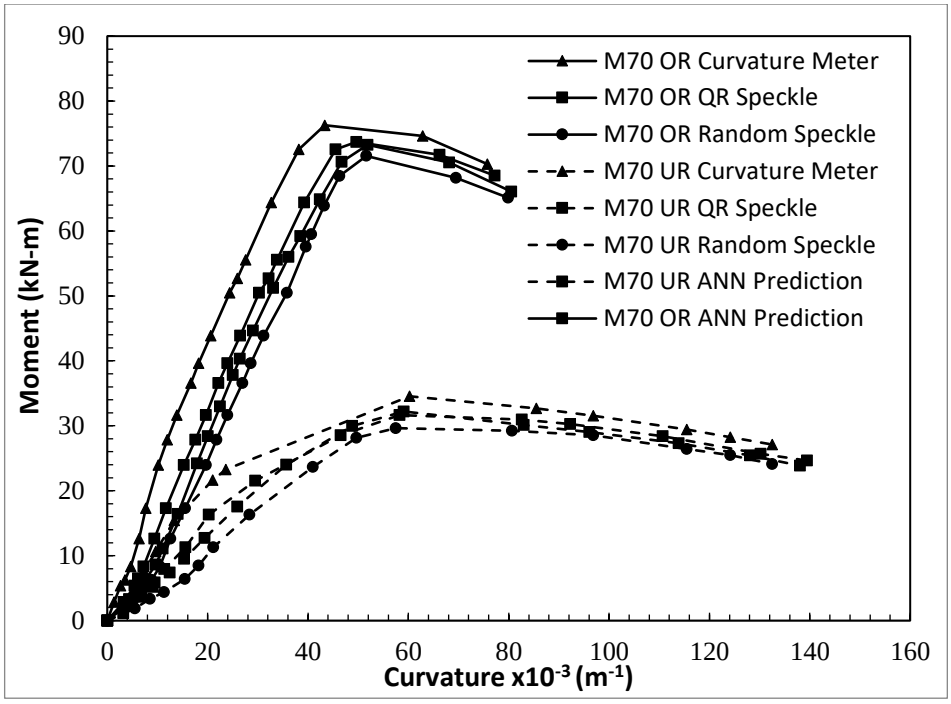

Figure 6.16 Moment (M)-Curvature (κ) for M70 beams

Based on the curvature meter readings obtained at top and bottom portion of the beam from the experiment, the Moment (M)-Curvature (κ) relationship is calculated. In Moment (M)-Curvature (κ) plots, shown in Figures 6.14, 6.15 and 6.16, it is observed that ANNs results compare well with experimental results. Based on ANNs results, residual moment capacity and DI are calculated and plotted. It is observed that the DI is sensitive to the curvature.

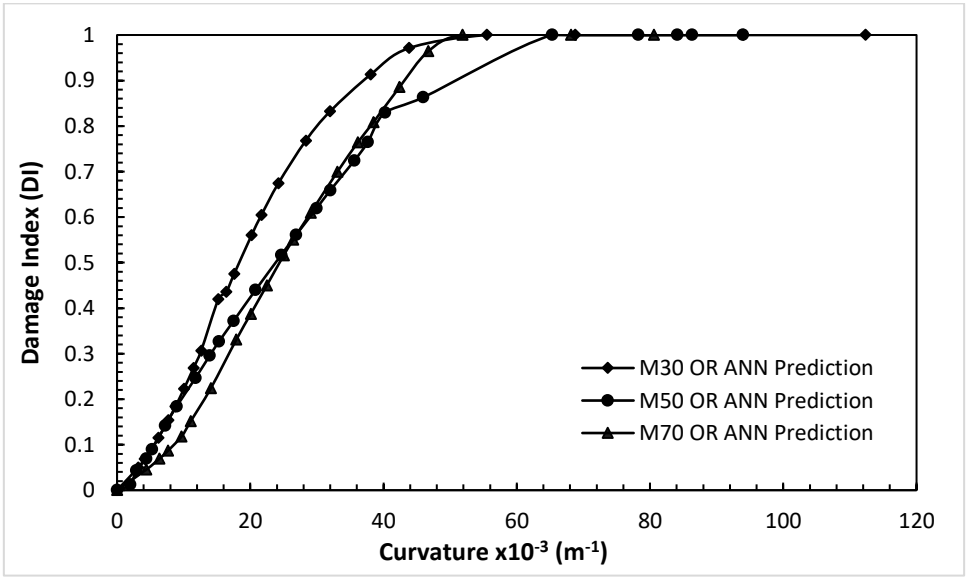

Figure 6.17 Damage Index (DI) vs Curvature for OR beams

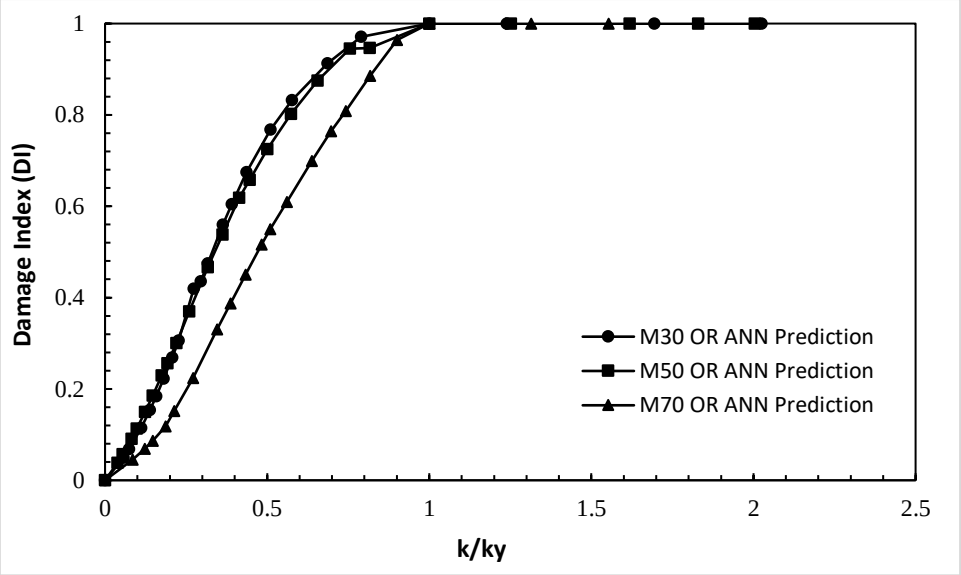

Figure 6.18 Damage Index (DI) vs Normalized Curvature for OR beams

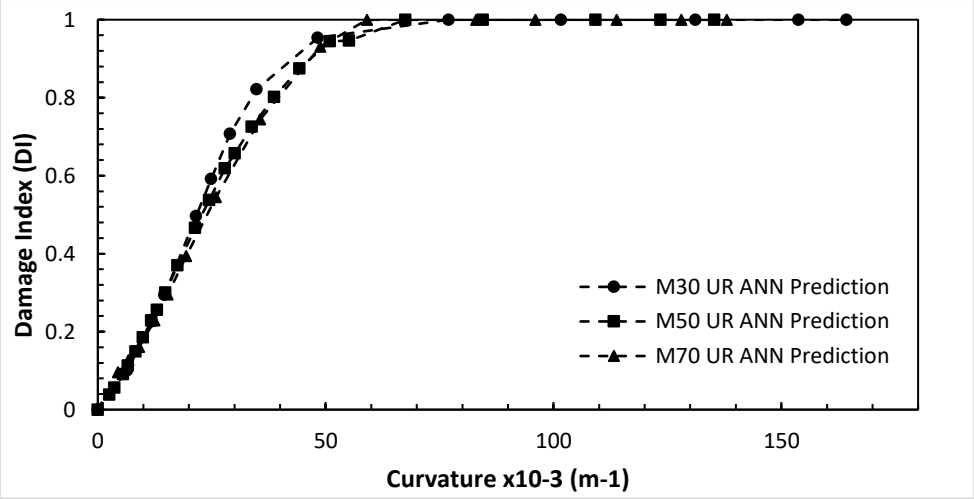

Figure 6.19 Damage Index (DI) vs Curvature for UR beams

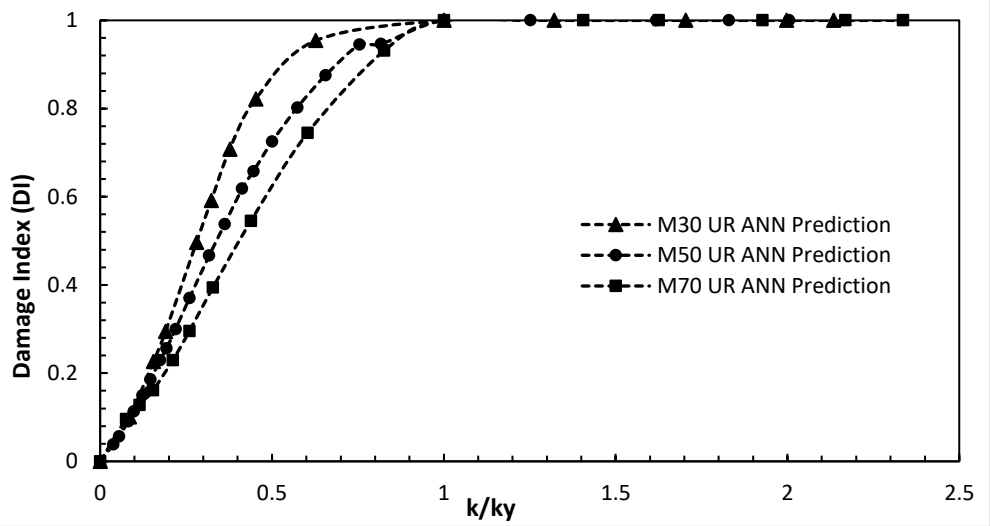

Figure 6.20 Damage Index (DI) vs Normalized Curvature for UR beams

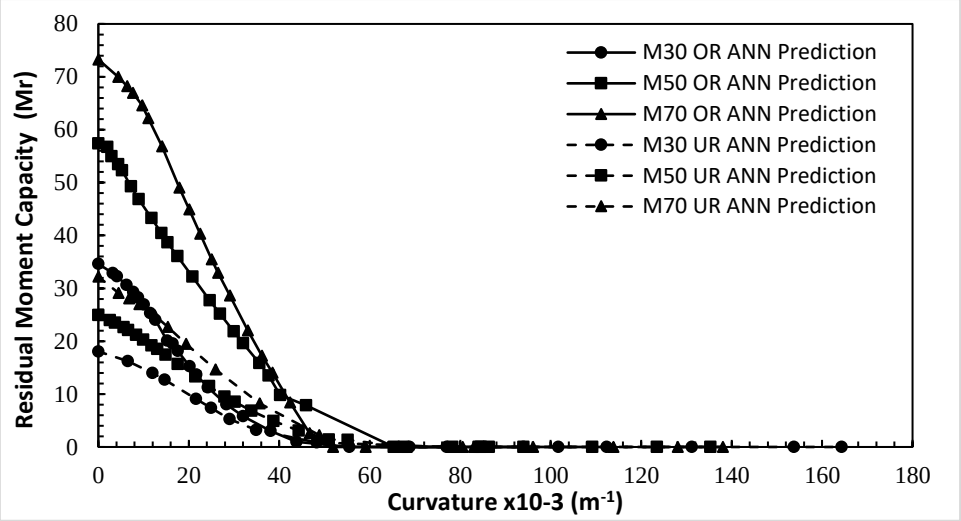

Figure 6.21 Residual Moment Capacity vs Curvature for RCC beams

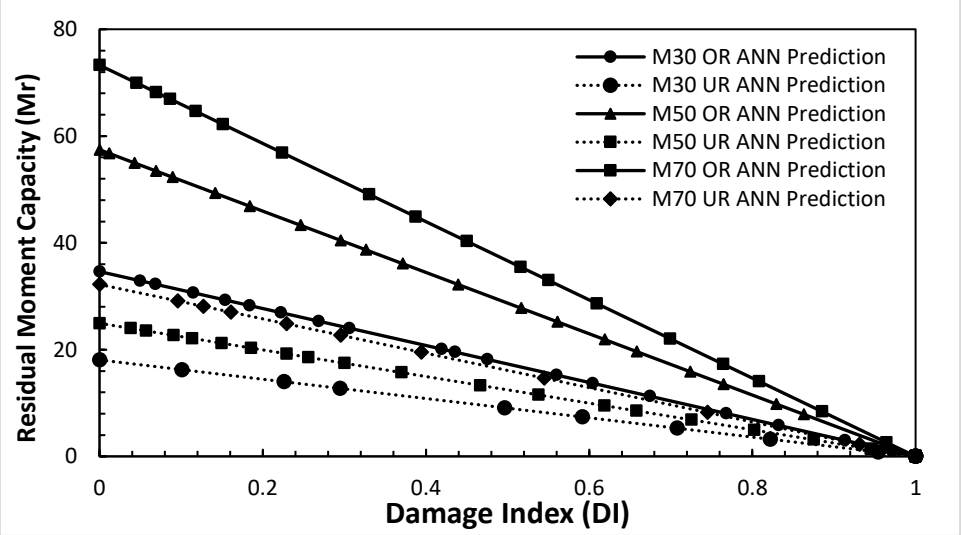

Figure 6.22 Residual Moment Capacity vs Damage Index for UR beams

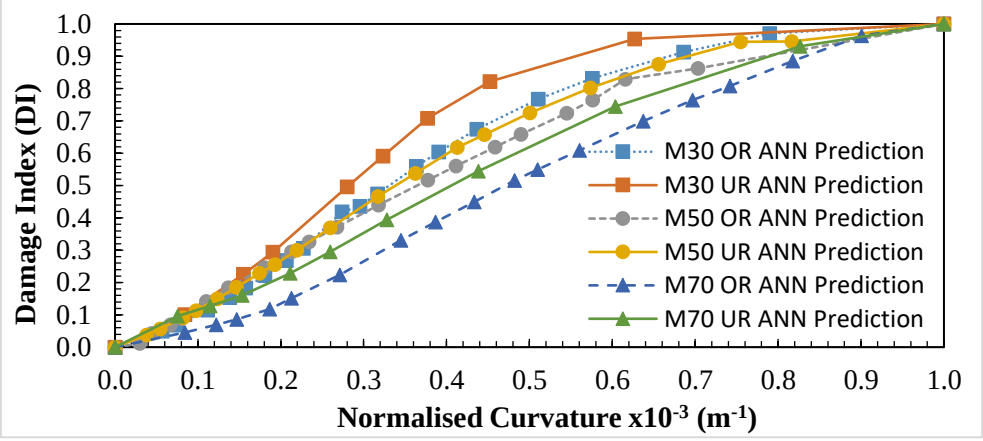

Figure 6.23 ANNs prediction of Damage Index (DI) vs Normalised Curvature for rectangular beams

Figures 6.17-6.23 show the relationship between curvature, residual moment capacity, DI, and Normalised curvature, where it is observed that the residual moment capacity converges to zero before reaching a curvature value of 0.065 m^{-1}. As the value of the DI increases, the residual moment capacity of the flexural dominated member decreases linearly.

Table 6.7 Comparison of experimental with ANNs results

Designation	Experimental			ANNs			Error in Moment (%)	Error in Load (%)
	Deflection (mm)	Moment (kN-m)	Load (kN)	Moment (kN-m)	Load (kN)	Curvature x10^{-3} m-1		
M30 (UR)	9.7	18.3	52.4	18.03	51.6	77	1.47	1.52
M50 (UR)	4.3	34.5	98.6	34.6	98.7	47.8	0.28	0.1
M70 (UR)	18.6	25.6	73.1	24.9	70.4	67.5	2.73	3.69
M30 (OR)	12.3	52.6	150.4	57.4	164	45.9	9.12	9.04
M50 (OR)	9.2	30.9	88.3	32.2	88.5	59	4.2	0.22
M70 (OR)	10.8	73.2	209.2	70.8	216.8	51.8	3.27	3.38

From the Table 6.7, it is clear that the error percentage is less than 5% for most of the samples.

6.4 T-Beams Conventional

To study the behaviour of the full-scale bridge girders, a scaled experimental study is conducted. An actual MoRTH bridge girder of span 24 m, is scaled down to 1:12 to enable testing under four-point flexural loading. From the experiment, moment-curvature is obtained, which helps in the calculation of DI based on which the condition of the girder is classified in terms of residual capacity. RCC T-beams of M30 grade of concrete for UR sections are cast and tested for deformations using dial gauges and LVDTs along with DIC technique. The cross-section size and typical reinforcement details of T-beam are shown in Figure 6.24.

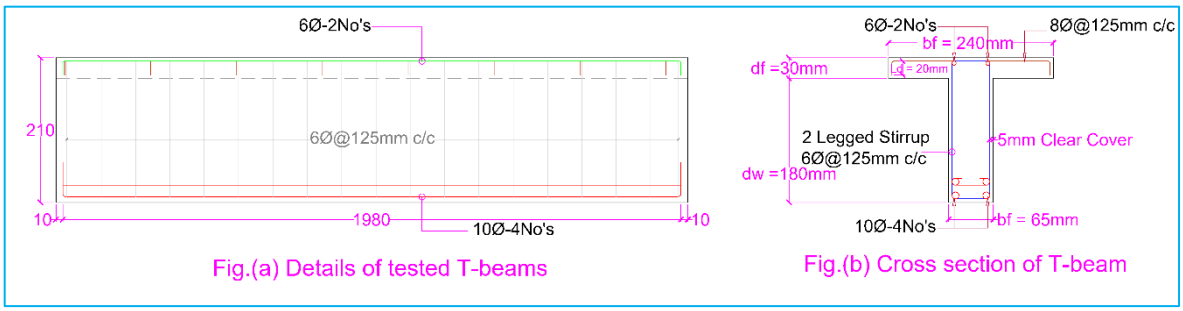

Figure 6.24 Reinforcement details of T-section

The supported length of the T-beam is 1800 mm. It was used to check the suitability of employing random speckle pattern and QR based random speckle pattern on either side of the test component. The component-level testing of RCC T-beam is performed under simply supported conditions and validated using SAP2000 software, as shown in Figure 6.25.

(a) **(b)**

Figure 6.25 Scaled T-beam (1:12) (a) Experimental specimen (b) SAP2000 model

Three T-beam specimens are cast for experimental studies, and after validation of experimental T-beam using SAP2000, four standard MoRTH Bridge girders shown in Table 6.8 are considered for modelling (Figures 6.27-6.28). Experimentally obtained nonlinear compressive stress-strain behaviour of a prism (1:2 cement to sand ratio) is given as material property in SAP2000, as shown in Figure 6.26. Young's modulus of the concrete material (M30) is considered as $5000\sqrt{f_{ck}}$ (IS 456:2000).

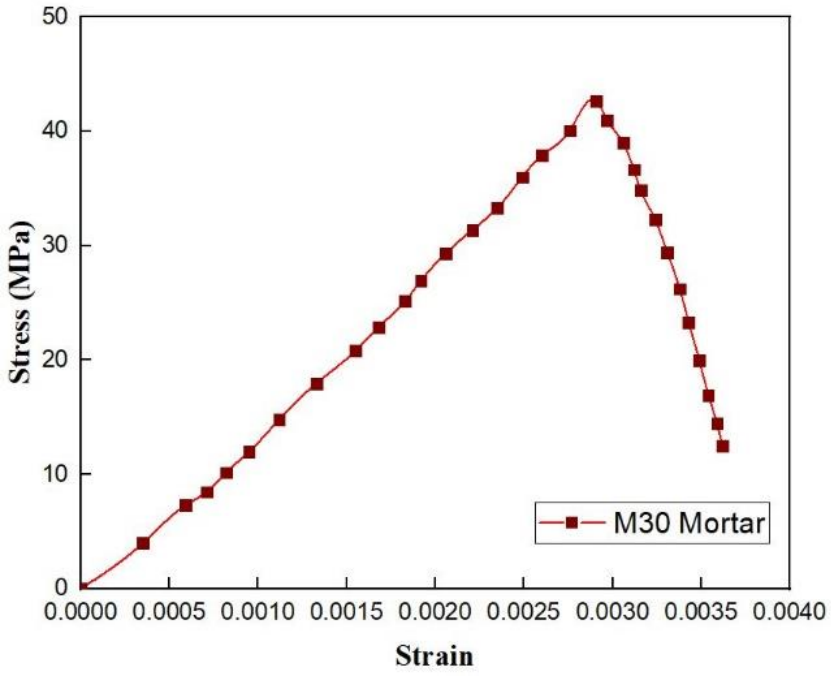

Figure 6.26 Stress-Strain relation for scaled M30 concrete

Table 6.8 Dimensions of standard MoRTH bridge girders used in SAP2000

SPAN (m)		Flange (b_f) mm	Flange (D_f) mm	Web (b_w) mm	Web (d) mm
Beam-1	24	2800	350	625	2055
Beam-2	24	2825	350	625	2055
Beam-3	21	2650	400	625	2105
Beam-4	21	2825	350	625	2055

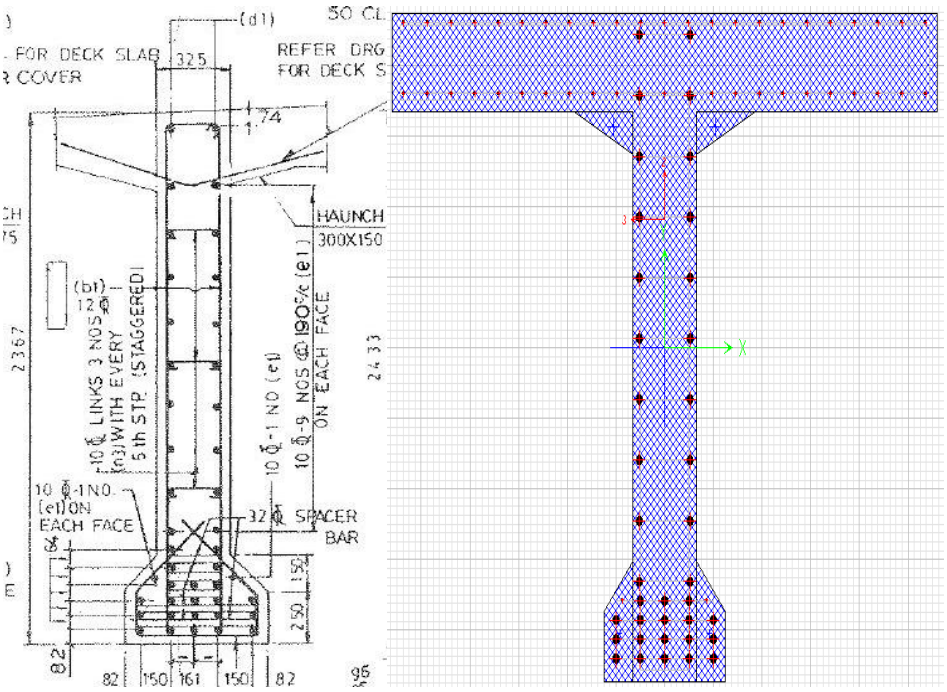

(a) Beam-1 (b)

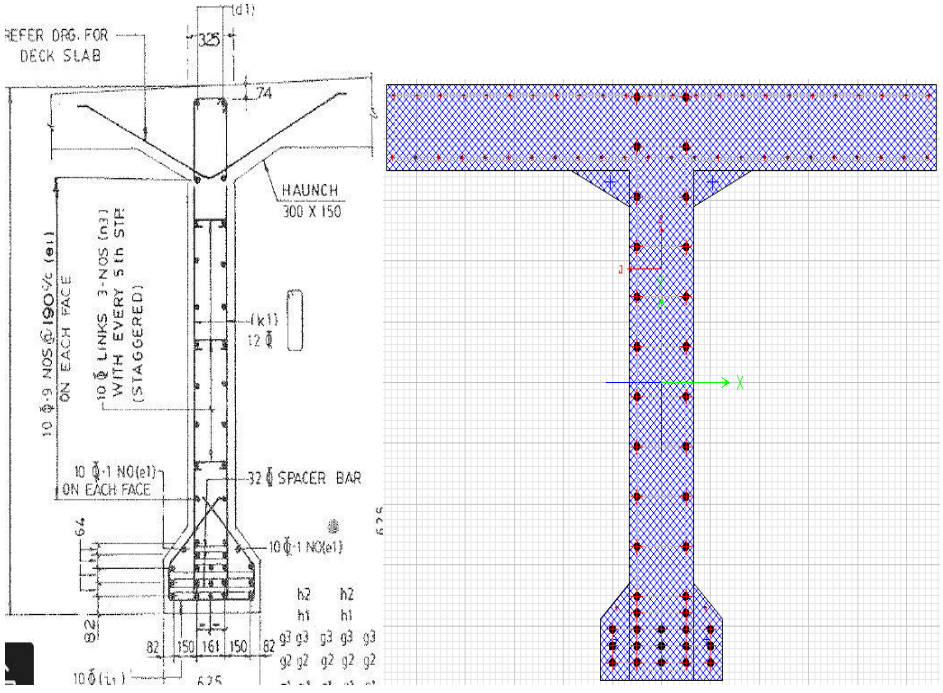

(a) Beam-2 (b)

Figure 6.27 MoRTH T-girder of 24 m span (a) Standard c/s drawings (b) SAP2000 model

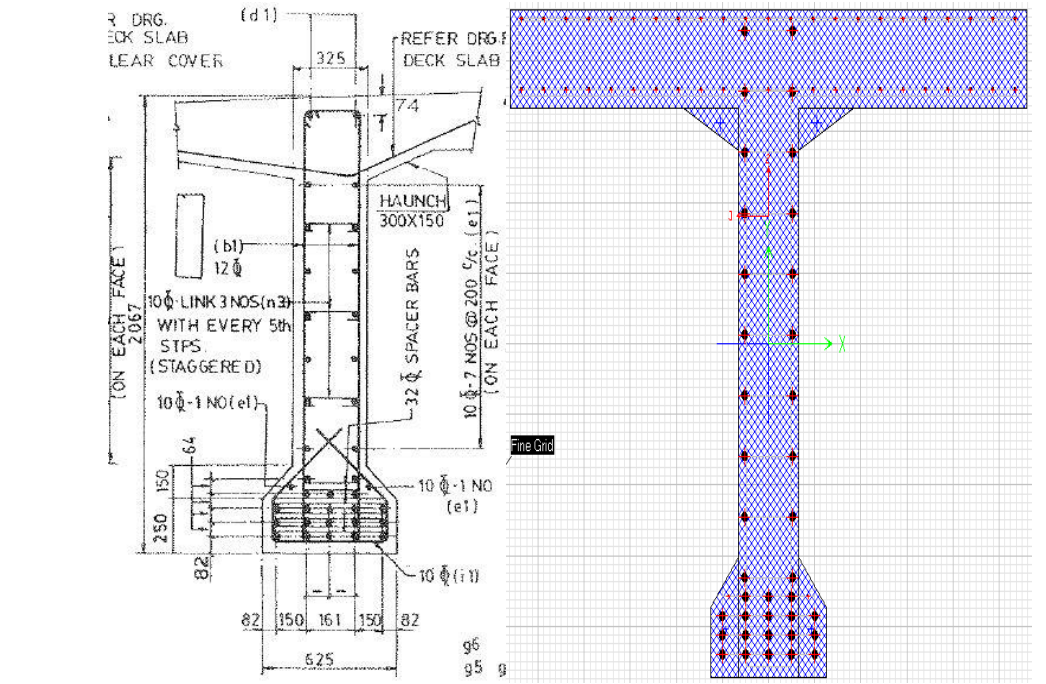

(a) Beam-3 (b)

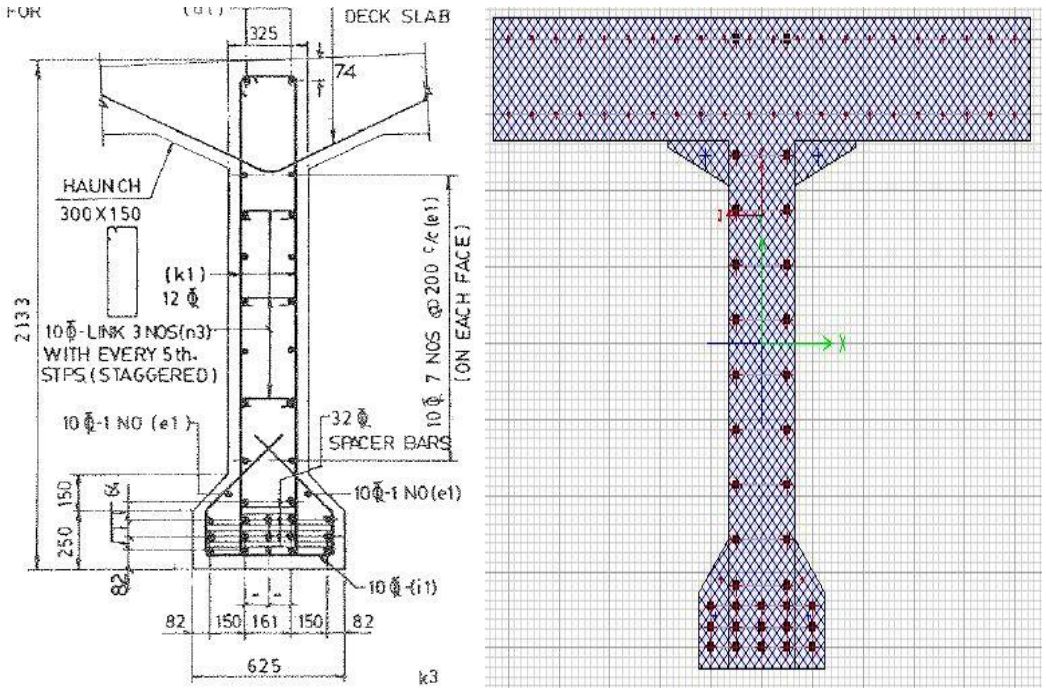

(a) Beam-4 (b)

Figure 6.28 MoRTH T-girder of 21 m span (a) Standard c/s drawings (b) SAP2000 model

6.4.1 Analytical prediction of M-κ for standard MoRTH bridge girders

Flexural behaviour of standard MoRTH bridge girders using analytical approach (MATLAB code) is estimated in this study, to generate more amount of data in addition to the experimental data for ANN training. A normal distribution of f_{ck} (characteristic compressive strength) is considered to generate M-κ curves in MATLAB as shown in Figure 6.29. A total number of

200 samples of full-scale MoRTH Bridge girders are used for training ANN, which are shown in Figure 6.30. Details of the MATLAB code are provided in Appendix-A.

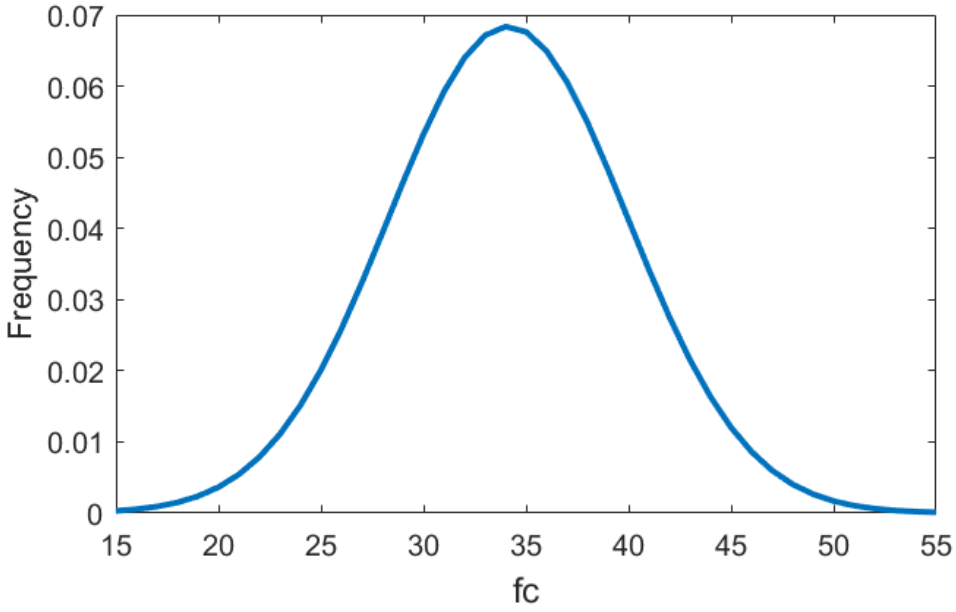

Figure 6.29 Normal distribution of f_{ck} values for M30 concrete

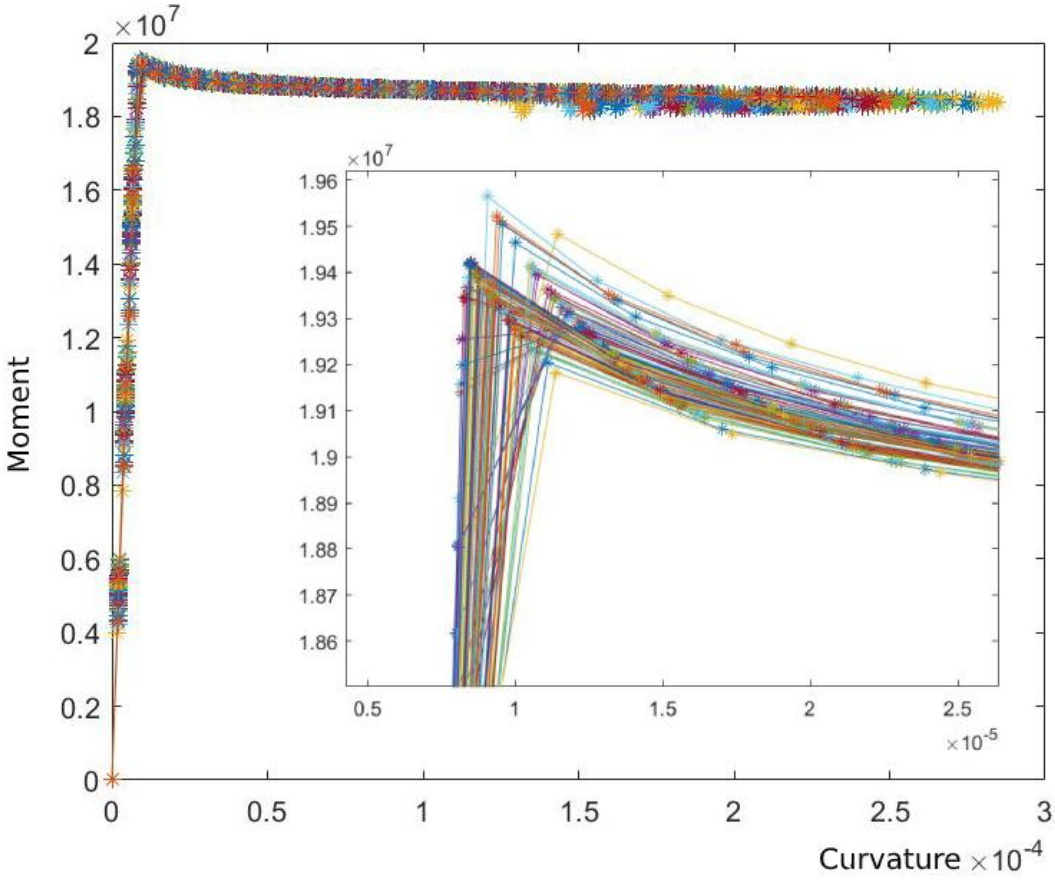

Figure 6.30 Prediction of M-κ curves for standard MoRTH bridge girders using MATLAB

6.4.2 ANN modelling for T-beams

Based on the simulation results of full-scale MoRTH bridge girders, ANN are trained, whose objective is to find out the DI. The typical ANN architecture for the T-beams is shown in Figure 6.31

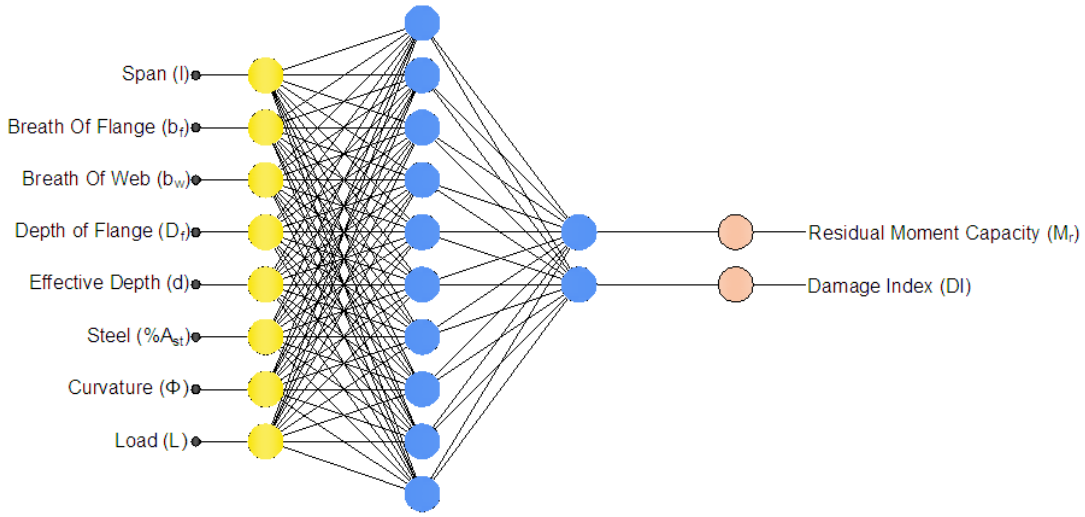

(a)

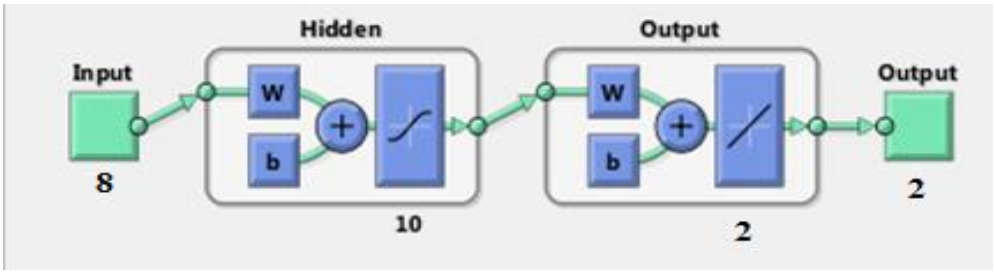

(b)

Figure 6.31 ANN architecture of full-scale T-beams (Ref: MATLAB R2018a *neural fitting* toolbox)

Input vectors are span (m), breath of the flange b_f (mm), breath of the web b_w (mm), depth of the flange D_f (mm), effective depth d (mm), % of tension reinforcement $\%A_{st}$, and curvature κ (m^{-1}), load (kN) whereas the output is in DI (0 to 1). The predicted output mainly depends upon these eight input vectors for the T-beams. The transfer function from input to hidden layers is *sigmoidal*, and from hidden layer to output layer it is *purelin*. Feed-forward back-propagation neural network is used, and Levenberg-Marquardt algorithm is used for training the neural network. There are other input parameters which are also used in addition to these parameters for prediction of DI. By performing a number of trials with various input parameters. Figure 6.32 shows that the neural networks stop training at 22^{nd} Epoch. The mean squared error (mse) is below 10^{-3}.

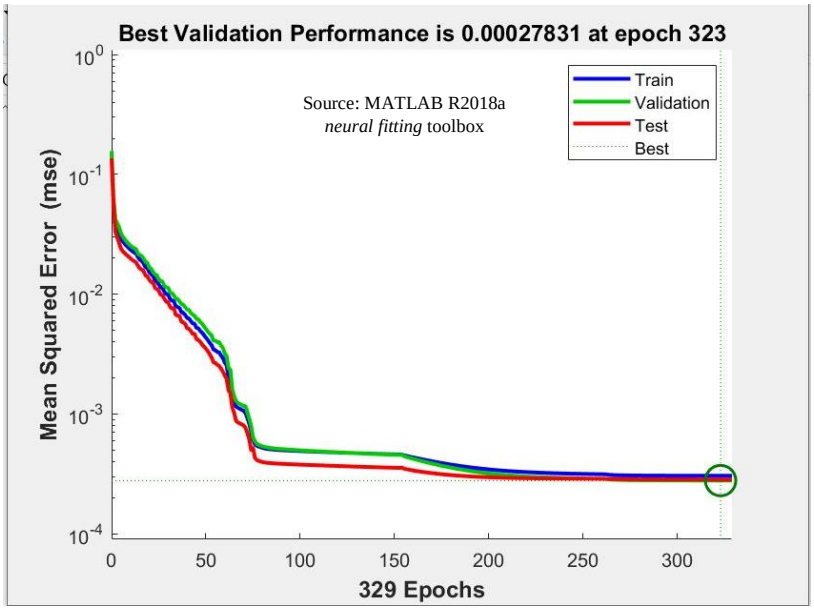

Figure 6.32 Performance graph of full-scale T-beams (Ref: MATLAB R2018a *neural fitting* toolbox)

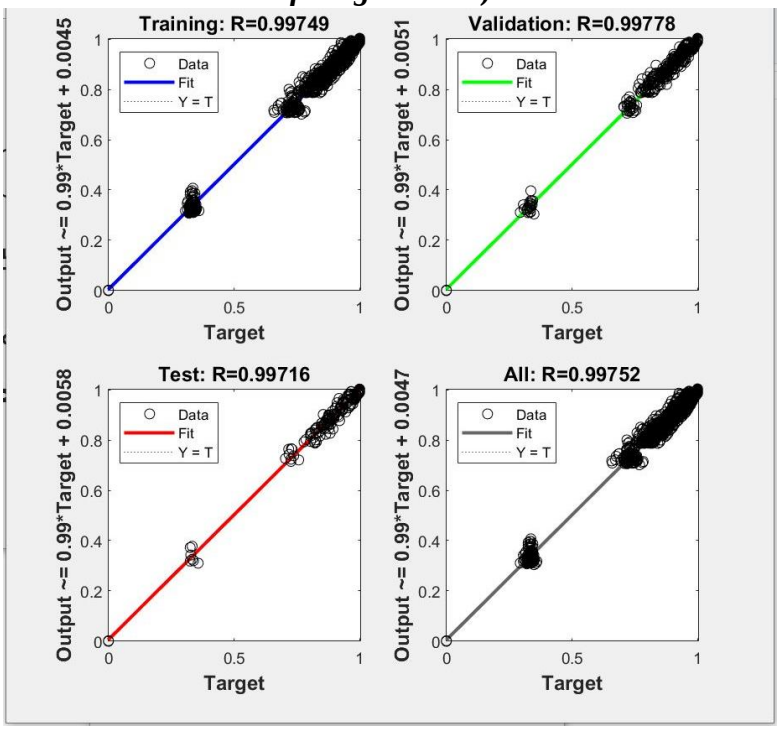

Figure 6.33 Regression plot for full-scale T-beams using ANN

From Figure 6.33 the value of R is 0.9975, which means most of the points are lie on the regression plot, which is a good fit.

6.4.3 Results obtained for T-beams using ANN

The T-beam sections are considered from MoRTH standard bridge drawings, and T-beam samples (3 no's) of scale (1:12) are cast and tested. Subsequently, FEM simulation for the reduced scale (1:12) is performed using SAP2000. The same material properties are used for

simulating full-scale T-beam girders. Experimentally examined RCC T-beams using Ncorr v1.2.2 is shown in Figure 6.34.

(a)

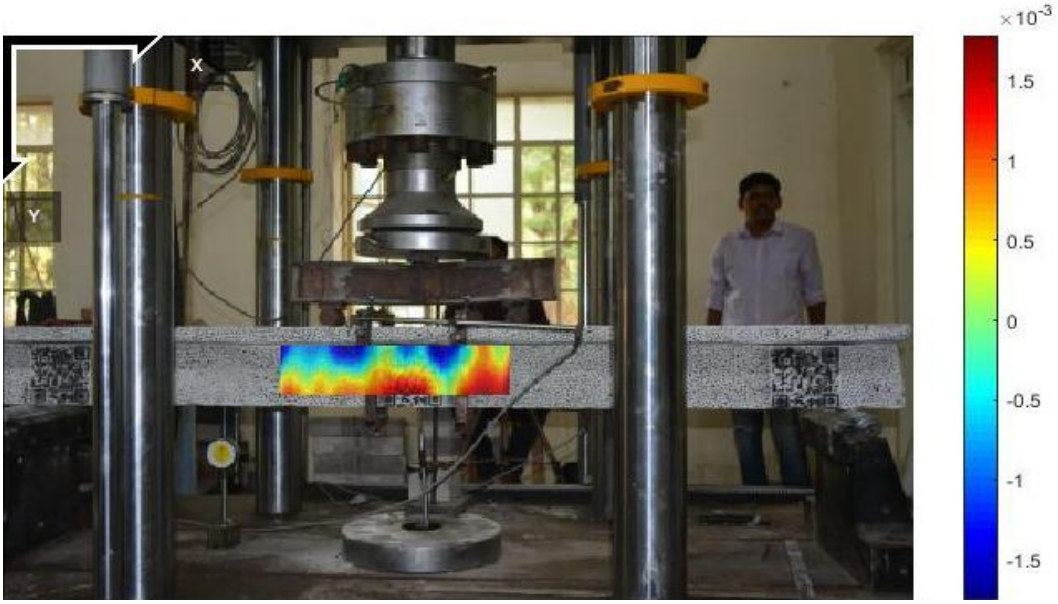

(b)

Figure 6.34 Deflection profile using Ncorr V1.2.2 for T-beams (a) Vertical displacement (mm) (b) Horizontal displacement (mm)

6.4.4 Experimental results and FEA simulation of reduced scale T-beams

From Figure 6.35 it is observed that simulation results compare well with experimental results. The same material properties are used in the simulation of full-scale T-beam girder. Later, ANN are trained for full-scale T-beam girder and then compared with FEA simulation results. Figure 6.36 shows the moment-curvature relationship for full-scale MoRTH bridges. Damage Index vs Curvature behaviour obtained from FEA simulation using SAP2000 is shown in

Figure 6.37 and Damage Index vs Curvature behaviour predicted using ANN shown in Figure 6.38.

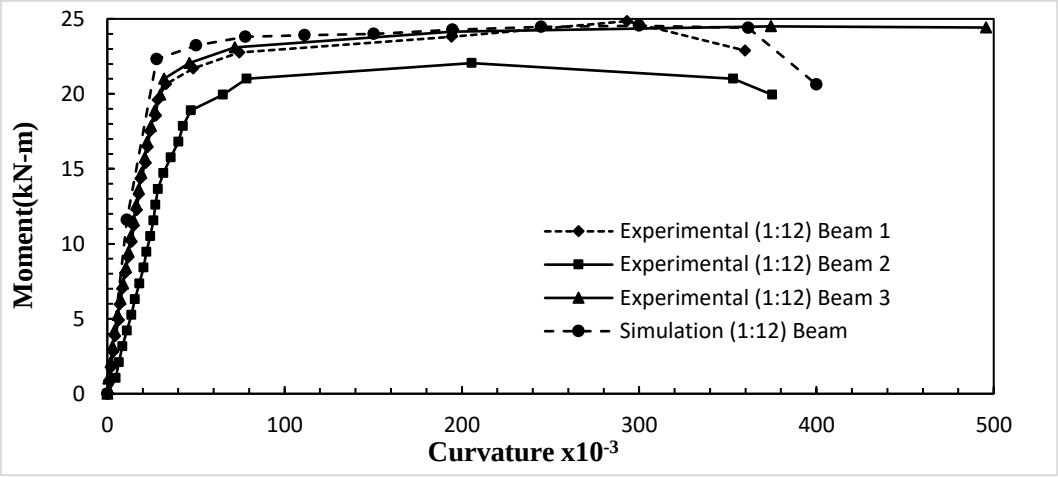

Figure 6.35 Moment (M)-Curvature (κ) for Reduced Scale (1:12) T-beams (experimental)

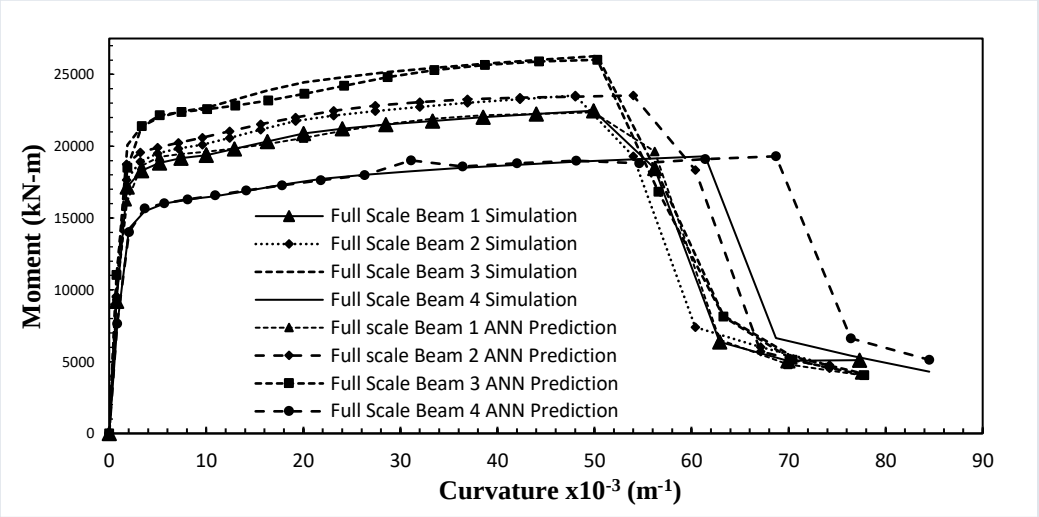

Figure 6.36 Moment (M)-Curvature (κ) for full-scale MoRTH bridges

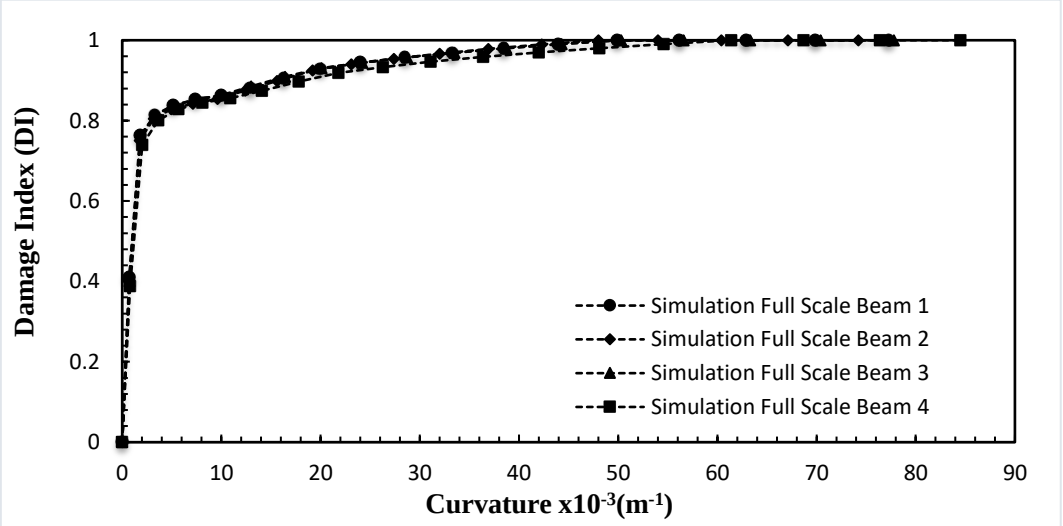

Figure 6.37 Damage Index (DI) vs Curvature for simulated (SAP2000) full-scale girders

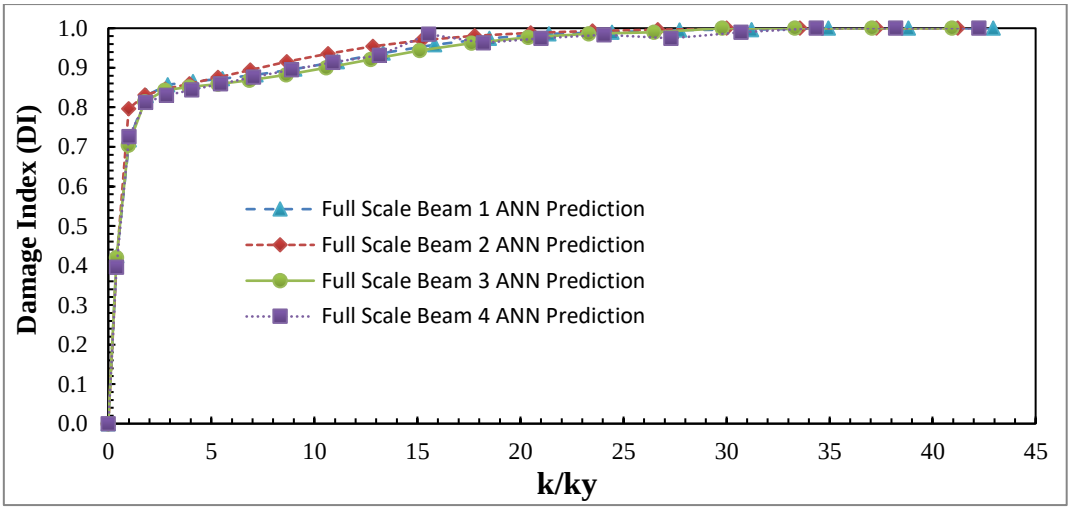

Figure 6.38 ANN prediction of Damage Index (DI) vs Normalised Curvature for full-scale MoRTH T-beams

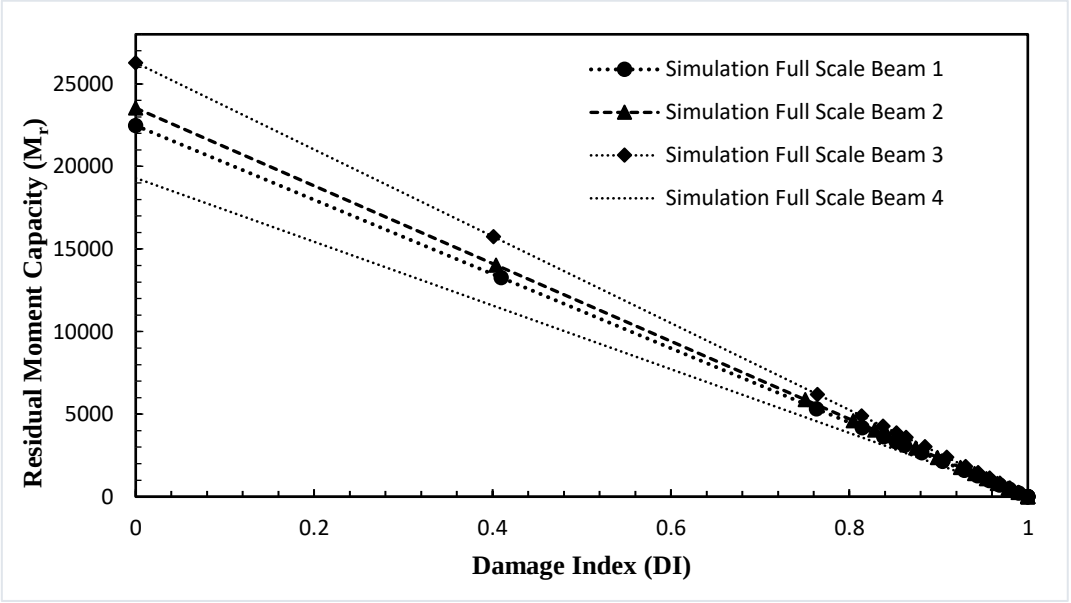

Figure 6.39 Residual Moment Capacity vs Damage Index (DI) for Full-Scale girders using (SAP2000)

Residual moment capacity vs DI for full-scale girders (Table 6.8) using (SAP2000) shown in Figure 6.39. Normalised Moment vs Curvature predicted for standard full-scale MoRTH bridges (backbone curve) shown in Figures 6.40 and 6.41.

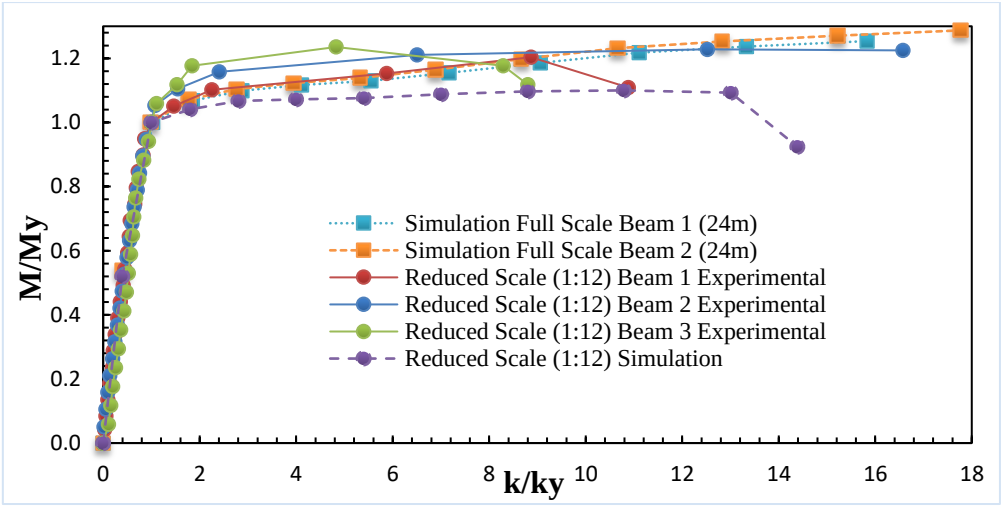

Figure 6.40 Normalised Moment vs Curvature predicted for full-scale MoRTH bridges (24m)

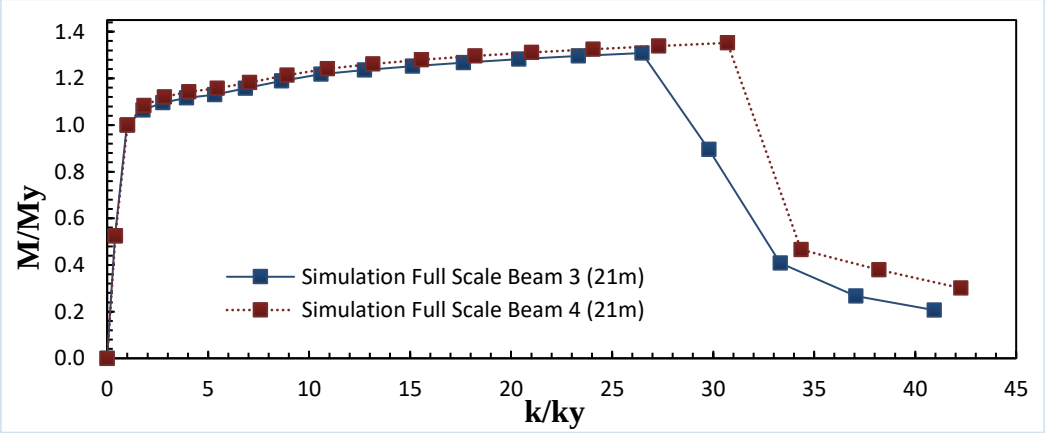

Figure 6.41 Normalised Moment vs Curvature predicted for full-scale MoRTH bridges(21 m)

The damage indices Cao Vui (2014) is employed in this study and corresponding CRN mapping are shown in Figure 6.42 and Table 6.9.

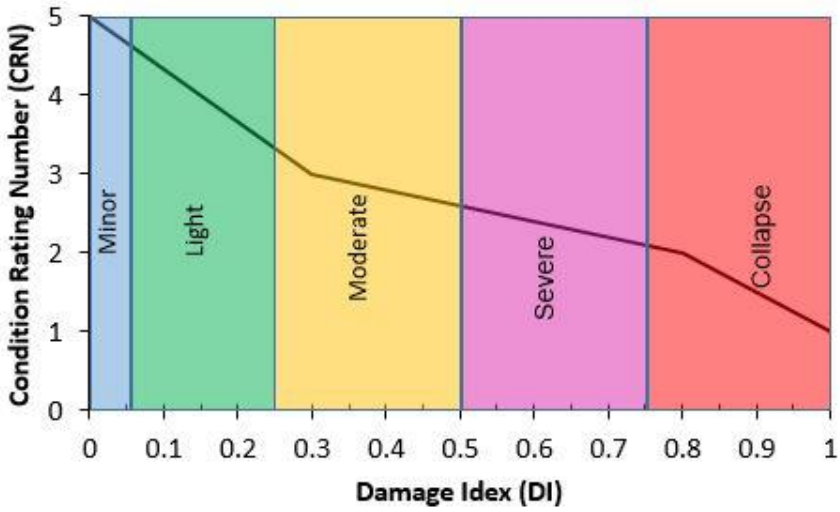

Figure 6.42 Mapping of Damage Index (DI) with Condition Rating Number (CRN)

Table 6.9 Proposed damage indices with CRN

CRN	DI	Normalized Residual Moment Capacity	Description	Action
1	0.75-1.0	0	Rebuilding/ Rehablitation Immediately	Collapse
2	0.50-0.75	0.07	Rebuilding/ Rehablitation on programed basis	Severe
3	0.25-0.50	0.23	Major/ Special Repair	Moderate
4	0.05-0.25	0.59	Routine Maintenance	Minor
5	0-0.05	1	Sound Condition	No Damage

6.5 Single ANN for flexural dominated beams

Based on the experimental, analytical and simulation results of flexurally dominated beams (rectangular and T-beams), ANN are trained, whose objective is to find out the DI and relative residual moment capacity. The typical ANN architecture for flexural dominated beams is shown in Figure 6.43

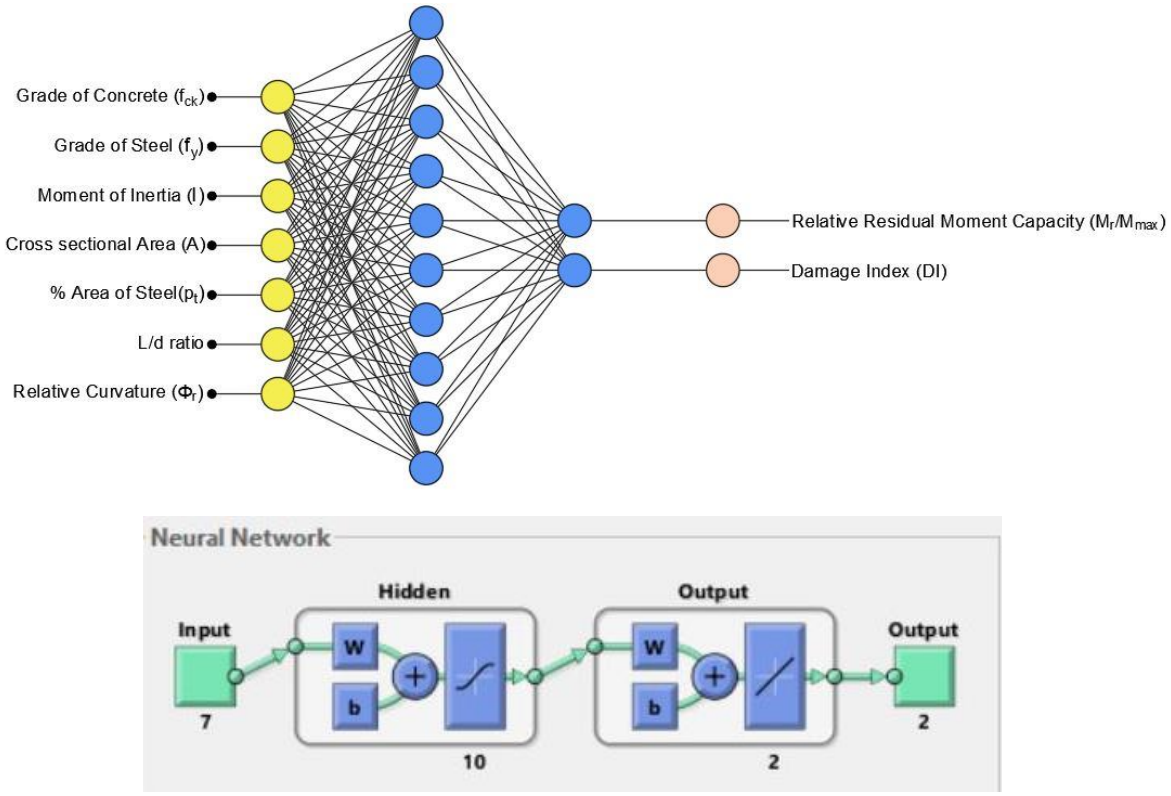

Figure 6.43 Schematic representation of ANNs architecture for flexural dominated beams (Ref: MATLAB R2018a neural fitting toolbox)

Input vectors are grade of concrete (f_{ck}), grade of steel (f_y), moment of inertia (I), cross sectional area (A), % of steel (p_t), L/d ratio, and relative curvature (κ_r), whereas the output is in DI (0 to 1) and relative residual moment capacity (M_r/M_{max}) . The predicted output mainly depends upon these seven input vectors for the beams. The transfer function from input to hidden layers is *sigmoidal*, and from hidden layer to output layer it is *purelin*. Feed-forward back-propagation neural network is used, and Levenberg-Marquardt algorithm is used for training the neural network. There are other input parameters which are also used in addition to these parameters for prediction of DI. By performing a number of trials with various input parameters. Figure 6.44 shows that the neural networks stop training at 22nd Epoch. The mean squared error (mse) is below 10^{-3}.

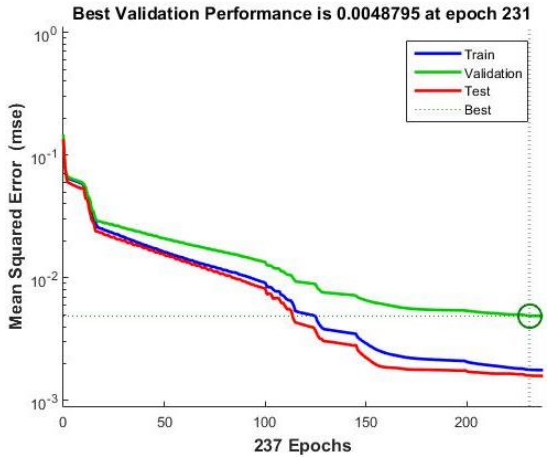

Figure 6.44 Performance graph of flexural dominated beams (Ref: MATLAB R2018a neural fitting toolbox)

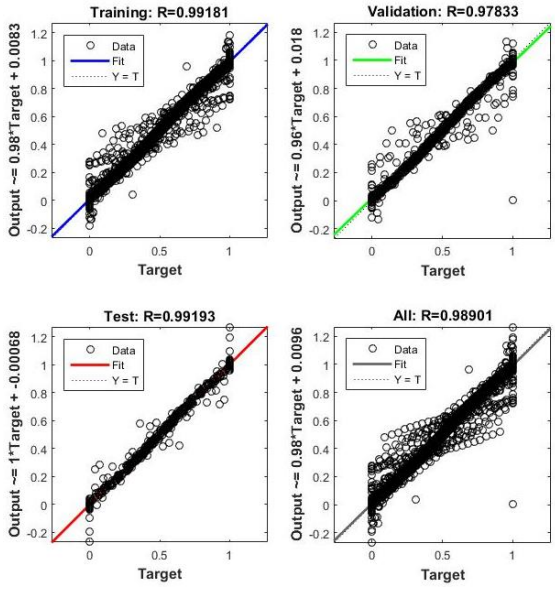

Figure 6.45 Regression plot for flexural dominated beams using ANN

From Figure 6.45 the value of R is 0.9783, which means most of the points are lie on the regression plot, which is a good fit.

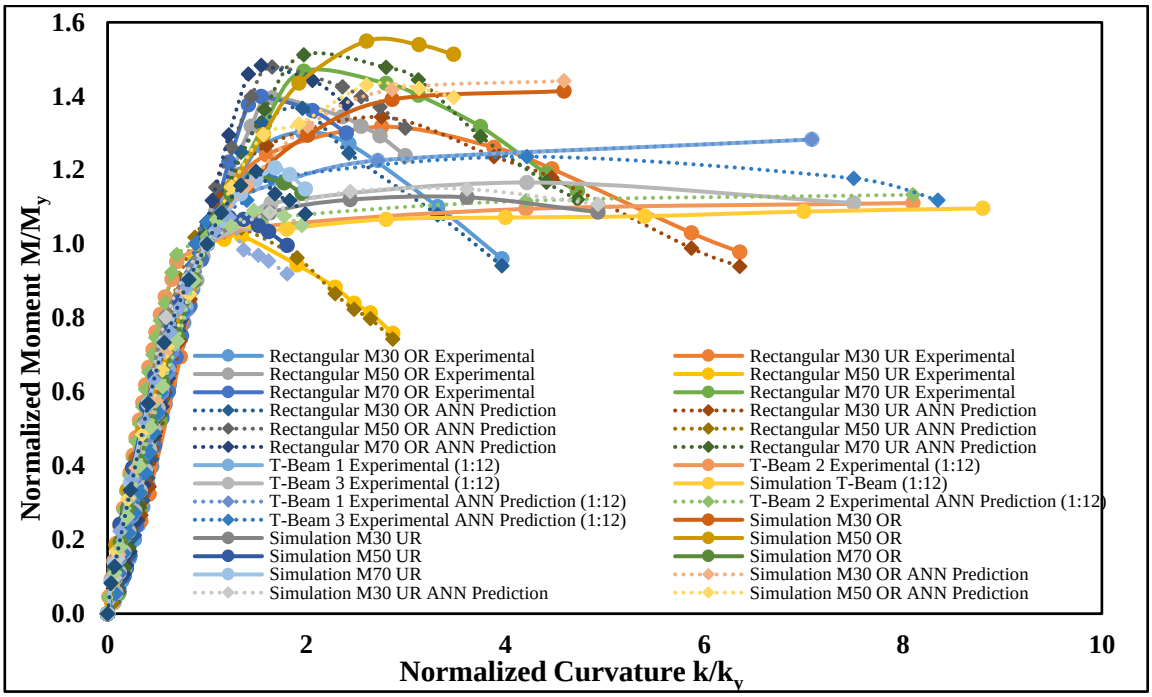

Figure 6.46 Normalised Moment vs Normalised Curvature predicted for bridge components

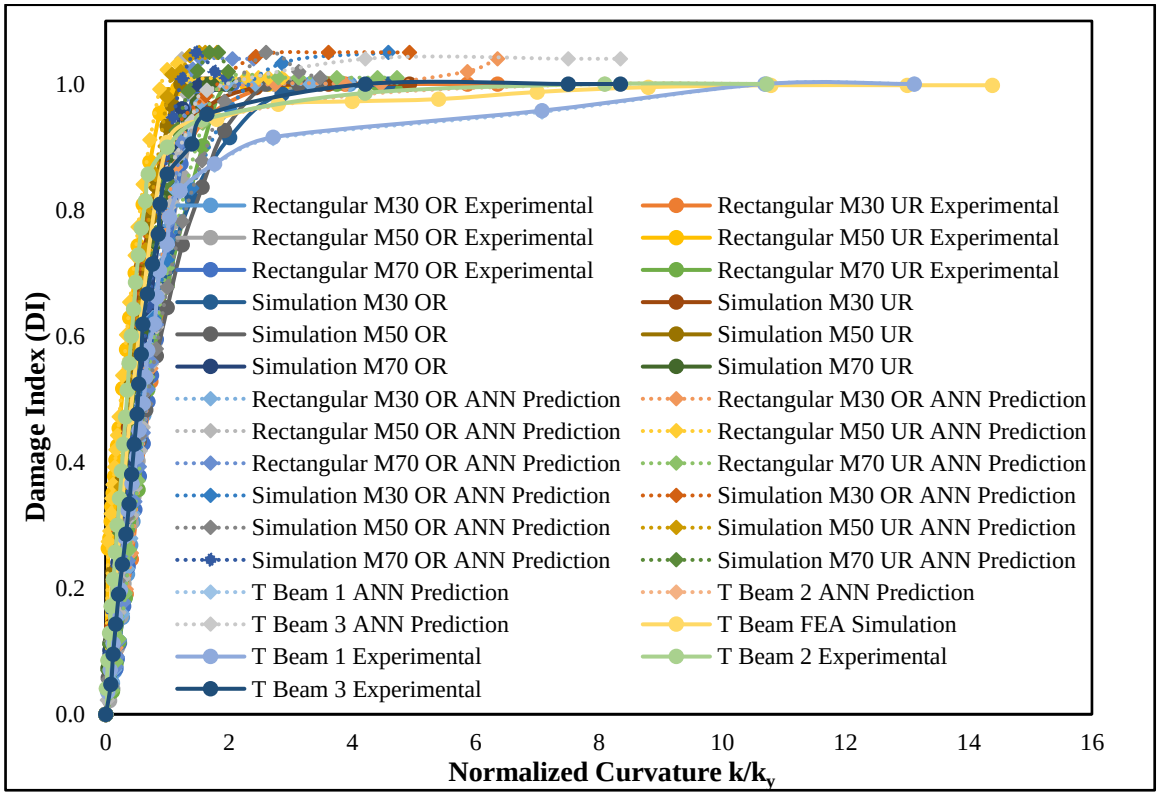

Figure 6.47 Damage Index (DI) vs Normalised Curvature predicted for experimental beams

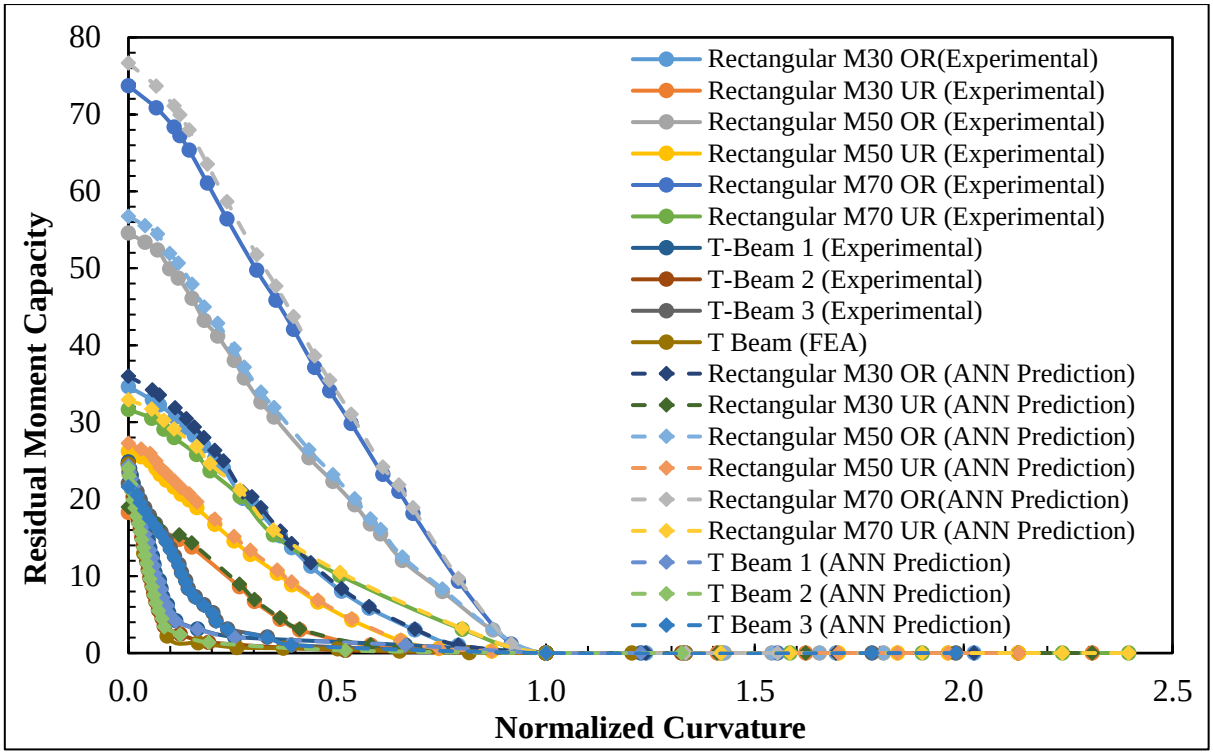

Figure 6.48 Residual Moment Capacity vs Normalised Curvature predicted for Experimental beams

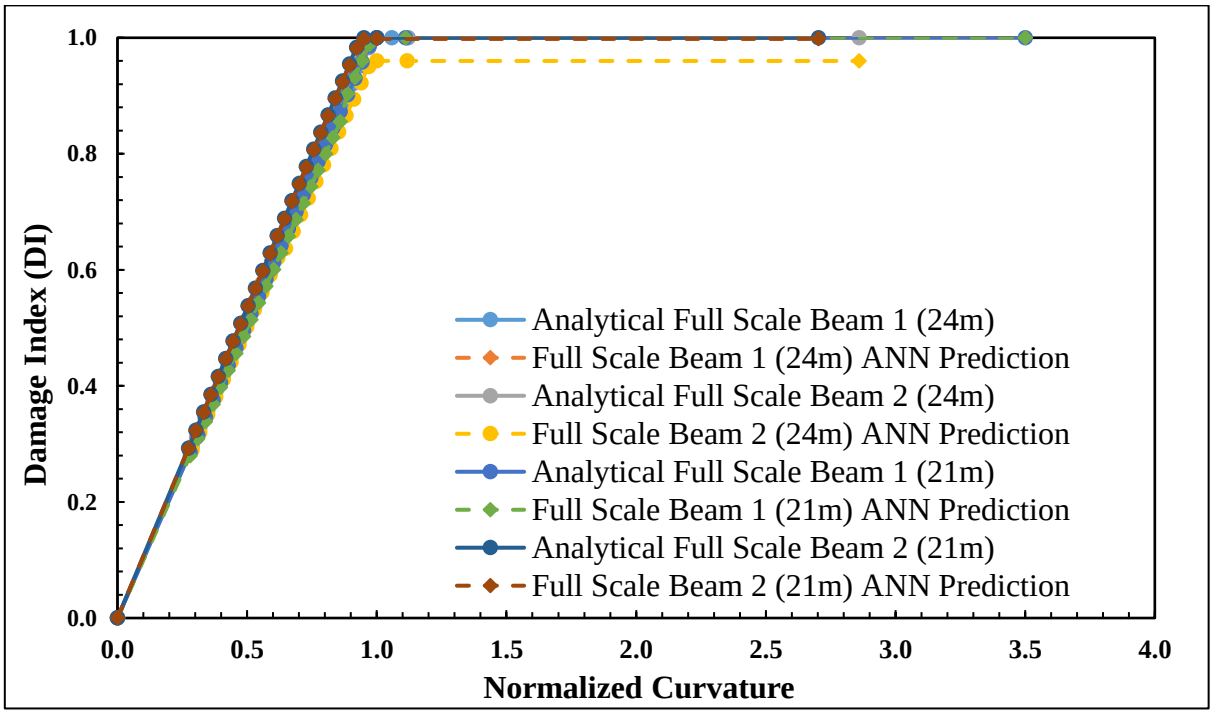

Figure 6.49 Damage Index (DI) vs Normalised Curvature predicted for full-scale MoRTH bridges

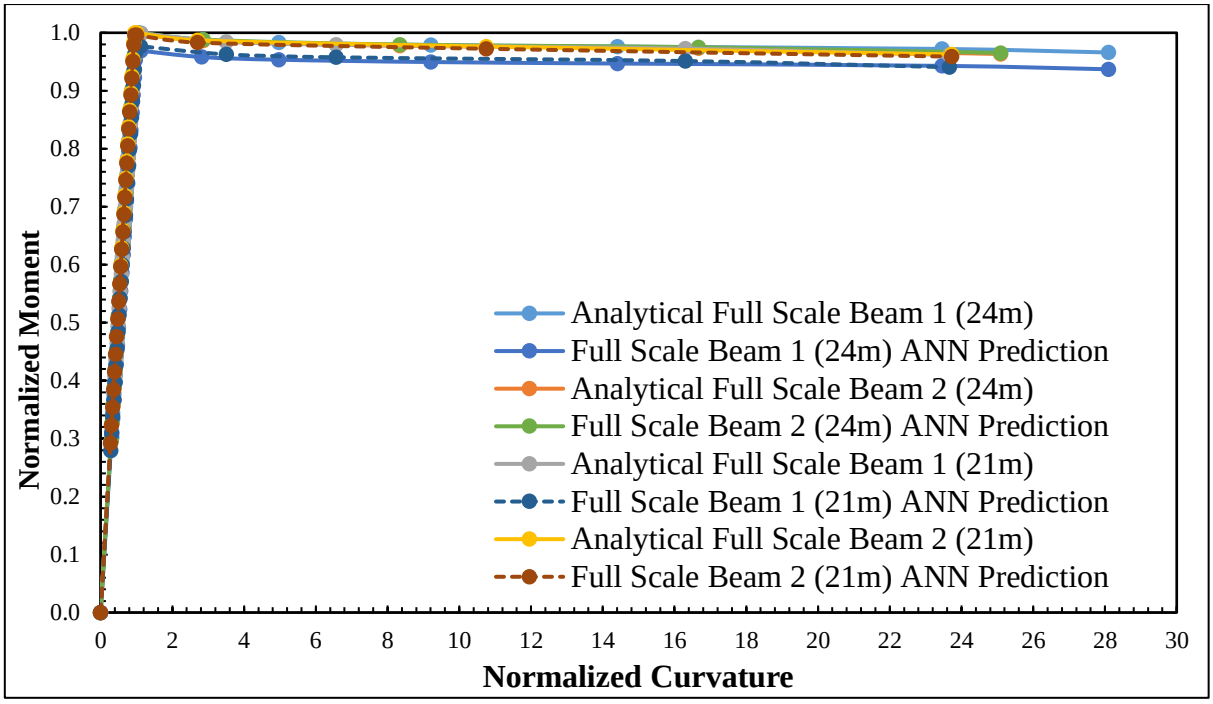

Figure 6.50 Normalised Moment vs Normalised Curvature predicted for full-scale MoRTH bridges

From Figures 6.46 to 6.50 it is observed that ANN results compare well with experimental, analytical and simulation results of flexurally dominated beams (rectangular and T-beams).

6.6 Conclusions Drawn from the Study

This part of the study presents the application of ANNs for image-based prediction of DI of reinforced concrete components. Based on the experiments, as well as FEA and ANN predictions, the following conclusions are drawn:

- In comparison with other ANN training algorithms, such as Bayesian Regularization, and Scaled Conjugate Gradient, the Levenberg-Marquardt algorithm gives acceptable results with fewer iterations and better accuracy.

- It is found that ANNs can correctly identify the magnitude of damage. DI for beams using ANNs is developed based on experimental and numerical simulation results obtained from Phase-I and Phase-II.

- The shape of the normalized moment-curvature relationship (backbone curve) is similar for the flexure dominated beams. This finding can be used to generalize the results of this study to full-scale bridges components.

- As the damage index increases, the residual moment capacity of the section falls linearly. Initially, the damage index for simulated full-scale girder changes rapidly at small values of curvature. Hence, the curvature is a sensitive indicator of residual capacity and damage in flexure dominated beams.

CHAPTER 7

Conclusions

7.0. Brief Conclusions from Each Phase

From the three phases of the study, it can be summarized that Quick Response (QR) code-based random speckle pattern compares well with conventionally obtained results. The more random the speckle pattern, the closer are the Digital Image Correlation (DIC) results in comparison with conventional measurements. An image-based damage prediction and classification methodology for condition assessment of Reinforced Cement Concrete (RCC) bridge girders is developed in this study. To assess the condition of structural components, a local damage index was developed. The development of a framework will enable global as well as localized measurements of structural deformation and provide data for periodic maintenance as well as condition classification of critical infrastructure. Based on the three phases of investigation, the following conclusions can be drawn.

A schematic diagram of the research methodology adopted along with the variables considered in each phase and corresponding outcomes are shown in Figure 7.1.

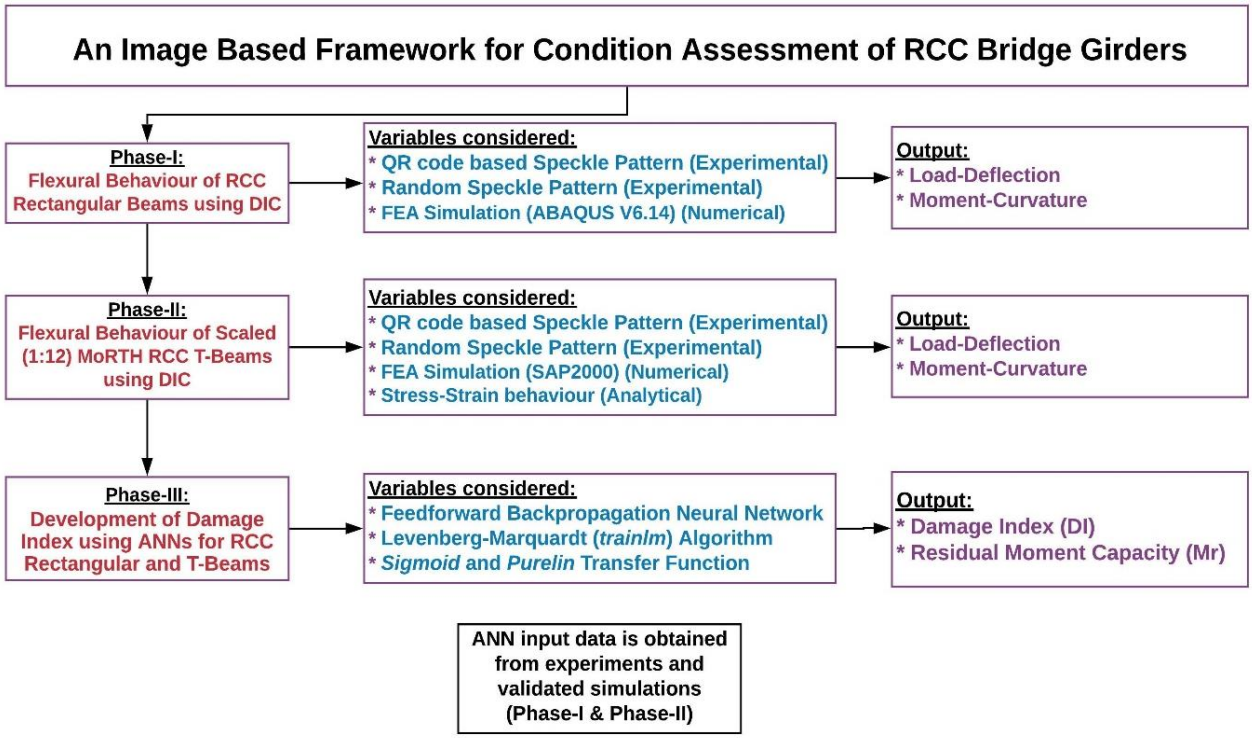

Figure 7.1 Schematic diagram of the research work

7.1. Phase-I

The following conclusions are drawn based on the flexural response extracted using conventional measurements and DIC technique on RCC rectangular beams.

- The M-κ relationships for RCC beams obtained from conventional curvature meters and deflections from crosshead readings compare well with DIC results obtained using different speckle patterns. An innovative approach to use QR code as a speckle pattern in the field of DIC is proposed with comparative results. Further, embedding data in a speckle pattern will enable integration with BIM.

- The M-κ values extracted using QR code-based speckle pattern compare well with conventionally obtained M-κ results. The ultimate moment carrying capacity of RCC beams extracted from QR code-based speckle pattern is more accurate, with less scatter while compared with the ultimate values obtained from M-κ random speckle pattern.

- The results of the FEA modelling procedures using CDP and non-linear geometry (NLGEOM) compare well with experimental results obtained for conventional methods as well as DIC.

- The non-linear constitutive modelling adopted herein is a CDP model applied in the finite element code, ABAQUS. This constitutive model is used to predict the realistic flexural nonlinear behaviour of RCC beams, and it is observed that M-κ results extracted using QR code-based speckle pattern closely match FEM simulation results.

- The more random the pattern is, the closer are the DIC results obtained from both FEM and conventional measurements.

- QR code-based speckle pattern serves a dual purpose of having an additional advantage of data encryption and may be used as consistent non-contact optical sensor in real-time structure health monitoring techniques.

7.2. Phase-II

The following conclusions are drawn based on flexural response extracted using conventional measurements, numerical, analytical and DIC technique on T- beams.

- ❖ The M-κ relationships for T-beams obtained from conventional dial gauge and crosshead readings compare well with DIC results obtained using different speckle patterns.

- ❖ The scaling factors are derived from the standard law of similitude procedure and their accuracy in satisfying the similarity conditions.

- ❖ The designed scaled-down T-beam is cast and tested in a four-point bending test configuration under incremental loads while DIC cameras measured the displacement field and calculated the strain distribution of the T-beam.

- ❖ Analytical stress-strain relationship for scaled (1:12) RCC T-beam is validated based on experimental results.

- ❖ The QR code serves the dual purpose of embedding data in the structural component as well as functioning as a random pattern for DIC which is helpful for non-contact sensor-based condition monitoring, as well as the integration of component-level data with BIM.

7.3. Phase-III

This part of the study presents the application of ANNs for image-based prediction of Damage Index (DI) of reinforced concrete components. Based on the experiments, as well as FEA and ANNs predictions, the following conclusions are drawn:

- ❖ In comparison with other ANN training algorithms, such as Bayesian Regularization, and Scaled Conjugate Gradient, the Levenberg-Marquardt algorithm gives acceptable results with fewer iterations and better accuracy.

- ❖ It is found that ANNs can correctly identify the magnitude of damage. DI for beams using ANNs is developed based on experimental and numerical simulation results obtained from Phase-I and Phase-II.

- ❖ The shape of the normalized moment-curvature relationship (backbone curve) is similar for the flexure dominated beams. This finding can be used to generalize the results of this study to full-scale bridges.

- ❖ As the damage index increases, the residual moment capacity of the section falls linearly. Initially, the damage index for simulated full-scale girder changes rapidly at small values of curvature. Hence, the curvature is a sensitive indicator of residual capacity and damage in flexure dominated beams.

7.4 Specific Contributions Made in this Research Work

The following are the major contributions:

- ❖ An innovative approach to using QR code as a speckle pattern in the field of DIC is established with comparative results. QR code-based speckle pattern may be used as an integrated non-contact optical sensor for Structural Health Monitoring (SHM) and data embedment for BIM.

- ❖ An image-based condition assessment methodology is developed to enable quantification of existing damage and residual moment capacity based on curvature for flexure dominated RCC Bridge T-girder.

- ❖ Correlation between mechanistic based superstructure Damage Index (DI) and bridge Condition Rating Number (CRN) is established.

- ❖ The methodology presented in this study enables image-based condition assessment and damage quantification for flexure dominated structural components.

7.5 Future Scope of the Investigation

Further study may be attempted in the following focuses:

- ❖ Development of ruggedized rig and data processing system utilizing two cameras for 3D DIC as well as photogrammetry.

- ❖ Behaviour of scaled RCC T-beams for Shear dominated and axial structural components using DIC.

- ❖ Study on sensor instrumented buildings and bridges (field trials) in conjunction with painted (optimized) speckle patterns.

- For large input datasets deep learning algorithms like (convolution neural network, long short-term memory neural network) are preferred rather than normal ANNs, to reduce the computational burden.

CHAPTER 8

References

1. Ab Ghani, A. F., Ali, M. B., DharMalingam, S., & Mahmud, J. (2016). Digital image correlation (DIC) technique in measuring strain using opensource platform Ncorr. *Journal of Advanced Research in Applied Mechanics*, *26*(1), 10-21.
2. M Abd, A., D Salman, W., & W Ahmed, Q. (2015). ANN and statistical modelling to predict the deflection of continuous reinforced concrete deep beams. *Diyala Journal of Engineering Sciences*, *8*(4), 134-143.
3. Altunisik, A. C., Kalkan, E., & Basaga, H. B. (2018). Structural response relationship between scaled and prototype concrete load bearing systems using similarity requirements. *Computers and Concrete*, *21*(4), 385-397.
4. Antoš, J., Nežerka, V., & Somr, M. (2017). Assessment of 2d-DIC stochastic patterns. *Acta Polytechnica CTU Proceedings*, *13*, 1-10.
5. Balawi, S., Shahid, O., & Mulla, M. A. (2015). Similitude and scaling laws-static and dynamic behaviour beams and plates. *Procedia Eng*, *114*, 330-337.
6. Blaber, J., Adair, B., & Antoniou, A. (2015). Ncorr: open-source 2D digital image correlation matlab software. *Experimental Mechanics*, *55*(6), 1105-1122.
7. Blaysat, B., Grediac, M., & Sur, F. (2016). On the propagation of camera sensor noise to displacement maps obtained by DIC-an experimental study. *Experimental Mechanics*, *56*(6), 919-944.
8. Bossuyt, S. (2013). Optimized patterns for digital image correlation. In *Imaging Methods for Novel Materials and Challenging Applications, Volume 3* (pp. 239-248). Springer, New York, NY.
9. Bridge Inspection and Maintenance, Manual by Indian Railways, Institute of Civil Engg., Fourth Edition -September 2014, 11-A, South Main Road, Koregaon Park, Pune 411 001.
10. BIS, I. (1970). 383 (1970) Specification for Coarse and Fine Aggregates from Natural Sources for Concrete. *Bureau of Indian Standards, New Delhi, India*.

11. BIS, I. (1987). 12269-1987: Specifications for 53 grade ordinary Portland cement. *Bureau of Indian Standards, New Delhi, India.*

12. Indian Standard. (2000). IS 456 2000: Plain and Reinforced Concrete. Code of Practice (4th revision). *Bureau of Indian Standards, New Delhi*.

13. Cao, V. V., Ronagh, H. R., Ashraf, M., & Baji, H. (2014). A new damage index for reinforced concrete structures. *Earthquakes and Structures*, *6*(6), 581-609.

14. Carter, J. L., Uchic, M. D., & Mills, M. J. (2015). Impact of speckle pattern parameters on DIC strain resolution calculated from in-situ SEM experiments. In *Fracture, Fatigue, Failure, and Damage Evolution, Volume 5* (pp. 119-126). Springer, Cham.

15. Chen, Z., Shao, X., Xu, X., & He, X. (2018). Optimized digital speckle patterns for digital image correlation by consideration of both accuracy and efficiency. *Applied optics*, *57*(4), 884-893.

16. Cofaru, C., Philips, W., & Van Paepegem, W. (2010). Improved Newton–Raphson digital image correlation method for full-field displacement and strain calculation. *Applied optics*, *49*(33), 6472-6484.

17. Cybenko, G. (1989). Approximation by superpositions of a sigmoidal function. *Mathematics of control, signals and systems*, *2*(4), 303-314.

18. De Villiers, J., & Barnard, E. (1993). Backpropagation neural nets with one and two hidden layers. *IEEE transactions on neural networks*, *4*(1), 136-141.

19. Deniaud, C., & Roger Cheng, J. J. (2003). Reinforced concrete T-beams strengthened in shear with fiber reinforced polymer sheets. *Journal of Composites for Construction*, *7*(4), 302-310.

20. Dutton, M., Take, W. A., & Hoult, N. A. (2014). Curvature monitoring of beams using digital image correlation. *Journal of Bridge Engineering*, *19*(3), 05013001.

21. El-Ariss, B. (2006). Effect of reducing coarse aggregates on concrete strength. *Construction and Building Materials*, *20*(3), 149-157.

22. Feng, D., Feng, M. Q., Ozer, E., & Fukuda, Y. (2015). A vision-based sensor for noncontact structural displacement measurement. *Sensors*, *15*(7), 16557-16575.

23. Fitzner, B., & Heinrichs, K. (2001). Damage diagnosis at stone monuments-weathering forms, damage categories and damage indices. *Acta-Universitatis Carolinae Geologica*, *1*, 12-13.

24. George, J., Rama, J. K., Kumar, M. S., & Vasan, A. (2017). Behavior of plain concrete beam subjected to three point bending using concrete damaged plasticity (CDP) model. *Materials Today: Proceedings*, *4*(9), 9742-9746.

25. Grassl, P., Xenos, D., Nyström, U., Rempling, R., & Gylltoft, K. (2013). CDPM2: A damage-plasticity approach to modelling the failure of concrete. *International Journal of Solids and Structures*, *50*(24), 3805-3816.

26. Hait, P., Sil, A., & Choudhury, S. (2019). Overview on damage assessment of structures. *Current Science*, *117*(1), 64.

27. Harilal, R. (2014). Adaptation of open source 2D DIC software Ncorr for solid mechanics applications. pp. 1-6.

28. Harris, H. G., & Sabnis, G. (1999). *Structural modeling and experimental techniques*. CRC press.

29. Harris, H. G., Sabnis, G. M., & White, R. N. (1966). *Small scale direct models of reinforced and prestressed concrete structures* (No. 326). Dept. of Structural Engineering, School of Civil Engineering, Cornell University.

30. HasançEbi, O., & Dumlupınar, T. (2013). Linear and nonlinear model updating of reinforced concrete T-beam bridges using artificial neural networks. *Computers & Structures*, *119*, 1-11.

31. Hecht-Nielsen, R. (1992). Theory of the backpropagation neural network. In *Neural networks for perception* (pp. 65-93). Academic Press.

32. Hung, P. C., & Voloshin, A. S. (2003). In-plane strain measurement by digital image correlation. *Journal of the Brazilian Society of Mechanical Sciences and Engineering*, *25*(3), 215-221.

33. Imam, A., Anifowose, F., & Azad, A. K. (2015). Residual strength of corroded reinforced concrete beams using an adaptive model based on ANN. *International Journal of Concrete Structures and Materials*, *9*(2), 159-172.

34. Indian Standard code of practice [IS: 2250 – 1981, Reaffirmed 2000] For Preparation and use of masonry mortars (First revision).

35. Jadid, M. N., & Fairbairn, D. R. (1996). Neural-network applications in predicting moment-curvature parameters from experimental data. *Engineering Applications of Artificial Intelligence*, *9*(3), 309-319.

36. Jankowiak, T., & Lodygowski, T. (2005). Identification of parameters of concrete damage plasticity constitutive model. *Foundations of civil and environmental engineering*, *6*(1), 53-69.

37. Jeyasehar, C. A., & Sumangala, K. (2006). Damage assessment of prestressed concrete beams using artificial neural network (ANN) approach. *Computers & structures*, *84*(26-27), 1709-1718.

38. Kalyana Rama, J. S., Chauhan, D. R., Sivakumar, M. V. N., Vasan, A., & Murthy, A. R. (2017). Fracture properties of concrete using damaged plasticity model-A parametric study. *Structural Engineering and Mechanics*, *64*(1), 59-69.

39. Kanwar, V., Kwatra, N., & Aggarwal, P. (2007). Damage detection for framed RCC buildings using ANN modeling. *International Journal of Damage Mechanics*, *16*(4), 457-472.

40. Kappos, A. J. (1997). Seismic damage indices for RC buildings: evaluation of concepts and procedures. *Progress in Structural Engineering and materials*, *1*(1), 78-87.

41. Karamodin, A., Kazemi, H. H., & Akbarzadeh-T, M. R. (2008, October). Damage Index Monitoring of Structures Using Neural Networks. In *14th World Conference on Earthquake Engineering*.

42. Knappett, J. A., Reid, C., Kinmond, S., & O'Reilly, K. (2011). Small-scale modeling of reinforced concrete structural elements for use in a geotechnical centrifuge. *Journal of Structural Engineering*, *137*(11), 1263-1271.

43. Kozicki, J., & Tejchman, J. (2007). Experimental investigations of strain localization in concrete using Digital Image Correlation (DIC) technique. *Archives of Hydro-Engineering and Environmental Mechanics*, *54*(1), 3-24.

44. Lecompte, D., Sol, H., Vantomme, J., & Habraken, A. (2006, September). Analysis of speckle patterns for deformation measurements by digital image correlation.

In *SPECKLE06: Speckles, From Grains to Flowers* (Vol. 6341, p. 63410E). International Society for Optics and Photonics.

45. Lee, J., & Fenves, G. L. (1998). Plastic-damage model for cyclic loading of concrete structures. *Journal of engineering mechanics*, *124*(8), 892-900.

46. Liang, Z., Yin, B., Liu, H., Mo, J., & Wang, S. (2015). Displacement measurement of specimen surfaces with damaged areas by digital image correlation. *Measurement*, *76*, 183-188.

47. Long, X., Fu, S., Qi, Z., Yang, X., & Yu, Q. (2013). Digital image correlation using stochastic parallel-gradient-descent algorithm. *Experimental Mechanics*, *53*(4), 571-578.

48. Lu, H., & Cary, P. D. (2000). Deformation measurements by digital image correlation: implementation of a second-order displacement gradient. *Experimental mechanics*, *40*(4), 393-400.

49. Lubliner, J., Oliver, J., Oller, S., & Oñate, E. (1989). A plastic-damage model for concrete. *Int. J. Solids and Structures*. pp. 299-326.

50. Lucas, B. D., & Kanade, T. (1981). An iterative image registration technique with an application to stereo vision.

51. Meadati, P., & Irizarry, J. (2018). BIM and QR Code for Operation and Maintenance. In *Computing in Civil Engineering 2015* (pp. 556-563).

52. Mechbal, N., & Rebillat, M. (2017, June). Damage indexes comparison for the structural health monitoring of a stiffened composite plate. J. R. A. Güemes, A. Benjeddou, J. Leng (Eds.), 8th ECCOMAS Thematic Conference on Smart Structures and Materials (SMART 2017), Madrid, Spain, pp. 436-444.

53. Ministry of Surface Transport. (1991). Standard plans for highway bridges—RCC T-beam and slab super structure.

54. MLV, P., & Kumar Rathish, P. (2012). Moment-curvature relationship of glass fiber reinforced self-compacting recycled aggregate concrete. *Journal of Environmental Research And Development*, *7*(2A).

55. Moon, H. G., & Kim, J. H. (2011). Intelligent crack detecting algorithm on the concrete crack image using neural network. *Proceedings of the 28th ISARC*, 1461-1467.

56. Mudassar, A. A., & Butt, S. (2016). Improved digital image correlation method. *Optics and Lasers in Engineering*, *87*, 156-167.

57. Nguyen, V. T., Kwon, S. J., Kwon, O. H., & Kim, Y. S. (2017). Mechanical properties identification of sheet metals by 2D-digital image correlation method. *Procedia Engineering*, *184*, 381-389.

58. Onal, O., & Ozturk, A. U. (2010). Artificial neural network application on microstructure–compressive strength relationship of cement mortar. *Advances in Engineering Software*, *41*(2), 165-169.

59. Pan, B. (2014). An evaluation of convergence criteria for digital image correlation using inverse compositional Gauss–Newton algorithm. *Strain*, *50*(1), 48-56.

60. Pan, B., Qian, K., Xie, H., & Asundi, A. (2009). Two-dimensional digital image correlation for in-plane displacement and strain measurement: a review. *Measurement science and technology*, *20*(6), 062001.

61. Petry, S., & Beyer, K. (2012). Testing unreinforced masonry structures at reduced scale. In *Proceedings of the 15th World Conference on Earthquake Engineering* (No. CONF).

62. S. Philip Bamiyo, O. Austine and M. Adamu. (2016). "Study of Load-Deflection of two way Slab using artificial neural networks". In *Journal of Civil Engineering*.

63. Hung, P. C., & Voloshin, A. S. (2003). In-plane strain measurement by digital image correlation. *Journal of the Brazilian Society of Mechanical Sciences and Engineering*, *25*(3), 215-221.

64. Salmanpour, A., & Mojsilovic, N. (2013, December). Application of Digital Image Correlation for strain measurements of large masonry walls. In *Conference Proceedings. APCOM & ISCM, Singapore*.

65. Shih, M. H., & Sung, W. P. (2013). Application of digital image correlation method for analysing crack variation of reinforced concrete beams. *Sadhana*, *38*(4), 723-741.

66. Simitses, G. J., Starnes, J. H., & Rezaeepazhand, J. (2001). Structural similitude and scaling laws for plates and shells: A review. In *Advances in the Mechanics of Plates and Shells* (pp. 295-310). Springer, Dordrecht.

67. Simulia, D. S. (2011). Abaqus 6.11 theory manual. *Providence, RI, USA: DS SIMULIA Corp*.

68. Srikanth, M. G. R. K., Rajesh, K. G., & Giri, S. (2007). Moment curvature of reinforced concrete beams using various confinement models and experimental validation. *Asian Journal of Civil Engineering*, pp. 247-265.

69. Stoilov, G., Kavardzhikov, V., & Pashkouleva, D. (2012). A comparative study of random patterns for digital image correlation. *Journal of Theoretical and Applied Mechanics*, *42*(2), 55-66.

70. Stubbs, N., & Kim, J. T. (1996). Damage localization in structures without baseline modal parameters. *AIAA journal*, *34*(8), 1644-1649.

71. Su, C., & Anand, L. (2003). A new digital image correlation algorithm for whole-field displacement measurement. Proceedings of Singapore-MIT Alliance Symposium of Innovation in Manufacturing Systems and Technology.

72. Sung, Y. C., Miyasaka, T., Lin, T. K., Wang, C. Y., & Wang, C. Y. (2012). A case study on bridge health monitoring using position-sensitive detector technology. *Structural Control and Health Monitoring*, *19*(2), 295-308.

73. Suryanto, B., Tambusay, A., & Suprobo, P. (2017). Crack mapping on shear-critical reinforced concrete beams using an open source digital image correlation software. *Civil Engineering Dimension*, *19*(2), 93-98.

74. Sutton, M. A., Wolters, W. J., Peters, W. H., Ranson, W. F., & McNeill, S. R. (1983). Determination of displacements using an improved digital correlation method. *Image and vision computing*, *1*(3), 133-139.

75. Schreier, H., Orteu, J. J., & Sutton, M. A. (2009). *Image correlation for shape, motion and deformation measurements: Basic concepts, theory and applications* (Vol. 1). Boston, MA: Springer-Verlag US.

76. Swamy Naga Ratna Giri, P., Rajesh Kumar, G., Sri Rama Chand, M., & Rathish Kumar, P. (2017). Stress–strain model for tie-confined self-curing self-compacting concrete. *Proceedings of the Institution of Civil Engineers-Structures and Buildings*, *170*(7), 465-480.

77. Swamy Naga Ratna Giri, P., Rajesh Kumar, G., Sri Rama Chand, M., & Rathish Kumar, P. (2018). Flexural behaviour of tie-confined self-curing self-compacting concrete. *Magazine of Concrete Research*, *70*(23), 1232-1242.

78. Syed, A. M., Javed, M., & Alam, B. Similitude Analysis of Concrete Scaled Bridge Columns for Quasi-Static and Free Vibration Testing.

79. Tong, W. (2005). An evaluation of digital image correlation criteria for strain mapping applications. *Strain*, *41*(4), 167-175.

80. Vassoler, J. M., & Fancello, E. A. (2010). Error analysis of the digital image correlation method. *Mecánica Computacional*, *29*(61), 6149-6161.

81. Wang, G., Liu, X., Wei, C., Zhang, Z., & Wang, W. (2017). Experimental Study on Flexural Capacity of Reinforced Concrete Beam after Collision. *Journal of Engineering Science & Technology Review*, *10*(1).

82. White, R. N. (1964). Small-scale Models of Concrete structures. American Society of Civil Engineers.

83. Wittevrongel, L., Lava, P., Lomov, S. V., & Debruyne, D. (2015). A self adaptive global digital image correlation algorithm. *Experimental Mechanics*, *55*(2), 361-378.

84. Wolowicz, C. H., Brown Jr, J. S., & Gilbert, W. P. (1979). Similitude requirements and scaling relationships as applied to model testing. NASA, Tech. Rep. 1435.

85. Wu, D., & Xiong, Y. (2017). Tests study of a 1: 20 scale steel-concrete hybrid structure. *Procedia engineering*, *210*, 441-448.

86. Wu, X., Ghaboussi, J., & Garrett Jr, J. H. (1992). Use of neural networks in detection of structural damage. *Computers & structures*, *42*(4), 649-659.

87. Yaofeng, S., & Pang, J. H. (2007). Study of optimal subset size in digital image correlation of speckle pattern images. *Optics and lasers in engineering*, *45*(9), 967-974.

88. Yuan, Y., Huang, J., Fang, J., Yuan, F., & Xiong, C. (2015). A self-adaptive sampling digital image correlation algorithm for accurate displacement measurement. *Optics and Lasers in Engineering*, *65*, 57-63.

89. Zyung, T., Kim, H., Postlewaite, J. C., & Dlott, D. D. (1988). Ultrafast Imaging of Optical Damage in PMMA. In *Laser Induced Damage in Optical Materials: 1987*. ASTM International.

Appendix

Appendix-A

MoRTH T-girder of 24 m span beam-1

```
% Program for Moment-Curvature of T-Beam
% Modified by: Dr.T.P.Tezeswi
%=========================================================================
clear all
clc
format long
%-------------------------------------------------------------------------
---
% Generate distribution of Concrete properties
%-------------------------------------------------------------------------
---
fck=30; % Characteristic strength of concrete
ssigma=5 % Standard Deviation Ref: IS456, Table 8
ftarg =1.65*ssigma+fck % mean value
fdata=[fck,ftarg]';
pd=fitdist(fdata, 'Normal')% Fit normal distribution to the given data
xx=0:1:1000;
pdf =pdf (pd, xx); % Generate normally distributed samples of fc
figure(1)
plot(xx,pdf,'linewidth',2);
rr=ftarg+ssigma.*randn(500,1);% Generate 1000 normally distributed
samples of fc
%-------------------------------------------------------------------------
--
% Generate Moment-curvature based on stress block equilibrium
%-------------------------------------------------------------------------
--
e_o=0.003; % Max strain in concrete
f_y=415;   % Yield Strength of Steel
A_st=17981;% Area of Steel
b_f=2800;  % Width of Flange
d_f=350;   % Depth of flange
b_w=625;   % Width of web
d_w=2055;  % Depth of web
n=0.5*dw; % Thickness of layer
z=1;       %
pp=35     % number of strain increments
for jj=1:500;
fci(jj)=rr(jj);
fc=fci(jj);
    i=1;
    for ii=[0.003 1:pp]
        ecc=0.0001*ii;
        check=0;
        TS=0;
        MTS=0;
        while check==0
            TC=0;
            TMC=0;
            for j=1:100
                cstrip=(n/55)*j-(n/150);
```

```
                ec=cstrip*ecc/n;
                CS=fck*(2*ec/eo-(ec/eo)^2);
                CF=CS*bf*n/100;
                MC=CF*cstrip;
                TC=TC+CF;
                TMC=TMC+MC;
            end
            est=(dw-n)*ecc/n;
            if est>(fy/200000)
                sst=fy;
            else
                sst=est*200000;
            end
            TS=sst*Ast;
            MTS=TS*(dw-n);
            TT=TS;
            MT=MTS;
            M=TMC+MT;
            phi=ecc/n;
            if TC>TT
                n=n-0.1;
            else if TC<TT
                    n=n+0.1;
                end
            end
            err=TC-TT;
            perr=abs(100*err/TC);
            if perr<1
                check=1;
            end
        end
        fperr(i)=perr;
        fn(z,i)=n;
        fTC(i)=TC;
        fT(i)=TT;
        fTMC(i)=TMC;
        fMT(i)=MT;
        fM(z,i)=M;
        fphi(z,i)=phi;
        i=i+1;
    end
   figure(2)
   plot(fphi(z,:),fM(z,:), '-*') % Plot individual M-Phi curves
   hold on
   %Storage of data
   fphijj(z,:,jj)=fphi(z,:);
   fMjj(z,:,jj)=fM(z,:);
end
```

MoRTH T-girder of 24 m span beam-2

```
% Program for Moment-Curvature of T-Beam
% Modified by: Dr.T.P.Tezeswi
%=========================================================================
clear all
clc
format long
%-------------------------------------------------------------------------
---
% Generate distribution of Concrete properties
%-------------------------------------------------------------------------
---
fck=30; % Characteristic strength of concrete
ssigma=5 % Standard Deviation Ref: IS456, Table 8
ftarg =1.65*ssigma+fck % mean value
fdata=[fck,ftarg]';
pd=fitdist(fdata, 'Normal')% Fit normal distribution to the given data
xx=0:1:1000;
pdf =pdf (pd, xx); % Generate normally distributed samples of fc
figure(1)
plot(xx,pdf,'linewidth',2);
rr=ftarg+ssigma.*randn(500,1);% Generate 1000 normally distributed
samples of fc
%-------------------------------------------------------------------------
--
% Generate Moment-curvature based on stress block equilibrium
%-------------------------------------------------------------------------
--
eo=0.003; % Max strain in concrete
fy=415;   % Yield Strength of Steel
Ast=17981;% Area of Steel
bf=2825;  % Width of Flange
df=350;   % Depth of flange
bw=625;   % Width of web
dw=2055;  % Depth of web
n=0.5*dw; % Thickness of layer
z=1;      %
pp=35     % number of strain increments
for jj=1:500;
fci(jj)=rr(jj);
fc=fci(jj);
    i=1;
    for ii=[0.003 1:pp]
        ecc=0.0001*ii;
        check=0;
        TS=0;
        MTS=0;
        while check==0
            TC=0;
            TMC=0;
            for j=1:100
                cstrip=(n/55)*j-(n/150);
                ec=cstrip*ecc/n;
                CS=fck*(2*ec/eo-(ec/eo)^2);
                CF=CS*bf*n/100;
                MC=CF*cstrip;
                TC=TC+CF;
```

```
            TMC=TMC+MC;
        end
        est=(dw-n)*ecc/n;
        if est>(fy/200000)
            sst=fy;
        else
            sst=est*200000;
        end
        TS=sst*Ast;
        MTS=TS*(dw-n);
        TT=TS;
        MT=MTS;
        M=TMC+MT;
        phi=ecc/n;
        if TC>TT
            n=n-0.1;
        else if TC<TT
                n=n+0.1;
            end
        end
        err=TC-TT;
        perr=abs(100*err/TC);
        if perr<1
            check=1;
        end
    end
    fperr(i)=perr;
    fn(z,i)=n;
    fTC(i)=TC;
    fT(i)=TT;
    fTMC(i)=TMC;
    fMT(i)=MT;
    fM(z,i)=M;
    fphi(z,i)=phi;
    i=i+1;
 end
figure(2)
plot(fphi(z,:),fM(z,:), '-*') % Plot individual M-Phi curves
hold on
%Storage of data
fphijj(z,:,jj)=fphi(z,:);
fMjj(z,:,jj)=fM(z,:);
end
```

MoRTH T-girder of 21 m span beam-3

```
% Program for Moment-Curvature of T-Beam
% Modified by: Dr.T.P.Tezeswi
%=========================================================================
clear all
clc
format long
%-------------------------------------------------------------------------
---
% Generate distribution of Concrete properties
%-------------------------------------------------------------------------
---
fck=30; % Characteristic strength of concrete
ssigma=5 % Standard Deviation Ref: IS456, Table 8
ftarg =1.65*ssigma+fck % mean value
fdata=[fck,ftarg]';
pd=fitdist(fdata, 'Normal')% Fit normal distribution to the given data
xx=0:1:1000;
pdf =pdf (pd, xx); % Generate normally distributed samples of fc
figure(1)
plot(xx,pdf,'linewidth',2);
rr=ftarg+ssigma.*randn(500,1);% Generate 1000 normally distributed
samples of fc
%-------------------------------------------------------------------------
--
% Generate Moment-curvature based on stress block equilibrium
%-------------------------------------------------------------------------
--
eo=0.003; % Max strain in concrete
fy=415;   % Yield Strength of Steel
Ast=18419;% Area of Steel
bf=2650;  % Width of Flange
df=400;   % Depth of flange
bw=625;   % Width of web
dw=2105;  % Depth of web
n=0.5*dw; % Thickness of layer
z=1;      %
pp=35     % number of strain increments
for jj=1:500;
fci(jj)=rr(jj);
fc=fci(jj);
    i=1;
    for ii=[0.003 1:pp]
        ecc=0.0001*ii;
        check=0;
        TS=0;
        MTS=0;
        while check==0
            TC=0;
            TMC=0;
            for j=1:100
                cstrip=(n/55)*j-(n/150);
                ec=cstrip*ecc/n;
                CS=fck*(2*ec/eo-(ec/eo)^2);
                CF=CS*bf*n/100;
                MC=CF*cstrip;
                TC=TC+CF;
```

```
                TMC=TMC+MC;
            end
            est=(dw-n)*ecc/n;
            if est>(fy/200000)
                sst=fy;
            else
                sst=est*200000;
            end
            TS=sst*Ast;
            MTS=TS*(dw-n);
            TT=TS;
            MT=MTS;
            M=TMC+MT;
            phi=ecc/n;
            if TC>TT
                n=n-0.1;
            else if TC<TT
                    n=n+0.1;
                end
            end
            err=TC-TT;
            perr=abs(100*err/TC);
            if perr<1
                check=1;
            end
        end
        fperr(i)=perr;
        fn(z,i)=n;
        fTC(i)=TC;
        fT(i)=TT;
        fTMC(i)=TMC;
        fMT(i)=MT;
        fM(z,i)=M;
        fphi(z,i)=phi;
        i=i+1;
    end
   figure(2)
   plot(fphi(z,:),fM(z,:), '-*') % Plot individual M-Phi curves
   hold on
   %Storage of data
   fphijj(z,:,jj)=fphi(z,:);
   fMjj(z,:,jj)=fM(z,:);
end
```

MoRTH T-girder of 21 m span beam-4

```
% Program for Moment-Curvature of T-Beam
% Modified by: Dr.T.P.Tezeswi
%=========================================================================
clear all
clc
format long
%-------------------------------------------------------------------------
---
% Generate distribution of Concrete properties
%-------------------------------------------------------------------------
---
fck=30; % Characteristic strength of concrete
ssigma=5 % Standard Deviation Ref: IS456, Table 8
ftarg =1.65*ssigma+fck % mean value
fdata=[fck,ftarg]';
pd=fitdist(fdata, 'Normal')% Fit normal distribution to the given data
xx=0:1:1000;
pdf =pdf (pd, xx); % Generate normally distributed samples of fc
figure(1)
plot(xx,pdf,'linewidth',2);
rr=ftarg+ssigma.*randn(500,1);% Generate 1000 normally distributed
samples of fc
%-------------------------------------------------------------------------
--
% Generate Moment-curvature based on stress block equilibrium
%-------------------------------------------------------------------------
--
eo=0.003; % Max strain in concrete
fy=415;   % Yield Strength of Steel
Ast=17981;% Area of Steel
bf=2825;  % Width of Flange
df=350;   % Depth of flange
bw=625;   % Width of web
dw=2055;  % Depth of web
n=0.5*dw; % Thickness of layer
z=1;      %
pp=35     % number of strain increments
for jj=1:500;
fci(jj)=rr(jj);
fc=fci(jj);
    i=1;
    for ii=[0.003 1:pp]
        ecc=0.0001*ii;
        check=0;
        TS=0;
        MTS=0;
        while check==0
            TC=0;
            TMC=0;
            for j=1:100
                cstrip=(n/55)*j-(n/150);
                ec=cstrip*ecc/n;
                CS=fck*(2*ec/eo-(ec/eo)^2);
                CF=CS*bf*n/100;
                MC=CF*cstrip;
                TC=TC+CF;
```

```
                TMC=TMC+MC;
            end
            est=(dw-n)*ecc/n;
            if est>(fy/200000)
                sst=fy;
            else
                sst=est*200000;
            end
            TS=sst*Ast;
            MTS=TS*(dw-n);
            TT=TS;
            MT=MTS;
            M=TMC+MT;
            phi=ecc/n;
            if TC>TT
                n=n-0.1;
            else if TC<TT
                    n=n+0.1;
                end
            end
            err=TC-TT;
            perr=abs(100*err/TC);
            if perr<1
                check=1;
            end
        end
        fperr(i)=perr;
        fn(z,i)=n;
        fTC(i)=TC;
        fT(i)=TT;
        fTMC(i)=TMC;
        fMT(i)=MT;
        fM(z,i)=M;
        fphi(z,i)=phi;
        i=i+1;
    end
   figure(2)
   plot(fphi(z,:),fM(z,:), '-*') % Plot individual M-Phi curves
   hold on
   %Storage of data
   fphijj(z,:,jj)=fphi(z,:);
   fMjj(z,:,jj)=fM(z,:);
end
```

Appendix-B

Mix design for RCC scaled (1:12) T-beams

Trial	Mix Ratio (Cement : Fine Aggregate)	7 days lbs	7 Days MPa	Avg MPa	28 days lbs	28 Days MPa	Avg MPa
1	1:6	32000	6.32	6.46	49000	9.69	9.82
		31000	6.13		51000	10.08	
		35000	6.92		49000	9.69	
2	1:1	93000	18.39	20.10	174000	34.41	34.93
		105000	20.76		172000	34.01	
		107000	21.16		184000	36.38	
3	1:1.5	112000	22.15	24.06	170000	33.62	35.53
		128000	25.31		187000	36.98	
		125000	24.72		182000	35.99	
4	1:2	123000	24.32	24.26	195000	38.56	38.63
		121000	23.93		199000	39.35	
		124000	24.52		192000	37.97	

Appendix-C

Nonlinear Optimization used in DIC analysis

The overall goal of DIC is to obtain displacement and strain fields within a region of interest (ROI) for a material sample undergoing deformation. DIC uses image-processing techniques in an attempt to solve this problem. Basically, images of a sample are taken as it deforms; these images are used as inputs to a DIC program. The idea is to somehow obtain a one-to-one correspondence between material points in the reference (initial un-deformed picture) and current (subsequent deformed pictures) configurations. DIC does this by taking small subsections of the reference image, called subsets, and determining their respective locations in the current configuration.

For each subset, we obtain displacement and strain information through the transformation used to match the location of the subset in the current configuration. Many subsets are picked in the reference configuration, often with a spacing parameter to reduce computational cost (also note that subsets typically overlap as well). The end result is a grid containing displacement and strain information with respect to the reference configuration, also referred to as Lagrangian displacements/strains. The displacement/strain fields can then either be reduced or interpolated to form a "continuous" displacement/strain field. Further details are shown in section 4.2.2.

To be more specific, subsets are essentially a group of coordinate points; the idea of subsets in the reference and current image is shown below:

Correlation Coefficient (refer section 4.2.1)

```
img1= rgb2gray(imread('DSC_0009.jpg'));
img2= rgb2gray(imread('DSC_0022.jpg'));
c = normxcorr2(img2,img1);
figure, surf(c), shading flat
[ypeak, xpeak] = find(c==max(c(:)));
```

Correlation Process (Blaber et al. 2015)

Nonlinear Optimization used in DIC analysis

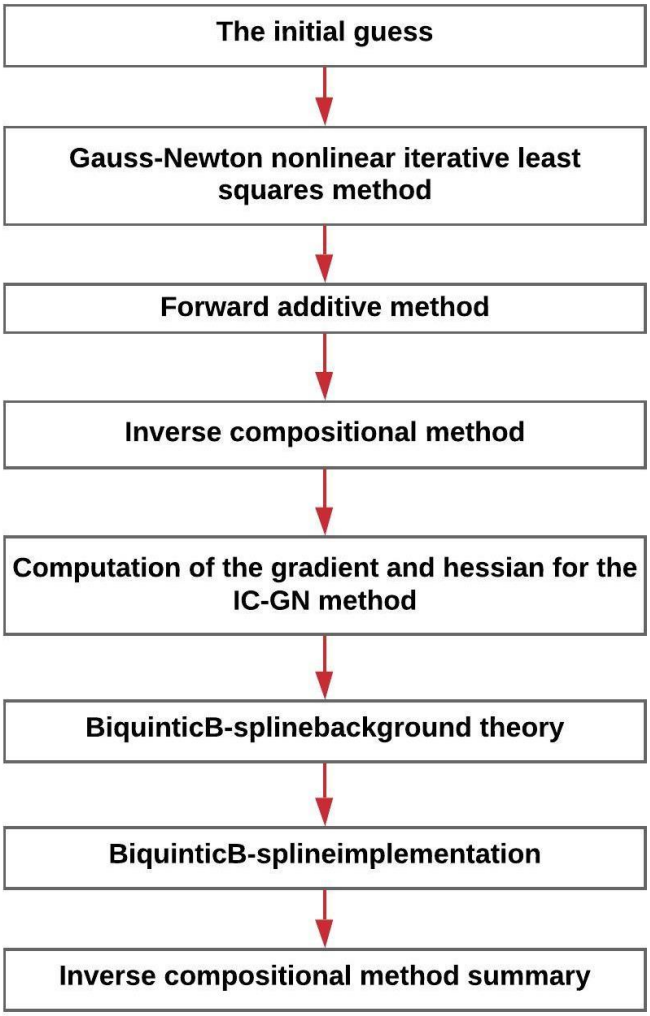

Figure C-1 Details and formulations used in Ncorr V1.2.2 tool for nonlinear optimization

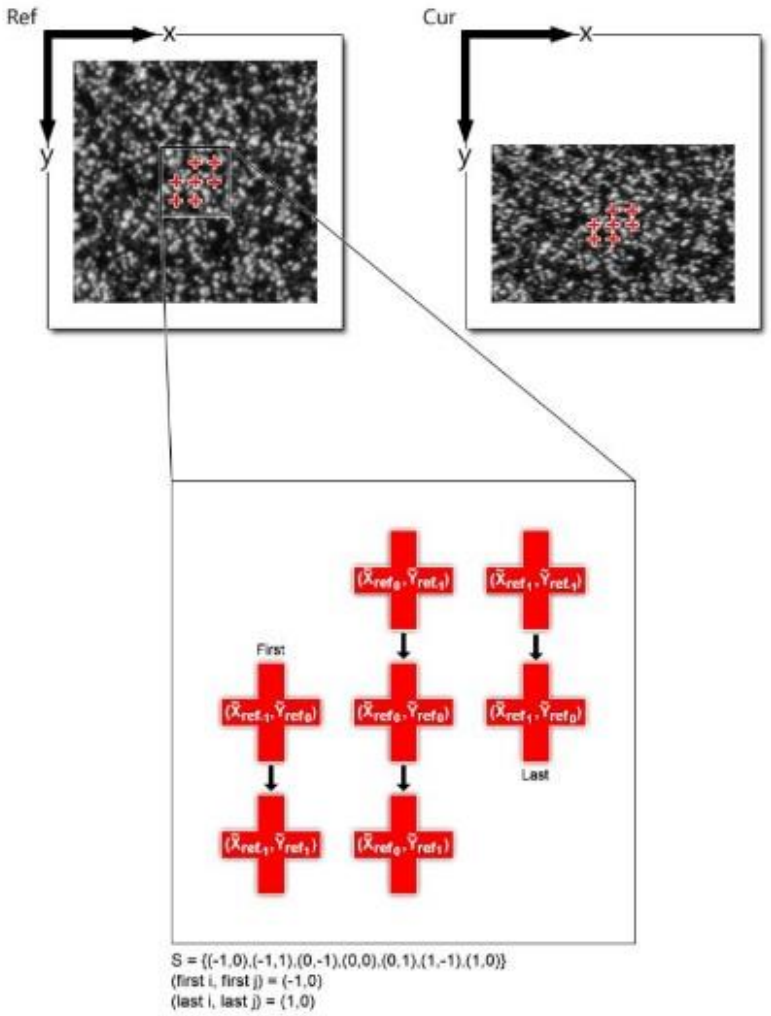

The subset's coordinates are shown as red crosses in the above figure

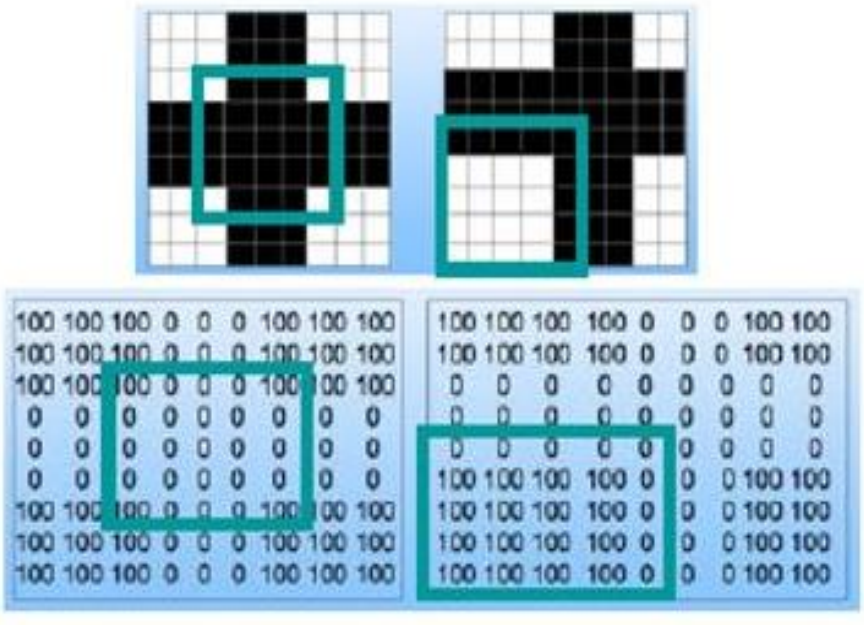

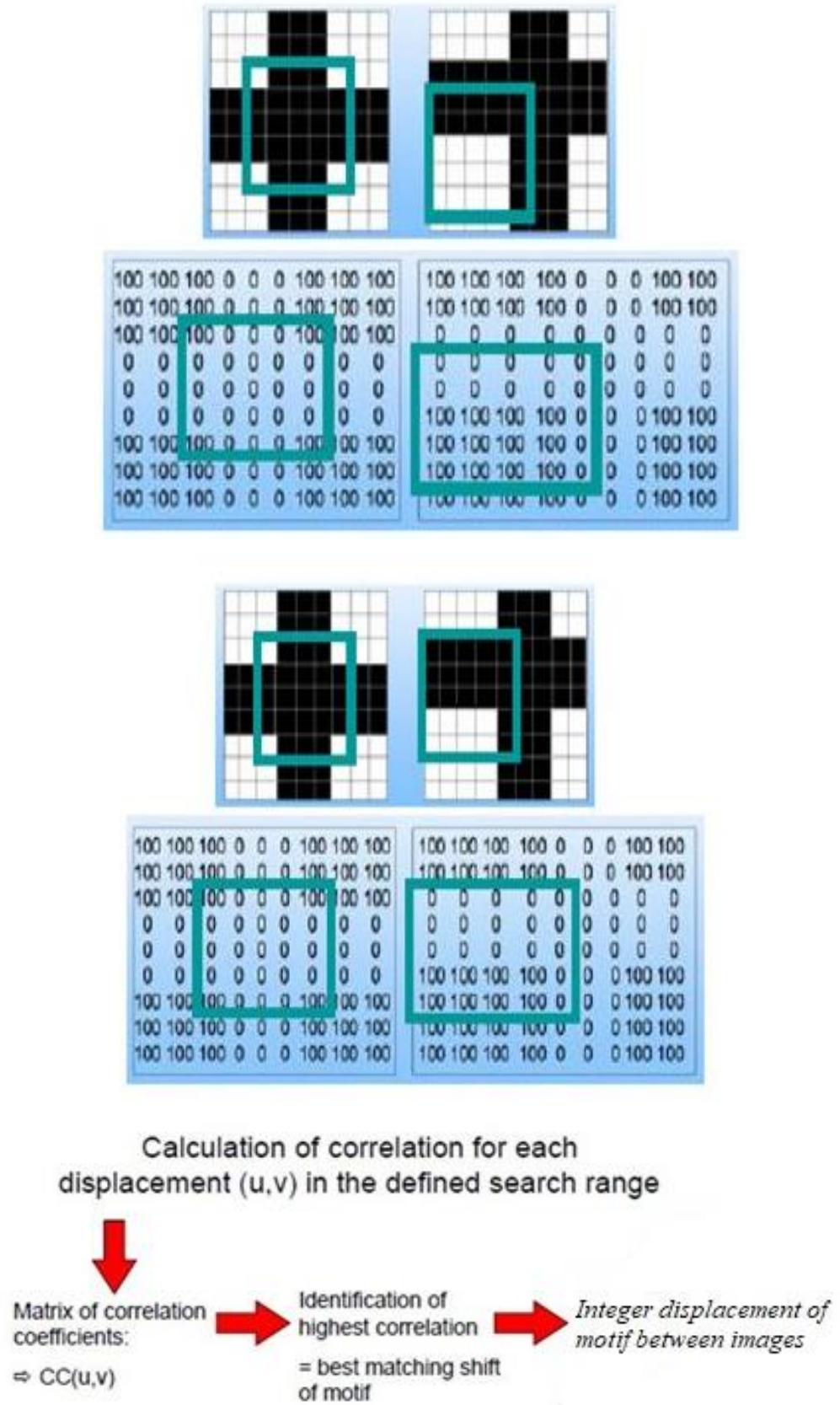

Figure C-2 Calculation of correlation for each coordinate in the given image

Nonlinear Optimization

Gauss-Newton nonlinear iterative least squares method

The Gauss-Newton method is used to find the roots of a function in the case that an analytic solution is not available. This scenario can be extrapolated to optimization by finding the roots of the derivative of a function. Even further, it can be generalized to multivariate optimization by using the gradient in place of the derivative, and then determining where the norm of the gradient converges to zero.

Forward additive method

The FA-GN method is essentially the standard application of a Gauss-Newton iterative solver. In this situation, the final reference subset location remains constant and p_{rr} is set to 0 for every iteration. On the other hand, the final current subset location is allowed to deform and p_{rc} is set to pold at the beginning of every iteration, where pold is the deformation parameters found from the previous iteration, using the forward additive technique or the initial guess.

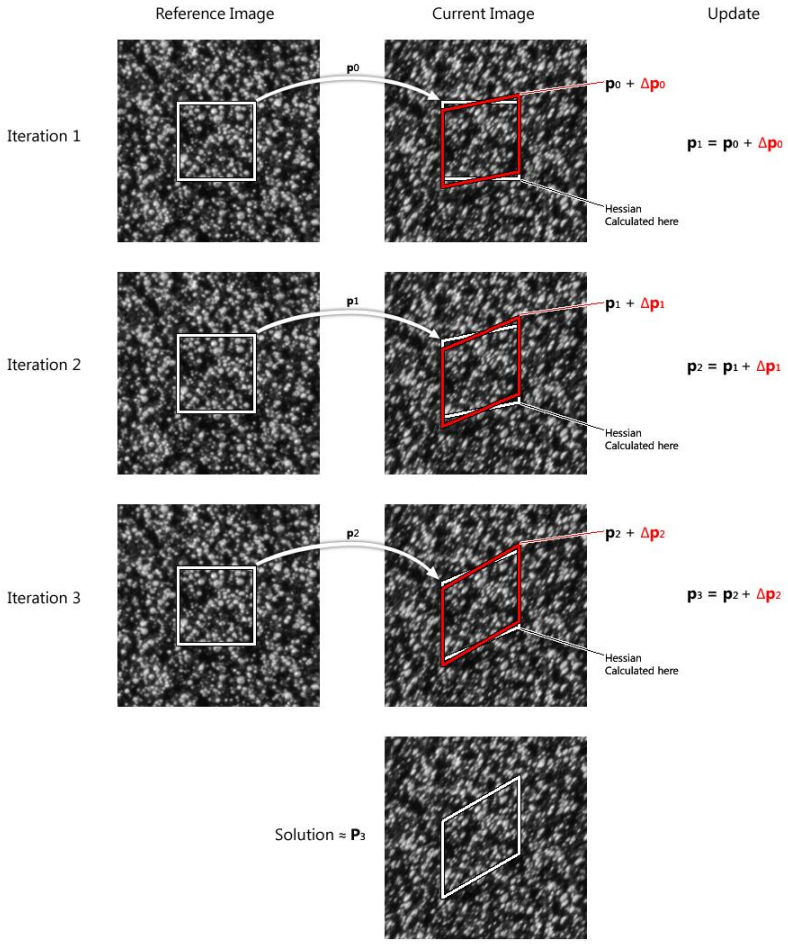

This is a graphical representation of the FA-GN method for image alignment. The reference image has a shear applied to it. The most important thing to note here is where the hessian is evaluated at the current image for every iteration. This quantity is the computational bottleneck of the algorithm and provides good insight to understanding the effectiveness of the IC-GN method.

Inverse compositional method

The act of doing this determines the direct transformation from the final reference subset to the final current subset. A graphical figure is shown below:

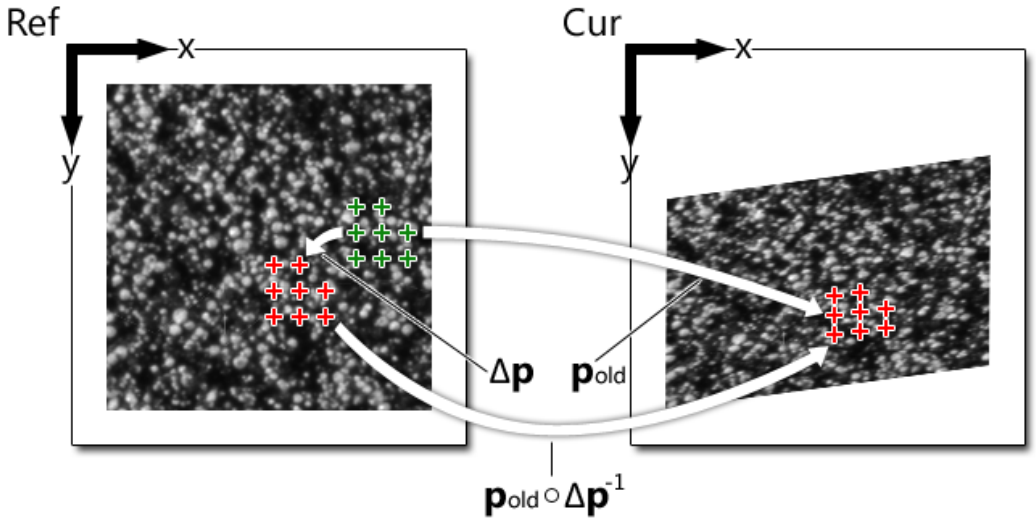

This a graphical representation of the inverse compositional update. p_{rr} is equal to Δp and p_{rc} is equal to p_{old}. As long as the translational component of Δp is small in magnitude, the composition of p_{old} and the inverse of Δp should be closer to than p_{old}. A detailed description is shown in Ncorr website.

Appendix-D

Shannon entropy

Entropy gives a statistical measure of randomness, which can be used to depict the texture of the image. Shannon entropy is given by the formula

Entropy= -sum (p.*log2 (p))

Here, p corresponds to the normalized histogram counts.

Shannon entropy can be used for global image assessment. An image with a high Shannon entropy needs a greater amount of ‘bits’ to form an adequate representation of a digital image. Higher entropy indicates broadness in grey scale distribution, high level of texture which are beneficial for maximizing the correlation peak for obtaining a correct match. The Shannon entropy for QR code printed pattern and randomly marked pattern is evaluated to be 6.343 and 6.211 respectively for the same spatial resolution. This implies that image correlation with QR code printed pattern produces lesser computational errors compared to the randomly marked pattern.

For both QR and Random speckle patterns, we adopted Ncorr software for analyzing the patterns. The size of the QR code is 150 mm by 150 mm, which was sprayed on the flexural portion of the beam. The minimum radius of the subset considered in this study is 1.5 mm escribed circle with a step size of 1.5 mm up to 21 mm (as there was no significant difference in the results after 18 mm until 21 mm). The optimal radius of subset was found to be 13 mm with a subset spacing of 6 based on the results obtained, which are in good agreement with conventional measurement technique (LVDTs/dial gauges).

Appendix-E

Training and Simulated Test Data Generated from 200 Random Samples

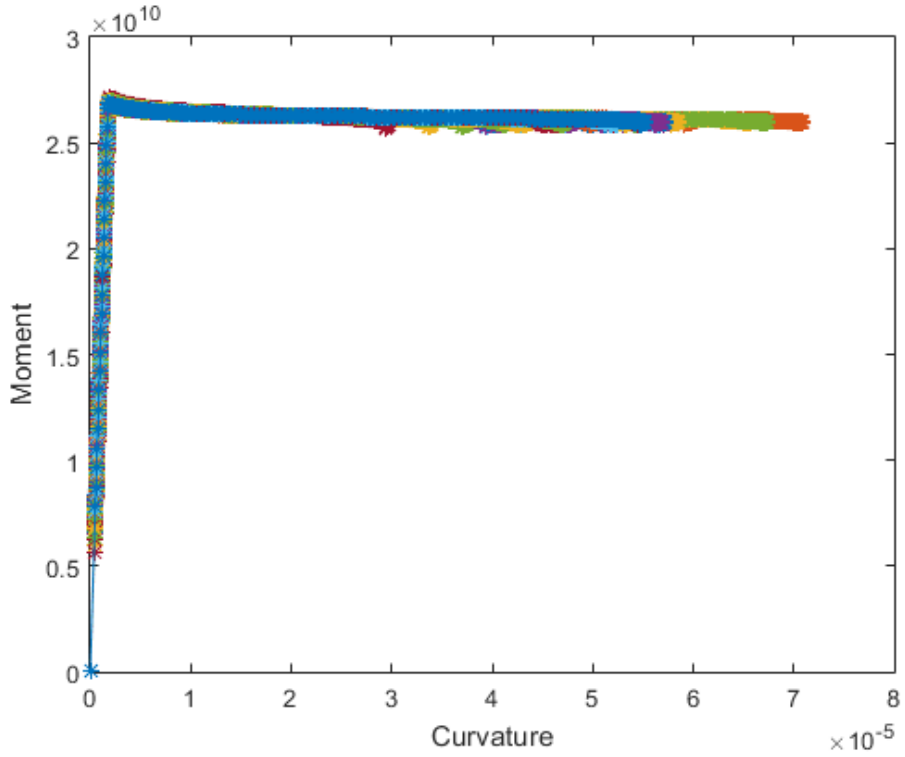

Figure E-1 Prediction of M-κ curves for standard MoRTH bridge girders of 24 m span 1 using MATLAB

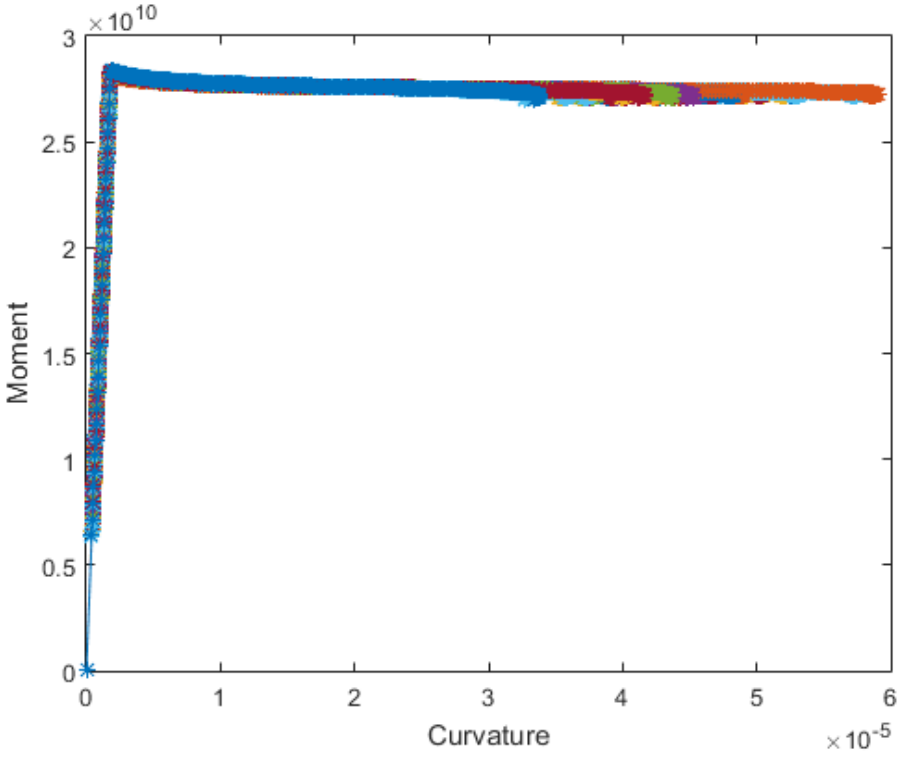

Figure E-2 Prediction of M-κ curves for standard MoRTH bridge girders of 24 m span 2 using MATLAB

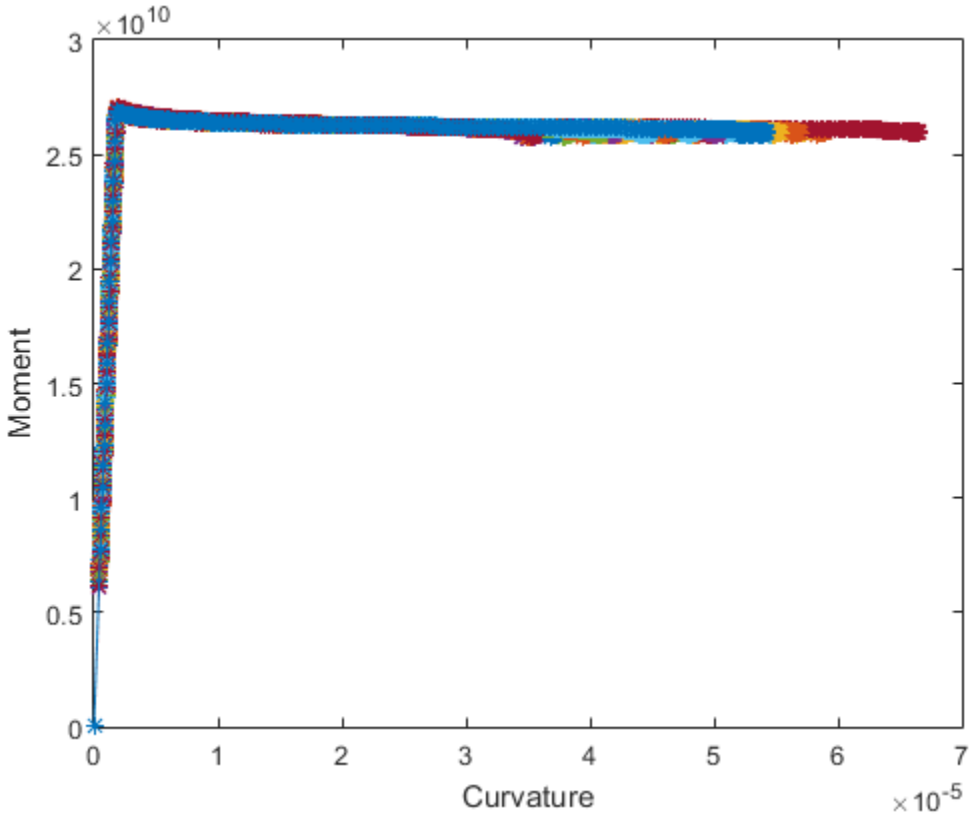

Figure E-3 Prediction of M-κ curves for standard MoRTH bridge girders of 21 m span 1 using MATLAB

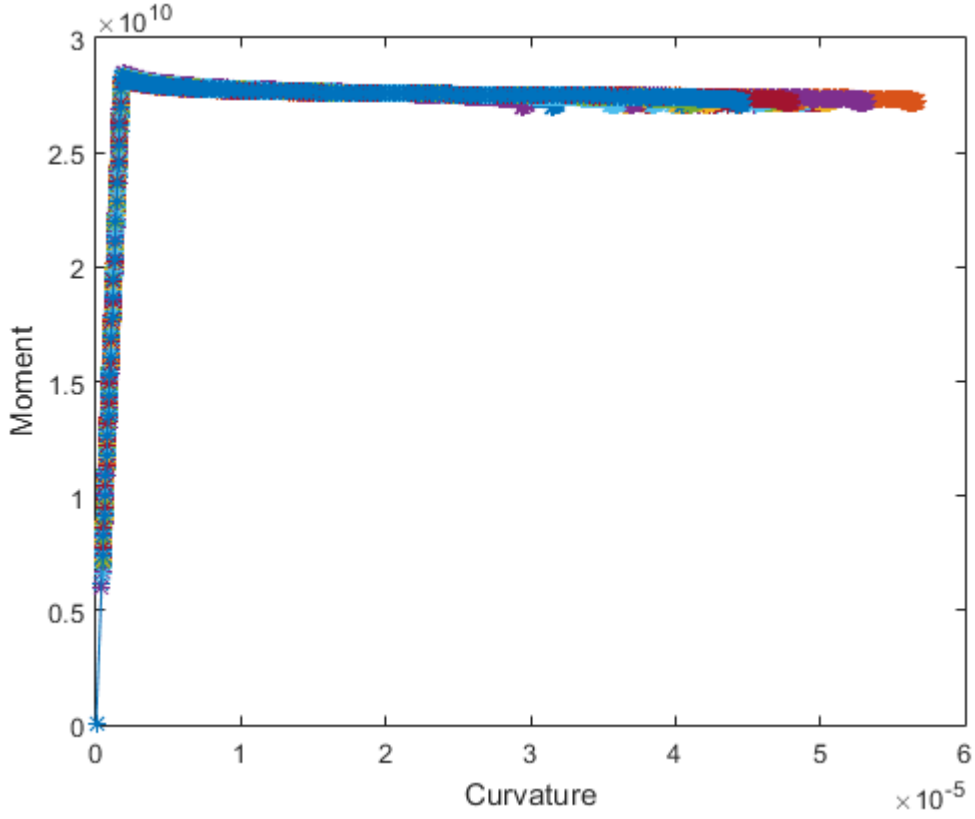

Figure E-4 Prediction of M-κ curves for standard MoRTH bridge girders of 21 m span 2 using MATLAB

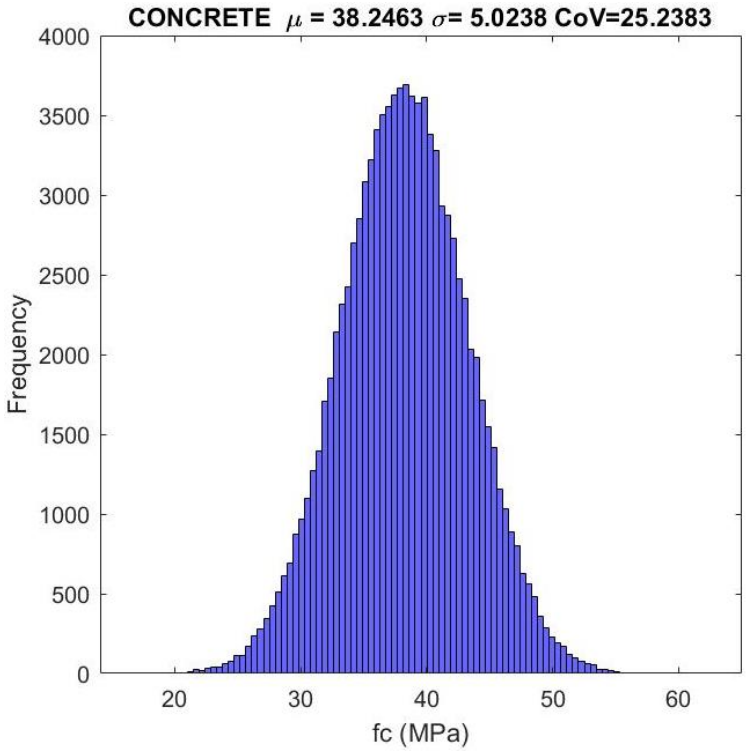

Figure E-5 Statistical distribution of compressive strength for M-30 concrete

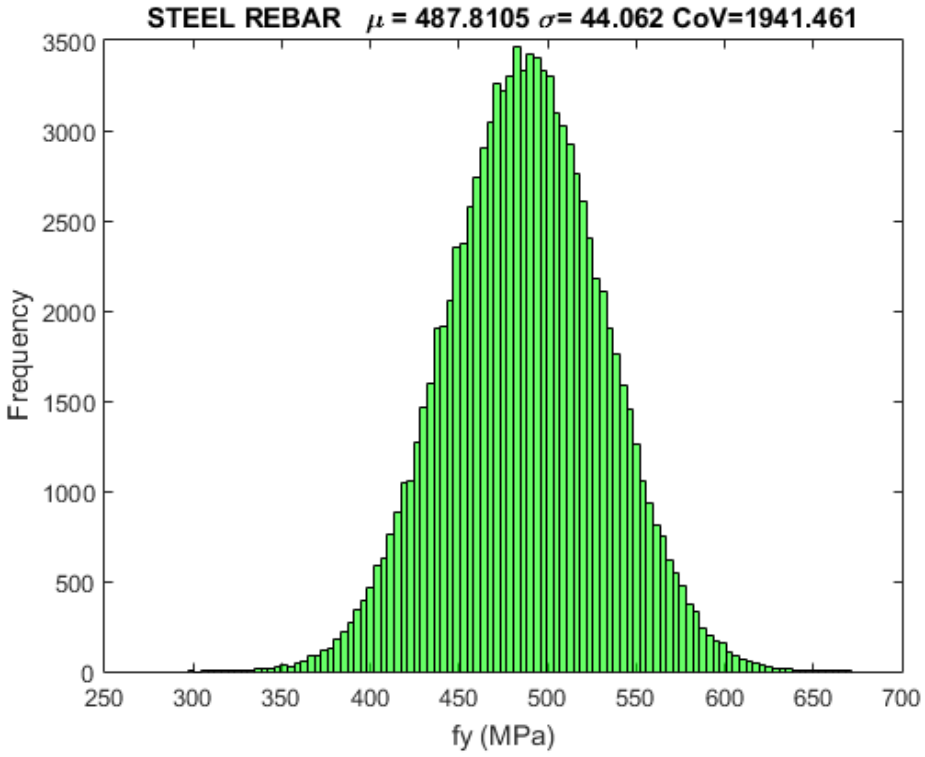

Figure E-6 Statistical distribution of yield strength for Fe-415 rebar steel

Training and Test Data Sets for 222 Samples are incorporated in the attached CD copy along with the thesis.

Appendix-F

Properties of QR code based speckle pattern

The optimal size of the QR pattern depends upon several factors like:

a) Distance from the target
b) Optical zoom Lens
c) Resolution of the camera
d) Size of the component to be monitored

Based on the above parameters one can calculate the size of the speckle as shown below.

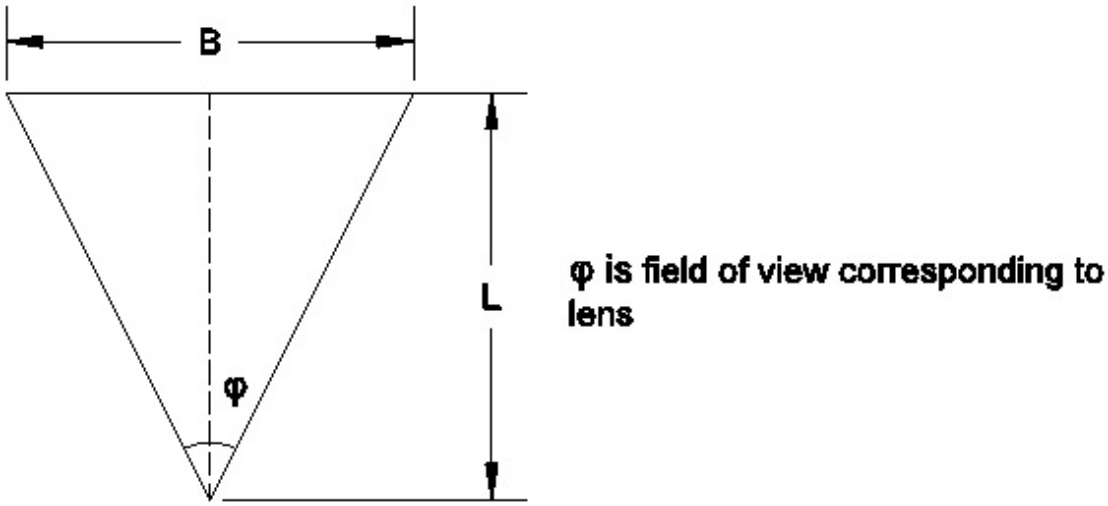

Figure F-1 Field of view for monitoring the structure

For example, using nikon field of view simulator for the camera model AF-S DX NIKKOR 18-55mm f/3.5-5.6G VR the angle of view for 18mm lens is 76° 10' and for 55mm lens is $28^{o}\ 50^{1}$ (https://imaging.nikon.com/lineup/lens/simulator).

i. $\frac{B/_2}{L} = \tan \theta/_2$

ii. No. of pixels = 6000 (width) x 4000 (depth) = 24 Mega Pixels

Therefore minimum pixel size @ L $_{meter}$ = $\frac{B}{6000}$

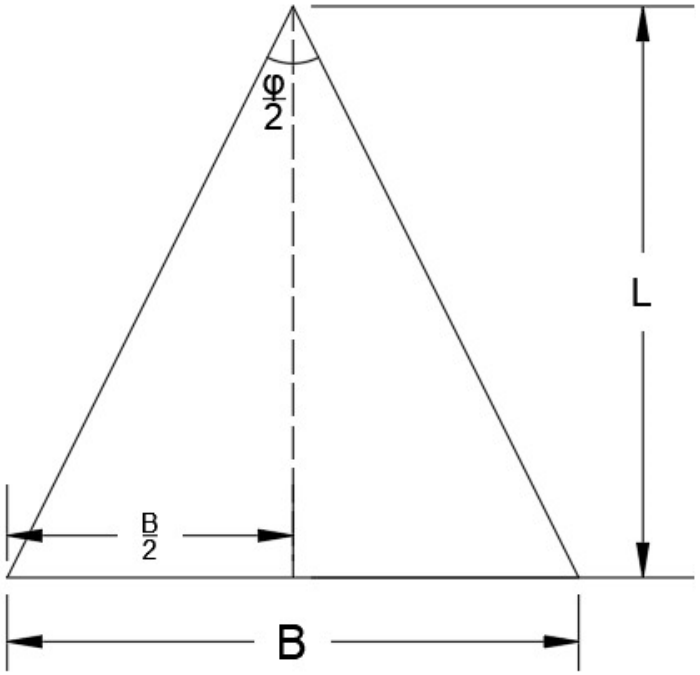

Table F-1 Properties of QR code based speckle pattern

Zoom Lens Type :	**AF-S DX NIKKOR 18-55mm f/3.5-5.6G VR**			**AF-S DX NIKKOR 18-140 mm F/3.5-5.6 G ED VR**
Focal length	18 mm	55 mm	55 mm	140 mm
Distance from camera	2 m	2 m	100 m	100 m
Field of view (θ)	76° 10'	28° 50'	28° 50'	11° 30'
Pixel size (mm)	0.522	0.171	8.568	3.356
Minimum speckle size (3 x Pixel size) (mm)	1.567	0.514	25.706	10.069
Min. Dimension of (n x n) QR pattern = (Min. Speckle size) x n (mm)	45.450	14.909	745.492	292.01

Multi-Scale Speckle Pattern

Innovation in this thesis work is to develop a multi-scale QR speckle pattern that can capture both local and global deformations. Speckle size, shape, and density heavily influence the randomness of a speckle pattern. Typically, in random speckle patterns, the smaller speckles are more similar in shape, and larger speckles have a greater number of shapes, uniquely defined within the pattern. There is a constraint on maximising the uniqueness, which is the number of speckles in a subset.

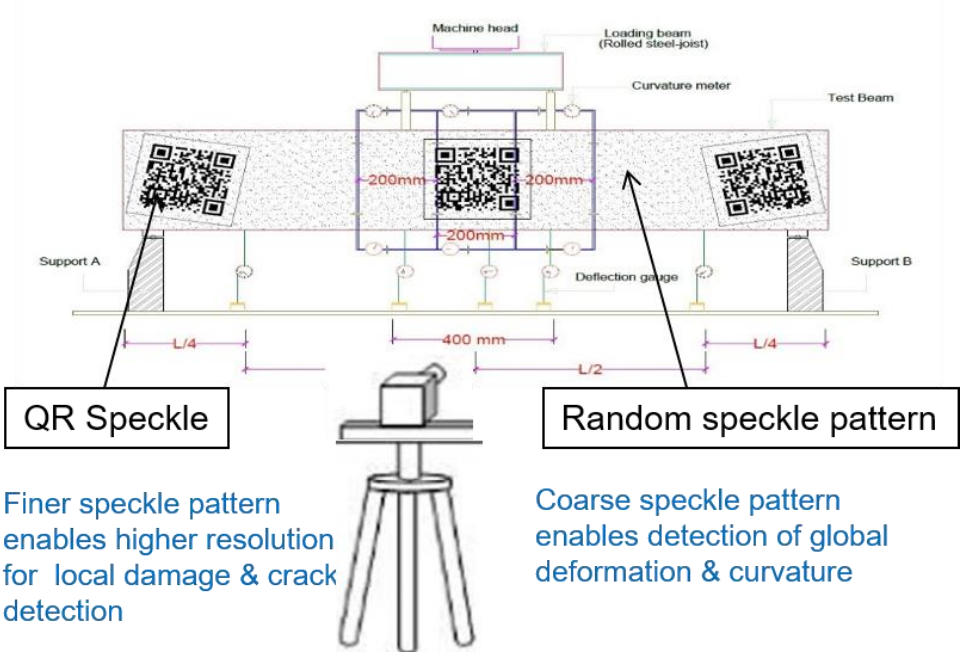

Figure F-2 Multi-Scale speckle pattern

Case-1: ***When structure is accessible***

In order to monitor full-scale structures from a short distance, there is no requirement to enlarge the multi-scale QR pattern. In this case, each pattern is representative of a particular critical region of the structure. A high level of unique features reduces the uncertainty in matching, thereby increasing the accuracy.

Case-2: ***When structure is not accessible***

In order to monitor full-scale structures from a significant distance (~ 100 m), the multi-scale QR pattern need not be enlarged. The larger position markers as well as alignment markers, serve the purpose of speckles at a large distance.

Appendix-G

Details and formulations used in Ncorr V1.2.2 MATLAB tool stepwise procedure

To load the images into Ncorr GUI, one of the ways to load reference images is to do it through the MATLAB terminal. The reference image can be set up by typing "handles_ncorr.set_ref" (data). The reference image will be stored here as an array. By following the above step, it will be convenient to load it directly than to save it, but there are few problems associated with it. Finally, when the reference image is loaded, it will appear as shown below.

Note: The reference image can also be called an unstrained image.

If this is the case, Ncorr has most likely installed correctly, and the installation should be completed. The next time you open MATLAB, you can open Ncorr again by typing" handles_ncorr=ncorr" into the MATLAB terminal, and the GUI should appear without having to repeat the installation process. If the installation proceeded correctly, then you can go to the user guides in section 2.

The other way to load a reference image is to do it through the MATLAB terminal. You can set the reference image by typing "handles_ncorr.set_ref (data)," where "data" is a 2D matrix (of type double, uint16, or uint8) containing image grayscale values, as shown below:

Loading Reference Image and current images

This feature is provided because sometimes the reference image is obtained through a series of images, which are averaged together or processed in some way. If this is the case, the reference image will be stored as an array in the base workspace, and it is much more convenient to load it directly than to save it as an image, which can also lead to loss of data through image compression or binning of grayscale values. Lastly, when the reference image is loaded, it should appear as shown below:

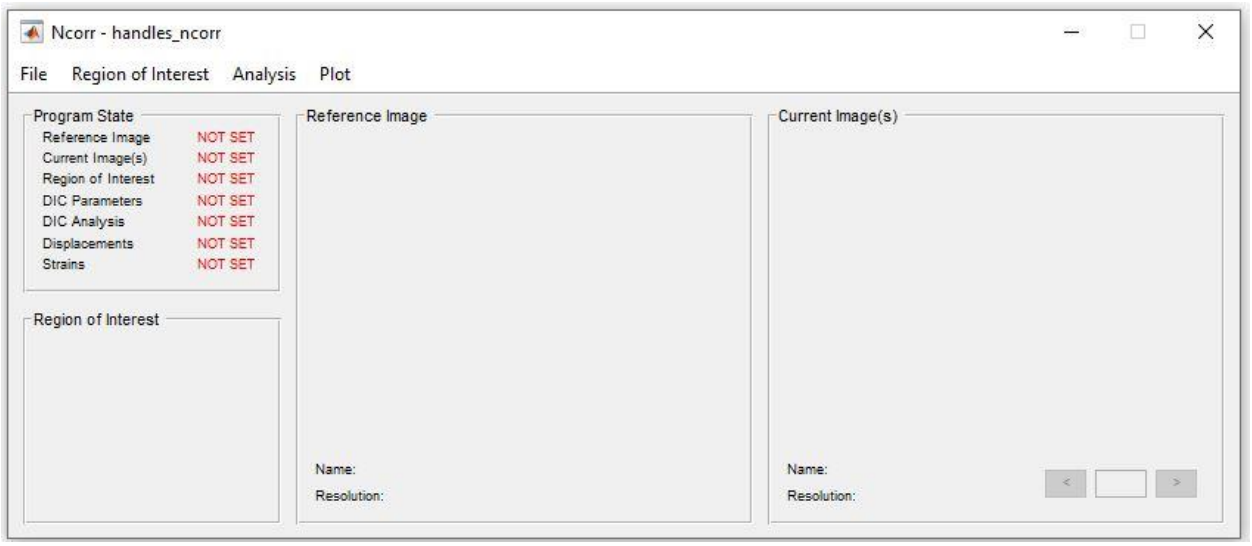

There are two ways to set the reference image. The first way is to use the Ncorr GUI by the following steps.

Go to File > Load reference image. The result is shown in the below image.

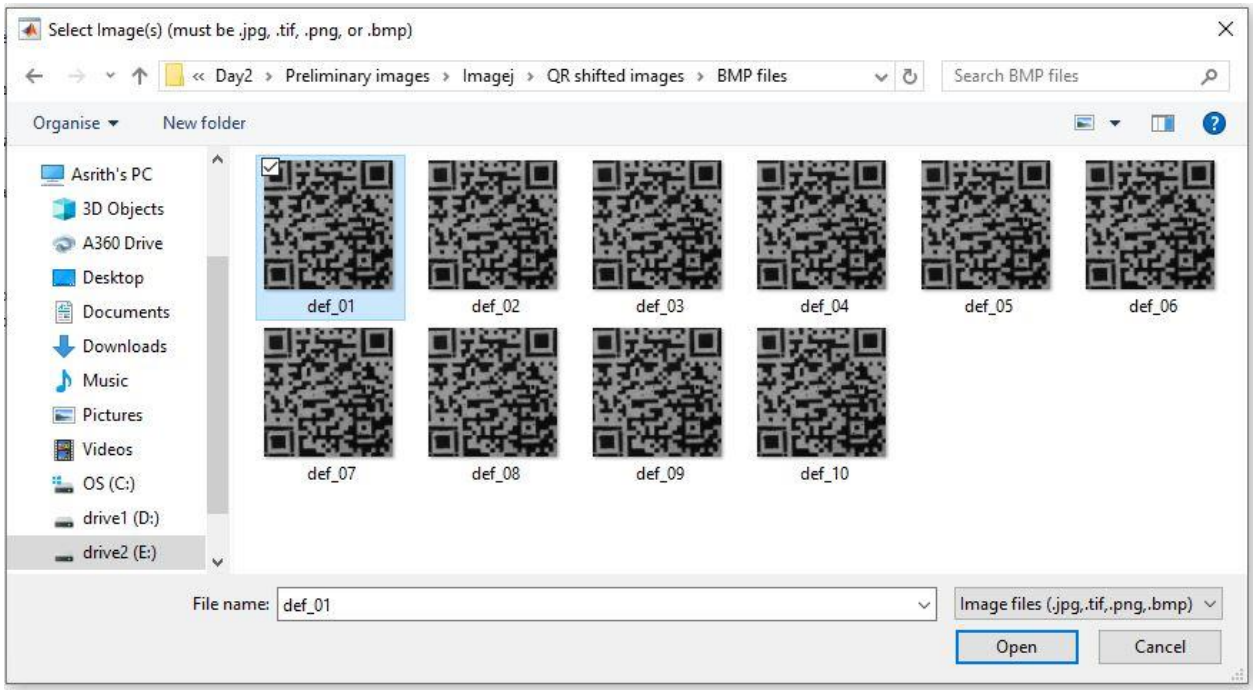

Next step is to select the very first image among the above images.

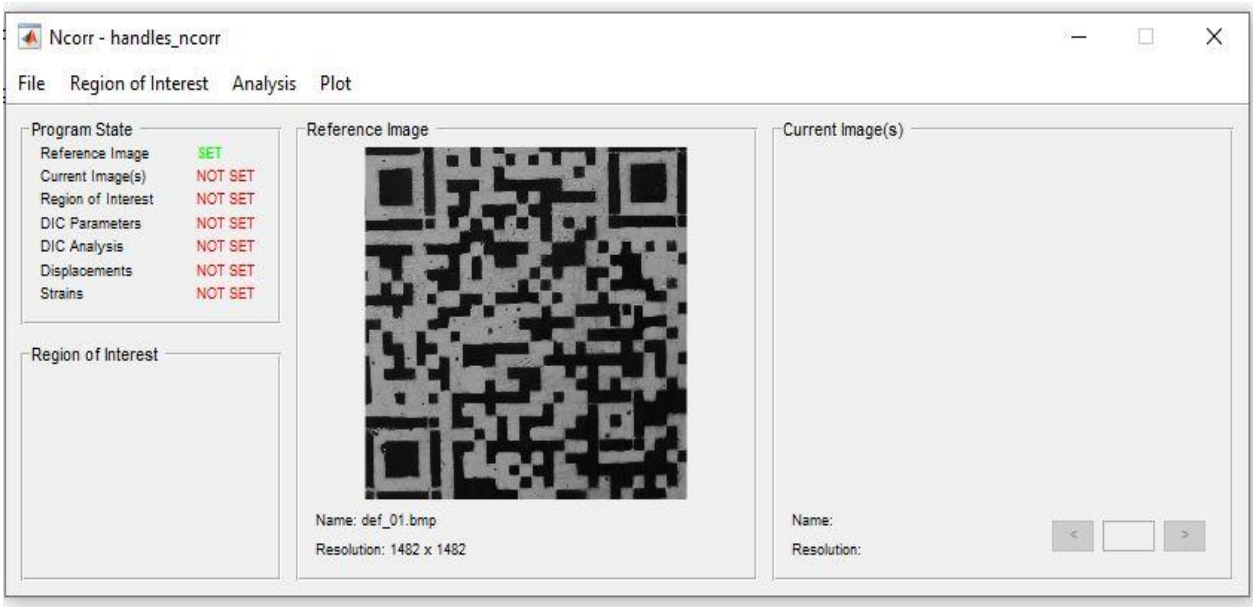

When loading through the GUI, the following window must appear.

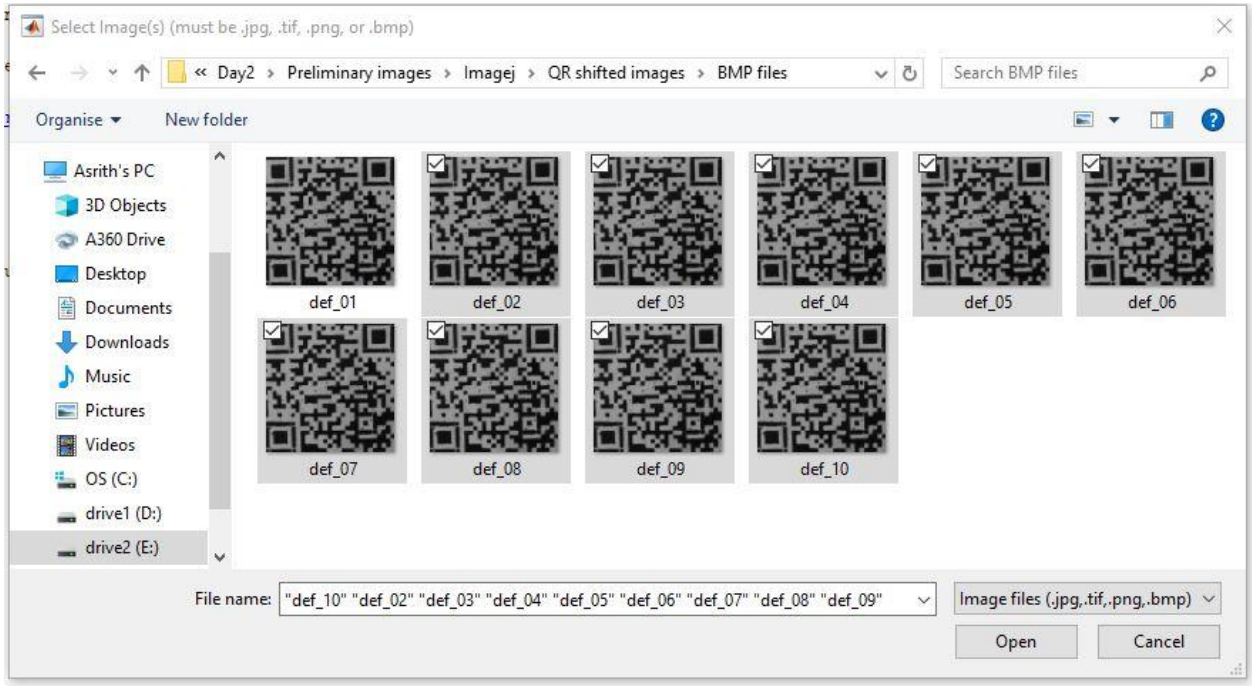

The present images should be kept in order according to their numbers, and the last image in the sequence will appear initially by default. It's a good check to ensure the order accuracy.

The current images should be appropriately ordered according to their number, and the last image in the sequence will appear initially by default. It's a good check to scroll through them to ensure the order is correct.

Start by setting the reference image to the first image of the set. Next, load the current images by using "Lazy Load". Finally, set the reference ROI to the ROI given in the image set. If successful, then GUI should appear as shown below. Also, in the program set, reference image, current image options will be highlighted as "SET".

Draw Region of Interest (ROI):

Region of Interest is the part on the specimen (specimen can be a bar, beam, cable, etc.) where the parameters such as strain, displacement, angular distortions etc. are evaluated. This size of ROI may vary depending on the type of specimen.

The second way to set the ROI is to draw the ROI directly in MATLAB by using region of interest> set reference ROI> Press "Draw ROI option. This is the preferred method for preliminary analysis because it can be done quickly. An example ROI is shown below and was constructed using "+Poly" followed by "-Ellipse," where the "+" prefix indicates adding portions to the ROI; "-"subtracts regions:

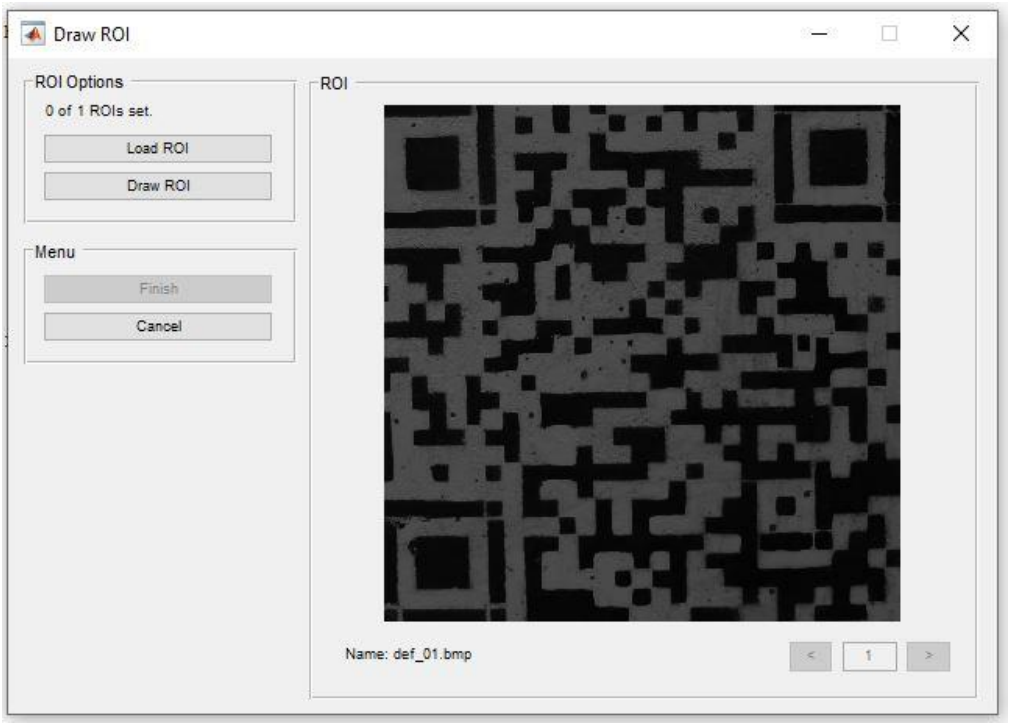

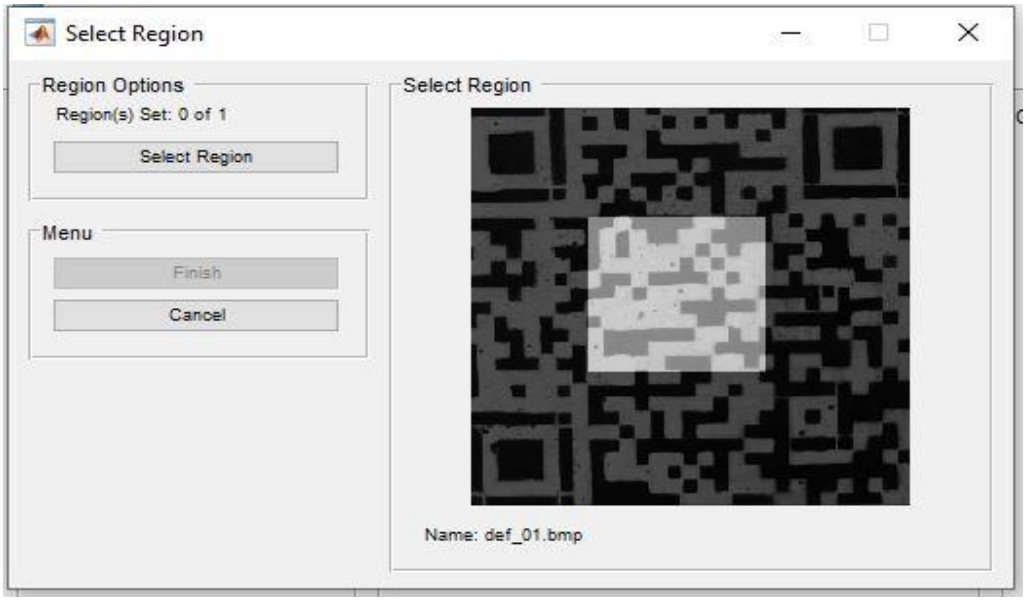

Next step is to select "region" in the image obtained in GUI.

To get better precision when drawing ROI's, various drawing options like +rec, -rec etc. are available in draw ROI window. In addition, zoom pan is available to zoom in or zoom out of the image.

After setting ROI, a region of interest option will be highlighted as SET.

Setting DIC Parameters

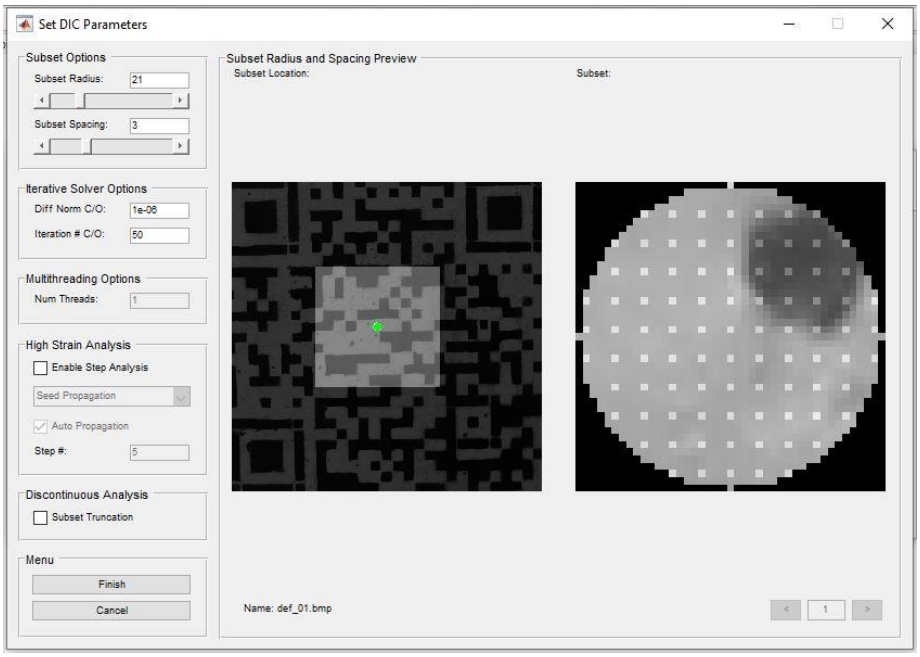

Next step is to set DCI parameters. Put subset radius as 21, subset spacing as 3, a number of iterations can also be chosen as per the requirement. A green point is placed in the axes labelled "subset Location", which is draggable and is the centre point of the subset shown on the right side. This highlighted point is the position where the centre of the subset is located.

There are several key components to this GUI. The first is obviously the menus on the left, but it is also important to note that the subset preview is interactive. A green point (highlighted by a red square) is placed in the axes labelled "Subset Location." This point is draggable and is the centre point of the subset shown on the right. The subset on the right gives an idea of what the subset spacing (space between the two dots within the red squares) and subsets will appear like. It's important to note that these highlighted points are where the subset locations will be, and not part of the speckle pattern in the uploaded image.

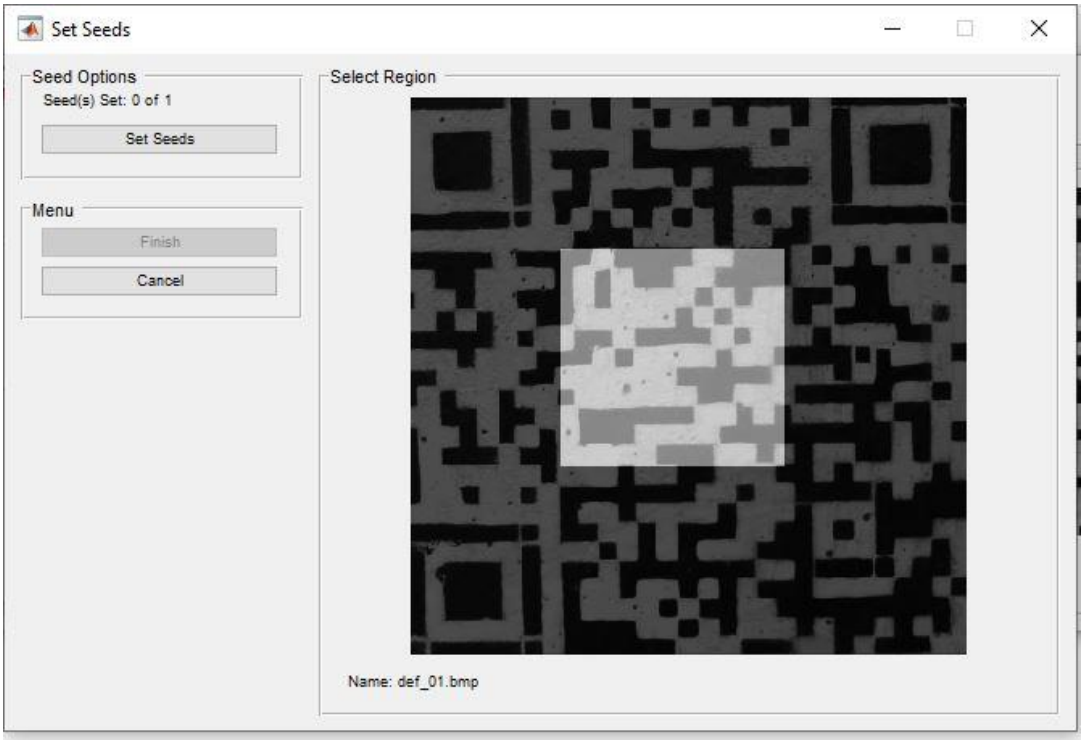

Now set seeds by clicking set seeds options on the right side.

In the program state, DIC analysis will be highlighted as SET.

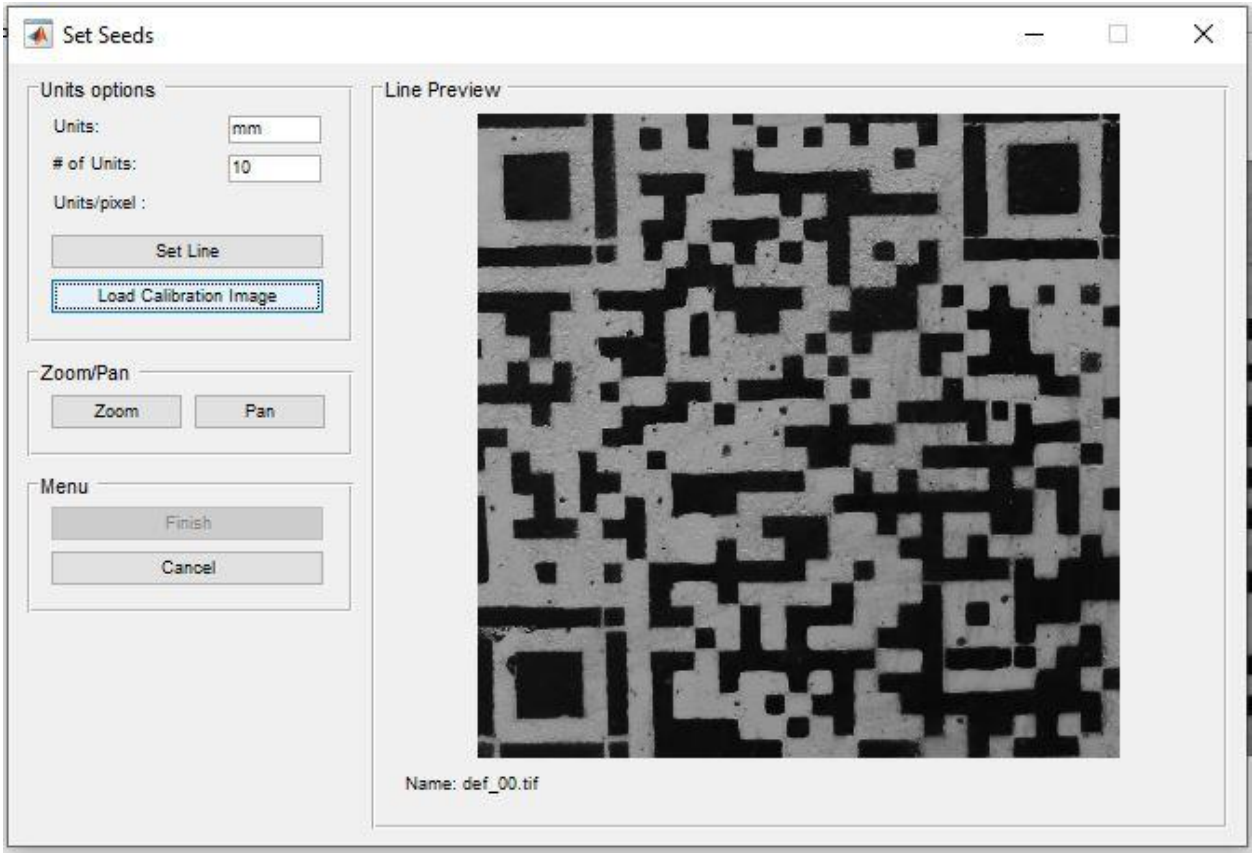

Unit options: Now open set seeds and then set up the units as mm, number of units as 10, and then select load calibration image. A line preview of the image is shown on the left side, i.e., GUI. These options are used to convert the displacements from pixels to real units. These options are used to convert the displacement from pixels to real units. You can either input the value directly if you know it, or you can click the "Get Unit Conversion" button in order to load an image with a known dimension. Most tests are done with a regular camera on a sample, so the easiest way to take advantage of this feature is to, after the experiment incomplete, replace the sample with a ruler so you can measure what the unit conversion is. An example of the GUI is shown below:

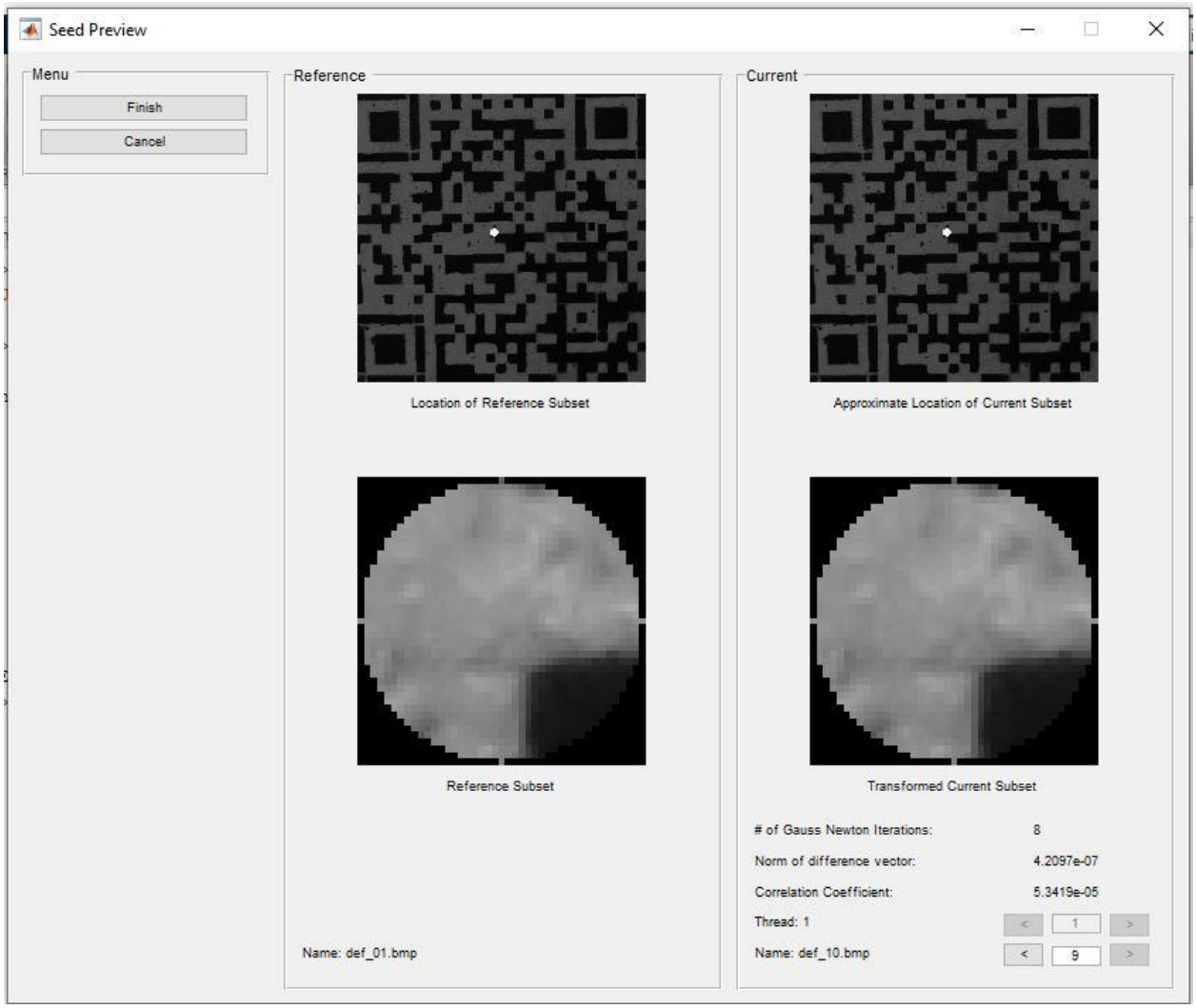

Notice that all the seed locations in the reference image seem to match appropriately with the locations in the current image. The reference subset and transformed the current subset look very similar. Lastly, Correlation coefficient, number of iterations are obtained below the image, and the low value of Correlation coefficient implies a good and correct seed placement.

After completion of the analysis, we can view the corresponding results, as shown above.

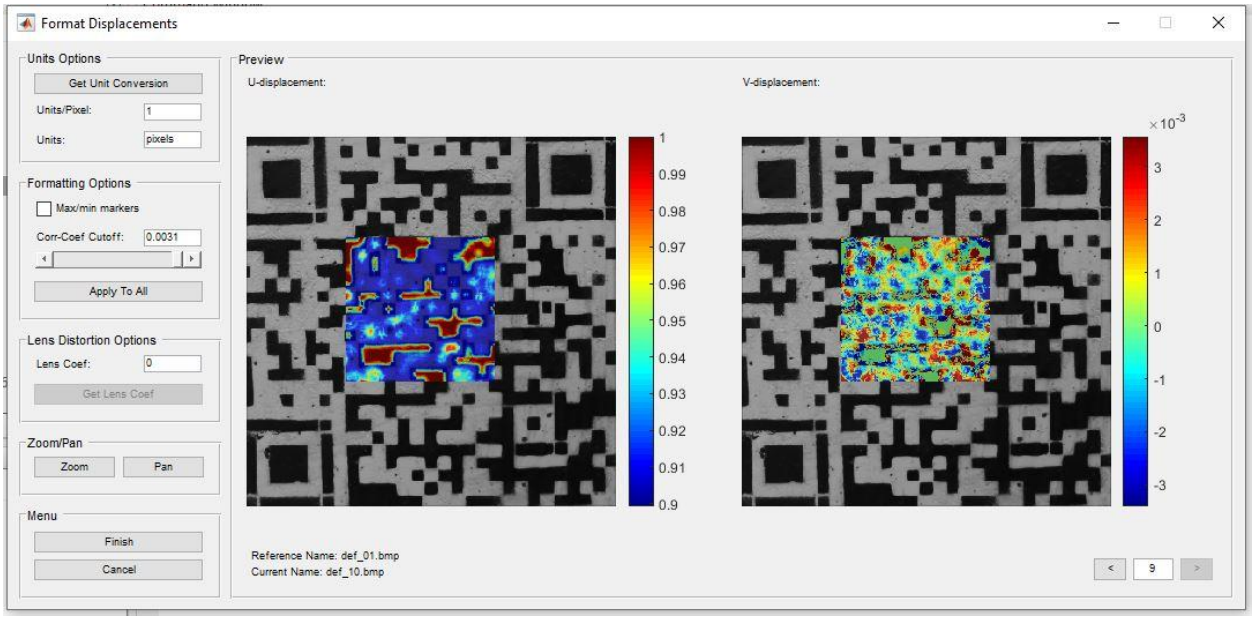

After following all the above steps, the above image will be obtained. This shows a preview of U-displacement, V-displacement. U displacements are displacements in horizontal and V-displacement are displacements in the vertical direction.

Plotting the results:

Strain options: Now set strain parameters like strain radius as 15, choose Lagrangian with U-displacement as the option. The only parameter you can vary here is the strain radius. This is the radius of a circle, which selects a group of points to fit a plane to. A preview is provided so the user can visualise the plane fitting. The selection of the ideal strain radius is similar to the selection of the ideal subset radius, in that the smallest radius is desired, which does not result in noisy strain data. The default radius is set to 15, but it is up to the user to select the most optimal radius for their data.

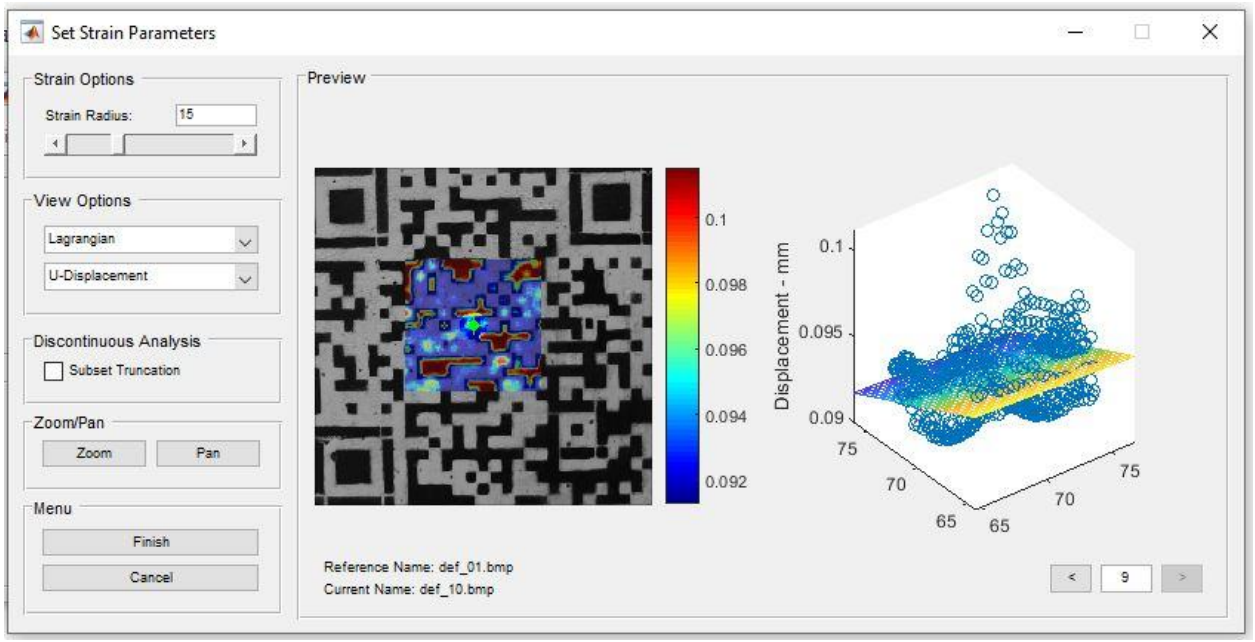

At this point, strains have been calculated. Plotting can be achieved by choosing plot> view displacement plots> view strain plots options in the main Ncorr GUI. This is the last step of the analysis.

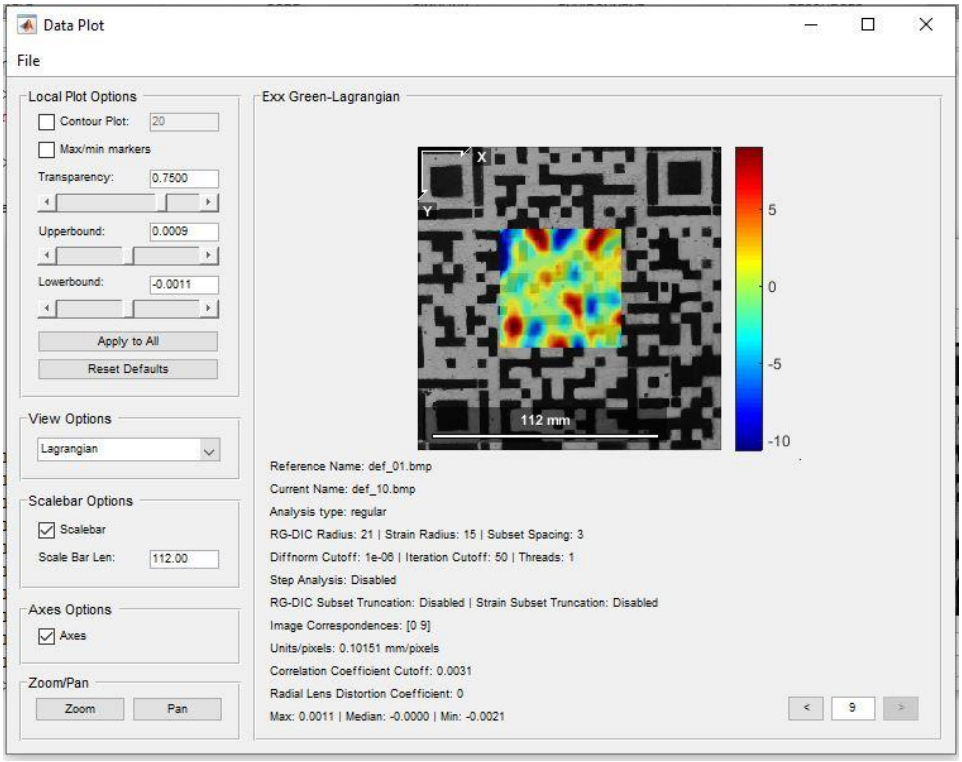

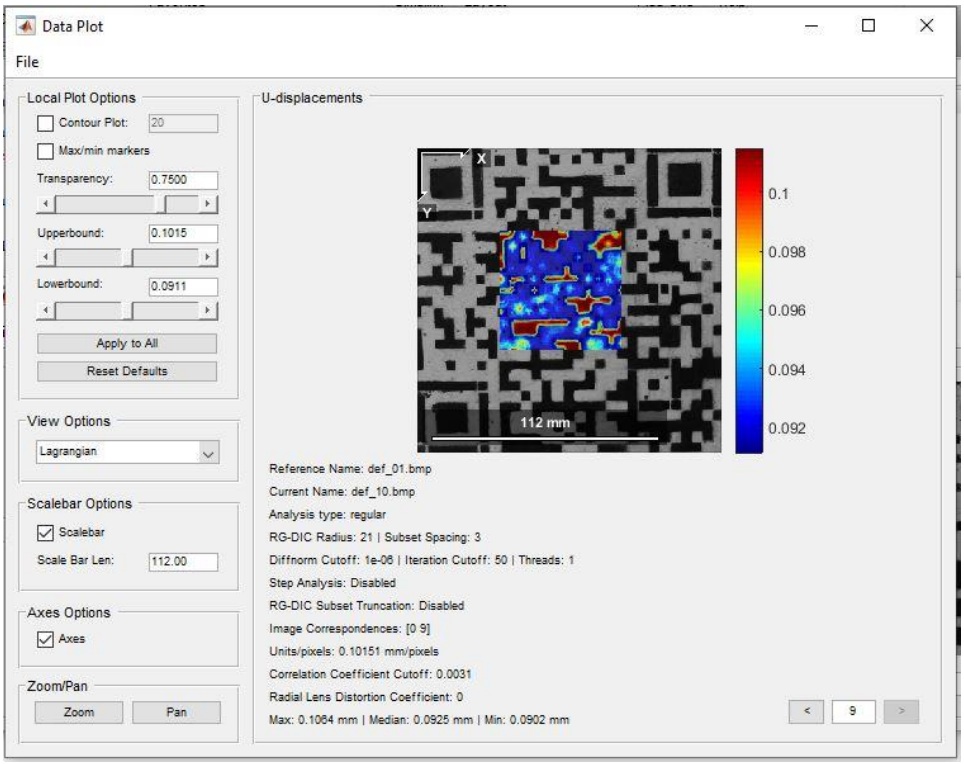

From the above image, the data plot for E_{xx} green Lagrangian and U-displacements are obtained and shown in the Ncorr GUI.

Publications Related to the Work

International Journals:

1. Krishna, B. M., Tezeswi, T. P., Kumar, P. R., Gopi Krishna, K., Siva Kumar, M. V. N., & Shashi, M. (2019). "QR code as speckle pattern for reinforced concrete beams using digital image correlation". In *Structural Monitoring and Maintenance*, vol. 6, no. 1, pp. 67-84. DOI: https:// doi.org/10.12989/smm.2019.6.1.067.
2. Krishna, B. M., Reddy, V. G. P., Shafee, M., & Tadepalli, T. (2020, February). "Condition assessment of RC beams using artificial neural networks". In *Structures* (vol. 23, pp. 1-12). Elsevier. https://doi.org/10.1016/j.istruc.2019.09.014.
3. Krishna, B. M., Reddy, V. G. P., Tadepalli, T., Kumar, P. R., Lahir Y. (2019). "Numerical and experimental study on flexural behavior of Reinforced Concrete beams: Digital Image Correlation approach". In *Computers and Concrete*, vol. 24, no. 6, pp. 561-570, Techno press. DOI: https://doi.org/10.12989/cac.2019.24.6.561.

National Conference:

1. B.Murali Krishna, T.P.Tezeswi, Y. Lahir, "Digital image correlation-based performance assessment of structural components" Proceedings of the 11th *Structural Engineering Convention* - 2018 Jadavpur University, Kolkata, India, December 19th-21st (2018); Paper No. 20180411, SHM Page no (44-50).